N° d'ordre : **40649**

UNIVERSITE LILLE 1 – SCIENCES ET TECHNOLOGIES

ECOLE DOCTORALE SCIENCES POUR L'INGENIEUR

THESE

présentée par

Bianca DE CARVALHO PINHEIRO

pour l'obtention du

TITRE DE DOCTEUR EN MECANIQUE

intitulée

ETUDE PAR DIFFRACTION DES RAYONS X DES MODIFICATIONS MICROSTRUCTURALES EN COURS DE FATIGUE

Soutenue **le 25 novembre 2011** devant le jury d'examen :

Directeur de thèse : **Jacky LESAGE**, Professeur, Université Lille 1

Co-encadrant : **Noureddine BENSEDDIQ**, Professeur, Université Lille 1

Rapporteurs : **Eli Saul PUCHI-CABRERA**, Professeur, Université Centrale du Venezuela (Caracas)
Jean-Louis ROBERT, Professeur, Université Clermont-Ferrand 2

Membres : **Ilson PARANHOS PASQUALINO**, Professeur, Université Fédérale de Rio de Janeiro
Edoardo BEMPORAD, Professeur, Université de Rome TRE

Titre en Français :

ETUDE PAR DIFFRACTION DES RAYONS X DES MODIFICATIONS MICROSTRUCTURALES EN COURS DE FATIGUE

Résumé :

Le travail présenté ici a pour but d'évaluer les mécanismes microstructuraux liés à l'amorçage de l'endommagement par fatigue d'un acier à usage pétrolier. Les microdéformations et les contraintes résiduelles (macrocontraintes) ont été déterminées par diffraction des rayons X en temps réel pendant des essais de fatigue en flexion alternée sur des éprouvettes plates prélevées dans la paroi d'un tube neuf. Les microdeformations sont estimées à partir de mesures de la largeur de corde à mi-hauteur (LCMH) d'un pic de diffraction et les contraintes résiduelles à partir du déplacement du pic. Les essais de fatigue sont réalisés pour cinq niveaux de contraintes différents. On observe trois stades de variation pendant l'évolution des microdeformations. On montre que leur amplitude et leur durée sont proportionnelles au niveau de contrainte alternée. Des variations similaires sont observées pour les contraintes résiduelles, avec des durées identiques à celles des microdéformations. Des évolutions dans la densité et la répartition des dislocations ont été observées par microscopie électronique en transmission à l'aide de la technique du faisceau d'ions focalisés. Pour comprendre le rôle de la structure initiale, des essais de fatigue sur éprouvettes recuites ont été réalisés dans les mêmes conditions d'essai. Là encore trois stades d'évolution sont observés mais avec un premier stade inversé du fait de l'état initial du réseau de dislocations. Les résultats obtenus sont très encourageants pour la prise en compte des évolutions microstructurales dans l'établissement d'un futur indicateur de dommage de la phase d'amorçage en fatigue à grand nombre de cycles des matériaux.

Mots-clés :

Fatigue ; Fatigue à grand nombre de cycles ; Amorçage de l'endommagement par fatigue ; Diffraction des rayons X ; Largeur de corde a mi-hauteur ; Microdéformations, Contraintes résiduelles ; Acier API 5L X60 ; Pipelines

Title in English:

X-RAY DIFFRACTION STUDY OF MICROSTRUCTURAL CHANGES DURING FATIGUE

Abstract:

The present work aims to evaluate the microstructural mechanisms associated with the initiation of fatigue damage of steels used in the petroleum industry. Microdeformations and residual stresses (macrostresses) were evaluated by X-ray diffraction in real time during alternating bending fatigue tests performed on flat test pieces taken from a pipe sample. Microdeformations were estimated from measurements of the full width at half maximum (FWHM) of the diffraction peak and residual stresses from the peak displacement. The fatigue tests were performed at five different stress levels. Three stages of changes during the evolution of microdeformation were detected. We show that their amplitude and duration are proportional to the level of alternating stress. Similar variations were observed for the residual stresses, with duration identical to those of the microdeformation. Changes in the density and distribution of dislocations were observed by transmission electron microscopy using the technique of focused ion beam. To understand the role of the initial structure, fatigue tests on annealed samples were performed under the same test conditions. Again, three stages of changes are observed but with an increase of the microdeformations instead of a decrease during the first stage due to the initial state of the dislocation network. The results are very encouraging for the consideration of the microstructural evolutions in the construction of a future counter of fatigue damage initiation in materials.

Keywords:

Fatigue; High cycle fatigue; Fatigue damage initiation; X-ray diffraction; Full width at half maximum; Microdeformations; Residual stresses; API 5L 60 grade steel; Pipelines

Laboratoire :

Laboratoire de Mécanique de Lille, LML URM 8107

Boulevard Paul Langevin

59655 VILLENEUVE D'ASCQ Cedex

FRANCE

Résumé en français étendu :

Les tubes utilisés pour le forage et l'exploitation pétrolière (pipelines), généralement fabriqués en aciers à haute résistance (tels que les aciers API 5L grades X60, X80 et X100, par exemple), sont soumis à des sollicitations cycliques qui peuvent provoquer leur rupture par fatigue. Outre les aspects financiers, celle-ci peut s'accompagner de graves dommages environnementaux. Pour assurer leur intégrité structurale et prévenir une rupture par fatigue, il est impératif de détecter et suivre l'endommagement par fatigue pendant leur usage.

L'endommagement par fatigue peut être divisé en deux phases : (1) une première phase d'incubation, pendant laquelle seules les évolutions microstructurales, la nucléation de microfissures et la microfissuration peuvent être observées ; (2) et une seconde phase de fissuration et propagation macroscopique, pendant laquelle l'identification et la quantification de l'endommagement du matériau peuvent être obtenues plus facilement. De ce fait, cette dernière phase a été largement étudiée ces dernières années, résultant de la proposition de différentes approches pour modéliser la propagation d'une fissure, comme la loi de Paris, par exemple, et d'un certain nombre de critères d'endommagement par fatigue concernant cette phase. En revanche, l'étude de la première phase est plus complexe, dès lors que l'endommagement par fatigue et les évolutions microstructurales ne peuvent pas être simplement dissociés. Pourtant, pour être physiquement fondé, un critère de fatigue doit nécessairement s'appuyer sur une approche locale, à l'échelle des dislocations, et prendre en compte les micromécanismes d'endommagement cyclique (microdeformations et évolutions microstructurales), qui précédent la fissuration macroscopique conduisant à la rupture.

Parmi les techniques de contrôle non-destructif (CND) disponibles pour l'évaluation des modifications microstructurales pendant la phase d'amorçage de l'endommagement par fatigue, la diffraction des rayons X, par l'étude de l'état du réseau des dislocations, se révèle l'outil d'analyse le mieux adapté. La technique de diffraction des rayons X renseigne sur l'état du réseau des dislocations et permet l'étude des évolutions microstructurales de l'endommagement, comprenant les microdeformations et les contraintes résiduelles (macrocontraintes). Durant ces dernières années, quelques auteurs ont étudié l'endommagement par fatigue par diffraction des rayons X. Bien que certaines de ces études soient parvenues à l'identification des modifications microstructurales en cours de fatigue, elles n'offrent pas de résultats quantitatifs en termes de sécurité et de prévision de la durée de vie avant fissuration macroscopique.

Le travail présenté ici a pour but d'évaluer et de quantifier les mécanismes microstructuraux liés à l'amorçage de l'endommagement par fatigue de l'acier API 5L X60 en vue du développement d'un indicateur de dommage de la phase d'amorçage en fatigue à grand nombre de cycles qui pourrait permettre une bonne prévision de la durée de vie résiduelle, avant fissuration macroscopique, et d'augmenter la fiabilité des pipelines sollicités en fatigue.

Des éprouvettes plates prélevées dans la paroi d'un tube neuf fabriqué en acier API 5L X60 ont été soumises à des essais de fatigue en flexion alternée. Les essais de fatigue ont été réalisés selon cinq niveaux de contraintes alternées différents, comprenant quatre chargements avec un rapport de contrainte R = -1 et un chargement avec R = -2.8. Au moins trois essais ont été réalisés pour chaque niveau de chargement. Les microdéformations et les contraintes résiduelles (macrocontraintes) ont été déterminées en temps réel pendant les essais de fatigue. Les microdeformations ont été estimées à partir de mesures de la largeur de corde à mi-hauteur (LCMH) d'un pic de diffraction, et les contraintes résiduelles à partir du déplacement du pic selon la loi des $\sin^2\psi$.

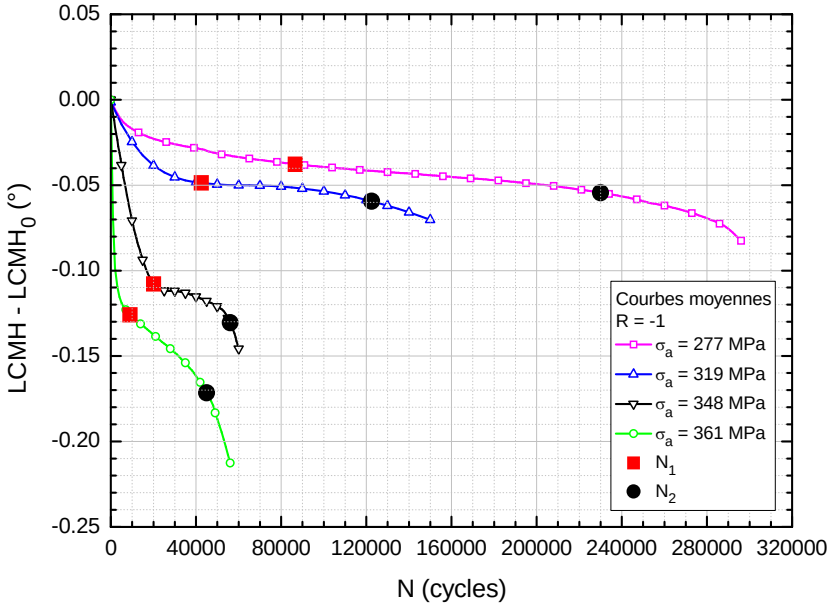

Figure 1. Courbes moyennes de l'évolution de la LCMH en fonction du nombre de cycles pour différentes contraintes alternées (R = -1).

Les courbes moyennes de l'évolution relative de la LCMH au cours des essais de fatigue sont présentées dans la Fig. 1 pour les différentes contraintes alternées appliquées avec R = -1. Pour toutes les contraintes alternées, l'évolution relative de la LCMH en fonction du nombre de cycles peut se décomposer en trois stades, dont les durées sont d'autant plus

courtes et les variations sont d'autant plus accentuées que la contrainte alternée est haute. Le Stade 1 se caractérise par une décroissance de la LCMH. Ce stade peut être relié à la multiplication de dislocations et réorganisation du réseau des dislocations initial, et à leurs interactions avec les éléments en insertion et les joints de grains. Le réseau des dislocations initial du matériau est supposé avoir été introduit par le processus de fabrication du tube. Durant le Stade 2, le taux de décroissance est réduit considérablement. La durée de ce stade concentre presque 50% de la durée de vie. Ce stade peut être relié au processus de nucléation de microfissures et microfissuration. Ce processus, qui entraine la création de nouvelles surfaces libres, peut être représenté par la propagation d'une fissure virtuelle, considérée comme la somme de microfissures individuelles se propageant à très basse vitesse (de l'ordre du nm/cycle). En admettant qu'à la fin du Stade 2 la fissure atteigne la longueur de l'ordre d'un ou de deux tailles de grain, i.e., 20-40 µm, il est possible d'estimer approximativement une vitesse apparente de propagation d'une microfissure pendant ce stade. Finalement, le Stade 3 a lieu au cours des derniers cycles avec une décroissance accentuée de la LCMH jusqu'à la rupture finale. Ce comportement peut être attribué à la relaxation de microcontraintes due à l'initiation et propagation d'une macrofissure (de l'ordre du µm/cycle). L'évolution des contraintes résiduelles (macrocontraintes) en fonction du nombre de cycles est aussi caractérisée par trois stades de mêmes durées que celles observées pour la LCMH. On montre que l'amplitude des variations et leur durée sont proportionnelles au niveau de contrainte. Un ajustement linéaire est observé entre les nombres de cycles délimitant les Stades 1 et 2 et les Stades 2 et 3 (N_1 et N_2, respectivement) et la contrainte alternée, comme présenté dans la Fig. 2.

Des évolutions dans la densité et la répartition des dislocations ont été observées par microscopie électronique en transmission (MET) à l'aide de la technique du faisceau d'ions focalisés. Dans les Figs. 3(a)-(d) il est possible d'observer l'effet de l'endommagement par fatigue, avec l'augmentation de la densité des dislocations et de la complexité du réseau des dislocations. En outre, des essais de fatigue sur des éprouvettes recuites ont aussi été réalisés pour étudier les effets de la restauration de l'état du réseau des dislocations, affecté par le processus de fabrication du tube (écrouissage). Là encore trois stades d'évolution sont observés mais avec un premier stade inversé du fait de l'état initial du réseau de dislocations. Les courbes moyennes de l'évolution relative de la LCMH au cours des essais de fatigue sur les éprouvettes recuites sont présentées dans la Fig. 4 pour deux contraintes alternées avec R = -1.

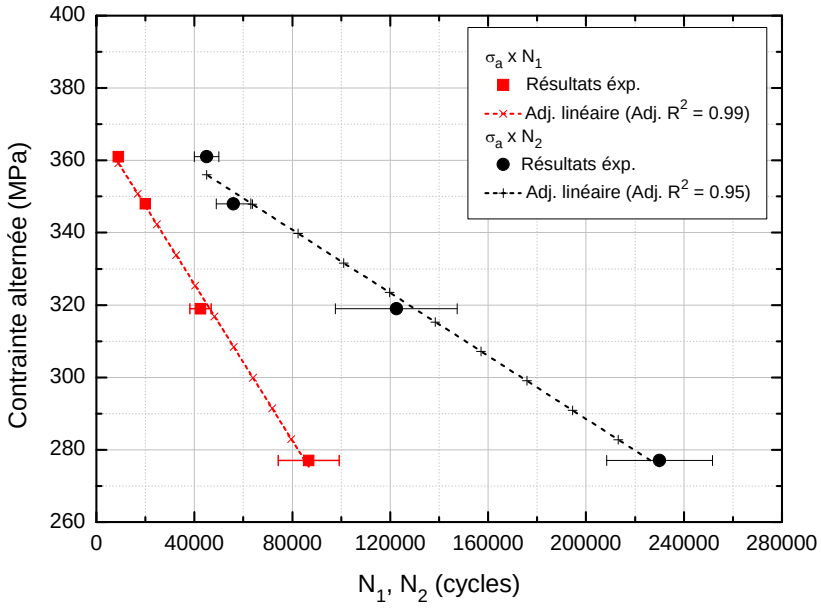

Figure 2. Paramètres N_1 et N_2 rapportés aux contraintes alternées.

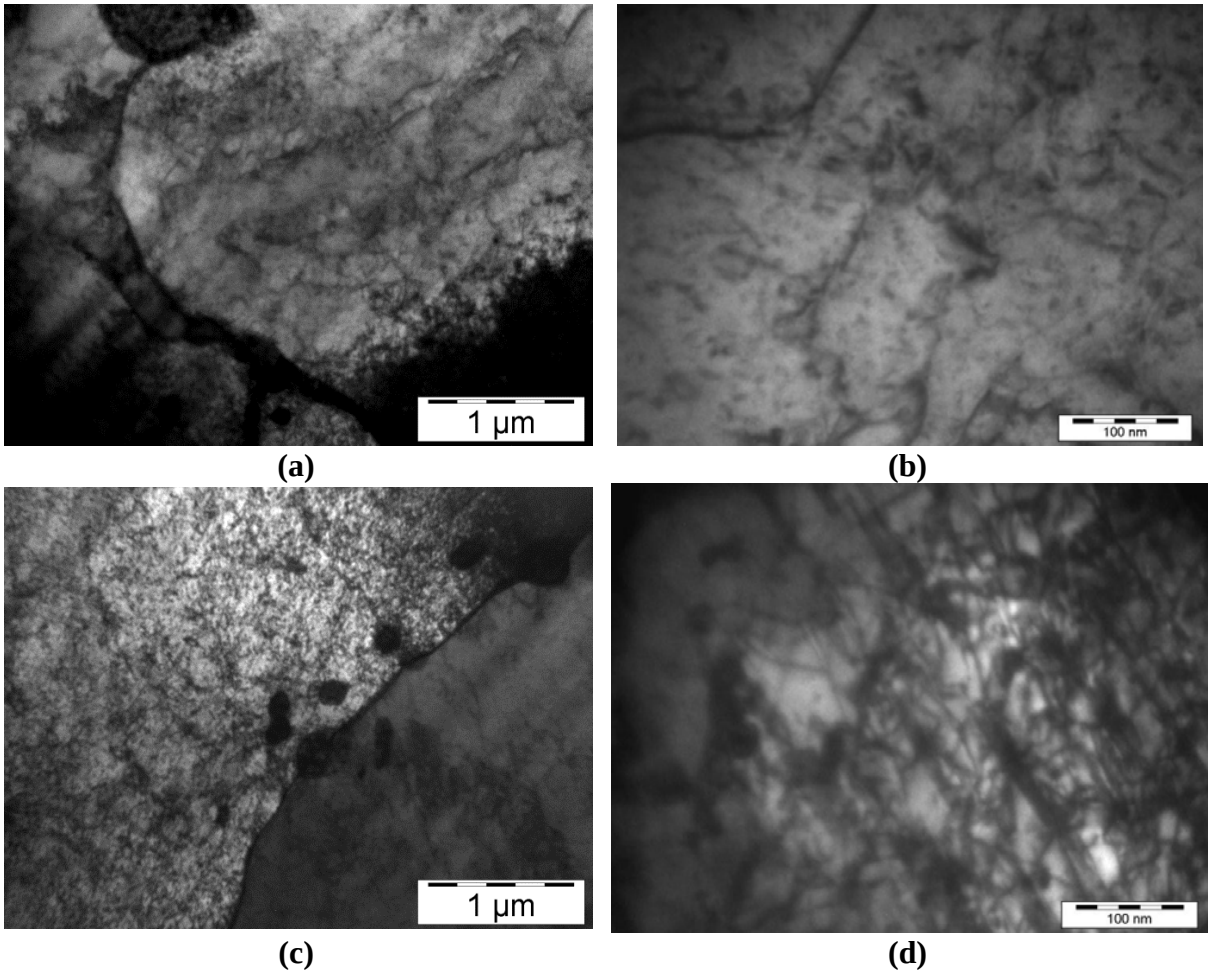

(a) **(b)**

(c) **(d)**

Figure 3. Structures des dislocations obtenues à partir des observations par MET sur éprouvettes fatiguées à une contrainte alternée de 319 MPa (R = - 1) jusqu'à (a)-(b) 20.000 cycles et (c)-(d) 120.000 cycles.

Dans le but de quantifier la phase d'initiation précédant la fissuration macroscopique, une nouvelle méthode est proposée simulant la propagation d'une fissure virtuelle pendant le Stade 2, qui peut permettre la prévision de la durée de ce stade. Les résultats obtenus sont très encourageants pour la prise en compte des évolutions microstructurales dans l'établissement d'un futur indicateur de dommage de la phase d'amorçage en fatigue à grand nombre de cycles des matériaux, qui doit permettre une bonne prédiction de la durée de vie résiduelle avant fissuration macroscopique.

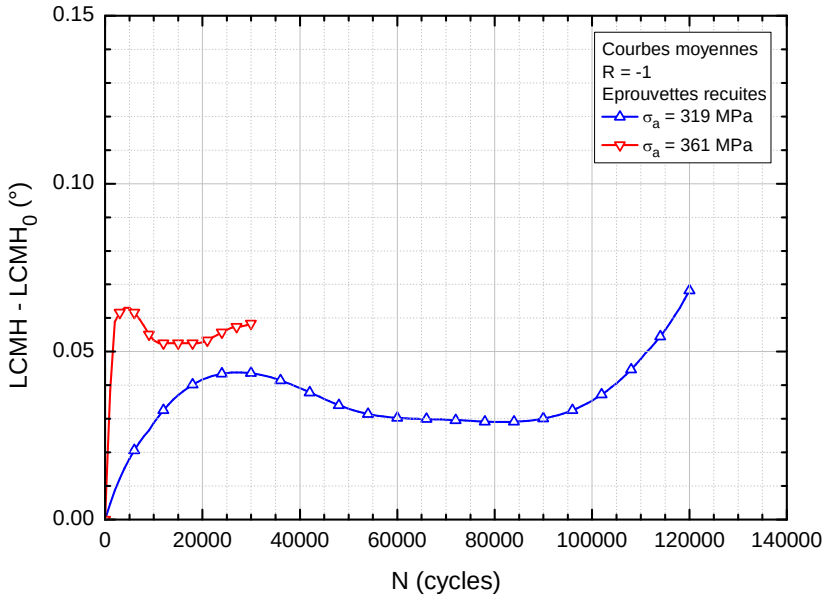

Figure 4. Courbes moyennes de l'évolution de la LCMH en fonction du nombre de cycles des éprouvettes recuites pour deux contraintes alternées (*R* = -1).

ACKNOWLEDGMENTS

First of all, I would like to express my sincere gratitude to my advisor, **Prof. Jacky Lesage**, for the continuous support to my work and for his motivation, inspiration, enthusiasm, and valuable expertise. His important guidance helped in my progress during the different phases of the work, from the understanding of the subject to the interpretation of results.

I am extremely thankful to my co-advisor, **Prof. Noureddine Benseddiq**, whose patience, encouragement, guidance and support helped me during all activities carried out. His insights were very important for the achievement of the work.

I would like to thank heartily the members of the jury, **Prof. Edoardo Bemporad**, from University of Rome TRE, **Prof. Eli Saul Puchi-Cabrera**, from Central University of Venezuela, **Prof. Ilson Pasqualino**, from the Federal University of Rio de Janeiro, and **Prof. Jean-Louis Robert**, from the University Clermont-Ferrand 2, for their time and dedication spent in the examination of the thesis, and their valuable contribution with insightful comments and questions. Particularly, I am extremely grateful to Professors Eli Saul Puchi-Cabrera and Jean-Louis Robert for their inestimable contribution with the reports.

I would like to show all my gratitude to Prof. Ilson Pasqualino and the whole administration and technical staff of the **Subsea Technology Laboratory (LTS)** of COPPE/Federal University of Rio de Janeiro for preparation of samples, execution of tension tests, and all support spent in different moments during the accomplishment of this work. Despite the distance, Prof. Ilson has always helped me with his insights, motivation, and encouragement. The periods he spent in the Laboratory of Mechanics of Lille were very fruitful and brought important contributions to the work.

I am extremely grateful to Prof. Edoardo Bemporad and the administration and technical staff of the **Interdepartmental Laboratory of Electron Microscopy (LIME)** of University of Rome TRE for the assistance in TEM analyses, and for the great opportunity I had to spend a time there to participate in the campaign of TEM analyses. Especially, I would like express my sincere thanks to **Danielle De Felicis**, **Mattia Piccoli**, **Vincenzo Mangione**, **Marco Sebastiani**, and **Luca Mazzola** for providing their valuable assistance in preparation of TEM lamellae and in TEM analyses.

I would like to thank **Eng. Jean-Marc Liekens**, from Lycée Camille-Claudel, for his valuable help with the annealing treatment of samples. I want to express my sincere gratitude

to **Dr. Patrick Flahaut**, from École des Mines de Douai, for the important assistance with metallographic analyses.

I would like to express all my gratitude to **Dr. Xavier Decoopman**, for sharing his friendship, helping me in several tasks, and sharing valuable insights and motivating conversations. I am also grateful to **Dr. Cosmin Gruescu**, **Prof. Didier Chicot**, **Dr. Francine Roudet,** and **Prof. Gérard Mesmacque** for helping with their valuable insights.

I would like to show my gratitude to **Bernard Christiaens** and **Michel Catteau** for providing assistance and helping several times with technical matters. I would like to express my gratitude to **Martine Slowinski** for always helping me with administrative questions.

My sincere thanks also go to all my colleagues and friends from the Laboratory of Mechanics of Lille: **Amar Belloula**, **Chen Shen**, **Jesus Martinez**, **Jhonny Mendoza**, **Josette Kozbial**, **Martine Slowinski**, **Pedro Cadenas**, **Ricardo Ambriz**, and **Ulises Sanchez** for supporting me with their friendship and important insights.

I am extremely thankful to the financial support from **CNPq** (Brazilian National Council for the Scientific and Technological Development) and **Roberto Rocca Education Program** (Tenaris Company), essential for the accomplishment of this work.

I would like to show my gratitude to everyone who helped me in different ways to offer me a wonderful and unforgettable time in France.

I would like to thank all my friends and family, and in special my parents, **Liana Ribeiro de Carvalho** and **Ivan Martins Pinheiro**, for supporting me throughout my life.

I want to express my kind regards to my partner **Jhon Quiroz** for always supporting me during the period of achievement of this work.

Finally, I offer my best regards to all of those who supported me and contributed in any aspect during the accomplishment of this work.

« Je suis de ceux qui pensent que la science a une grande beauté. Un savant, c'est aussi un enfant placé en face des phénomènes naturels qui l'impressionnent comme un conte de fées. »

Marie Curie, 1933

TABLE OF CONTENTS

LIST OF TABLES

LIST OF FIGURES

INTRODUCTION

INTRODUCTION

1. GENERAL INTRODUCTION

In 2007, the Brazilian government announced the discovery of potentially massive oil reserves in the “pre-salt” layer of Santos Basin. Brazil’s pre-salt layer, located approximately 170 miles off the coast at the Atlantic Ocean, is found at depths of up to 7,000 meters below the sea level with substantial oil and gas reserves. Petrobras estimates that the exploitation of these reserves will be able to double the volume of oil and gas production in Brazil, up to 5.7 million barrels per day by 2020 [1]. The activities of exploitation, production and distribution in the petroleum industry bring out several engineering issues and challenges.

Steel pipes used for oil and gas exploitation undergo the action of cyclic loads that can lead to fatigue failure. As a matter of fact, fatigue is one of the major causes of failure of such structures [2-5], which can be followed by catastrophic environmental damage and also significant financial loss. Subsea pipelines are usually made of high strength API 5L steels of different grades, as X60, X65, X70 and X80, for instance [6]. To assure their structural integrity and forewarn a fatigue failure it is important to be able to detect and follow the fatigue damage during operation.

Fatigue damage may be split in two phases: an incubation phase, during which only microstructural changes, microcracking and microcrack nucleation can be observed, and a propagation phase, characterized by macroscopic cracking and macrocrack propagation which lead to fatigue failure. During the second phase, fatigue damage (macrocrack propagation) is easier to be detected and followed. In addition, macrocrack propagation can be modeled by the classical Paris’s law [7] and modified versions within the linear elastic fracture mechanics (LEFM) approach. Moreover, risk-based inspections are supported by the probability of macrocrack detection, as in the case of steel pipelines [8]. Regarding the first phase, even if the mechanisms developed in early stages of fatigue are well known – multiplication of dislocations, formation of slip bands, extrusions, intrusions, and microcracks [9-11] – it is not always clear which microstructural changes, and to what extent, can be associated with fatigue damage. Another difficulty concerning this phase is related to the evaluation techniques employed. Since damage evolution, at least at the onset of fatigue, is associated with the movement, density and arrangement of dislocations, changes have to be observed at the nanoscale. The destructive character of the observation techniques available for this

purpose represents a real problem, since in this case it is not possible to perform a series of observations on a same sample during fatigue test. In addition, they require the extraction of very small samples or even thin lamellae from the test piece, which is technically complicated and very time-consuming.

Therefore, the use of nondestructive evaluation (NDE) techniques to investigate physical and microstructural changes associated with fatigue has greatly increased in the recent past. Among these techniques, thermography [12], ultrasonic testing [13,14], magnetic inspection [15,16], and X-ray diffraction [17-20] have indicated notable perspectives. Although most of the currently used NDE techniques may help to detect microstructural changes during the damage process, it is still not possible to correlate fatigue damage to these changes for damage quantification and prediction of the residual life of a component submitted to cyclic loading. Among available NDE techniques, though, X-ray diffraction (XRD) offers the more interesting perspectives, since it can deliver some important information about the dislocation network, microdeformation changes and residual stress state of a fatigued material. Moreover, this technique allows the use of portable systems to directly evaluate the surface of test pieces in real time during testing.

The aim of this work is to evaluate and quantify microstructural changes in real time during fatigue initiation and provide ground for the development of an indicator of fatigue damage initiation in order to allow the residual life prediction of a component submitted to cyclic loading, before macroscopic cracking. The material concerned in the study is the API 5L X60 grade steel, used in pipe manufacturing for the offshore petroleum industry. Fatigue test samples are cut off from an API 5L X60 grade steel pipe sample in the longitudinal direction. The X-ray diffraction technique is used to evaluate microdeformations, characterized by the full width at half maximum (FWHM) of the XRD peak, and macro residual stresses in real time during high cycle fatigue (HCF) tests under alternating bending loadings. Five different alternating stress amplitudes are applied in the fatigue tests. Thus, microstructural changes in terms of variations in FWHM and residual stresses are evaluated during fatigue cycling as a function of the loading level (stress amplitude). Samples fatigued at specific numbers of cycles are further examined by transmission electron microscopy (TEM) to investigate the correlation between FWHM changes and dislocation density. In addition, fatigue tests on annealed samples are also carried out to study the effects of restoration of the nonstressed dislocation network. The annealing treatment eliminates effects related to the dislocation network generated during pipe manufacturing by cold working. The experimental results obtained are analyzed in view of the development of an indicator of

fatigue damage initiation for the X60 grade steel that could allow evaluation of the residual life before macroscopic cracking and help to increase the reliability of pipelines submitted to cyclic loads.

2. STRUCTURE OF THE DISSERTATION

In Chapter 1 a literature review about fatigue of metals is presented. This chapter is divided in two parts. In the first part, a brief review of macroscopic aspects of fatigue is presented, focusing on the stress-life method of fatigue life evaluation and effects of mean stresses and residual stresses. The second part deals with fatigue damage mechanisms, which can be divided in three phases: initiation of microcracks, microcracking (microcrack propagation) and macrocrack propagation. The crack initiation phase and stage I (microcrack propagation) and stage II (macrocrack propagation) of crack growth are discussed.

Chapter 2 presents a literature review concerning the X-ray diffraction technique and its use in mechanical characterization of materials. The first part comprises a brief theoretical review of the technique, emphasizing its principles and practical engineering application for measurements of macro residual stresses and microdeformations. Macro residual stresses are usually estimated by the $\sin^2\psi$ method [21-23] and microdeformations can be studied quantitatively by mathematical theories, or peak profile analysis [24]. The two classical methods of peak profile analysis are the Warren-Averbach analysis and the Williamson-Hall plot [24-27]. Microdeformations can also be estimated by characterization of peak broadening according to parameters such as the integral width or the full width at half maximum (FWHM), which can give at least qualitative information upon the dislocation network state [28]. The second part describes the use of X-diffraction for characterization of material strength (hardness, fatigue limit and work hardening state, for example) and microstructural changes of materials under static, thermal and cyclic loadings based on results obtained in the literature. In a number of previous works reported in the literature, X-ray diffraction studies of fatigue damage, or at least changes in microstructural parameters, were carried out by the evaluation of the evolution of microdeformations and residual stresses with fatigue cycling [10,18-20,28-71]. In general, it was found that in the early stage of fatigue, the FWHM may increase for an annealed material, while for a hardened (cold worked) material the FWHM may decrease [10,18-20,28-71].

In Chapter 3 the experimental work is presented, comprising the characterization of material properties of the API 5L X60 grade steel, the preparation of fatigue test samples, the

experimental setup for the fatigue tests, and the X-ray diffraction study of changes in residual stresses and microdeformations during fatigue tests.

Chapter 4 presents and discusses the obtained results. For all applied stress amplitudes, three stages can be identified in FWHM changes during fatigue cycling. The first stage (Stage 1) takes place in the early cycles and is characterized by a fast decrease of FWHM. In the second stage (Stage 2), the rate of FWHM decrease is considerably reduced. This stage comprises the major fraction of fatigue life. Finally, the third stage (Stage 3) occurs in the last cycles with a rapid decrease in FWHM until complete fracture. Considering that the microstructural changes measured in terms of variations in FWHM present three regular successive stages, it can be supposed that a connection could exist between them and the three phases of fatigue damage mechanisms, namely initiation of microcracks, microcracking (microcrack propagation and coalescence), and macrocrack propagation. These results are discussed in view of the development of an indicator of fatigue damage initiation in order to allow the residual life prediction of a component submitted to cyclic loading, before macroscopic cracking.

Finally, the conclusions of the developed work and perspectives for future works are discussed.

CHAPTER I

FATIGUE OF METALS AND DAMAGE MECHANISMS

CHAPTER I

FATIGUE OF METALS AND DAMAGE MECHANISMS

This chapter is divided in two parts. The first part comprises a brief review of macroscopic aspects of fatigue, focusing on the stress-life method of fatigue life evaluation and effects of mean stresses and residual stresses. The second part deals with fatigue damage mechanisms, involving initiation of microcracks, microcracking and macrocrack propagation.

I. 1. FATIGUE OF METALS

I. 1.1. MACROSCOPIC ASPECTS OF FATIGUE [72,73]

A metal subjected to cyclic loadings can fail by fatigue at a stress well below the static ultimate strength of the material. In industrial fields, fatigue is one of the major mechanical causes of failure of components, parts or machines. Fatigue damage is particularly dangerous due to its progressive and localized character; it usually develops without any obvious warning. Variables such as stress concentration, surface finish, corrosion, temperature, load frequency, metallurgical structure and residual stresses can affect the material fatigue behavior.

The three major fatigue life methods used in design and analysis are the stress-life method, the strain-life method, and the linear elastic fracture mechanics (LEFM) method. These methods attempt to predict the life in number of cycles to failure, N, for a specific level of loading. The stress-life method is the most traditional method, since it is the easiest to implement for a wide range of design applications, has ample supporting data and represents high cycle applications adequately. However, care should be exercised when applying the method for low cycle applications, as the method does not account for the true stress-strain behavior when localized yielding occurs. The strain-life method involves more detailed analysis of the plastic deformation and is especially indicated for low cycle fatigue applications. The fracture mechanics method assumes that a crack is already present and detected. It is then employed to predict crack growth with respect to stress intensity. It is most practical when applied to large structures in conjunction with computer codes and a periodic inspection program. Only the stress-life method will be considered in this work.

I. 1.1.1. STRESS-LIFE METHOD

A cyclic loading is usually represented by the maximum stress σ_{max}, the minimum stress σ_{min}, the mean stress σ_m and the stress ratio R, which is defined as

$$R = \frac{\sigma_{min}}{\sigma_{max}} \quad \textbf{(I.1)}$$

Figure I.1 illustrates a typical cyclic loading of sinusoidal form. The alternating stress amplitude σ_a and the mean stress σ_m are given by

$$\sigma_a = \frac{\Delta\sigma}{2} = \frac{(\sigma_{max} - \sigma_{min})}{2} \quad \textbf{(I.2)}$$

and

$$\sigma_m = \frac{(\sigma_{max} + \sigma_{min})}{2} \quad \textbf{(I.3)}$$

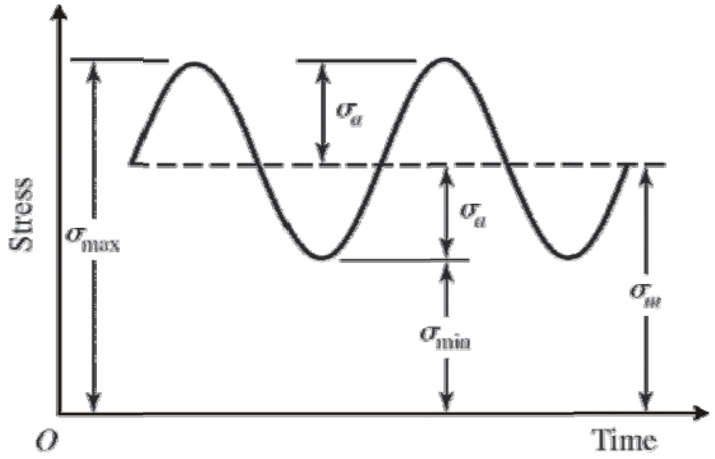

Figure I.1. Typical cyclic loading of sinusoidal form (adapted from [73]).

The curve relating fatigue life, or number of cycles N to failure, to fatigue strength S_f is called Wöhler curve, or S-N curve. The number of cycles should be plotted in logarithmic scale (abscise axis) and fatigue strength should be indicated in logarithmic or Cartesian scale (ordinate axis). To establish the fatigue strength of a material, quite a number of tests are needed due to the statistical nature of fatigue. The fatigue strength S_f is usually expressed in terms of alternating stress amplitude σ_a or maximum stress σ_{max}. Due to the considerable

variability of results of fatigue tests, several tests should be carried out for the same stress amplitude, and the set of results should be statistically treated. The number of cycles N is then referred to a probability of failure. Commonly, the S-N curve is defined for a probability of failure of 50% unless otherwise specified. Figure I.2 shows an example of an S-N curve plotted from results of completely reversed axial fatigue tests (material: normalized UNS G41300 steel) [73].

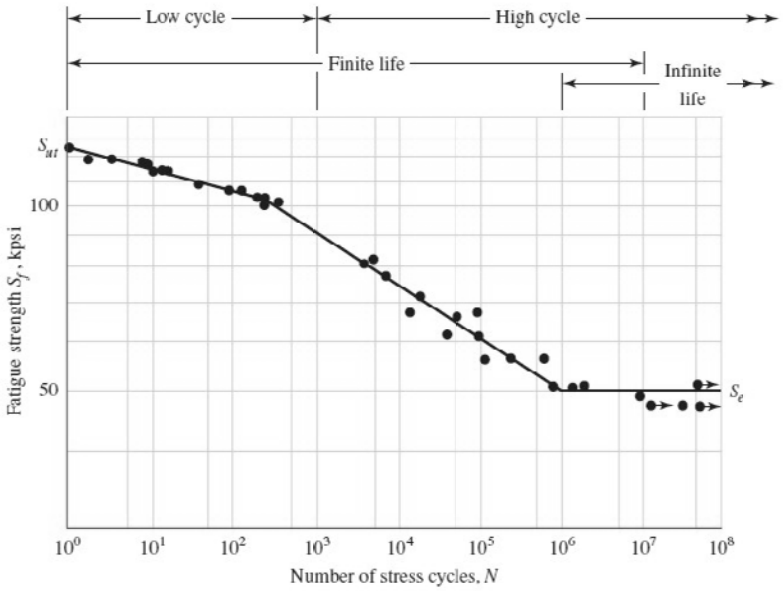

Figure I.2. S-N curve plotted from results of completely reversed axial fatigue tests. Material: normalized UNS G41300 steel [73].

Three domains of fatigue behavior can be distinguished in an S-N curve (Fig. I.2):

- **Low cycle fatigue (finite life)**: in this domain fatigue failures occur at low number of cycles (generally from N = 1 to 10^3 cycles) and are usually preceded by macroscopic plastic deformation. In this case, the significant plastic deformation makes interpretation difficult in terms of stress, and then fatigue tests are generally conducted with prescription of total deformation or plastic deformation instead of stress cycles. A cyclic stress-strain plot is shown in Fig. I.3(a) for the first few cycles of controlled cyclic strain for a high strength steel. In this case cyclic softening was observed. Figure I.3(b) shows a log-log plot relating fatigue life in reversals to failure to strain amplitude for hot-rolled SAE 1020 steel. The Coffin-Manson equation relates fatigue life to total strain amplitude:

$$\frac{\Delta\varepsilon}{2} = \frac{\sigma'_F}{E}(2N)^b + \varepsilon'_F(2N)^c \qquad \textbf{(I.4)}$$

where $2N$ is the number of strain reversals, E is Young's modulus, ε'_F is the fatigue ductility coefficient, σ'_F is the fatigue strength coefficient, and c is the fatigue ductility exponent (slope of the plastic-strain line). ε'_F and σ'_F are, respectively, the true strain and the true stress corresponding to fracture in one reversal. This domain is not concerned in this work.

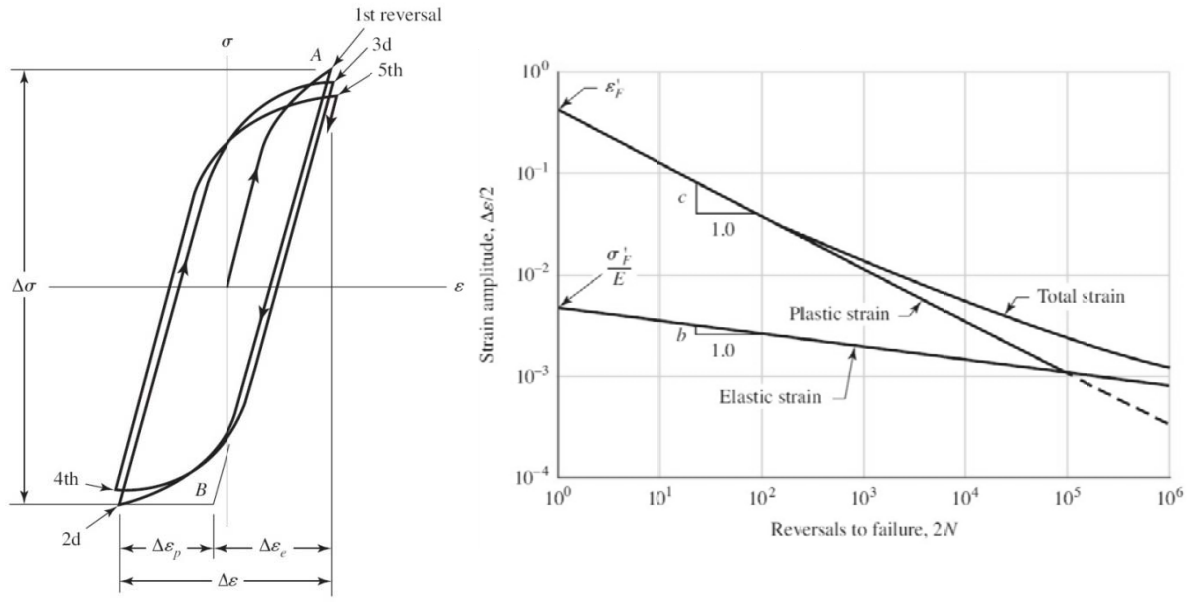

(a) **(b)**

Figure I.3. (a) True stress-true strain hysteresis loops showing the first five stress reversals for high strength steel. (b) Log-log plot relating fatigue life in reversals to failure to the true-strain amplitude for hot-rolled SAE 1020 steel [73].

- **High cycle fatigue (finite life):** concerns failures corresponding to stress cycles greater than 10^3 cycles. In high cycle fatigue, even if stresses are elastic at the macroscopic scale, highly localized deformations are observed in the material. In this case, stresses remain globally elastic and fatigue tests can be conducted either under stress control or strain control. The S-N curve in the high cycle fatigue is usually described by the Basquin equation

$$S_f = CN^b \qquad \textbf{(I.5)}$$

where S_f is the fatigue strength and b and C are empirical constants of the material.

- **Infinite life:** For some materials, such as steel and titanium, the S-N curve becomes horizontal at a certain limiting stress, called fatigue limit or endurance limit, below which the material presumably can endure an infinite number of cycles without failure (infinite life region). The boundary between the finite life and infinite life regions cannot be clearly defined except for a specific material; but it lies somewhere between 10^6 and 10^7 cycles for

steels. Most nonferrous metals, like aluminum, magnesium, and copper alloys, do not have a true fatigue limit and it is common practice to characterize the fatigue strength of these materials at an arbitrary number of cycles, for example, 10^8 cycles.

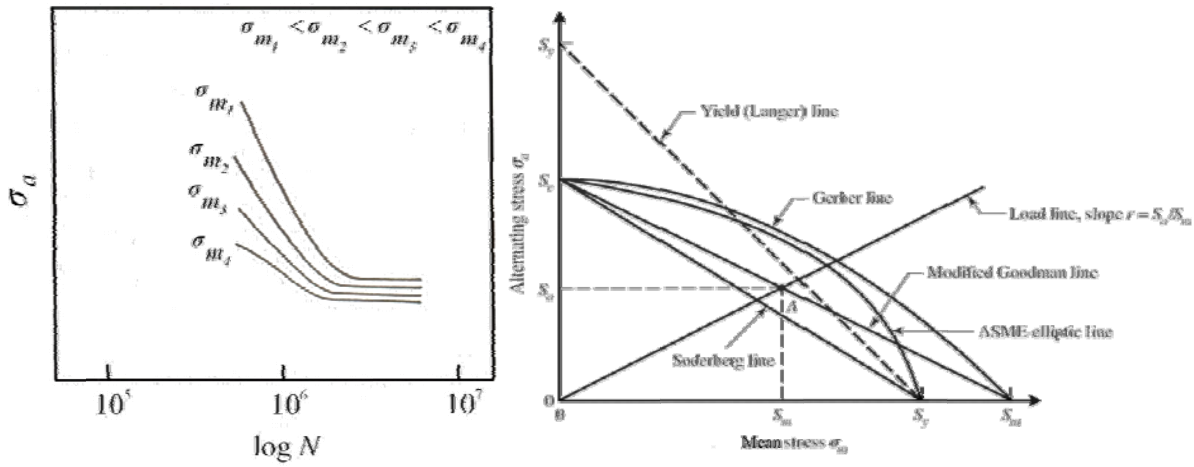

(a) **(b)**

Figure I.4. (a) Effect of mean stress on fatigue strength [72] and (b) current criteria of failure to account for the mean stress effect on fatigue strength [73].

Table I.1. Equations describing some criteria of failure that account for the mean stress effect on fatigue strength [73].

Criterion of failure	Equation	
Modified Goodman	$\frac{\sigma_a}{S_f} + \frac{\sigma_m}{S_u} = 1$	**(I.6)**
Gerber	$\frac{\sigma_a}{S_f} + \left(\frac{\sigma_m}{S_u}\right)^2 = 1$	**(I.7)**
Soderberg	$\frac{\sigma_a}{S_f} + \frac{\sigma_m}{S_y} = 1$	**(I.8)**
Yielding	$\sigma_a + \sigma_m = \sigma_y$	**(I.9)**

I. 1.1.2. EFFECT OF MEAN STRESS ON FATIGUE

Figure I.4(a) illustrates the effect of mean stress on fatigue strength. For a given number of cycles *N*, fatigue strength decreases with increasing mean stress. Some available methods allow the correction of the S-N curve for the condition of mean stresses different to zero. Figure I.4(b) presents the methods most commonly used to account for the mean stress effect on fatigue strength, including the criteria of modified Goodman, Gerber, Soderberg, and

yielding. The expressions describing these criteria are presented in Table I.1. For each criterion, points on or above the respective line indicate failure.

I. 1.2. EFFECT OF RESIDUAL STRESSES ON FATIGUE [19,20,25,69,74]

Fatigue strength of steels can be greatly influenced by macro and micro residual stresses present in the material. Residual stresses are generated during manufacturing processes such as forging, machining, heat treating, shot peening, and many others. These stresses result from nonuniformly distributed dimensional changes due to inhomogeneous plastic deformations, thermochemical treatments, and/or phase transformations. Residual stresses can be distinguished between first order stresses in the macroscopic scale (scale of a few grains), second order stresses in the grain scale, and third order stresses in the scale of the crystallographic network. Residual stresses in general are the superposition of these three kinds of stress, as schematically illustrated in Fig. I.5. Second and third order stresses, which are stresses in the microscopic scale, cannot be measured. In this case, only microdeformations can be determined.

Residual stresses can be either beneficial or detrimental to fatigue strength, depending on their sign, magnitude and stability as well as on the loading and environmental conditions. Compressive macro residual stresses in the surface region of materials with medium and high hardness increase the fatigue life and the fatigue limit. This improvement is caused by an increased resistance against crack initiation and, to a certain extent, against crack propagation if the residual stresses are sufficiently stable in areas of highest loading. Therefore, in many cases, compressive macro residual stresses are intentionally generated in near-surface regions by controlled heat treatments or by mechanical treatments, such as shot peening or deep rolling. In contrast, effects are detrimental for tensile stresses. Despite the number of studies already carried out over the last years, the influence of residual stresses in the fatigue life is still an opened engineering research issue. The difficulty of separating contributions of residual stresses and other metallurgical or geometrical parameters that follow the creation of these stresses and the different effects of macroscopic and microscopic residual stresses render the subject more complex [69].

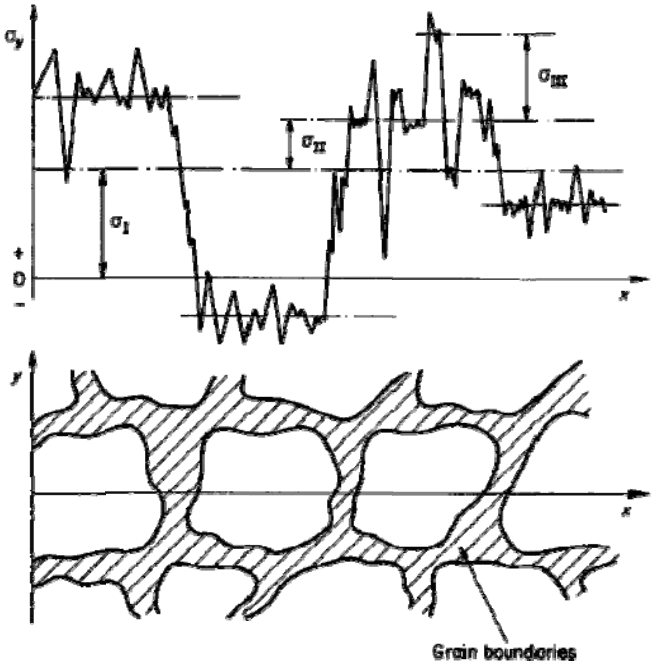

Figure I.5. The three residual stress orders [25].

I. 2. FATIGUE DAMAGE IN HIGH CYCLE FATIGUE

I. 2.1. PHASES OF DAMAGE MECHANISMS [70,72,73]

In general, three phases of damage mechanisms can be distinguished during the process of high cycle fatigue of a sample initially without cracks:

- **Phase 1: Initiation of microcracks**. This phase concerns the initiation of one or more microcracks, which often takes place at the surface of metals or at zones of high local stress concentration, such as interfaces precipitate-matrix or inclusion-matrix and grain boundaries. In this phase, strain localization leads to the formation of persistent slip bands (PSBs), which entail the development of extrusions and intrusions, where microcracks initiate.
- **Phase 2: Microcracking (microcrack propagation)**. This phase concerns the propagation of one or more microcracks, usually along PSBs or slip planes of the crystalline structure of high shear stress. This is frequently called stage I crack growth. The rate of microcrack propagation is very low (by the order of nm/cycle). At the end of this phase, microcracks start to coalesce to form a macrocrack, which propagates during phase 3.
- **Phase 3: Macrocrack propagation**. In this phase, macrocracking and macrocrack propagation take place. Macrocrack propagation (by the order of μm/cycle) occurs in a direction normal to the maximum applied tensile stress. This is usually called stage II crack

growth. Rupture occurs at the end of this phase when the crack reaches sufficient length so that the remaining cross section can no longer support the applied load.

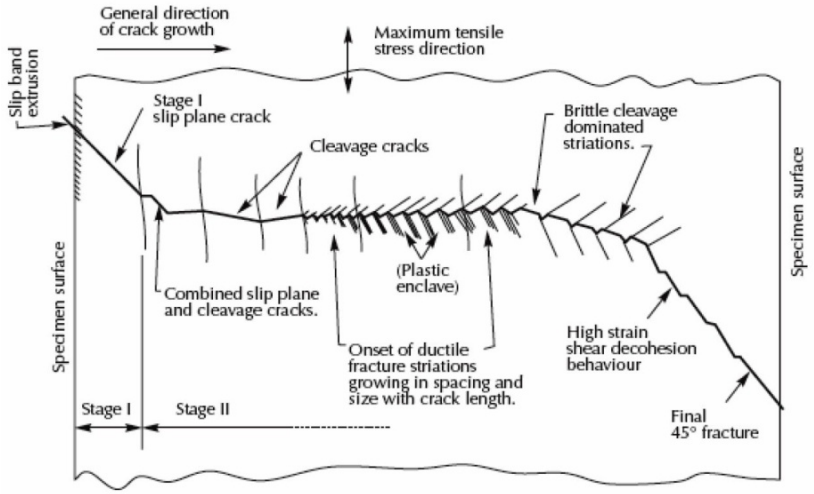

Figure I.6. Schema of stages I and II of fatigue crack growth in an AlZnMg alloy [75].

Figure I.6 schematically represents stages I and II of fatigue crack growth, showing the initiation of a microcrack from a slip band extrusion on the specimen surface, the microcrack propagation at a slip plane of high shear stress (stage I), the macrocrack propagation in a direction normal to the maximum applied tensile stress (stage II), and the final fracture at 45° to the surface.

I. 2.1.1. CRACK INITIATION

In this phase, intense deformation is observed at grains favorably oriented to shear slip and relatively less confined due to proximity to the surface, grains close to a local geometrical discontinuity (stress concentration), or grains affected by stress-corrosion effects. Figure I.7 schematically illustrates atomic rearrangements that accompany the motion of an edge dislocation as it moves in response to an applied shear stress. Dislocations are then arranged along dense crystalline planes giving rise to bands with high localized strain, called persistent slip bands (PSBs) [76], as schematically represented in Fig. I.8. PSBs multiply and interact with cycling. Sequential slip of adjacent PSBs results in the development of intrusions and extrusions [77], which act as initiation sites for microcracks.

A model for the mechanism of development of slip band extrusions and intrusions was proposed by Wood [78], considering that slip bands are the result of a systematic buildup of

free slip movements (of the order of 1nm). This model is schematically illustrated in Fig. I.9, where the fine structure of a slip band is represented at magnifications obtainable with electron microscope. The back-and-forth fine slip movements build up notches (Fig. I.9(b)) or ridges (Fig. I.9(c)) at the surface, which act as stress raisers and initiation sites for microcracks.

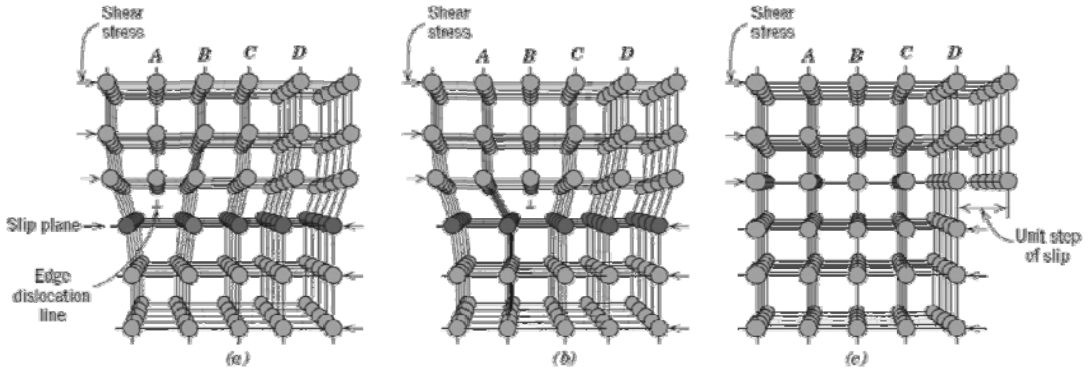

Figure I.7. Atomic rearrangements that accompany the motion of an edge dislocation as it moves in response to an applied shear stress [84].

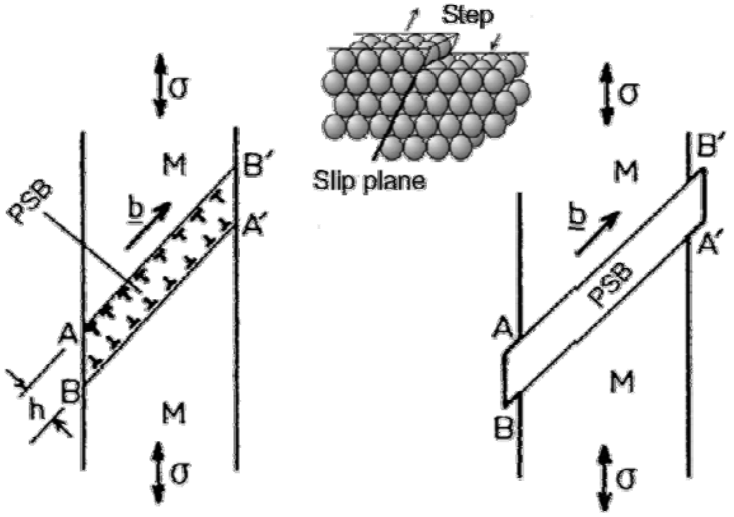

Figure I.8. Damage mechanism of development of a persistent slip band (PSB) and an irreversible step at the surface (adapted from [70]).

The basic premise of this model is that repeated cycling of the material leads to different amounts of net slip on different slip planes. The irreversibility of shear displacements along slip bands then results in roughening of the material surface and gradual development of a notch-ridge surface morphology. The “micro-notches” act as stress raisers and promotes additional slip [79]. Figure I.10 presents an example of fatigue crack initiation in a PSB in a copper single crystal [80].

Other authors proposed models for the mechanism of formation of intrusions and extrusions [75,77] from PSBs. For example, according to Cottrell et al. [77] intrusions and extrusions are formed from sequential slip movements of two intersecting PSBs in one stress cycle, as schematically illustrated in Fig. I.11. This model considers that one PSB becomes active before the other if it is more favorably oriented to the applied stress.

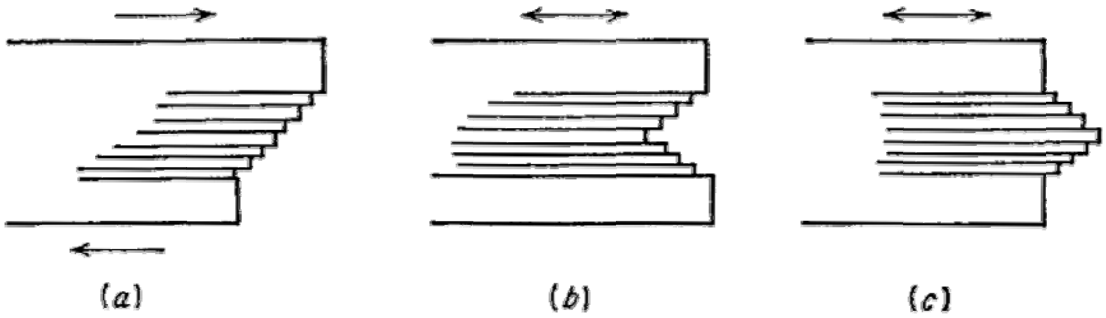

Figure I.9. Model for the mechanism of formation of slip band extrusions and intrusions proposed by Wood [78]. (a) Static deformation. Cyclic deformation leading to (b) surface notch (intrusion) and (c) surface ridge (extrusion).

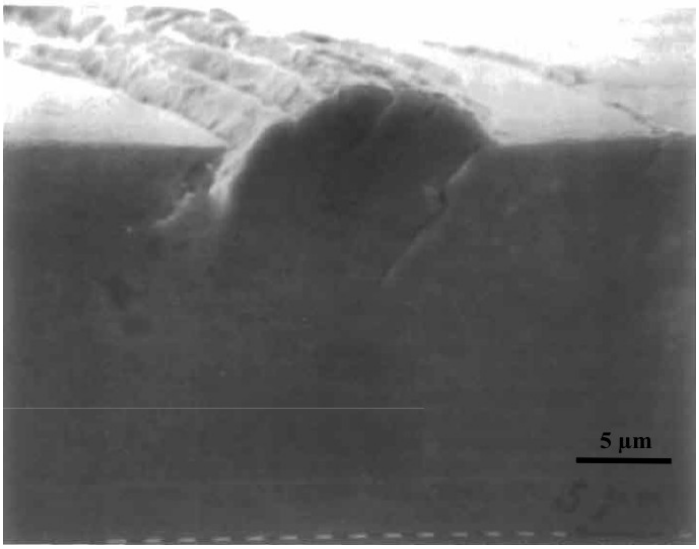

Figure I.10. Fatigue crack initiation in a PSB in a copper single crystal fatigued for 60,000 cycles at a plastic shear strain amplitude of 0.2% at room temperature [80].

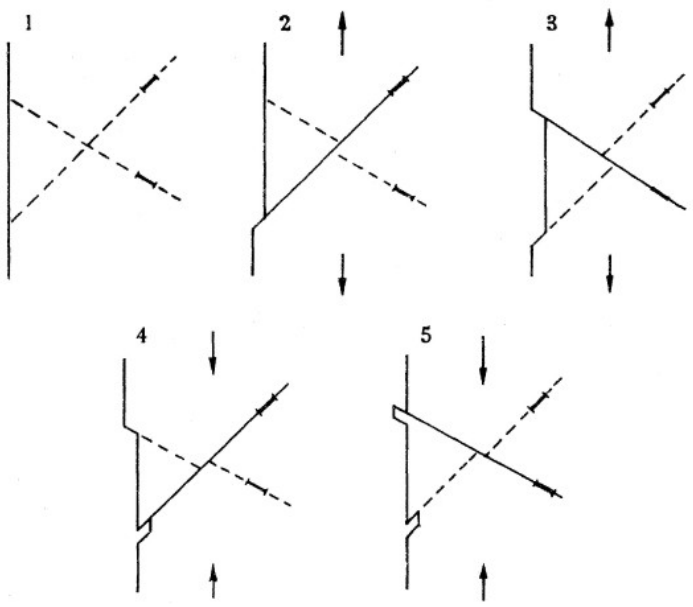

Figure I.11. Sequence of slip movements producing an extrusion and an intrusion according to the Cottrell and Hull model [77].

I. 2.1.2. STAGE I CRACK GROWTH [72]

After initiation, microcracks propagate gradually into the grains along persistent slip bands, representing the stage I crack propagation. In a polycrystalline metal, the crack may extend for only a few grain diameters before crack propagation changes to stage II. The rate of stage I crack propagation is generally very low, on the order of nm/cycle, compared to crack propagation rates in stage II (on the order of μm/cycle). Stage I crack propagation is limited to the near-surface zone of the material. Microcracks are frequently interrupted at grain boundaries that they cannot easily overcome, when adjacent grains are not favorably oriented. Microcracks are very difficult to be detected by nondestructive evaluation (NDE) techniques.

I. 2.1.3. STAGE II CRACK GROWTH [72]

Stage II progresses from microcracks to macrocracks, forming parallel plateau-like fracture surfaces separated by longitudinal ridges. Stage II crack propagation occurs in a direction normal to the maximum applied tensile stress. Stage II crack propagation occurs by plastic blunting process, which is schematically illustrated in Fig. I.12. At the beginning of the loading cycle the crack tip is sharp (Fig. I.12(a)). As the tensile load is applied, the small double notch at the crack tip concentrates the slip along planes at 45° to the plane of the crack

(Fig. I.12(b)), and the crack widens and its tip becomes blunter (Fig. I.12(c)).When the load changes to compression, the slip direction is reversed (Fig. I.12(d)), and the crack surface created in tension is forced into the plane of the crack, forming a resharpened crack tip (Fig. I.12(e)). The resharpened crack is then ready to advance and be blunted in the next stress cycle. In general, larger fatigue life fractions are involved with stage II crack propagation in low cycle fatigue than in high cycle fatigue, when, in contrast, stage I crack propagation comprises the major part of the fatigue life.

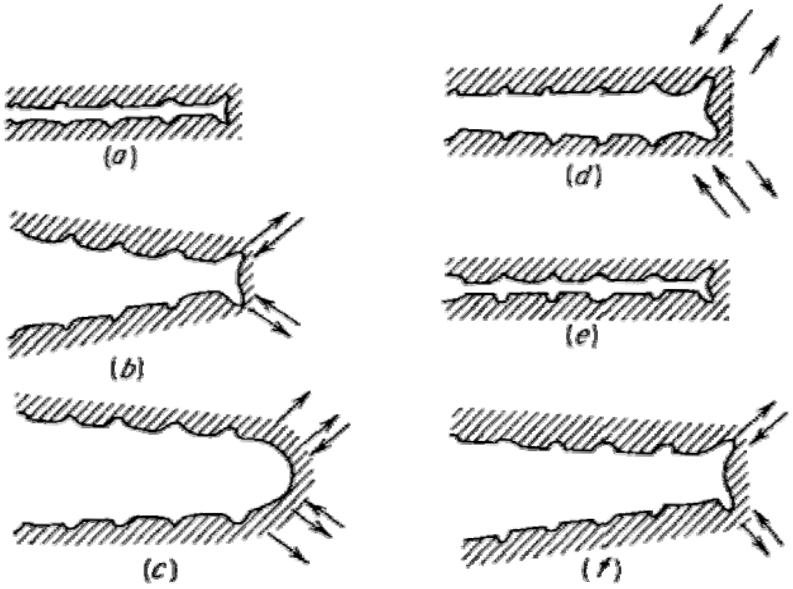

Figure I.12. Plastic blunting process of stage II fatigue crack growth [72].

When the macrocrack is formed, the stage II crack growth can be quantitatively studied by the linear elastic fracture mechanics (LEFM) approach, using the concept of stress intensity factor $K_{\mathrm{I}} = \beta\sigma\sqrt{\pi a}$, introduced by Irvin [81] and extended to fatigue by Paris et al. [7] in terms of the range $\Delta K_{\mathrm{I}} = K_{\mathrm{Imax}} - K_{\mathrm{Imin}}$

$$\Delta K_{\mathrm{I}} = \beta(\sigma_{\max} - \sigma_{\min})\sqrt{\pi a} = \beta\Delta\sigma\sqrt{\pi a} \qquad \textbf{(I.10)}$$

where β is a geometric factor, a is the crack length, and σ is the applied stress, with $\sigma_{\max}$ and $\sigma_{\min}$ as the maximum and minimum stresses, respectively. The relationship between fatigue crack growth rate and ΔK_{I} on a log-log scale has a sigmoidal shape and can be divided into three regions, as shown schematically in Fig. I.13. Region I is bounded by a threshold value $(\Delta K_{\mathrm{I}})_{\mathrm{th}}$, below which there is no observable fatigue crack growth. The crack growth in region II can be approximated by a linear equation, often referred to as Paris's law

$$\frac{da}{dN} = C(\Delta K_{\mathrm{I}})^m \qquad \textbf{(I.11)}$$

where m is the slope of the curve and C is the value found by extending the straight line to $\Delta K_{\mathrm{I}} = 1$ MPa m$^{1/2}$, with the use of SI units.

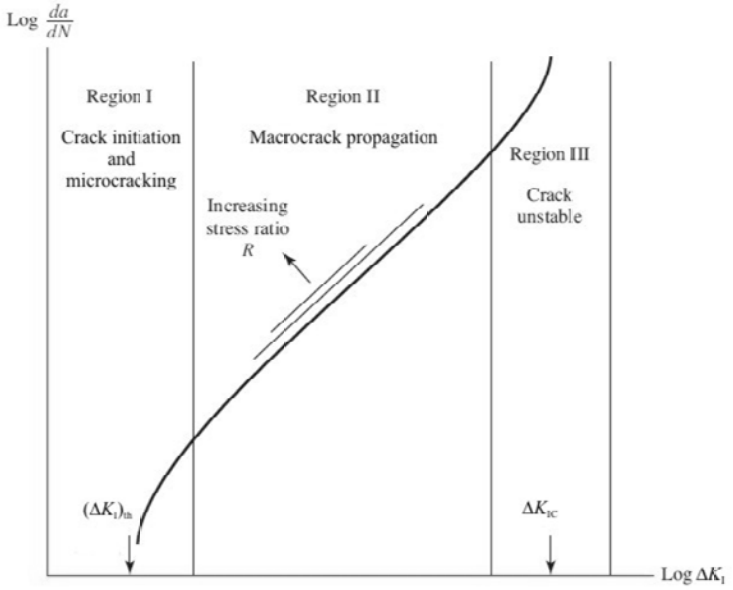

Figure I.13. Schematic plot of fatigue crack propagation rate *da*/*dN* versus stress intensity range ΔK_{I} showing regions I, II and III of crack growth (adapted from [73]).

The macrocrack is easier to be detected by nondestructive evaluation (NDE) techniques than microcracks, and the macrocrack can rapidly lead to fracture. Striations are often visible on fracture surfaces of stage II crack growth. Each striation represents the successive position of an advancing crack front.

Stage II crack growth occurs until a critical length is attained and the stress intensity factor reaches a critical value (K_{Ic}), when the crack becomes unstable with acceleration of crack propagation, and rupture occurs after few cycles. The critical stress intensity factor K_{Ic} is a material property, also called fracture toughness of the material. Region III is then associated with rapid acceleration of crack growth followed by sudden fracture.

I. 2.2. FATIGUE DAMAGE MODELS

Over the last decades, several fatigue damage models have been proposed to estimate fatigue damage. Among them, the Miner's rule [82] and the non-linear continuous fatigue

damage model of Chaboche [83] have wide acceptance. Nevertheless, the different mechanisms of fatigue damage are not distinguished by these models.

I. 2.2.1. MINER'S RULE

The linear cumulative damage rule, also called Miner's rule, assumes [82] that the total life of a part can be estimated by adding up the fatigue life fraction consumed by each stress cycle. Fatigue damage D is then calculated as

$$D = \sum \frac{n_{\mathrm{i}}}{N_{\mathrm{i}}} \qquad \textbf{(I.12)}$$

where n_{i} and N_{i} are, respectively, the number of cycles applied and the number of cycles to failure at a stress σ_{i}. Fatigue failure occurs for $D = 1$. Many variations from Miner's rule have been proposed, but none have gained wide acceptance.

I. 2.2.2. CHABOCHE MODEL

Based on continuum damage mechanics, the nonlinear continuum fatigue damage model proposed by Chaboche et al. [83] describes fatigue damage D as function of the maximum stress σ_{M} and the mean stress $\overline{\sigma}$

$$dD = f(\sigma_{\mathrm{M}}, \overline{\sigma}, D)dN \qquad \textbf{(I.13)}$$

with

$$D = \left(\frac{N}{N_{\mathrm{f}}}\right)^{1/1-\alpha},\ N_{\mathrm{f}} = \frac{1}{1-\alpha}\left[\frac{\sigma_{\mathrm{M}} - \overline{\sigma}}{M(\overline{\sigma})}\right]^{-\beta},\ \alpha = 1 - a\left(\frac{\sigma_{\mathrm{M}}}{\sigma_{\mathrm{b}}}\right)^{\lambda-\beta}, \text{ and } M(\overline{\sigma}) = M_0(1 - b\overline{\sigma})$$

where M_0, b, β, and a are material constants, λ is the slope of the fatigue stress versus life curve, and σ_{b} is the ultimate strength.

CHAPTER II

X-RAY DIFFRACTION AND MECHANICAL CHARACTERIZATION OF MATERIALS

CHAPTER II

X-RAY DIFFRACTION AND MECHANICAL CHARACTERIZATION OF MATERIALS

This chapter presents a literature review concerning the X-ray diffraction technique and its use in mechanical characterization of materials. The first part comprises a brief theoretical review of the technique, emphasizing its principles and practical engineering application for measurements of macro residual stresses and microdeformations. The second part describes the use of X-diffraction for characterization of material strength (hardness, fatigue limit and work hardening state, for example) and microstructural changes of materials under static, thermal and cyclic loadings based on results obtained in the literature.

II. 1. PRINCIPLES OF X-RAY DIFFRACTION [21-23]

The principles of X-ray diffraction (XRD) are not new; they have been used over the years for different purposes in physics, chemistry and engineering fields. The interaction of an X-ray radiation with a material produces the emission in all directions of a radiation with the same wavelength and coherent phase [21]. This phenomenon leads to scattered waves with very low amplitude in the case of scattering of X-rays by an electron or an atom. The scattering of X-rays by a material, i.e., a set of atoms, gives rise to an interference of coherent waves scattered by each atom. The directions for which the diffracted waves are in phase follow the Laue equations, which reduce to the Bragg's law [21].

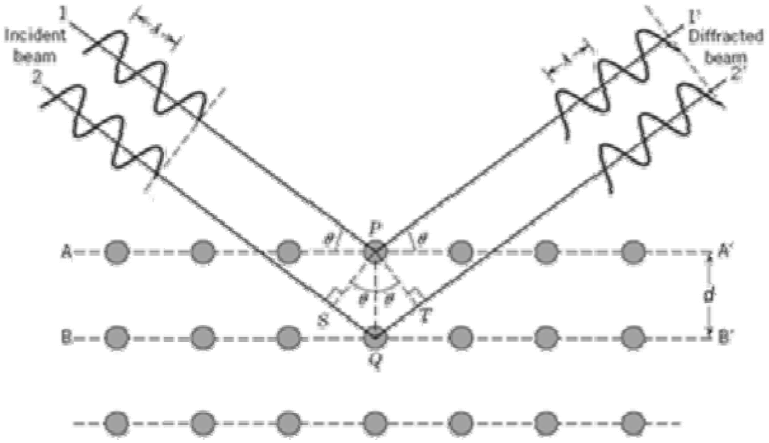

Figure II.1. Principle of X-ray diffraction according to the Bragg's law [84].

In a perfect crystalline material, the atoms constitute a periodic tridimensional arrangement. Schematically, a crystalline material may be considered as a multitude of regular pilling of atomic planes, called coherently diffracting domain (CDD). This system of geometrical ordering of atoms in crystallographic planes is well known to be indicated by the Miller indices (hkl) [84]. Each material is characterized by its distance between crystallographic planes, or lattice spacing, d_0 (nonstressed material), which is an intrinsic material property.

Monochromatic X-rays irradiated over the surface of a crystalline material can be diffracted with concentrated energy (diffraction peak) only if they are in agreement with the Bragg's law, expressed as

$$2d\sin\theta = n\lambda \qquad \textbf{(II.1)}$$

where λ is the wavelength of the incident radiation, θ is the diffraction angle (Bragg's angle), n is the order of diffraction (integer number), and d is the lattice spacing of diffracting planes. Figure II.1 describes the principle of X-ray diffraction according to the Bragg's law; the incident and diffracted beams are symmetrical to the normal to diffracting planes (measurement direction). A schema of X-ray diffraction measurement and resulting XRD peak are illustrated in Fig. II.2. The angular position of the X-ray diffraction peak (2θ) is given as a function of the lattice spacing d of diffracting planes, according to the Bragg's law (Eq. II.1).

The lattice deformation in a crystalline material can produce different effects on the XRD peak whether the deformation is uniform or nonuniform. A uniform deformation ($\varepsilon <$ 0.2%) results in first order residual stresses (macrostresses), which are homogeneous over large scale involving many grains, i.e., a few hundreds of microns. In this case, the angular position of the XRD peak is shifted according to the Bragg's law [21]. This is schematically shown in Fig. II.3(b). In the case of a nonuniform deformation, second and third order residual stresses (microdeformations) are concerned, being homogeneous over small domains such as a part of a grain, with dimensions of about tens of microns. When microdeformations are concerned, broadening of the XRD peak is observed (Fig. II.3(c)), owing to changes in the dislocation network [9]. Microdeformations are related to the degree of cold working or hardness of the material and result from imperfections in the crystal lattice [22]. Microdeformations vary from point to point within the crystals, producing a range of lattice spacing and broadening of the diffraction peak, as illustrated in Fig. II.3(c).

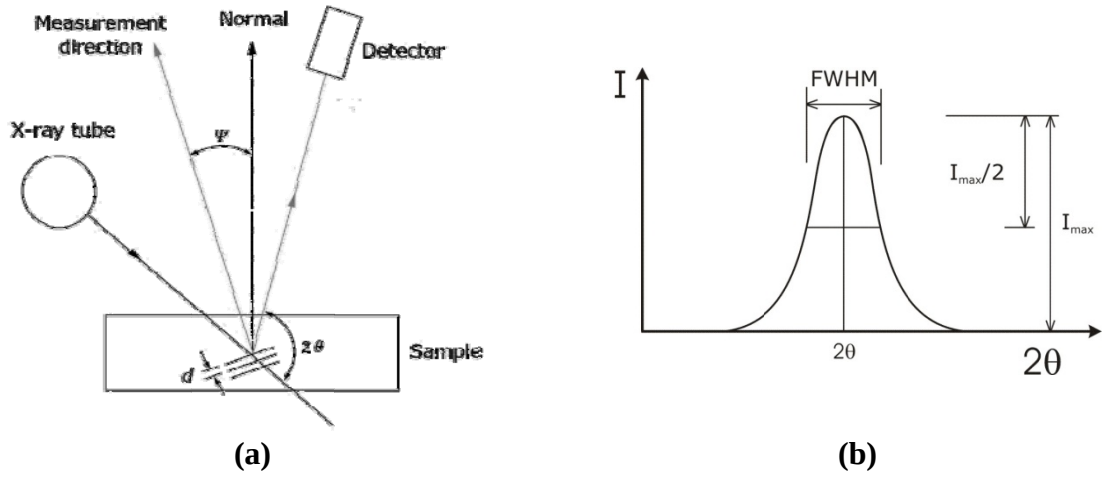

Figure II.2. (a) Schema of XRD measurement [21] and (b) XRD peak, characterized by the angular position 2θ and the full width at half maximum (FWHM).

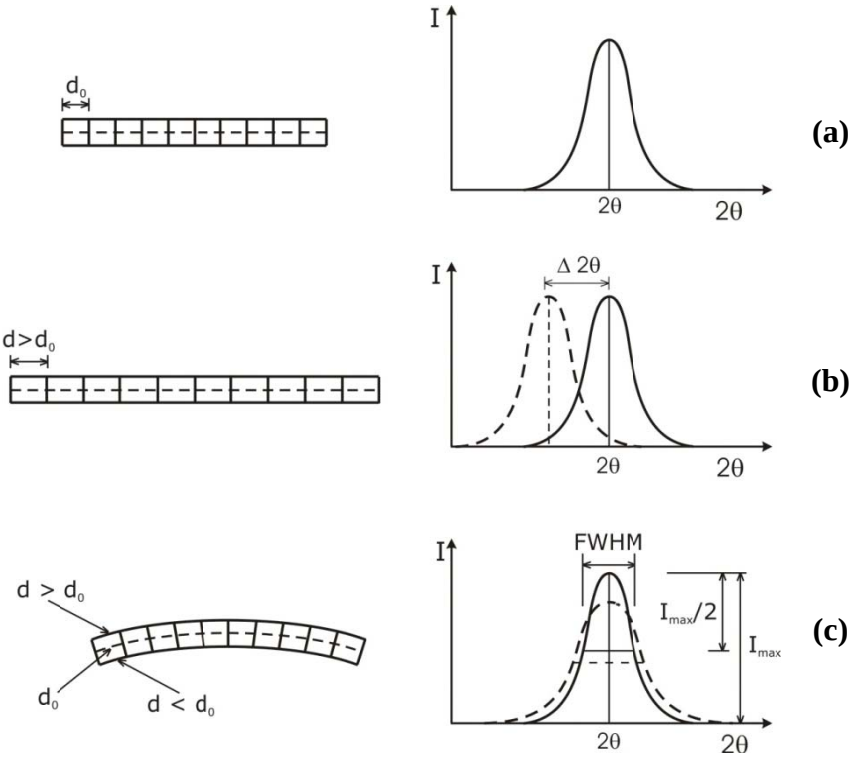

Figure II.3. Effects of lattice deformation on XRD peaks: (a) nondeformed material, (b) uniform deformation (macrostresses), and (c) nonuniform deformation (microdeformations).

X-ray diffraction is the only technique capable to determine independently macroscopic stresses and microdeformations: macroscopic stresses are measured by evaluation of the shift of the angular position of the XRD peak, and microdeformations are estimated by analysis of peak broadening. Therefore, the data obtained from XRD measurements are essentially two: the angular position of the X-ray diffraction peak and the

width (broadening) of the peak. The first one is directly related to macro residual stresses, while the second is related to distortion of the grains, dislocation density and micro residual stresses (microdeformations). This is represented in Fig. II.3, where the shift of the XRD peak allows the measurement of the elastic deformation of the crystal lattice space, while the peak broadening gives the deformation of the crystallographic planes. Macro residual stresses are usually estimated by the $\sin^2\psi$ method [21-23]. Peak broadening can be studied quantitatively by mathematical theories, or peak profile analysis, which allows the calculation of the coherently diffracting domain size D and microdeformations (distortion) $<\varepsilon^2>$ [24]. However, peak broadening can also be characterized by parameters such as the integral width (peak area/height ratio) or the full width at half maximum (FWHM) (Fig. II.2), which can give at least qualitative information upon the dislocation network state [28].

The application of X-ray diffraction for stress measurement in practical engineering problems began in the early 1950's [23]. The development of commercial diffractometers resulted in widespread application in the automotive and bearing industries in the 1960's. By the late 1970's, XRD residual stress measurement was routinely applied in aerospace and nuclear applications involving fatigue and stress corrosion cracking of nickel and titanium alloys, as well as aluminum and steels. Today, a variety of position sensitive detector instruments allows measurements to be routinely performed in the field and on massive structures. X-ray diffraction presents the following properties when applied to residual stress measurements:

- the technique is nondestructive;
- the technique can be applied only to crystalline materials, and
- measurements concern only the near-surface region of the material (< 10μm).

II. 1.2. MACRO RESIDUAL STRESSES: THE SIN$^2\psi$ METHOD

When a crystalline material is submitted to a uniform deformation (macrostresses), the lattice spacing is changed from d_0 (nonstressed material) to d due to expansion or contraction of the crystal lattice space, as illustrated in Fig. II.4. The elastic deformation can then be expressed in terms of changes in the crystal lattice spacing

$$\varepsilon_{\phi\psi} = \frac{\Delta d}{d_0} = \frac{d_{\phi\psi} - d_0}{d_0} \qquad \textbf{(II.2)}$$

where $d_{\phi\psi}$ is the lattice spacing measured in the direction normal to diffracting planes, defined by the angles ϕ and ψ (Fig. II.5). It can be considered that in a lattice space under uniform deformation the lattice spacing plays the role of a "strain gage" (Fig. II.4).

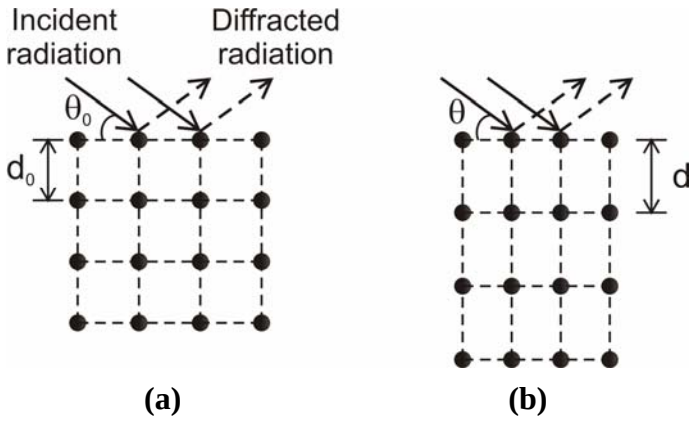

Figure II.4. Changes in the lattice spacing under uniform deformation: (a) nondeformed and (b) deformed lattice spaces.

With the measurement of the elastic deformation $\varepsilon_{\phi\psi}$ of the lattice space, the macroscopic stresses can be estimated by continuum mechanics. For an isotropic and linear elastic material submitted to a stress state given by principal stresses σ_1, σ_2 and σ_3, the components of the deformation $\varepsilon_{\phi\psi}$ in the principal directions are written as

$$\varepsilon_{11} = \frac{1+\nu}{E}\sigma_1 - \frac{\nu}{E}(\sigma_1+\sigma_2+\sigma_3)$$
$$\varepsilon_{22} = \frac{1+\nu}{E}\sigma_2 - \frac{\nu}{E}(\sigma_1+\sigma_2+\sigma_3) \qquad \textbf{(II.3)}$$
$$\varepsilon_{33} = \frac{1+\nu}{E}\sigma_3 - \frac{\nu}{E}(\sigma_1+\sigma_2+\sigma_3)$$

where ν is the Poisson's ratio and E is the Young's modulus. From Eqs. II.3 the deformation $\varepsilon_{\phi\psi}$ at an angle ψ to the surface normal N can then be defined as a function of the principal stresses

$$\varepsilon_{\phi\psi} = \frac{1+\nu}{E}(n_1^2\sigma_1 + n_2^2\sigma_2 + n_3^2\sigma_3) - \frac{\nu}{E}(\sigma_1+\sigma_2+\sigma_3) \qquad \textbf{(II.4)}$$

where n_1, n_2, and n_3 are the direction cosines (Fig. II.5)

$$n_1 = \sin\psi\cos\phi$$
$$n_2 = \sin\psi\sin\phi \qquad \textbf{(II.5)}$$
$$n_3 = \cos\psi$$

Since the penetration depth of X-rays is extremely shallow (< 10 μm), the diffracting volume can be considered to represent a free surface under plane stress [23], as schematically illustrated in Fig. II.5. Then, components of the stress tensor corresponding to the normal stress σ_{33} and shear stresses $\sigma_{13} = \sigma_{31}$ and $\sigma_{23} = \sigma_{32}$ acting out of the plane of the sample surface are assumed to be zero, and Eq. II.4 is simplified to

$$\varepsilon_{\phi\psi} = \frac{1+\nu}{E}(n_1^2\sigma_1 + n_2^2\sigma_2) - \frac{\nu}{E}(\sigma_1+\sigma_2) \qquad \textbf{(II.6)}$$

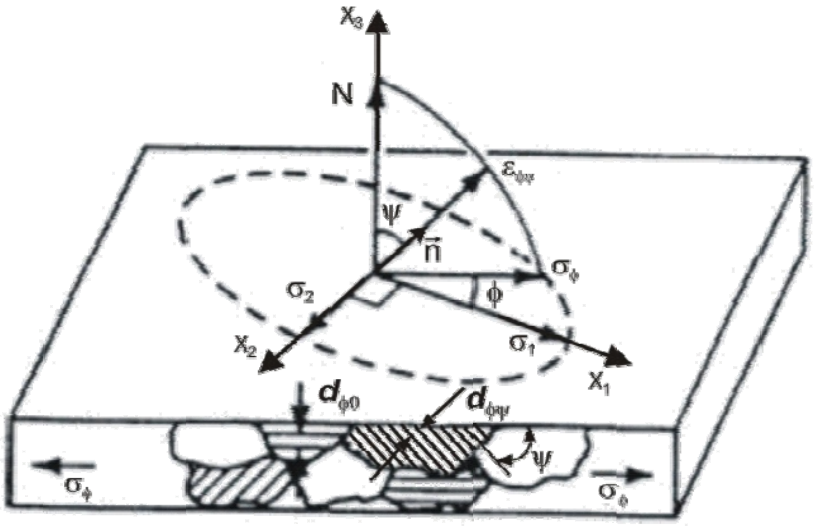

Figure II.5. Assumption of plane stress state (σ_3 = 0) at the free surface of the material (adapted from [23]).

Considering the direction cosines n_1 and n_2 given by Eqs. II.5, Eq. II.6 becomes

$$\varepsilon_{\phi\psi} = \frac{1+\nu}{E}\sin^2\psi(\sigma_1\cos^2\phi + \sigma_2\sin^2\phi) - \frac{\nu}{E}(\sigma_1+\sigma_2) \qquad \textbf{(II.7)}$$

Eq. II.7 can be rewritten as

$$\varepsilon_{\phi\psi} = \frac{1+\nu}{E}\sigma_\phi\sin^2\psi - \frac{\nu}{E}(\sigma_1+\sigma_2) \qquad \textbf{(II.8)}$$

where the stress σ_ϕ acting in the plane of the material surface at an angle ϕ to the maximum principal stress σ_1 is given by

$$\sigma_\phi = \sigma_1 \cos^2 \phi + \sigma_2 \sin^2 \phi \qquad \textbf{(II.9)}$$

Finally, the deformation $\varepsilon_{\phi\psi}$ can be written as a linear function of $\sin^2\psi$

$$\varepsilon_{\phi\psi} = \frac{1}{2} S_2 \sigma_\phi \sin^2 \psi + S_1(\sigma_1 + \sigma_2) \qquad \textbf{(II.10)}$$

where the elastic constants $S_1 = -\nu/E$ and $\frac{1}{2} S_2 = (1+\nu)/E$ where introduced. Considering that $\varepsilon_{\phi 0} = S_1(\sigma_1 + \sigma_2)$, Eq. II.10 becomes

$$\varepsilon_{\phi\psi} = \frac{1}{2} S_2 \sigma_\phi \sin^2 \psi + \varepsilon_{\phi 0} \qquad \textbf{(II.11)}$$

The deformation $\varepsilon_{\phi 0}$ perpendicular to the sample surface ($\psi = 0$) is also given by

$$\varepsilon_{\phi 0} = \frac{d_{\phi 0} - d_0}{d_0} \qquad \textbf{(II.12)}$$

Substituting Eq. II.12 in Eq. II.11, the following expression relates the stress state in the sample surface to the lattice spacing $d_{\phi\psi}$

$$\sigma_\phi = \left(\frac{1}{2} S_2\right)^{-1} \frac{d_{\phi\psi} - d_0}{d_0} \frac{1}{\sin^2 \psi} \qquad \textbf{(II.13)}$$

where d_0 replaces $d_{\phi 0}$ considering that their values differ by less than ± 0.1%, since $E \gg (\sigma_1 + \sigma_2)$, and then σ_ϕ may be approximated to this accuracy.

The sample is assumed to consist of a large number of small grains or crystals, nominally randomly oriented (Fig. II.5). The crystal lattice consists of planes of atoms identified by their Miller indices (hkl). The spacing between a given set of lattice planes, for example (211) planes in steels, will be constant regardless of the orientation of the lattice planes relative to the sample surface in a stress-free sample. The lattice spacing will be expanded or contracted elastically under deformation of the sample (by an amount dependent upon the orientation of the lattice planes). Elastic constants $S_{1(hkl)}$ and $\frac{1}{2} S_{2(hkl)}$ defined for the (hkl) planes become

$$S_{1(\mathrm{hkl})} = -\frac{\nu_{(\mathrm{hkl})}}{E_{(\mathrm{hkl})}} \qquad \textbf{(II.14)}$$

and

$$\frac{1}{2}S_{2(\mathrm{hkl})} = \frac{1+\nu_{(\mathrm{hkl})}}{E_{(\mathrm{hkl})}} \qquad \textbf{(II.15)}$$

where $\nu_{(\mathrm{hkl})}$ is the ratio between the deformation in the planes (hkl) and the deformation in the crystallographic direction [hkl], and $E_{(\mathrm{hkl})}$ is the stress-strain ratio in the direction [hkl], normal to the (hkl) planes. Elastic constants for the (hkl) planes can be determined empirically, according to the standard ASTM E1426 [23], and may differ significantly (commonly as much as 40%) from the values obtained by mechanical testing due to elastic anisotropy [23]. Using the elastic constants $S_{1(\mathrm{hkl})}$ and ½ $S_{2(\mathrm{hkl})}$ given by Eqs. II.14 and II.15, Eq. II.13 becomes

$$\sigma_\phi = \left(\frac{1}{2}S_{2(\mathrm{hkl})}\right)^{-1} \frac{d_{\phi\psi(\mathrm{hkl})} - d_0}{d_0} \frac{1}{\sin^2\psi} \qquad \textbf{(II.16)}$$

In Eq. II.16, the stress σ_ϕ is expressed as a function of the lattice spacing $d_{\phi\psi}$ and elastic constants for the (hkl) planes used for stress measurement at any angle ψ to the sample surface normal. Solving Eq. II.16 for the lattice spacing $d_{\phi\psi}$ gives

$$d_{\phi\psi(\mathrm{hkl})} = d_0\left(1 + \frac{1}{2}S_{2(\mathrm{hkl})}\sigma_\phi \sin^2\psi\right) \qquad \textbf{(II.17)}$$

which is the fundamental equation of the $\sin^2\psi$ method, showing that the lattice spacing $d_{\phi\psi}$ measured at any angle ψ to the surface normal varies linearly as a function of $\sin^2\psi$, assuming the plane stress condition. Eq. II.16 can be also written as

$$\sigma_\phi = \left(\frac{1}{2}S_{2(\mathrm{hkl})}\right)^{-1} \varepsilon_{\phi\psi(\mathrm{hkl})} \frac{1}{\sin^2\psi} \qquad \textbf{(II.18)}$$

where the deformation $\varepsilon_{\phi\psi(\mathrm{hkl})}$ is measured in the direction normal to the (hkl) planes and expressed as

$$\varepsilon_{\phi\psi(\mathrm{hkl})} = \frac{d_{\phi\psi(\mathrm{hkl})} - d_0}{d_0} \qquad \textbf{(II.19)}$$

Finally, defining

$$\varepsilon_{\phi(\mathrm{hkl})} = \varepsilon_{\phi\psi(\mathrm{hkl})} \frac{1}{\sin^2 \psi} \qquad \textbf{(II.20)}$$

Eq. II.18 becomes

$$\sigma_\phi = \left(\frac{1}{2} S_{2(\mathrm{hkl})} \right)^{-1} \varepsilon_{\phi(\mathrm{hkl})} \qquad \textbf{(II.21)}$$

If σ_ϕ is a tensile stress, the spacing between lattice planes parallel to the surface will be reduced by Poisson's ratio contraction, while the lattice spacing of planes tilted into the direction of the tensile stress will be expanded.

Differently from other techniques, such as ultrasonic and Barkhausen noise, no stress-free reference standards are required to determine d_0 for the $\sin^2\psi$ method applied to the X-ray diffraction technique [23]. The stress σ_ϕ is determined from elastic constants and the lattice spacing measured at $\psi = 0$. The stress state within the penetration depth of X-rays can then be determined by measuring the lattice spacing at different orientations to the sample surface. If the stress is determined in at least three different directions, the principal stresses and their directions can be calculated and the full stress tensor can be defined.

The residual stress determined by X-ray diffraction is the average stress in a volume of material defined by the irradiated area, which may vary from square centimeters to less than a square millimeter, and the penetration depth of X-rays. The linear absorption coefficient of the material for the radiation employed governs the penetration depth. For the techniques commonly used for steel, nickel, and aluminum alloys, 50% of the radiation is diffracted from a layer with less than 5 μm in depth. The shallow penetration depth and small irradiated area allow measurements of residual stress distributions with spatial and depth resolution exceeding all other methods [23].

II. 1.3. MICRODEFORMATIONS: METHODS OF PEAK BROADENING ANALYSIS [24-27]

On a very small scale, a plastically deformed metal can be considered as divided into small crystallites called coherently diffracting domains (CDDs); these domains being themselves elastically distorted. Each domain is formed from a group of cell columns, whose length L is perpendicular to the diffracting planes. The mean value of the column length L is

the size D of the CDD. The distortion of each column can be expressed by $\varepsilon_L = \Delta L/L$ and, considering the same length L for all columns, the microstrain is defined as $<\varepsilon_L^2>^{1/2}$, which is called the root mean square (RMS) strain.

Distortions of the regular crystal lattice as well as the size D of the coherently diffracting domain lead to peak broadening. Separation of the distortion (strain) effect from the size effect becomes possible considering that the diffraction order dependence of each effect is different. This can be done from analysis of the diffraction peak broadening described by physical models of the individual types of broadening. In the peak profile analysis, peak broadening is studied quantitatively by mathematical theories that allow the calculation of the coherently diffracting domain size D and microdeformations (distortion) $<\varepsilon^2>$. Different methods for peak profile analysis have been proposed. Two different models have been developed to separate strain and size broadening correctly: (i) the phenomenological model based on the elastic anisotropy of crystals, and (ii) the dislocation model based on the mean square strain of dislocated crystals. The latter takes into account that the effect of dislocations on strain broadening depends on the relative orientations between the line and Burgers vectors of dislocations and the diffraction vector.

Peak profile analysis has proven to be a powerful tool to obtain a number of relevant microstructural parameters. The method can quantitatively determine the dislocation density and assess the coherently diffracting domain size distribution in good accordance with other methods (e.g., transmission electron microscopy), but over larger sample volumes and with better statistics. The total dislocation density ρ_t can be estimated by the following expression

$$\rho_t = \frac{2\sqrt{3}}{b}\frac{<\varepsilon_L^2>^{1/2}}{D} \qquad \textbf{(II.22)}$$

where b is the magnitude of the Burgers vector. Eq. II.22 is only valid if the mean strain is caused only by dislocations with a restrictedly random distribution and if the influence of solute alloying atoms on $<\varepsilon_L^2>^{1/2}$ and of interfaces on D is negligible. From the microstrain $<\varepsilon_L^2>^{1/2}$ it is also possible to determine a mean micro residual stress using the Hooke's law

$$\sigma_{micro}^{rs} = E_{(hkl)} <\varepsilon_L^2>^{1/2} \qquad \textbf{(II.23)}$$

where $E_{(hkl)}$ is the crystallographic Young's modulus for the (hkl) planes.

The two classical methods of peak profile analysis are the Warren-Averbach analysis and the Williamson-Hall plot. For the different methods proposed, different profile data are concerned:

- the lowest order Fourier coefficients in the Warren-Averbach analysis and variants;
- the full width at half maximum (FWHM) or integral width in the Williamson-Hall plot and its modified version;
- fitting of the Fourier coefficients, or
- the intensity distribution of the profile in the momentum method.

Strain anisotropy and sometimes shape anisotropy can complicate the peak profile analysis. Strain anisotropy means that neither the Fourier coefficients nor the width of diffraction profiles are monotonous functions of the diffraction angle or of the magnitude of the diffraction vector g. Further difficulty is encountered by the fact that $<\varepsilon_{g,L}^2>$ is never a constant, neither as a function of g or the Fourier length L. The use of average contrast factors to characterize strain anisotropy has been suggested to account for these difficulties.

Peak broadening can also be characterized by the integral width or the FWHM, which can give at least qualitative information upon the dislocation network state.

WARREN-AVERBACH ANALYSIS [24,25,27,85]

Warren-Averbach analysis is the basis of the X-ray profile analysis. In this method, the diffracted intensity of the peak is obtained by convolution of size and distortion broadening. Fourier coefficients A_L of the physical profile of the diffraction peak are given by

$$A_{\mathrm{L}} = A_{\mathrm{L}}^{\mathrm{S}} A_{\mathrm{L}}^{\mathrm{D}} = A_{\mathrm{L}}^{\mathrm{S}} \exp(-2\pi^2 L^2 g^2 <\varepsilon_{\mathrm{g,L}}^2>) \qquad \textbf{(II.24)}$$

where $A_{\mathrm{L}}^{\mathrm{S}}$ and $A_{\mathrm{L}}^{\mathrm{D}}$ are Fourier coefficients related to size and distortion broadening, respectively, L is the Fourier variable (length), g is the magnitude of the diffraction vector and $<\varepsilon_{\mathrm{g,L}}^2>$ is the mean square strain. The Fourier variable L is written as

$$L = n\lambda / [2(\sin\theta_2 - \sin\theta_1)] \qquad \textbf{(II.25)}$$

where n are integers and $\lambda/[2(\sin\theta_2\text{-}\sin\theta_1)]$ is the unit of the Fourier length in the direction of the diffraction vector (peak profile measured in the angular range θ_2-θ_1), and λ is the wavelength of X-rays. Size and distortion broadening can be separated by plotting $\ln A_{\mathrm{L}}$ versus g for the lowest order Fourier coefficients. The average length of the CDD in the direction of

the diffraction vector is given by the initial slope of the plot of A_L^S versus L. The second derivative of this plot gives the CDD distribution. Distortion broadening coefficients are given by $A_L^D = \exp(-2\pi^2 L^2 g^2 < \varepsilon_{g,L}^2 >)$.

MODIFIED WARREN-AVERBACH ANALYSIS [24,25,27]

For strains caused by dislocations, Wilkens computed the mean square strain assuming a restrictedly random dislocation distribution in the modified Warren-Averbach analysis

$$< \varepsilon_{g,L}^2 > = -\left(\frac{b}{2\pi}\right)^2 \pi\rho C f(\eta) \qquad \textbf{(II.26)}$$

where ρ is the dislocation density, b is the magnitude of the Burgers vector, f(η) is the Wilkens function, and C is the contrast factor of dislocations to account for strain anisotropy. $\eta = L/R_e$, where R_e is the effective outer cut-off radius of dislocations. For $\eta \leq 1$ the Wilkens function can be approximated by a logarithmic function, and then

$$< \varepsilon_{g,L}^2 > \cong \frac{\rho C b^2}{4\pi} \ln\left(\frac{R_e}{L}\right) \qquad \textbf{(II.27)}$$

Contrast factors should be averaged over factors from edge and screw dislocations

$$\overline{C} = A - BH^2 \qquad \textbf{(II.28)}$$

where constants A and B depend on elastic constants of the material and on the character of dislocations (edge or screw), and H^2 is a function of the Miller indices (hkl)

$$H^2 = \frac{(h^2k^2 + h^2l^2 + k^2l^2)}{(h^2 + k^2 + l^2)^2} \qquad \textbf{(II.29)}$$

A is the average contrast factor corresponding to the h00 diffraction, i.e., $A = \overline{C}_{h00}$. Introducing Eq. II.27 into Eq. II.24, the modified Warren-Averbach equation is written as

$$A_L = A_L^S A_L^D \cong A_L^S \exp\left(-\frac{\pi}{2} L^2 g^2 b^2 \rho \overline{C} \ln\left(\frac{R_e}{L}\right)\right) \qquad \textbf{(II.30)}$$

Ungar et al. have also successfully considered effects of stacking faults and twins in the modified Warren-Averbach analysis by adding one more parameter to Eq. II.30 [86].

WILLIAMSON-HALL PLOT [24,25,27]

Williamson-Hall plot is the most direct method of X-ray profile analysis. Williamson and Hall calculated the integral width of a Bragg's peak [87] from the work of Warren and Averbach [85]. In the classical Williamson-Hall method, with the plot of the FWHM or integral width of the peak profile against the magnitude of the diffraction vector, size and distortion broadening effects can be separeted if an average particle size accurately describes the CDD distribution. Assuming that broadenig is predominatly caused by dislocations, the modified Williamson-Hall plot is written as

$$\Delta K \approx \frac{0.9}{D} + \left(\frac{\pi}{2}\right)^{1/2} Mb\rho^{1/2} K\overline{C}^{1/2} \qquad \textbf{(II.31)}$$

which gives the peak width ΔK in terms of $K = (2 \sin\theta)/\lambda$, where θ is the diffraction angle, D is the average CDD size, α is 0.9 or 1 for FWHM or integral width, respectively, ρ is dislocations density, b is the length of the Burgers vector, $\overline{C}$ is the average contrast factor of dislocations, and M is a constant related to the dislocation arrangement which depends on the effective outer cut-off radius of dislocations R_e. The disadvantage of a peak width based method is that, for a CDD distribution different from one average crystallite size, distortion and size effects cannot be separated.

FITTING OF FOURIER COEFFICIENTS [27]

Physical models presented in the Warren-Averbach analysis can be fitted to the low order Fourier coefficients computed from experimental data by software algorithms. The fitting parameters would be, for example, q or q_1 and q_2, for the average contrast factor, or ρ and R_e describing the dislocation arrangement.

MOMENTUM METHOD [27,88]

The momentum method (or variance method), first proposed by Wilson [89], uses a different approach to separate size and strain effects to peak broadening and to determine microstructural parameters. The momentum method takes into account the asymptotic behavior of the second and fourth order restricted moments of the intensity distribution and has been extended to include the size contribution. No assumptions are made for the shape of the CDD. The restricted moment of order k is defined as

$$M_k(q) = \frac{\int_{-q}^{q} q'^k I(q')\mathrm{d}q'}{\int_{-\infty}^{\infty} I(q')\mathrm{d}q'} \qquad \textbf{(II.32)}$$

in which $I(q)$ is the intensity distribution of the profile as a function of the scattering parameter $q = [2(\sin\theta - \sin\theta_0)]/\lambda$, where θ is the diffraction angle, θ_0 is the Bragg's angle, and λ is the wavelength of X-rays. Groma [90] derived a generalized version of the variance method using only analytical properties of displacement field of straight dislocations, without making assumptions on dislocation distribution. The advantage of this method is that the contributions to peak broadening can be observed immediately by plotting $M_2(q)$ and $M_4(q)/q^2$ versus q, due to the relatively simple dependence of microstructural parameters.

QUALITATIVE OR SEMI-QUANTITATIVE METHOD: FULL WIDTH AT HALF MAXIMUM (FWHM)

Analysis of peak broadening by measurement of the full width at half maximum (FWHM), or even the integral width, of the diffraction peak is a qualitative or semi-quantitative method. The FWHM is expressed by the angular deviation at the half-width of the peak. This method does not directly distinguish the two causes of broadening (size and distortion). However, if the instrumental errors of peak broadening are negligible, the FWHM can be used to estimate the average size D of the CDD by the Scherrer's equation [91]

$$D = \frac{k\lambda}{\mathrm{FWHM}\cos\theta} \qquad \textbf{(II.33)}$$

where k is the Scherrer's constant, λ is the wavelength of X-rays, θ is the diffraction angle and FWHM is expressed in radians. The Scherrer's constant k was found to vary between 0.89 and 1.39 according to Azaroff [91]. Assuming a Gaussian distribution for the diffraction peak, Warren obtained the value of 0.9 for k [92]. For its simplicity of measurement, the FWHM represents an interesting parameter to study the dislocation network state. The more common application of the method is the characterization of the work hardening state of materials. The study of the evolution of the FWHM is usually accompanied by observation of dislocation structures by transmission electron microscopy (TEM). The FWHM is adopted in this work to estimate changes in microdeformations with fatigue cycling.

II. 2. X-RAY DIFFRACTION APPLIED TO MECHANICAL CHARACTERIZATION OF MATERIALS

This section is dedicated to the literature review about the use of X-ray diffraction for mechanical characterization of materials.

X-ray diffraction technique is highly sensitive to changes in the crystalline structure of materials. The shape and position of an X-ray diffraction peak depend on microstructural parameters such as crystallite size, residual stresses, microstrains, stacking faults etc. [28]. The analysis of broadened XRD peaks can be used to study microstructural changes of plastically deformed crystalline materials [25]. The FWHM can be used to characterize the work hardening state of a material. An increase in FWHM results from increasing work hardening level [38,39], which is related to development of microdeformations in the material, mainly built up by increased dislocation density [39]. Microdeformations and lattice defects are one of the main mechanisms that result in increase of FWHM [66].

X-ray diffraction technique can be used to evaluate microstructural changes of a material under fatigue cycling, since they are expected to manifest as changes in XRD peak shape and position. The response of X-rays diffracted from a fatigued metallic material gives a great amount of information concerned with changes in crystallographic parameters ranging from microscopic to macroscopic scale.

It is well known that the residual stress state and the dislocation density in the near-surface zone of a material can drastically change as a function of the load cycles. The residual stress distribution, both micro and macro, which develops during fatigue cycling has far-reaching implications in phenomena related to reverse plastic flow, such as stress relaxation, Bauschinger effect and inelastic effects [47]. Within individual grains, dislocation pile-ups at obstacles are believed to be the primary origin of easily reversed plastic flow. Initial compressive macro residual stresses can be significantly relaxed during fatigue loading. Relaxation of macro residual stresses is related to redistribution and annihilation of dislocations and thus is also related to dislocation density [39].

Since fatigue fracture occurs as a result of deterioration of lattice structure, the progress of fatigue damage could be characterized by a parameter connected to lattice deterioration. The integral width β or the FWHM (also referred to as halfwidth b) of an X-ray diffraction peak have been proposed earlier by Taira [58] and Goto [68] as parameters characterizing fatigue damage. The FWHM parameter can be used in fatigue investigations allowing estimation of changes in micro residual stresses (microdeformations), dislocation density, work hardening state, and amount of plastic deformation [18-20,25,28,43,47,49]. The

XRD study of the evolution of residual stresses and microdeformations (characterized by the FWHM) can inform about the level of fatigue damage reached by a cyclically loaded material [51].

X-ray diffraction can also be used to perform a fatigue failure analysis. Residual stress measurements on fatigue fracture surfaces can provide important data to interpret fatigue failure and to determine working conditions that lead the part to fail [51].

X-ray diffraction technique presents two main interests for the study of microstructural changes during fatigue. Considering that X-ray penetration depth reaches about 5-10 μm, measurements are restricted to the near-surface zone of the material and the technique is particularly suitable, since during fatigue process the major microstructural evolutions take place in this zone. Additionally, this technique is nondestructive and can be employed several times during fatigue test. The use of modern portable systems extends the feasibility of the technique for in-service fatigue damage assessment of structural components.

Obviously, X-ray diffraction technique cannot elucidate the whole nature of fatigue damage and must be supported by data gained by other evaluation techniques, of macroscopic, sub-macroscopic and microscopic aspects, to increase the understanding of this complex phenomenon. Nevertheless, X-ray diffraction could be one of the most useful means of bridging the seemingly dissociated macroscopic and microscopic approaches to fatigue studies that have been usually carried out independently until now.

In a number of previous works reported in the literature, X-ray diffraction studies of fatigue damage, or at least changes in microstructural parameters, were carried out by the evaluation of the evolution of microdeformations and residual stresses with fatigue cycling [10,18-20,28-72].

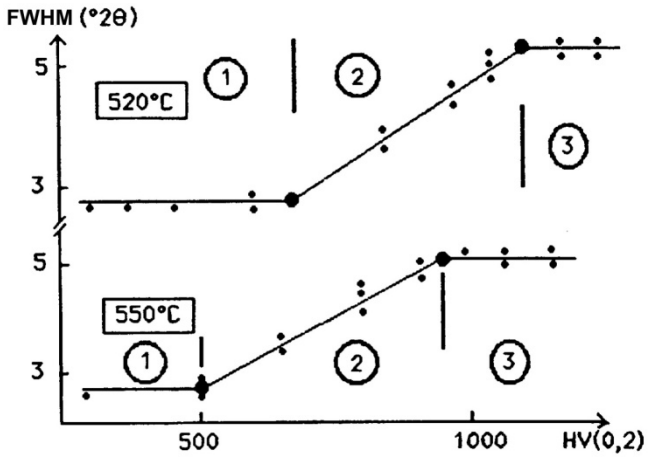

Figure II.6. FWHM versus microhardness for two different nitrided steels [94].

II. 2.1. INFLUENCE OF THE MATERIAL AND ITS PREPARATION PROCESS

A linear relationship between hardness and microdeformation in several nitrided steels was found by Mittemeijer [93]. However, Barralis have shown that this relationship is not always linear and monotonic, and that it can be described by three stages [94], as shown in Fig. II.6. Stage 1, which corresponds to the transition between the diffusion zone of the nitrogen and the base metal, is associated with hardening by solid solution of nitrogen and increasing microhardness, even at constant FWHM. In stage 2, local high microdeformations are created by nitride precipitates that gradually appear, which lead to increasing FWHM. In stage 3, there is a saturation of microdeformations in the near-surface zone and hardening is related to the formation of other types of nitrides.

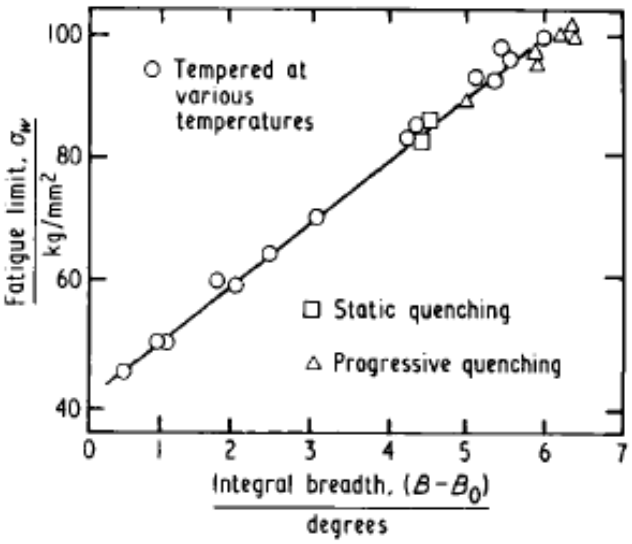

Figure II.7. Relation between fatigue limit and integral width (integral breadth) for induction-hardened 0.45% carbon steel bars [67].

Since the fatigue strength of a metal is intimately related to its microstructure state, the assessment of the fatigue strength on the basis of microstructural parameters given by X-ray diffraction was proposed in [67]. In Fig. II.7 the fatigue limit is shown as a function of the integral width of the XRD peak measured before fatigue test [67]. The influence of macro and micro residual stresses on the fatigue strength depends on the initial microstructure of the material. For low hardness materials (< 280 HV) the greater influence are exerted by micro residual stresses; macro residual stresses tend to relax. For high hardness materials (> 800 HV) the influence of macro residual stresses and their distribution are more significant; macro residual stresses are not relaxed and microdeformations have no significant influence. For

materials with intermediate hardness values, both behaviors are observed, but with moderate influence [69].

Microstructural changes during the early stages of fatigue are connected to multiplication, movement and rearrangement of dislocations and strain localization. From a macroscopic point of view, these changes are characterized by cyclic hardening or softening, depending on the initial structural state of the material [10]. Fatigue cycling can involve the decay in the dislocation density, or cold work (work hardening), characterized by a reduction in the FWHM of diffraction peaks. The decrease in FWHM values was related to cyclic softening in peak- and over-aged AA6110 aluminum alloy, while cyclic hardening and increase in FWHM was observed for as-quenched and under-aged AA6110 aluminum alloy [34]. The evolution of FWHM was found to decrease in regular successive stages during fatigue process of cold worked, shot peened, deep rolled, and laser-shock peened (hardened) steel samples [19,36-44]. However, if the initial state of a material is annealed, then cyclic loading will most likely increase lattice distortion and lead to the formation of cell dislocation configurations. The increase in lattice distortion is caused by an increase in the dislocation density from dislocation regeneration. Therefore, in general, in the early stage of fatigue, the FWHM may increase for an annealed material, while for a hardened (cold worked) material the FWHM may decrease [10,18-20,28-71].

X-ray diffraction has been widely applied to study the stability of residual stresses and work hardening state (characterized by FWHM) induced on metallic materials by mechanical surface treatments, such as shot peening, deep rolling, and laser-shock peening [18,36-39,59,65,66,68]. Near-surface macroscopic compressive residual stresses and work hardening state induced by these treatments relax during mechanical and/or thermal loading when elastic residual strains can be converted into microscopic plastic strains (dislocation movement, rearrangement and annihilation as well as micro/macroscopic crack initiation) [66]. Residual stress relaxation is strongly affected by the cyclic deformation behavior of the material. A strong correlation between residual stresses, FWHM and plastic strain amplitudes was observed [37,39,65,66]. Effects of dynamic and/or static strain ageing in combination with mechanical surface treatments result in more stable near-surface stress states and microstructures due to solute atoms or fine precipitates which impede the migration of dislocations and increase the resistance to local plastic flow [41]. Relaxation of residual stresses in surface treated steels is slightly faster than that of FWHM values, since for relaxation of macro residual stresses dislocation movement is sufficient, whereas for a distinct relaxation of micro residual stresses additional dislocation annihilation is necessary [66].

Since the hard near-surface regions have lower plastic flow (less dislocation movement) than the soft core, the FWHM values should show slighter changes than residual stresses [41]. The effectiveness of mechanical surface treatments is governed by cyclic and thermal stability of the near-surface work hardening state rather than compressive residual stresses. Residual stress relaxation increases with increasing test temperature, since dislocation movement and rearrangement as well as micro/macroscopic crack initiation are enhanced [31]. Fatigue cycling at high temperatures caused the almost complete relaxation of residual stresses in deep rolled and laser-shock peened Ti-6Al-4V titanium alloy samples, while FWHM values remained essentially stable with cycling at room and high temperatures [54].

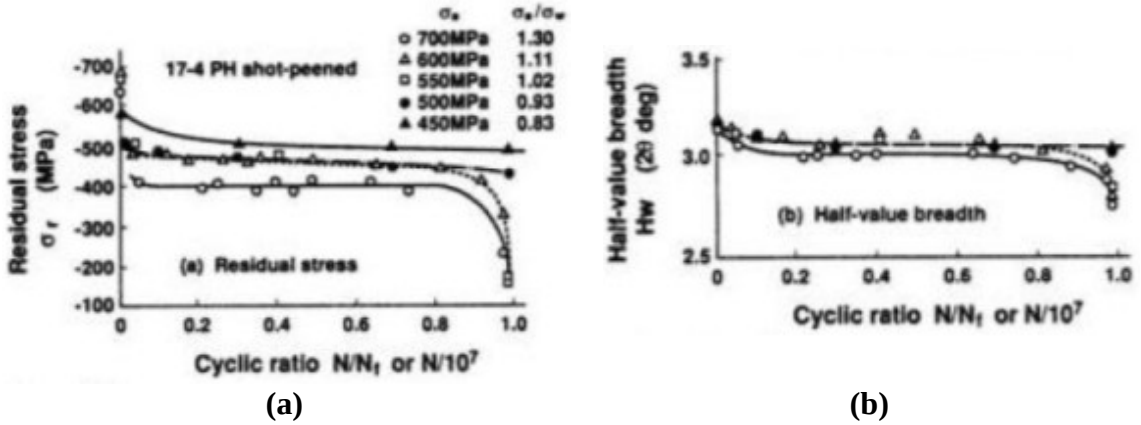

(a) **(b)**

Figure II.8. Evolution of (a) residual stresses and (b) FWHM (half-value breadth) with the fatigue life fraction (N/N_f) of shot peened 17-4 PH stainless steel samples under high cycle fatigue at different stress amplitudes [68].

In [68] the evolution of residual stresses and FWHM during high cycle fatigue on shot peened 17-4 PH stainless steel samples was found to follow a regular three-stage decreasing behavior, as shown in Fig. II.8. Figure II.9(a) shows that the plastic strain amplitude controlled the residual stress relaxation during cyclic deformation of shot peened normalized SAE 1045 steel samples [65]. When cyclic plastic deformation set in, macro residual stresses relaxed almost completely and micro residual stresses (FWHM) also considerably relaxed. These changes were caused by rearrangement of tangled dislocations, induced in near-surface regions by shot peening, into cell structures. The decrease in FWHM was related to the lower dislocation density inside the cells. Cyclic softening by annihilation processes gave rise to further decrease of FWHM until sample fracture. The stability of dislocation arrangements (FWHM values) and residual stresses of shot peened samples with cycling depended strongly on the stress amplitude (Fig. II.9(b)).

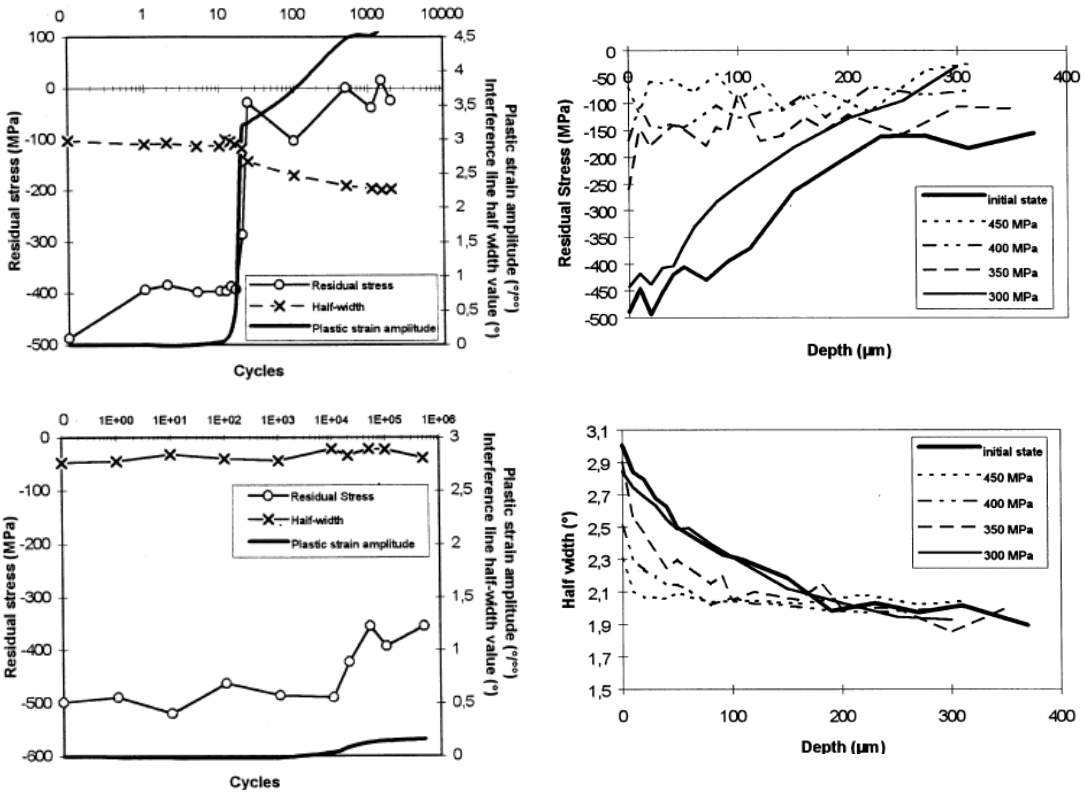

Figure II.9. (a) Evolution of residual stresses, FWHM and plastic strain amplitudes with cycling (σ_a = 300, above, and 450 MPa, below) and (b) depth profiles of residual stress and FWHM at $N = N_f/2$ in shot peened normalized SAE 1045 steel samples [65].

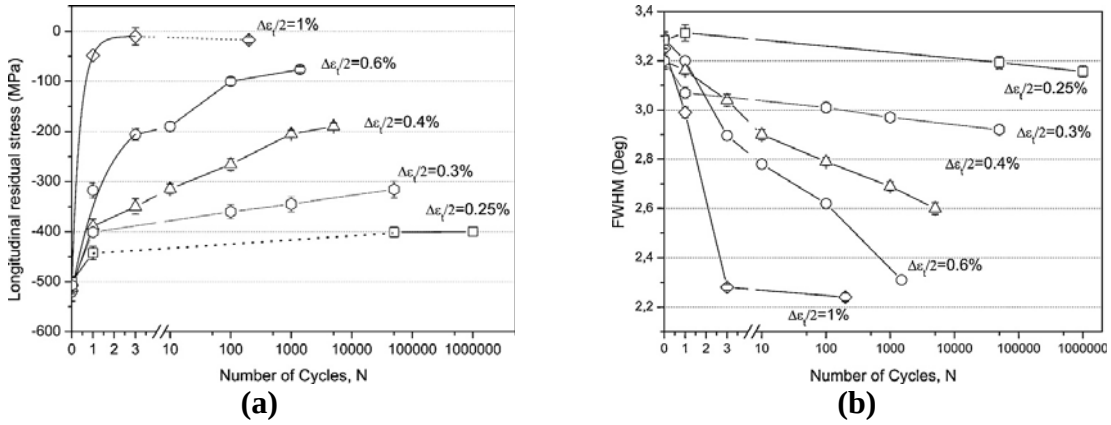

Figure II.10. Relaxation of (a) residual stresses and (b) work hardening in shot peened near pearlitic carbon steel samples up to $N = N_f/2$ at different strain amplitudes [39].

In [38,39] the relaxation of compressive residual stresses and recovery of work hardening in surface layers of shot peened microalloyed near pearlitic carbon steel samples under strain controlled push-pull loading were studied. At high strain amplitudes the denser dislocation network created led to cyclic hardening, while at low strain amplitudes the looser and consequently more flexible network created resulted in cyclic softening in the early

cycles. Compressive residual stresses and work hardening (FWHM) at the surface decreased with the number of cycles and increasing strain amplitude, as depicted in Fig. II.10. A linear relation between FWHM, compressive residual stresses and work hardened layer depth was observed at any strain amplitude.

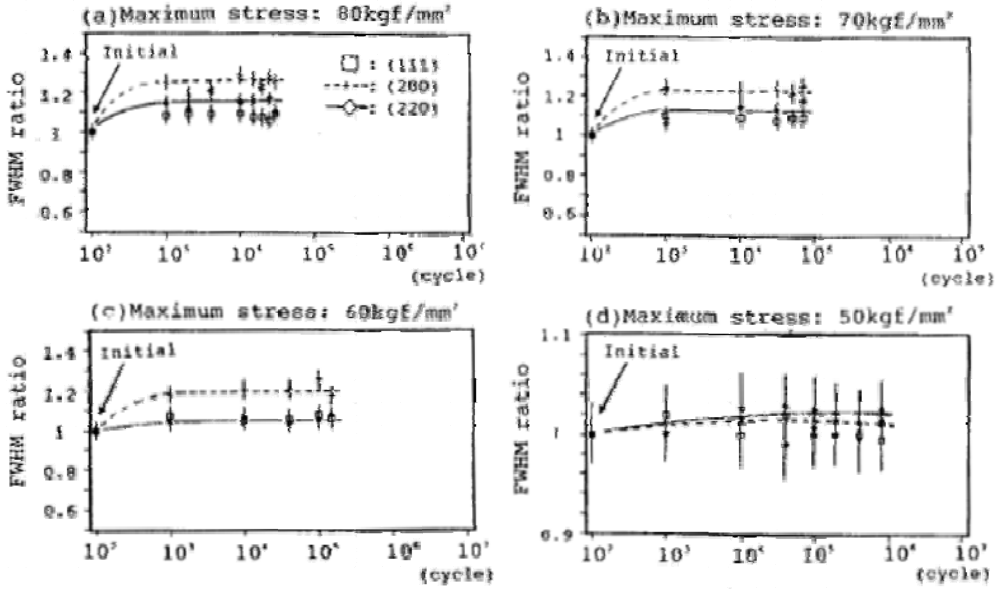

Figure II.11. Evolution of FWHM ratio with fatigue cycling of mill-annealed nickel-chromium alloy 718 samples [18].

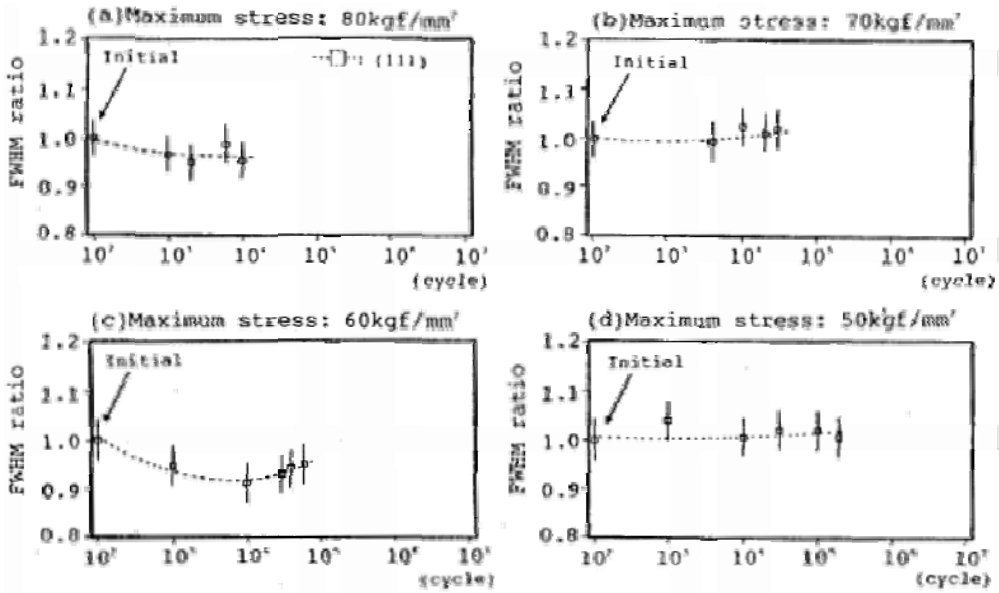

Figure II.12. Evolution of FWHM ratio with fatigue cycling of shot peened nickel-chromium alloy 718 samples [18].

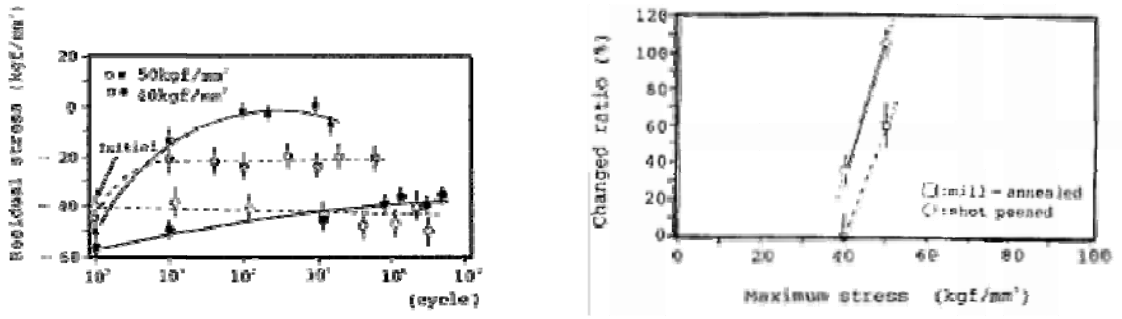

(a) **(b)**

Figure II.13. Changes in residual stresses with fatigue cycling in nickel-chromium alloy 718 samples (open symbols: mill-annealed; solid symbols: shot peened) [18].

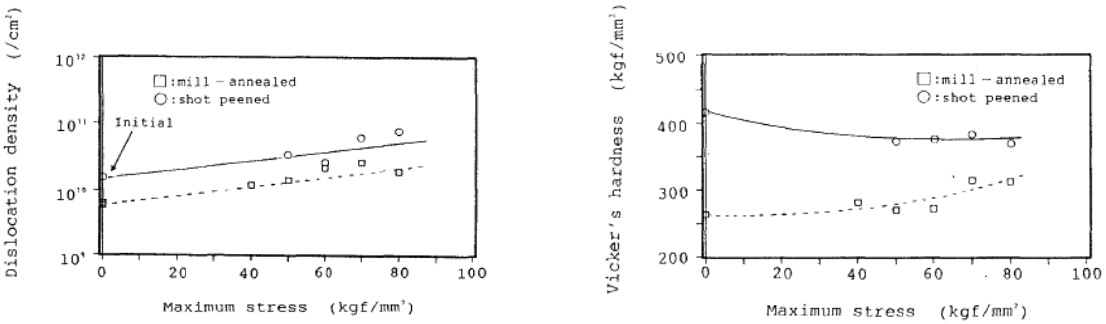

(a) **(b)**

Figure II.14. (a) Dislocation density and (b) Vickers microhardness of fatigued samples at various maximum stress levels [18].

In [18] fatigue damage in mill-annealed and shot peened nickel-chromium alloy 718 samples under repeated tensile fatigue was evaluated by X-ray diffraction. Different diffraction planes were considered for X-ray diffraction measurements to study the angular dependence of XRD parameters with fatigue cycling. For both mill-annealed and shot peened samples, the evolution of the FWHM ratio ($FWHM/FWHM_0$) with cycling depended strongly on applied stresses and lattice planes. FWHM increased with fatigue cycling for mill-annealed samples (cyclic hardening), while FWHM decreased for shot peened samples (cyclic softening), as depicted in Figs.II.11 and II.12. Changes in residual stresses in shot peened samples were more significant than that of mill-annealed samples for high applied stresses (Fig. II.13). For both mill-annealed and shot peened samples, the residual stress was more sensitive to high cycle fatigue damage than FWHM. The change in residual stresses was suggested as a damage indicator for mill-annealed and shot peened nickel-chromium alloy 718 samples under high cycle fatigue. As observed by TEM (transmission electron microscopy), the dislocation density increased during fatigue cycling with increasing applied stress for both types of samples (Fig. II.14(a)). At the same applied stress, shot peened

samples showed higher dislocation density than mill-annealed samples. Vickers microhardness measurements confirmed that mill-annealed samples showed cyclic hardening with fatigue cycling, and instead shot peened samples showed cyclic softening (Fig. II.14 (b)).

Relaxation of residual stresses induced by shot peening in AISI 4140 steel samples, normalized and quenched and tempered, under fatigue cycling at high temperatures was studied in [36]. Higher compressive residual stresses were induced on the quenched and tempered state. While FWHM values in the surface region of normalized samples increased as a result of shot peening, no significant change of FWHM was observed in quenched and tempered samples. In the quenched and tempered state, the Bauschinger effect resulted in lower compressive yield strength at the surface in comparison to the core region due to work softening induced by shot peening at the surface layer. In the normalized state, the deformation during shot peening led to a strongly work hardened surface, related to locally increased dislocation densities, and higher yield strengths at the surface than in the core material, as a consequence of the weaker Bauschinger effect. Higher residual stress relaxation was observed for the normalized state, in which compressive residual stresses relaxed during heating up and waiting for temperature compensation, and then the critical compressive loading stress necessary for the start of mechanical relaxation increased. In contrast, in the quenched and tempered state the critical compressive loading stress decreased considerably with the test temperature because of the stronger Bauschinger effect and the weaker effects of dynamic strain ageing due to significantly higher dislocation densities.

In [59] the residual stress relaxation in shot peened Udimet 720Li polycrystalline nickel base alloy samples under strain controlled isothermal low cycle fatigue tests at high temperatures was investigated. Irrespective of the testing temperature, the first cycle caused the maximum compressive residual stress to relax by more than 50%, as shown in Fig. II.15(a). Relaxation of compressive residual stresses would be expected to occur readily by plastification over the compressive half of the cycle (reverse straining), intensified by the Bauschinger effect, since in compression the yield strength at the work hardened near-surface region is lower than that in the bulk material. At higher numbers of cycles, the residual stress relaxation was controlled by temperature dependent mechanisms, in contrast to the relaxation occurring after the first cycle. The extent of residual stress relaxation upon further cycling was increased with increasing temperature. Instead of cyclic hardening at low temperatures, cyclic softening was observed at higher temperatures. Consequently, the integral width of the XRD peak increased at low temperatures and decreased at high temperatures (Fig. II.15). The reduction in the integral width in the first cycle was due to a thermally activated mechanism

of redistribution of metastable lattice defects induced by shot peening, and with further cycling it was controlled by both thermal and mechanical processes.

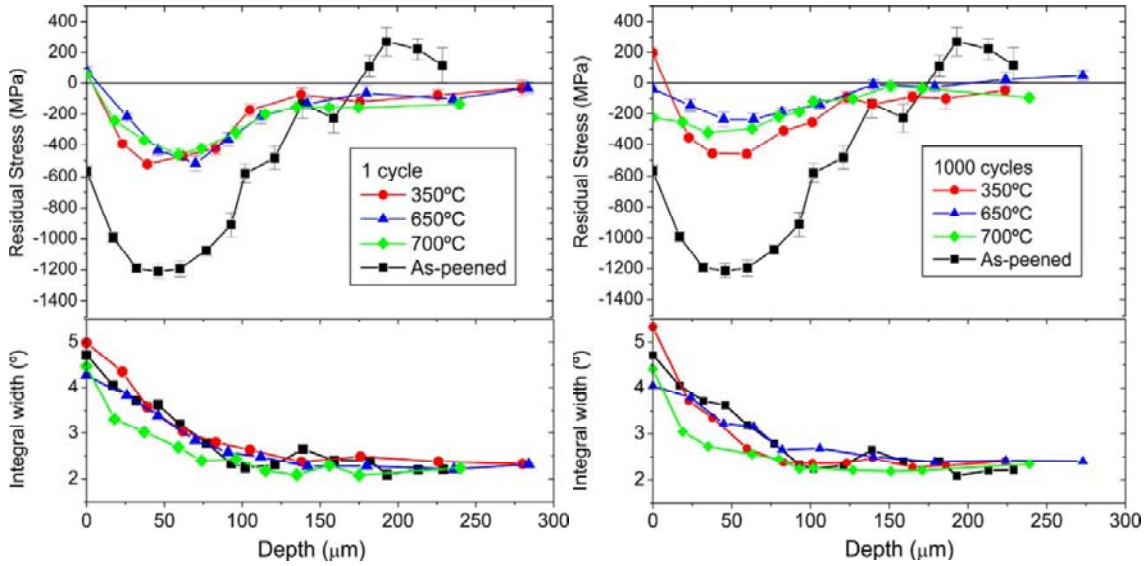

Figure II.15. Depth profiles of residual stresses and FWHM after (a) 1 cycle and (b) 1000 cycles of 1.2% strain controlled isothermal fatigue at different temperatures [59].

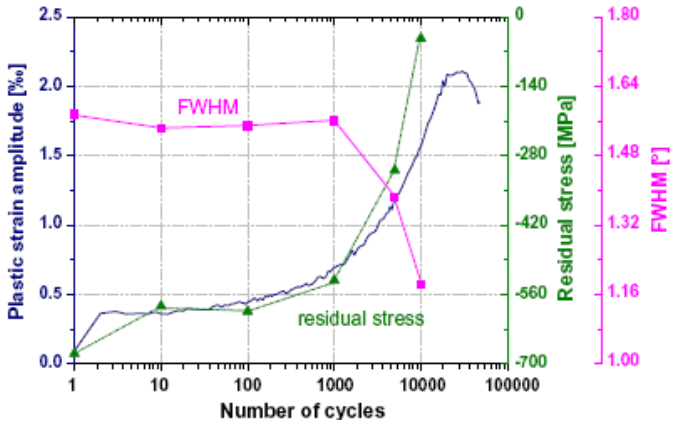

Figure II.16. Correlation between plastic strain amplitude and relaxation of residual stresses and FWHM values in function of the number of cycles (stress amplitude of 340 MPa) [42].

Relaxation of near-surface residual stresses and work hardening in deep rolled AISI 304 austenitic stainless steel samples during isothermal fatigue was strongly dependent on the number of cycles, stress amplitude and temperature [42]. Relaxation of residual stresses and FWHM values followed the cyclic softening of the material, as shown in Fig. II.16. At high temperatures, the relaxation was independent of the test temperature and depended only on the stress amplitude.

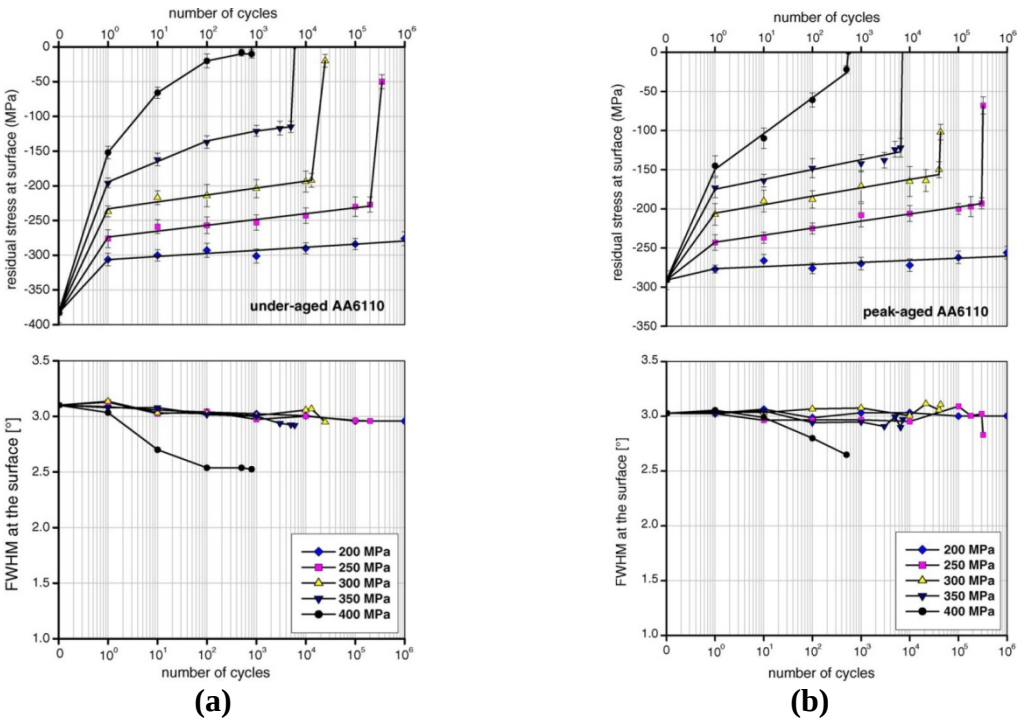

Figure II.17. Relaxation of residual stresses and FWHM at the surface of (a) under- and (b) peak-aged deep rolled AA6110 with cycling at different stress amplitudes [30].

Figure II.17 shows the relaxation of residual stresses and FWHM values on under- and peak-aged deep rolled AA6110 aluminum alloy samples [29,30]. Residual stress relaxation in deep rolled AA6110 aluminum alloy samples at elevated temperatures can be separated into mechanical and thermal control relaxation mechanisms [31]. Residual stress relaxation during fatigue tests at elevated temperatures was controlled by mechanical process until approximately 10^3 cycles and by thermal mechanical process for higher number of cycles.

Residual stresses in quenched and tempered AISI 4140 steel samples submitted to alternating bending fatigue tests relaxed more in the conventional shot peening condition than in the warm shot peening and consecutive conventional peening and annealing conditions [37], as shown in Fig. II.18. FWHM at the surface induced by warm shot peening and consecutive conventional peening and annealing were much higher than that induced by conventional shot peening. FWHM decreased linearly with the logarithm of the number of cycles in samples conventionally shot peened, while warm-peened and consecutive peened and annealed materials showed practically no relaxation of micro residual stresses, since their dislocation arrangements were considerably more stable. This was due to static strain ageing induced by annealing after conventional shot peening, and dynamic strain ageing produced by warm shot peening. Relaxation of macro residual stresses in warm shot peening and consecutive shot peening and annealing conditions was mainly due to dislocations that were

newly generated with cyclic loading, which is suggested by the increase of FWHM values for wide intervals of $N > 1$ (cyclic hardening) (Fig. II.18). Stress amplitude thresholds below which residual stresses and FWHM values remained unaltered by fatigue cycling were defined. For each shot peening state, the threshold for FWHM relaxation was several hundred MPa higher than that for residual stress relaxation. Thresholds for the conventional shot peening state were lower than for the other states.

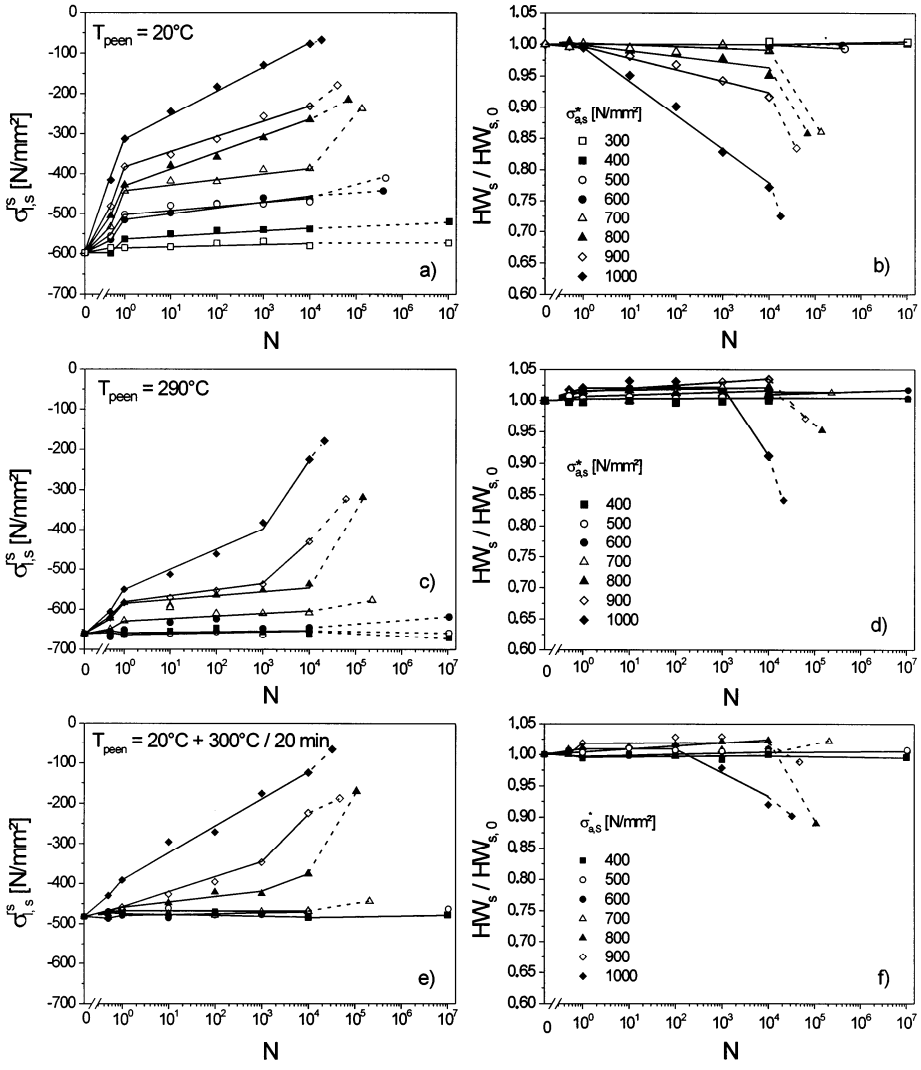

Figure II.18. Relaxation of residual stresses (a, c, e) and FWHM values (b, d, f) with fatigue cycling at different stress amplitudes for samples under conventional shot peening, warm shot peening and consecutive shot peening and annealing states [37].

In [62] effects of deep rolling temperature on the fatigue behavior of AISI 304 steel were investigated. Deep rolling at low temperatures as well as above 400°C led to relatively small compressive residual stresses, as shown in Fig. II.19. FWHM values at the surface

decreased continuously with increasing deep rolling temperature, but at greater depths higher FWHM values were found for deep rolling at high temperatures (Fig. II.19).

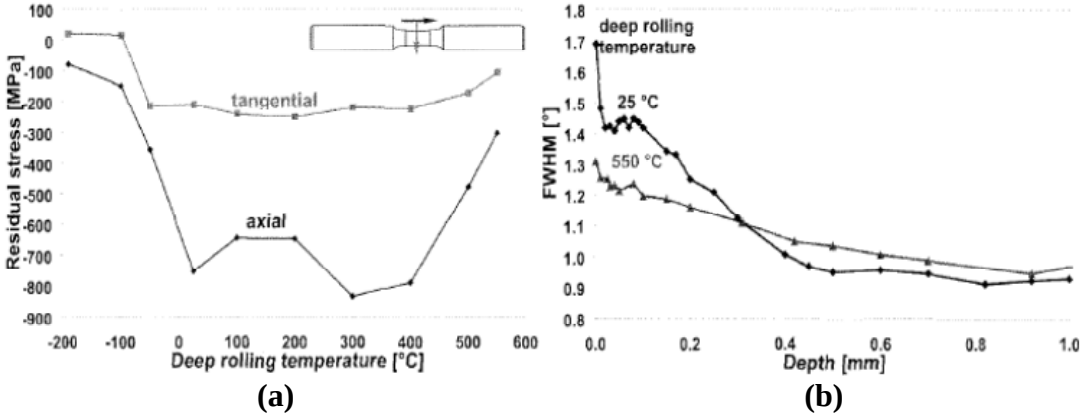

Figure II.19. (a) Residual stresses at the surface as a function of the deep rolling temperature and (b) depth profiles of FWHM values at different temperatures of deep rolled AISI 304 steel samples [62].

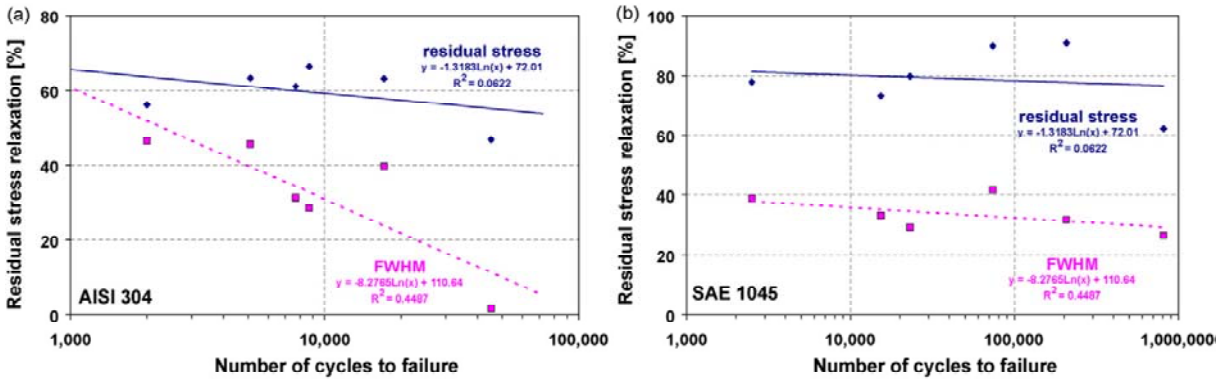

Figure II.20. Correlation between residual stress and FWHM at half of lifetime to failure ($N_f/2$) and the number of cycles to failure for deep rolled (a) AISI 304 and (b) SAE 1045 steel samples [41].

Consecutive deep rolling and annealing and high temperature deep rolling produced more stable near-surface stress states (lower relaxation of residual stresses and FWHM), lower plastic strain amplitudes, and consequently higher fatigue life improvement than conventional deep rolling in AISI 304 austenitic stainless steel and SAE 1045 ferritic-pearlitic steel samples under stress-controlled low cycle fatigue [41]. This was due to, respectively, static and dynamic strain ageing effects introduced by consecutive deep rolling and annealing and high temperature deep rolling. Due to higher work hardening level induced by deep rolling, SAE 1045 steel showed more stability of residual stresses and work hardening than AISI 304 steel, even if initial higher compressive residual stresses were induced by deep

rolling in AISI 304 steel samples. It was suggested that the residual stress can be used to evaluate the fatigue damage state in deep rolled AISI 304 and SAE 1045 steel samples under stress-controlled cyclic loading, according to plots shown in Fig. II.20.

Relaxation of compressive residual stresses and recovery of cold work at the surface of shot peened 2024-T351 aluminum alloy samples under tension-tension cyclic loading were studied in [60,61] for different shot peening intensities. Compressive residual stresses and cold work level were greater for higher shot peening intensities. The relaxation rate of residual stresses and reduction of cold work increased with increasing shot peening intensity, as shown in Fig. II.21.

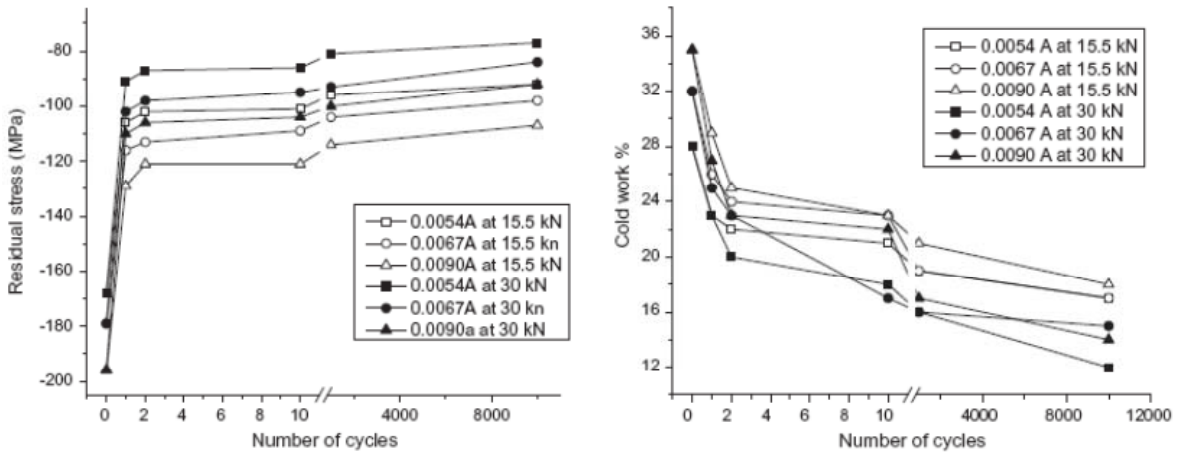

(a) (b)

Figure II.21. (a) Residual stress relaxation and (b) cold work reduction at the surface of shot peened 2024-T351 aluminum alloy samples submitted to different shot peening intensities at different applied loads [60].

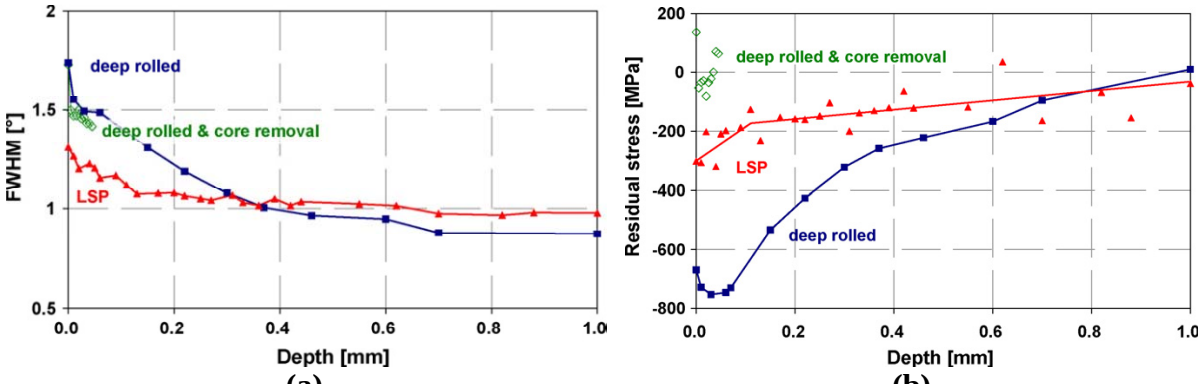

(a) (b)

Figure II.22. Depth profiles of (a) FWHM values and (b) residual stresses for deep rolled and laser-shock peened AISI 304 samples before fatigue tests [43].

In [43] samples were specially prepared by removing the core material (hollow samples) to investigate near-surface microstructures of laser-shock peened and deep rolled AISI 304 austenitic stainless steel samples without any surface-core interactions. In hollow samples, effects caused by different depths of affected zones were avoided. After core removal, near-surface residual stresses relaxed almost completely in deep rolled hollow samples, while FWHM values remained almost identical to the deep rolled round samples, as shown in Fig. II.22. This indicated that the FWHM value was not sensitive to long-range residual stresses. At high temperatures, deep rolled samples presented more stable microstructure.

In [56] the evolution of fatigue damage on untreated and laser surface treated (melting) AISI 316L austenitic stainless steel samples under high cycle fatigue tests was associated with progressive work hardening at the material surface, estimated by the integral width β of the XRD peak. Work hardening at the surface increased with fatigue cycling, and at each fatigue life fraction a maximum work hardening level (β_{max}) was reached, as shown in Fig. II.23(a). β_{max} increased continuously up to a critical value β^*, when the highest level of work hardening withstood by the material was reached and fracture occurred. In untreated samples, surface work hardening increased gradually and quite uniformly over the gage length during fatigue life up to fracture. This behavior was associated with the homogenous microstructure of untreated samples, which was well defined and independent of the applied load or number of cycles. In laser treated samples, surface work hardening increased uniformly for most of fatigue life and at end of fatigue life, a sharp peak developed at the fracture point (Fig. II.23(a)). This behavior was associated with a non-homogeneous microstructure in laser treated samples, with nonuniform distribution of potential sites for damage nucleation. In general, values of β were lower in laser treated than in untreated samples for all applied loads, indicating the smaller amount of work hardening and lower density of slip lines at the surface accumulated during fatigue in laser treated samples, as a consequence of the initial work hardening induced by the surface treatment. For both types of samples, β_{max} increased with increasing fatigue life fraction (N/N_f) and applied load, as shown in Fig. II.23(b). The integral width β was proposed as a fatigue damage parameter, and the correlation between β_{max} and the fatigue life fraction was proposed to be used for prediction of the remaining life of untreated and laser treated AISI 316L steel samples, if reference curves representing the initial state of the same material are considered.

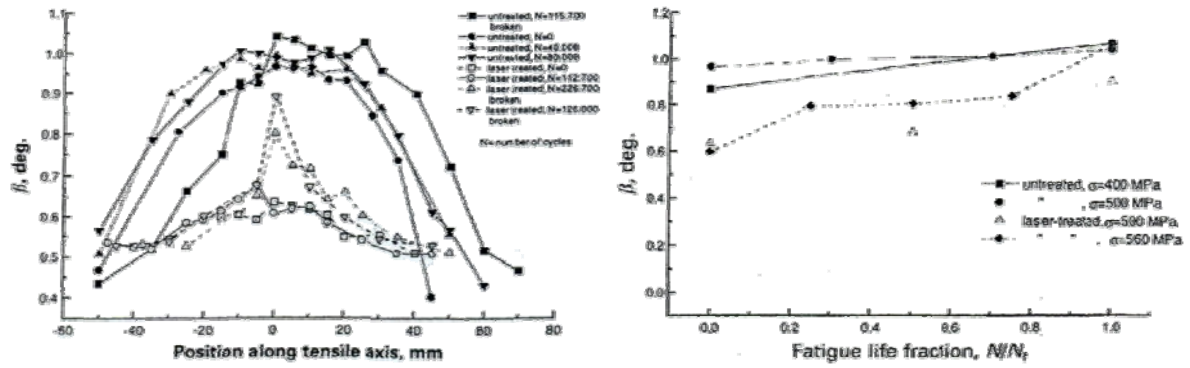

(a) **(b)**

Figure II.23. Integral width β of fatigue cycled untreated and laser treated AISI 316L steel samples (a) along gage length at applied load of 500 MPa and (b) as a function of fatigue life fraction (N/N_f) at different applied loads [56].

Residual stresses relaxed with increasing number of cycles of thermal shock load in hot-work tool AISI H11 steel samples in hard turned, electroeroded, weak shot peened, coarse shot peened and deep rolled surface conditions [49], as shown in Fig. II.24. FWHM values decreased with increasing number of cycles of thermal shock load in mechanically treated samples, but in eroded samples FWHM values were almost not affected. This results from more stable dislocation structures of electroeroded samples against thermal load.

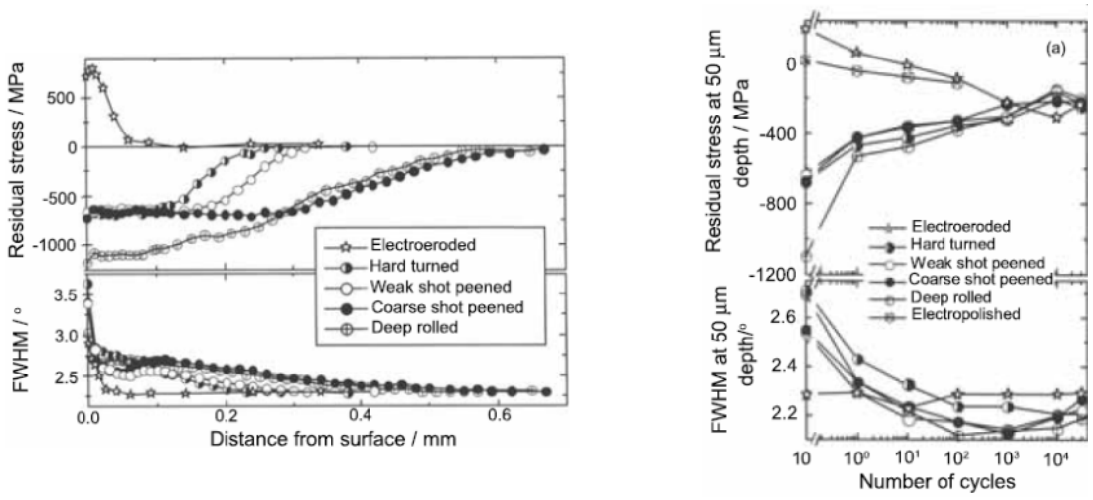

(a) **(b)**

Figure II.24. (a) Residual stress and FWHM depth profiles and (b) residual stresses and FWHM values at 50 µm depth versus number of cycles of thermal shock load in hot-work tool AISI H11 steel samples with different surface conditions [49].

In [51] the evolution of fatigue damage in shot peened carburized and hardened 16CrNi4 steel spur gear teeth subjected to rolling contact fatigue tests under operative

conditions was evaluated by X-ray diffraction. At the dedendum, FWHM values at the surface were progressively increased as a function of the number of cycles and were stabilized after 2/3 of the total duration of the test, as shown in Fig. II.25. The grain distortion induced by shot peening was considered as the cause of an uncertain trend in the evolution of FWHM values at the addendum surface observed with fatigue cycling.

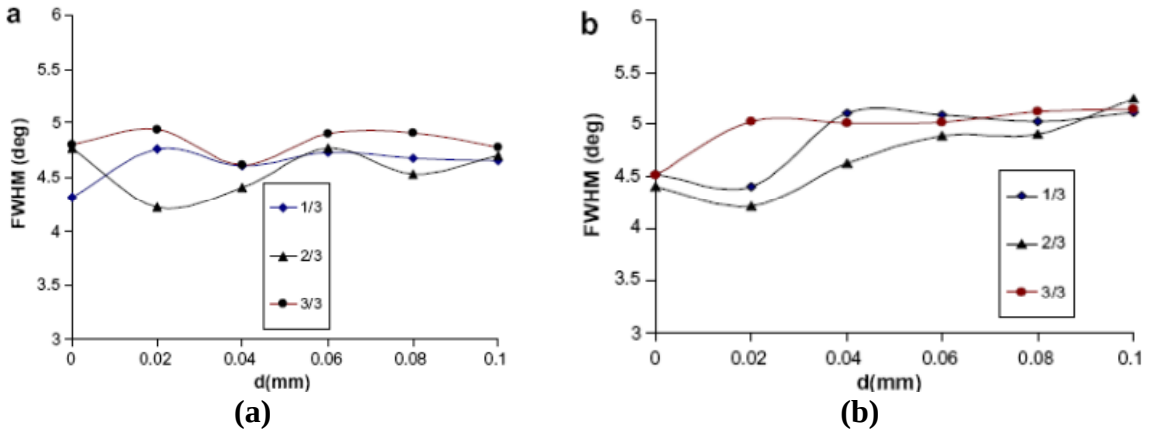

Figure II.25. Depth profiles of FWHM values at 1/3, 2/3 and 3/3 of the total number of cycles in shot peened carburized and hardened 16CrNi4 steel spur gear teeth at the (a) dedendum and (b) addendum [51].

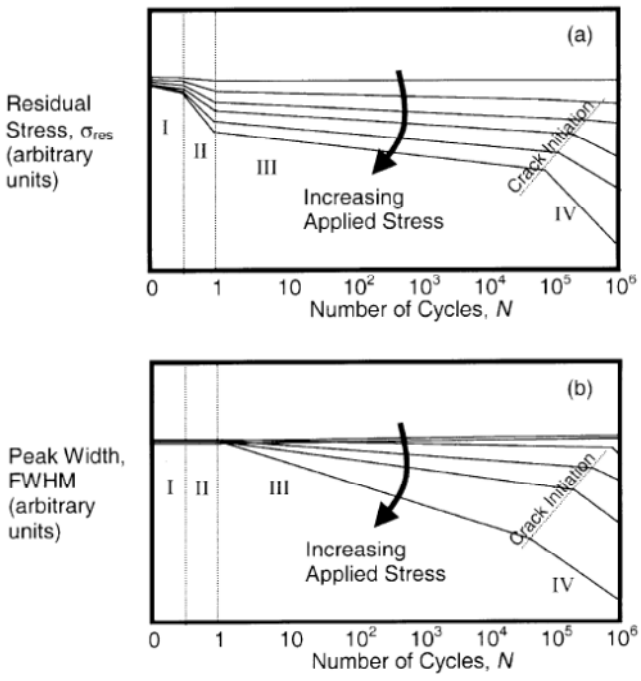

Figure II.26. Schematic illustration of the relaxation behavior of (a) residual stresses and (b) FWHM as a function of applied stress and number of cycles in mechanically surface treated metallic samples [35].

Figure II.26 schematic illustrates the relaxation of (a) residual stresses and (b) work hardening state (FWHM) as a function of applied stress and number of cycles observed in mechanically surface treated metallic samples [35,66]. During the first cycle the load reversal leads to relaxation of long-range residual stresses, and then, with further cycling, short-range residual stresses are relaxed by microstructural processes in near-surface regions when cyclic softening sets in. In general, the relaxation of macro residual stresses can be divided in four phases [35-37,66]: (I) quasi-static relaxation during the first half-cycle (tensile portion of the first cycle); (II) quasi-static relaxation during the second half-cycle due to load reversal (compressive portion of the first cycle); (III) cyclic relaxation up to crack initiation (N_i = number of cycles to crack initiation), which usually leads to linear reduction of residual stresses as function of the logarithm of the number of cycles, and (IV) cyclic relaxation after crack initiation and until failure ($N_i \leq N \leq N_f$) for sufficiently high applied stress amplitudes, which is enforced in the plastic zones at the tips of surface cracks.

Residual stress relaxation occurring at $1< N < N_i$ is thought to be related to cyclic softening and is typically associated with reordering of the dislocation substructure. Thus, arrangements of dislocations generated by mechanical surface treatments are changed to configurations typical for fatigue loading. Upon formation and propagation of a surface crack, the relaxation rate can increase, presumably due to the stress-concentrating effect and plasticity associated with the crack. For each of the four phases, there is a material dependent stress amplitude threshold below which no relaxation is seen. The rate of relaxation of FWHM and residual stresses is accentuated with increasing applied stress.

II. 2.2. INFLUENCE OF THE LOADING TYPE

II. 2.2.1. MONOTONIC (STATIC) LOADINGS

In the case of mechanical testing as tension or compression tests, it was shown that variations in FWHM are influenced by the plastic deformation level and also by loading conditions (plastic deformation rate and temperature, for example) [9,95], as illustrated schematically in Fig. II.27. In compression, and at low plastic deformations, the formation of dislocation cells is observed, and their observation increases with increasing deformation rate. With increasing deformation rate, dislocations walls progressively increase and become less dense. For deformation testing carried out on coppers, it was found the presence of a recrystallization zone of copper grains associated with increasing temperature [70]. This

phenomenon entails a decrease in the dislocation density, accompanied by lower FWHM values (Fig. II.27). In tension, the FWHM presents the same evolution under plastic deformation, which suggests a similar process of deformation.

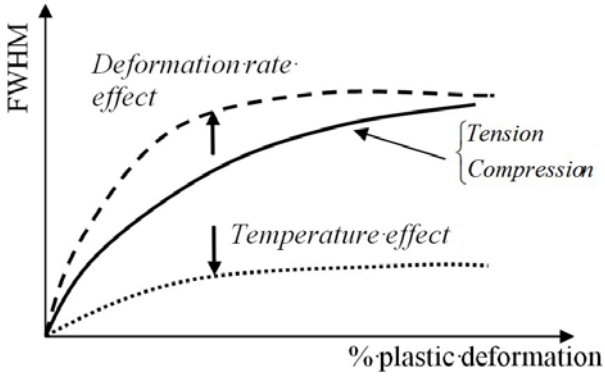

Figure II.27. Schema of variations of FWHM in tension and compression tests as a function of the plastic deformation rate and temperature (adapted from [70]).

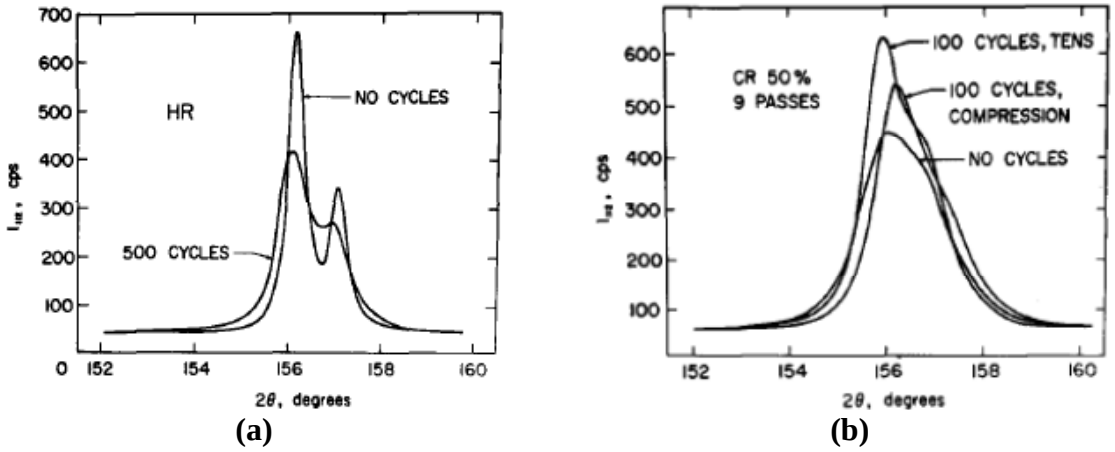

Figure II.28. Diffraction peaks of (a) hot-rolled (HR) and (b) 50% cold-rolled (CR 50%) steel samples under strain-controlled cyclic deformation [47].

II. 2.2.2. LOW CYCLE FATIGUE LOADINGS

The residual stress relaxation of high strength low alloy (HSLA) steel samples in hot-rolled (HR) and 50% cold-rolled (CR 50%) conditions during strain controlled fatigue tests (tension-compression loading) was studied in [47]. Hot-rolled steel samples exhibited a stable stress response (neither cyclic hardening nor softening) and broadening of the XRD peak (increase in FWHM) during fatigue cycling, as shown in Fig. II.28(a); before cycling the peak was sharp, characteristic of an annealed material. Sharpening of the XRD peak (decrease in FWHM) with cyclic softening was observed during fatigue cycling of cold-rolled steel

samples (Fig. II.28(b)), indicating that the distortion introduced by cold rolling was relieved with cyclic deformation. This was associated with the reduction in the dislocation density through formation of dislocations cells, which was verified by transmission electron microscopy. The initial high compressive macro residual stresses at the surface were released with cyclic deformation. At each strain reversal, the sign of macro residual stresses was opposite to the previous released strain, as shown in Fig. II.29. The rate of residual stress release increased with increasing strain amplitude.

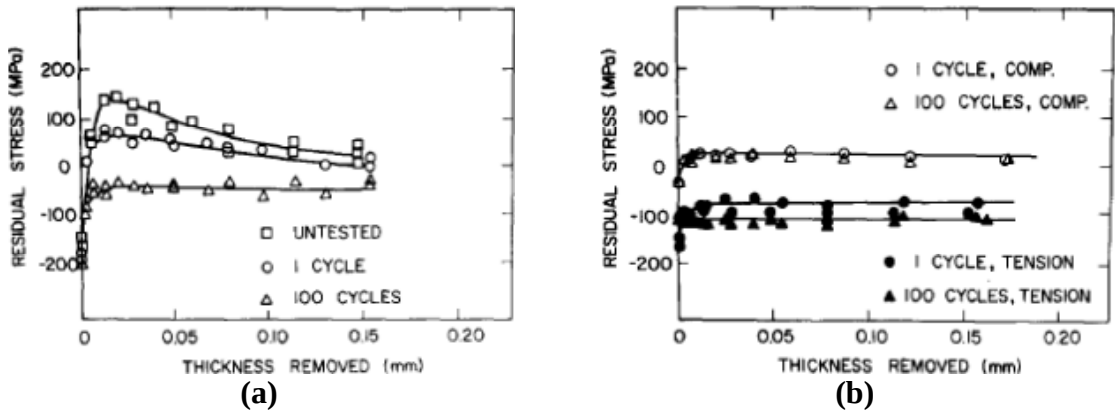

Figure II.29. Depth profiles of macro residual stresses of CR 50% samples under strain-controlled cyclic deformation at strain amplitudes of (a) 0.25% (release from tension) and (b) 1% (release from both tension and compression) [47].

In [57] the surface work hardening in 80 C4 steel samples submitted to thermal fatigue and isothermal low cycle fatigue tests was estimated from measurements of the XRD peak width. It was found that the peak width *B* (measured at 2/5 of the peak height) can be qualitatively correlated to microstructural evolutions of the material (dislocation density) evaluated by TEM. Despite the dispersion of results, a correlation between work hardening and the stress amplitude was found in low cycle fatigue tests, independent of both deformation mode and temperature, as shown in Fig. II.30(a). It was then suggested that the peak width *B* can be used as a parameter to predict the fatigue life under both isothermal low cycle fatigue and thermal fatigue. The lifetime prediction under thermal fatigue was based on the correlation between the level of work hardening of the material and the number of cycles to failure in isothermal fatigue tests, and on the introduction of the concept of an equivalent temperature. The equivalent temperature (20°C) was defined as the temperature under which the fatigue life of a sample submitted to isothermal fatigue is similar to that of a sample submitted to thermal fatigue (Fig. II.30(b)). It was found that the peak width in fatigued samples was inversely proportional to the number of cycles to failure.

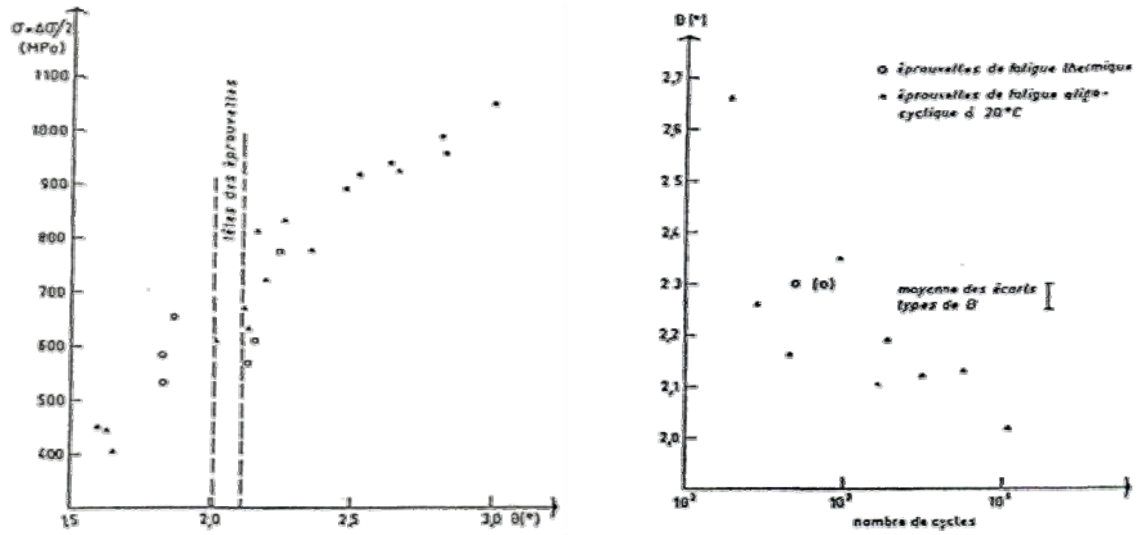

(a) **(b)**

Figure II.30. (a) Correlation between the peak width *B* and (a) the stress amplitude at different deformation modes and temperatures, and (b) number of cycles to failure for samples under isothermal low cycle fatigue and thermal fatigue at 20°C [57].

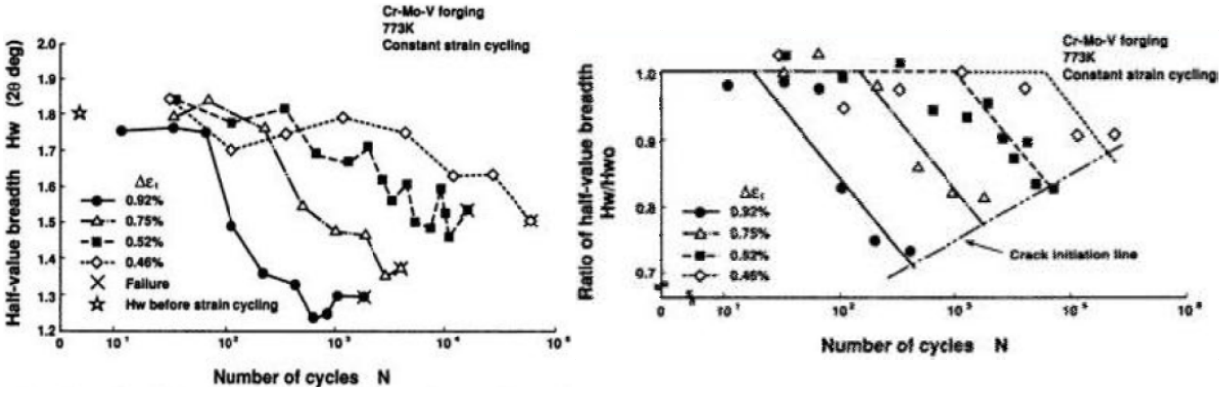

(a) **(b)**

Figure II.31. Changes in (a) H_w during fatigue life and (b) H_w/H_{wo} before crack initiation in Cr-Mo-V forged steel samples under high temperature low cycle fatigue [68].

In [68] the evolution of FWHM (half-value breadth, H_w) in Cr-Mo-V forged steel samples during high temperature low cycle fatigue under strain control was investigated. It was found that, except at the initial stage, the relation between the half-value breadth ratio (H_w/H_{wo}, where H_{wo} is the half-value breadth at $N = 0$) and the number of cycles can be represented by straight lines with a constant slope for different strain amplitudes on a log graph, as shown in Fig. II.31(a). The relation between the half-value breadth ratio and the number of cycles at crack initiation was represented by the "crack initiation line" (Fig. II.31(b)). A method was proposed for fatigue life prediction, as illustrated in Fig. II.32(a): the interception of the constant slope straight line through the point defined by the half-value

breadth ratio H_w/H_{wo} measured at a giving number of cycles N (point A) with the crack initiation line (point B) gives the number of cycles at crack initiation N_c. The fatigue damage is then estimated as N/N_c and the residual fatigue life as N_c-N. In Fig. II.32(b) fatigue life fractions of Cr-Mo-V forged steel samples obtained experimentally and estimated by the proposed method are compared. It was found that all data, except at extremely small life-fraction values, were located within the bounds of a factor of 2. It should be mentioned that the method is restricted to the material and testing conditions employed and a scatter factor of 2 must be taken into account.

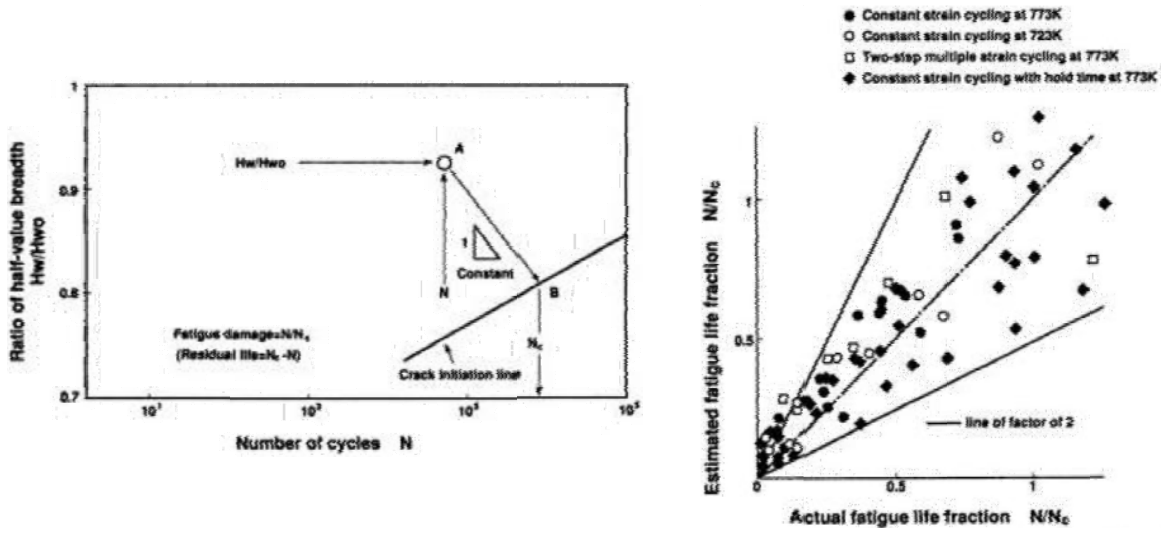

(a) **(b)**

Figure II.32. (a) Scheme of the method proposed for fatigue life estimation and (b) comparison between estimated and actual fatigue life fraction of Cr-Mo-V forged steel samples under high temperature strain-controlled low cycle fatigue [68].

In [20] the X-ray diffraction technique is used to study the low cycle fatigue (LCF) behavior of normalized and tempered 9Cr–1Mo ferritic steel samples through measurements of FWHM under strain-controlled fully reversed cyclic loadings. Initial high compressive macro residual stresses were relieved in the first cycles, and low (approximately zero) residual stresses were present throughout fatigue cycling. Different stages of LCF deformation and damage of normalized and tempered 9Cr–1Mo steel could be observed during the evolution of FWHM and tensile stress amplitude with fatigue cycling, as presented in Fig. II.33. These stages are associated with initial cyclic hardening, followed by gradual cyclic softening, saturation, and crack initiation and propagation. At all strain amplitudes, it was observed a rapid increase in FWHM in the early fatigue cycles, which corresponds to initial cyclic hardening and can be attributed to dislocation-dislocation and precipitate-dislocation

interactions resulting in the increase of dislocation tangles and dislocations entangled with matrix precipitates. Increasing the strain amplitude intensified the initial cyclic hardening, accentuating the FWHM increase. In the cyclic softening stage, which occurred during the major fatigue life fraction, the gradual decrease in stress values with increasing number of cycles could arise from the annihilation of dislocations introduced during martensitic transformation, development of cell structure within the martensite laths and transformation of original lath structure to cell structure. Since this new dislocation arrangement would lead to regions of high dislocation density (cell walls) and regions of low dislocation density (cell interior), no significant change in FWHM was observed during the softening stage. The saturation stage occurred at higher number of cycles with constant stress response over a large number of cycles. Since this stage results from a balance between cyclic hardening and cyclic softening and a stable dislocation substructure, no significant changes in FWHM values were observed. Only a marginal increase in FWHM was observed at high strain amplitudes, attributed to the accumulation of plastic strain. The saturation stage persisted until crack initiation and propagation impaired the load bearing capacity of the sample, as indicated by a rapid drop in the cyclic stress response. This was followed by a fast decrease in FWHM due to relaxation of microdeformations. Since the stage of crack propagation would take smaller number of cycles for sample fracture, it was suggested that the rapid decrease in FWHM in this stage could be used as a LCF life criterion, remaining within 10% of the fatigue life for the final failure.

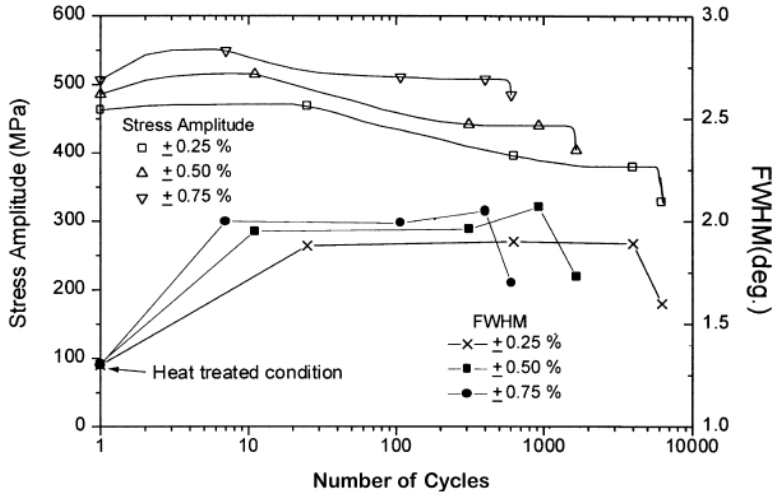

Figure II.33. Changes in tensile stress amplitude and FWHM with cycling of normalized and tempered 9Cr–1Mo ferritic steel samples at different strain amplitudes [20].

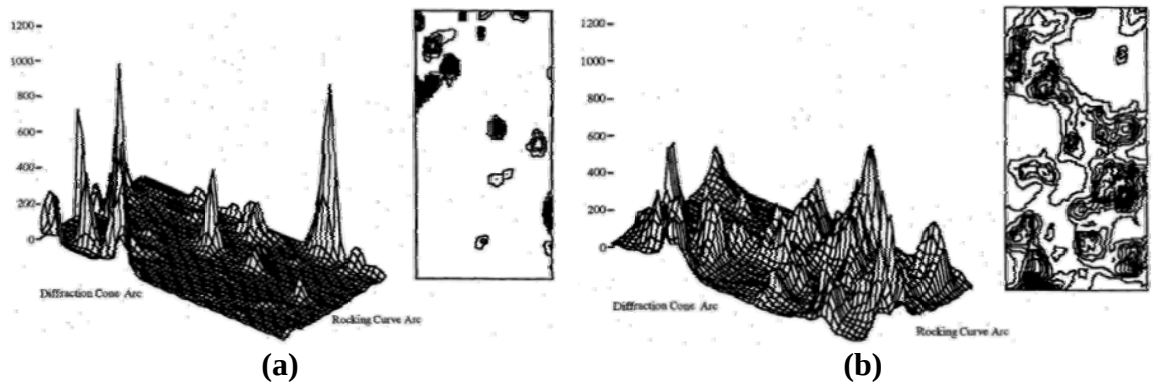

(a) **(b)**

Figure II.34. Contour plots of XRDCD data from the near-surface of AISI 304 steel samples under cyclic deformation at $\Delta\varepsilon$ = 1.20% at (a) initial and (b) failure states [55].

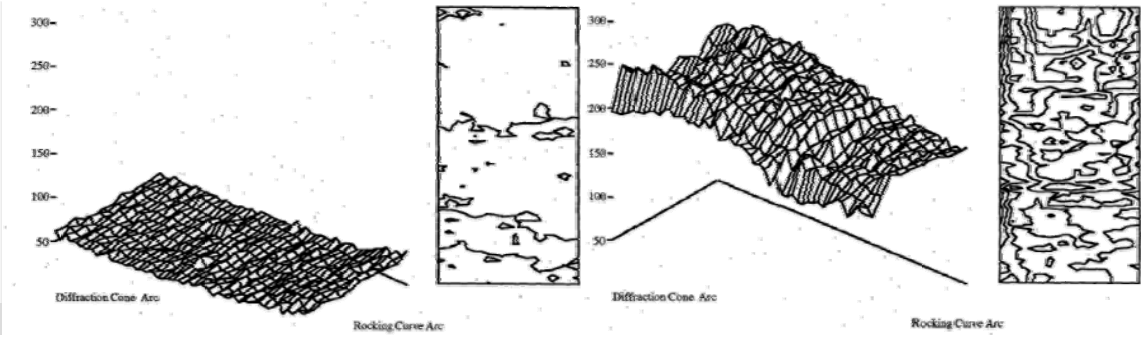

(a) **(b)**

Figure II.35. Contour plots of XRDCD data from the near-surface of SA 508 steel samples under cyclic deformation at $\Delta\varepsilon$ = 0.78% at (a) initial and (b) failure states [55].

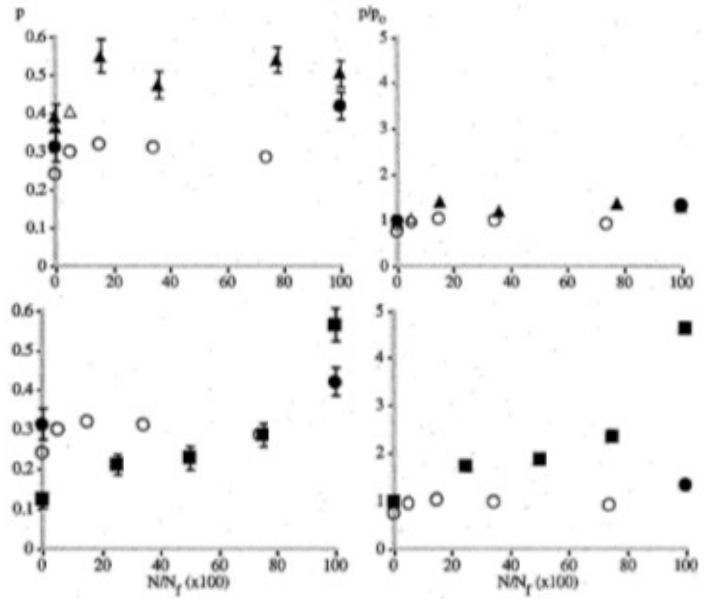

Figure II.36. Individual peak analysis of XRDCD data for AISI304 steel: absolute (left column) and normalized (right column) values of the estimator. •(○) $\Delta\varepsilon$ = 0.60%, near-surface; ▲(△) $\Delta\varepsilon$ = 1.20%, near-surface, and ■(□) $\Delta\varepsilon$ = 0.60%, bulk [55].

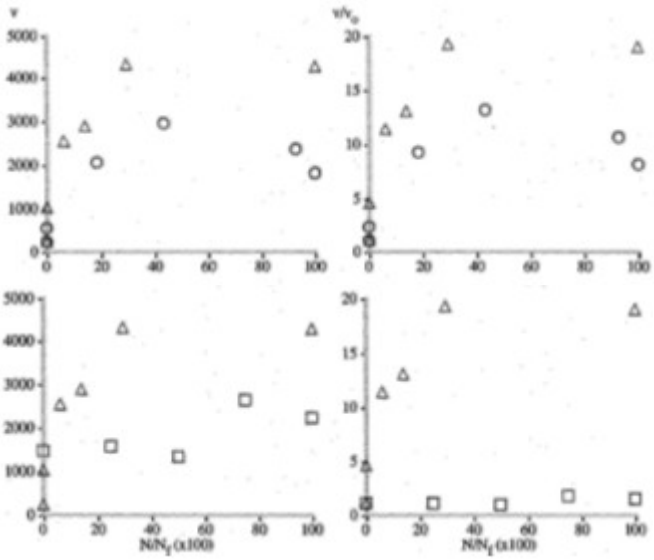

Figure II.37. Variance analysis of XRDCD data for SA508 steel. ○ $\Delta\varepsilon$ = 0.48%, near-surface; ▵ $\Delta\varepsilon$ = 0.78%, near-surface, and ▫ $\Delta\varepsilon$ = 0.78%, bulk [55].

In [55] X-ray double crystal diffractometry (XRDCD) was used to assess cyclic microstructural deformation on annealed AISI 304 steel samples and on quenched and tempered SA 508 steel samples submitted to tension-compression fatigue loading. Data obtained from XRDCD measurements were evaluated according to two different methods, the individual peak analysis and the variance analysis. In the individual peak analysis, an individual diffraction peak was identified and the integral breadth was measured. Identification and deconvolution of individual diffraction peaks from XRDCD data require several mathematical operations. As an alternative to individual peak analysis, an aggregate analysis of the same data provides a mathematically simple, but less sensitive approach. Since diffraction peaks broaden or contract with microstructural deformation, the deviation of each data point from the mean intensity of all data points will also change, then a variance analysis of XRDCD data was proposed. Plots of XRDCD data from the near-surface region showed that AISI 304 steel samples exhibited peak broadening, while SA 508 steel samples exhibited peak sharpening, as indicated in Figs. II.34 and II.35. Figure II.36 shows results from individual peak analysis of XRDCD data of AISI 304 steel samples, where the population proportion estimator, defined as the proportion of integral breadths that exceed the initial average integral breadth, was used to quantify the change in integral breadth distributions. Solid symbols represent results that have a statistically significant difference from the initial state, while open symbols represent results with no statistically significant difference from the initial state. Initially, the annealed AISI 304 steel had a low dislocation density as compared to a cold worked material. During cyclic loading, dislocation regeneration occurred to

accommodate the imposed strains. The increase in the dislocation density enhanced the development of cell dislocation structures as the dislocations reconfigured into lower energy states. As a result, the integral breadths of X-ray diffraction peaks increased with cycling. Initially, the free surface attracts dislocations and allows them to egress, but the increase in the near-surface strain energy due to the increase in dislocation density begins to repel dislocations rather than attract them. Therefore, the increase in integral breadths was greater in the bulk and subsurface than in the near-surface. It was also found that integral breadths increased as the strain amplitude ($\Delta\varepsilon$) increased. On the other hand, the quenched and tempered SA 508 steel contains ferrite laths that confer a high initial density of randomly oriented dislocations. Cyclic loading provided energy for the dislocations to glide and reconfigure into lower strain energy configurations. During this process, dislocation annihilation and egress at the free surface occurred. Therefore, the dislocation density and lattice distortion decreased, and then the integral breadths of X-ray diffraction peaks reduced with fatigue cycling. This is indicated by the increase in the variance parameter, as shown in Fig. II.37. Due to egress of dislocations at the free surface, the decrease in lattice distortion was greater in the near-surface region than in the bulk region. The reduction in lattice distortion increased with increasing strain amplitude.

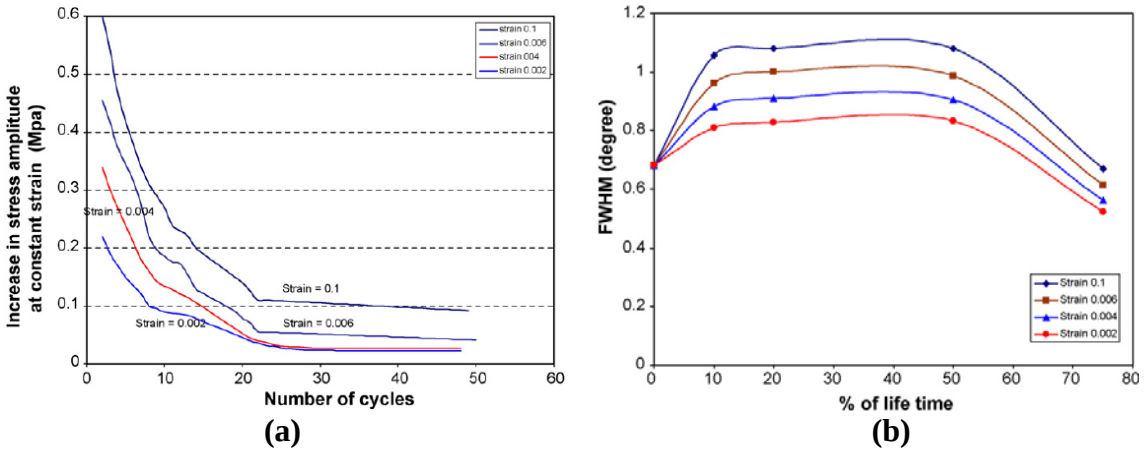

Figure II.38. (a) Cyclic hardening behavior of DP600 steel samples at the first 50 cycles and (b) evolution of FWHM with fatigue cycling at different stain amplitudes [50].

In [50] the evolution of fatigue damage and the low cycle fatigue (LCF) behavior of DP600 dual-phase (martensite and ferrite) high strength steel samples under fully reversed strain-controlled tension-compression loading were investigated from measurements of FWHM. The LCF life of DP600 steel was characterized by three stages: a high cyclic hardening during the first few cycles, followed by a gradual hardening for most of fatigue life

and finally a rapid drop in stress carrying capability prior to final failure. The rate of hardening at the first stage increased with increasing strain amplitude, as shown in Fig. II.38(a). The cyclic deformation behavior of the DP600 steel was correlated to the evolution of FWHM. It was found that sources of LCF behavior and XRD peak broadening were similar, and the main source was related to microstructure changes in the material with fatigue cycling. The basic mechanisms leading to fatigue hardening are dislocation structure changes and dislocation movement barriers during cycling. An increase in dislocation density by multiplication and rearranging of dislocation substructure in the soft matrix makes obstacles to dislocation movements and lead to fatigue hardening. A significant increase in FWHM was observed in the initial cycles, followed by a small change for large numbers of cycles, and a sharp decrease in FWHM prior to final fracture, as shown in Fig. II.38(b). The rapid initial increase in FWHM values in the first cycles was associated to the high initial cyclic hardening and can be ascribed to dislocation-dislocation and second phase-dislocation interactions, which increase microdeformations and then the FWHM. XRD peak broadening was sensitive to the strain amplitude and the fraction of fatigue life (damage) of the sample: FWHM values increased with increasing strain amplitude and number of cycles. Further straining changed dislocation arrangement and dislocation structure gradually, and therefore FWHM exhibited small changes. The rapid decrease in FWHM near the end of LCF tests was attributed to relaxation of microdeformations due to crack initiation and propagation.

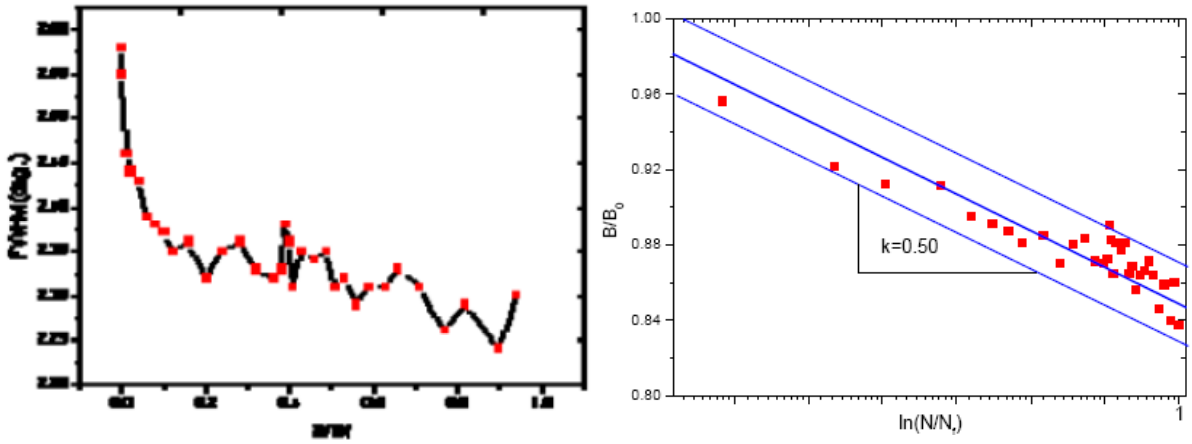

(a) (b)

Figure II.39. Variation of (a) FWHM and (b) B/B_0 with life consumption rate N/N_f in the base metal (strain amplitude of 0.4%) [53].

In [53] the evolution of FWHM of XRD peaks during strain-controlled low cycle fatigue of P92 steel samples was studied. The work investigated the relation between fatigue

damage and FWHM and proposed a method for fatigue life assessment of high temperature P92 steel pipelines. FWHM values decreased rapidly in the first cycles until 20% of the fatigue life. With further cycling, FWHM remained almost constant in the softening and saturation stages, and at about 90% of the fatigue life, a rapid decrease in FWHM was observed (Fig. II.39(a)). As shown in Fig. II.39(b), a linear relationship between the FWHM ratio (B/B_0) and the fatigue life ratio (N/N_f) was observed and expressed as

$$B / B_0 = k \ln(N / N_f) + C \qquad \textbf{(II.34)}$$

where B and B_0 are respectively FWHM values measured at the number of cycles N and before cycling, k is the slope of the linear equation, and C is a material constant given by the FWHM ratio at failure. It was suggested that this relationship can give direct prediction of the life consumption ratio, providing that the initial and current values of FWHM are known.

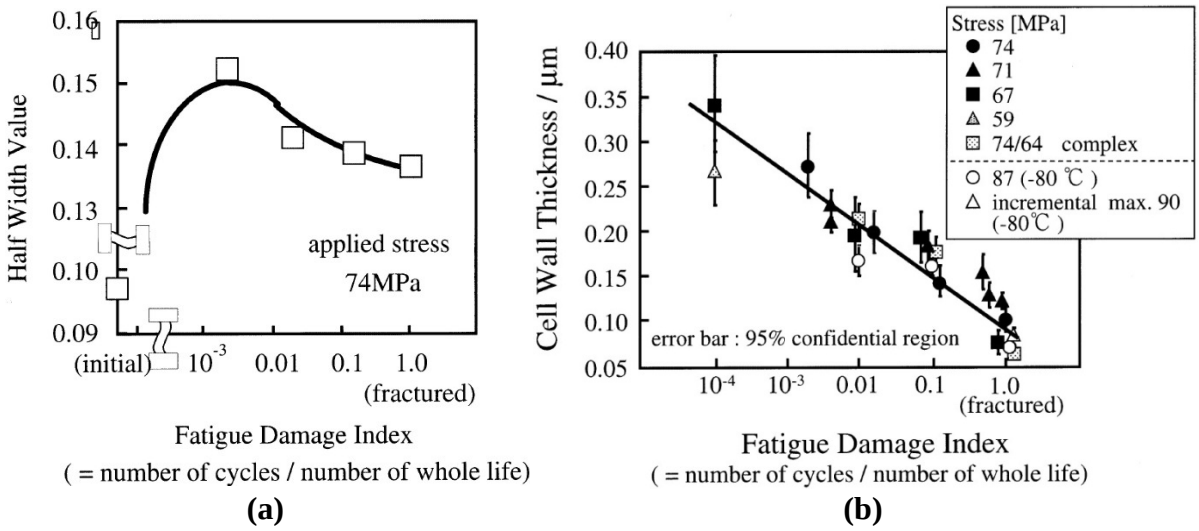

Figure II.40. (a) Evolution of FWHM values of AA 3003 aluminum alloy under low cycle fatigue and (b) cell wall thickness as a function of fatigue damage index (number of cycles/number of cycles of whole life) at different applied stress amplitudes [52].

In [52] microstructural evolutions during low cycle fatigue of AA 3003 aluminum alloy under tension-compression loading were investigated and a parameter to indicate fatigue damage prior to crack initiation was proposed. Microstructural changes were studied from examination of dislocation structures by transmission electron microscopy (TEM) and measurement of FWHM of XRD peaks during fatigue cycling. In the first few cycles the dislocation density increased until the distribution of dislocations in a rough cell structure. With further cycling, dislocations were rearranged forming a clear cell or sub-grain structure,

which was followed by a decrease in the dislocation density. The decrease in dislocation density was explained by the process of dynamic recovery of dislocations: at each cycle, dislocations in the cell interior move and, if opposite dislocations exist nearby, annihilation of dislocations takes place. The dislocation density decreased first in the cell interior and then within cell walls. Consequently, the FWHM increased in the first cycles and then decreased when a cell structure was formed, as shown in Fig. II.40(a). Finally, the cell wall was rearranged and the cell wall thickness decreased with increasing number of cycles. The cell wall thickness was suggested as a parameter to evaluate fatigue damage when the cell structure is formed. A fatigue damage index was proposed as the ratio of the number of cycles to the number of cycles to failure, which is inversely proportional to the average cell wall thickness, regardless of the applied stress level (Fig. II.40(b)).

II. 2.2.3. HIGH CYCLE FATIGUE LOADINGS

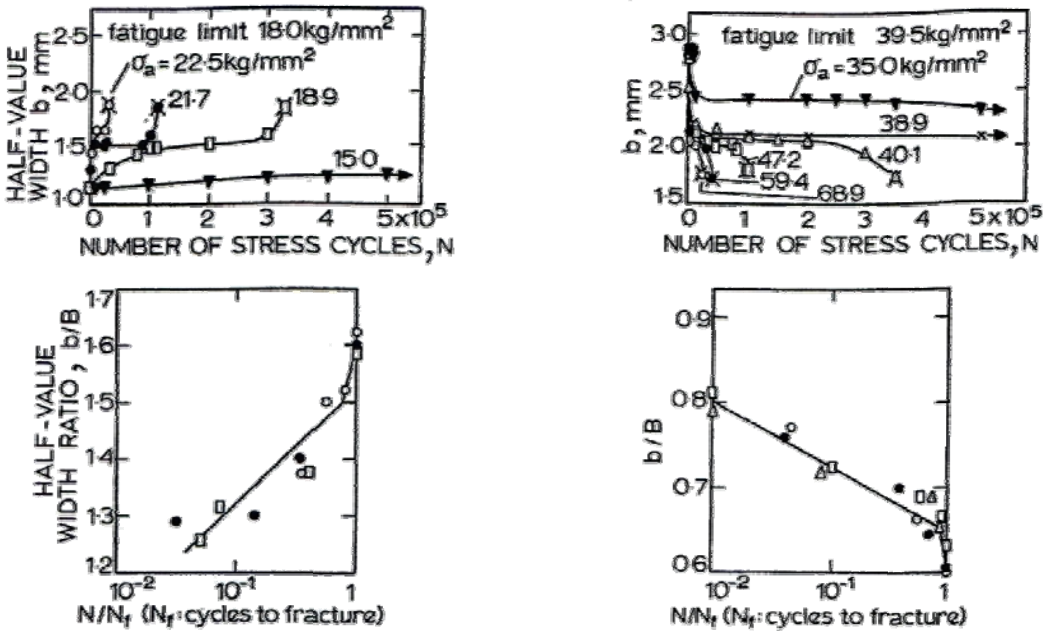

Figure II.41. Change in the integral breadth *b* during fatigue cycling of (a) annealed 0.76% C steel samples and (b) hardened 0.79% C steel samples [58].

In [58] it was found that both the integral width and the half-value width (FWHM) of the XRD peak measured in a fatigue cycled material are closely related to the amount and type of fatigue damage. Results of changes in the integral width *b* during fatigue cycling on hardened (cold worked) and annealed steel samples were presented. For annealed samples,

three successive increasing stages were observed in the evolution of the integral breadth *b* with increasing number of cycles (Fig. II.41(a)). However, for hardened samples, broader XRD peaks were detected before fatigue cycling, and instead the evolution of the integral breadth *b* with cycling comprised three regular and successive decreasing stages (Fig. II.41(b)). In both cases, the amplitude of variations of *b* was increased with increasing stress amplitude. A nondimensional linear relationship between the breadth ratio b/B (where B is the initial integral width) and the fatigue life fraction N/N_f (where N_f is the number of cycles at failure) was observed during fatigue life, regardless of the applied stress, as shown in Fig. II.41. The use of the curve b/B versus N/N_f was suggested for fatigue life prediction. In this case, some limitations should be taken into account: for example, the total amount of decrease in the integral width during fatigue is reduced as the hardness of the material increases.

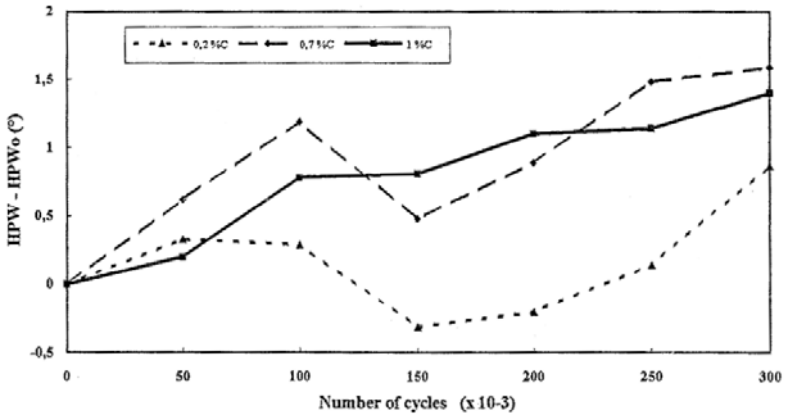

Figure II.42. Evolution of FWHM (HPW) with fatigue cycling on steel samples with different carbon contents: 0.2%, 0.7% and 1% C [10].

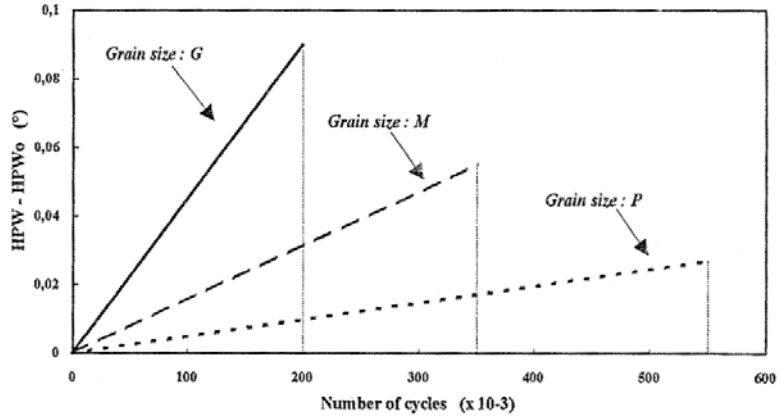

Figure II.43. FWHM (HPW) changes during stage I for middle carbon steel with different grain sizes [10].

In [10,70,71] the effects of the content of interstitial atoms and of the grain size on the movement of dislocations and microstructural changes during high cycle fatigue of low carbon steel samples were studied from X-ray diffraction measurements of FWHM values. Samples were submitted to different treatments to obtain different carbon contents at the surface and different grain sizes. Carburizing and induction hardening treatments were carried out in order to obtain samples with martensitic structure and three different carbon contents: 1% C carburized, 0.7% C carburized, and 0.2% C hardened samples. For the three different treated samples, the evolution of FWHM with fatigue cycling was characterized by three consecutive stages preceding macroscopic cracking, as shown in Fig. II.42. The first stage (stage I) is related to the multiplication of dislocations and cyclic hardening of the material, which results in a fast increase of the FWHM values in the early cycles. In this stage, the rate of FWHM increase was greater for lower carbon contents. This is explained by the effect produced by interstitial carbon atoms, which act as an obstacle to dislocation movement. Greater increases in FWHM are related to improved dislocation movements. In the second stage (stage II), FWHM values decreased (0.2% C and 0.7% C samples) or remained constant (1% C sample). The amplitude of decrease of FWHM and the duration of this stage were accentuated for lower carbon contents. It was considered that in this stage the rearrangement of the dislocation network by dislocation annihilation was preponderant. Finally, FWHM values increased in the third stage (stage III) up to macroscopic cracking. The rate of FWHM increase was greater for higher applied stresses and lower carbon contents (Fig. II.42). The effect of the grain size on the multiplication of dislocations and on the rate of FWHM increase, during the first stage was investigated for a 0.4% C steel. Three different grain sizes were obtained by different annealing treatments, producing 0.4% C steel samples with small (P), medium (M) and large (G) grain sizes. In all annealed samples, FWHM increased almost linearly with the number of cycles in the stage I, as shown in Fig. II.43. This confirms that the first stage of the evolution of FWHM is essentially linked to the multiplication of dislocations, intensification of their interactions, and hardening of the material. The rate of increase in FWHM is accentuated for greater grain sizes. The total increase of FWHM at the end of the first stage (ΔFWHM) is inversely proportional to the $1/\sqrt{d}$ ratio, where d is the grain size, corresponding to a Hall-Petch relationship (Fig. II.44)

$$\Delta\mathrm{FWHM} = \Delta\mathrm{FWHM}_0 + kd^{-1/2} \qquad \textbf{(II.35)}$$

where $\Delta FWHM_0$ is the total increase of FWHM for the greatest grain size of the plot and k depends on the applied stress.

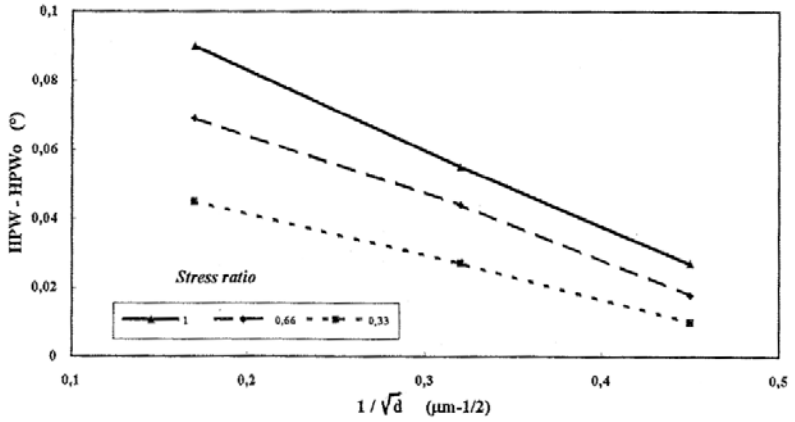

Figure II.44. Influence of the grain size on the FWHM (HPW) evolution with fatigue cycling on steel samples with different carbon contents: 0.2%, 0.7% and 1% C [10].

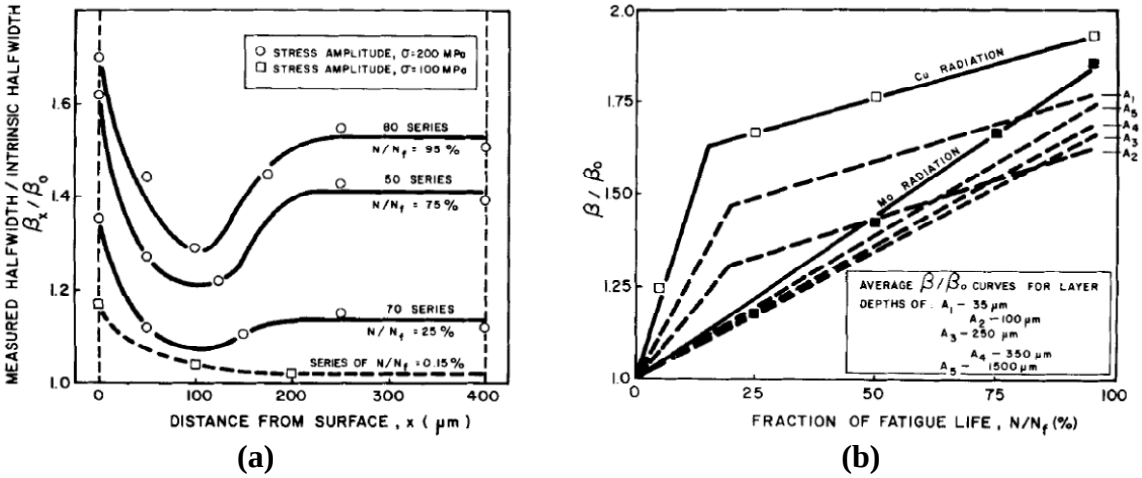

(a) **(b)**

Figure II.45. (a) Depth profiles at various fatigue life fractions of AA2024 samples (Cu Kα radiation). (b) Curves of β/β_0 versus N/N_f (Cu Kα and Mo Kα radiations) and average curves obtained by integration of depth profiles in (a) [63].

The work hardening in the surface layer and bulk material in AA2024 aluminum alloy samples cycled to different fractions of their fatigue life in tension-compression load cycling was investigated in [63]. During the first half-cycle of fatigue load a surface layer was formed, featuring larger half-width (β) values than those measured for the bulk material. Further cycling produced an increase in both surface and bulk half-widths. Results revealed that the surface layer work hardened more rapidly during fatigue life than the bulk material, and the half-width β at the surface remained higher than that in the bulk throughout the fatigue life. Fig. II.45(a) shows depth profiles of the β_x/β_0 ratio obtained with Cu Kα radiation

for AA2024 alloy samples fatigued to several fatigue life fractions, where β_0 represents the average half-width value prior to fatigue cycling, and β_x refers to the average half-width value measured at a depth x from the surface. A half-width plateau was observed for depths greater than 250 μm into the bulk. It was considered that the surface layer acts in such a manner as to oppose the motion of dislocations by providing a barrier to support a piled-up array of dislocations of like sign. When the barrier becomes sufficiently strong, fracture occurs if the local stress field, associated with an accumulation of excess dislocations, exceeds the fracture strength. The blocking aspect developed in the surface layer is clearly demonstrated in Fig. II.46. The curves in Fig. II.46(b) show that after removal of a 400 μm thickness layer in samples previously cycled to 75 and 95% of N_f, a clear decrease in β/β_0 values was observed upon initial recycling. This indicates that after removal of the surface layer the dislocation structure and arrangement in the bulk became unstable during cycling. Further cycling gave rise to an increase of β/β_0 values since a new, work hardened surface layer was being formed. In a second depth profile analysis carried out after recycling to 5% of the fatigue life, very low half-width values were measured for the sample originally cycled to 75% of N_f, as shown in Fig. II.46(c); these values approached that of the virgin sample. It was concluded that the remarkable extension of fatigue life observed after surface removal was ascribed, therefore, not to the removal of microcracks, but principally to the removal of the blocking effect due to the work hardened surface layer. In addition, results obtained with the use of two different X-radiations (Cu Kα and Mo Kα) were compared. Application of Cu Kα radiation, which penetrates only a portion of the work hardened surface layer, gave rise to a rapid increase of β/β_0 early in the fatigue life, followed by a gradual increase from 20 to 90% of the fatigue life, with nearly a plateau appearance. Beyond 90% of the fatigue life, the half-widths expanded rapidly again up to a critical value $(\beta/\beta_0)^*$ at failure. By contrast, the Mo Kα radiation, which penetrates grains at the surface as well as in the bulk, gave rise to a straight line that had a pronounced slope up to the critical value $(\beta/\beta_0)^*$. β/β_0 values for the surface and bulk converged to $(\beta/\beta_0)^*$ at the later fractions of life (Fig. II.45(b)). The steep, single-stage curve obtained with the Mo Kα radiation resulted from the added contribution of the bulk to X-ray measurements. This is revealed by the plot of average β/β_0 values produced by integrating depth profiles of Fig. II.45(a), obtained with Cu Kα radiation, to different depth limits. Curves obtained by integration to depths greater than the depth corresponding to the beginning of the half-width plateau (> 250 μm) approximately coincided with that obtained using Mo Kα radiation. It was proposed that the β/β_0 value, measured for a sample cycled to

an unknown extent, could be compared with the critical value $(\beta/\beta_0)^*$ to estimate the remaining fatigue life fraction before failure.

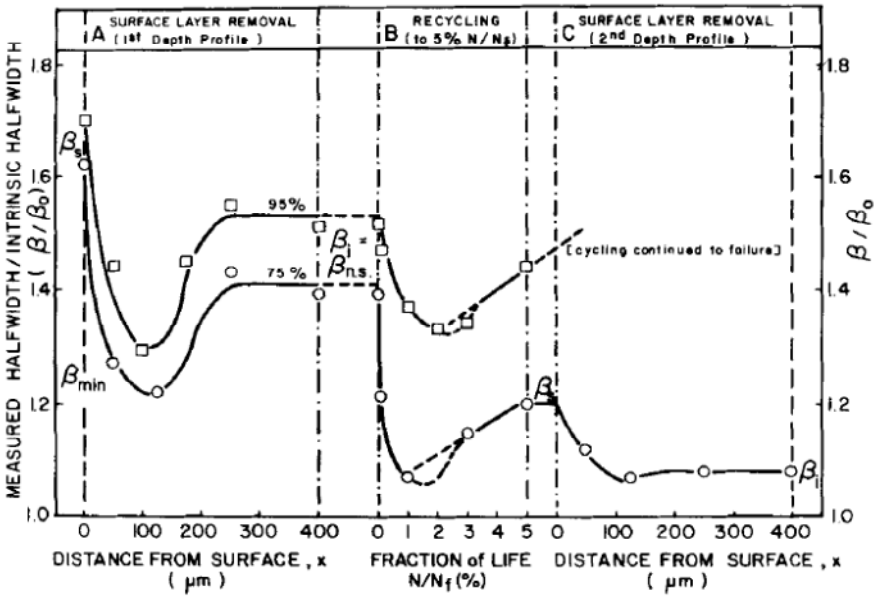

Figure II.46. Depth profiles of AA2024 samples (a) fatigue cycled to 75 and 95% of N_f at stress amplitude of 200 MPa, (b) recycled after 400 µm thickness surface layer removal to 5% of N_f, and (c) a second depth profile analysis [63].

In [45,46] an sample of aluminum alloy reinforced with SiC particles (SiCp/Al2024) was submitted to fatigue tests under stress control. Residual stresses in the composite were developed due to a mismatch of coefficients of thermal expansion between reinforcing particles and matrix. The phase residual stresses of the aluminum matrix and of the SiC particles were defined as the difference between the principal stresses σ_1 and σ_3 in the directions parallel to the loading axis and normal to the sample surface, respectively. Since the macrostress σ_3' is zero at the sample surface, the macrostress σ_1' was determined by the rule of mixture

$$\sigma_1' = (1-V_f)\langle\sigma_1-\sigma_3\rangle_m + V_f\langle\sigma_1-\sigma_3\rangle_p \quad \textbf{(II.36)}$$

where $\langle\sigma_1-\sigma_3\rangle_m$ and $\langle\sigma_1-\sigma_3\rangle_p$ are the phase stresses of aluminum matrix and SiC particles, respectively, and V_f is the volume fraction of particles. Residual stresses were measured by X-ray diffraction in each constituent phase and the macro residual stress $\langle\sigma_1-\sigma_3\rangle_R$ was calculated by Eq. (II.36). Compressive residual stresses in both phases and

the macro residual stress increased with increasing number of stress cycles, as shown in Fig. II.47(a). The evolution with the number of cycles of the difference between macro residual stresses measured at the maximum applied stress and at zero applied stress $\Delta\langle\sigma_1 - \sigma_3\rangle$ can be divided into four regions (Fig. II.47(b)). The first decrease (region B) resulted from residual stress release due to crack initiation and increase in the crack density, and the final decrease (region D) occurred from rapid residual stress release due to crack propagation just before the final failure. Although the scatter was large, it was found that in both phases the FWHM (half-value breadth) of the XRD peak increased with the number of cycles just before final failure, as shown in Fig. II.48. Peak broadening was caused by inhomogeneous strains induced by fatigue cracks and plastic deformation.

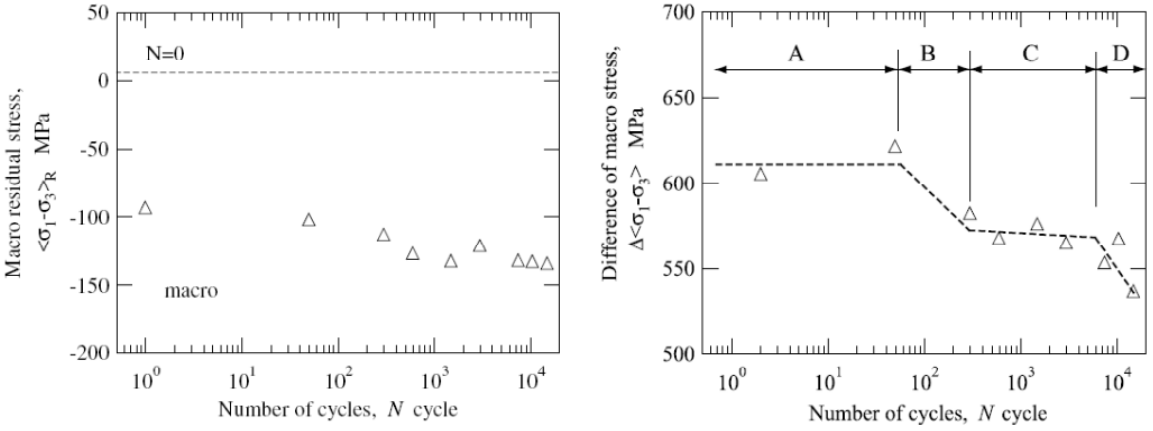

Figure II.47. Changes (a) of macro residual stresses (measured at zero applied stress) and (b) of the difference between macro residual stresses measured at the maximum applied stress and at zero applied stress with the number of cycles [45].

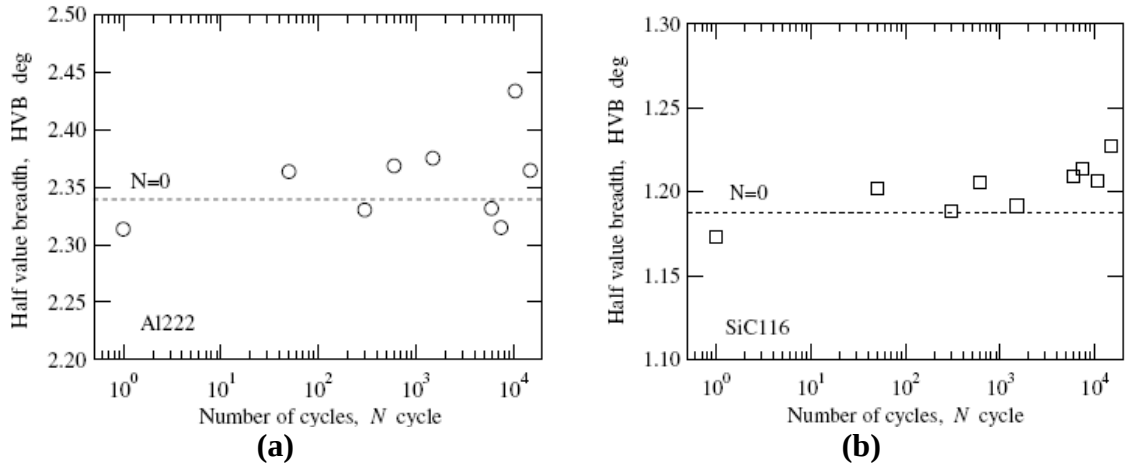

Figure II.48. Evolution of FWHM (half-value breadth) values with the number of cycles at (a) the Al phase and (b) at the SiC phase [45].

In [28] the fatigue behavior of annealed polycrystalline aluminum samples was analyzed from the evolution of FWHM (half-width) with fatigue cycling. Two different loading types were adopted: tension-tension axial loading at constant stress amplitude and stress spectrum loading representing an aircraft flight. The crystallite size (D) and microstrains ($<\varepsilon^2>$) were calculated at various stages of fatigue cycling using the single line method and the multiple line analysis. In the single line method, it is assumed that the Cauchy and Gaussian components represent respectively contributions from crystallite size and microstrains. In the multiple line method, a Cauchy-Gaussian approximation was used to describe the diffraction profile. D, $<\varepsilon^2>$ and the integral width β were related by the expression

$$\beta^2 / \tan^2\theta = (k\lambda / D)(\beta / \tan\theta \sin\theta) + 16 < \varepsilon^2 > \quad \textbf{(II.37)}$$

where the Scherrer constant k is close to unity, θ is the Bragg's angle and λ is the wavelength of X-rays. The angular dependence of peak broadening during fatigue cycling was established by measuring integral widths β over different crystallographic planes. As shown in Fig. II.49(a), the β/β_0 ratio increased with glancing angle and number of cycles, where β_0 refers to the integral width before fatigue cycling. Since during fatigue cycling higher integral widths were found for (422) planes, these planes was chosen for XRD measurements. Sensitivities of the integral width β and half-width b to fatigue cycling were compared (Fig. II.49(b)). The marked slope of the curve $(b/b_0)/(\beta/\beta_0)$ in the first cycles indicates a higher sensitivity of half-width values, and with further cycling sensitivities of b and β became comparable. The evolution of the b/b_0 ratio with N could be represented by a three-stage mean curve, as shown in Fig. II.50. Stage I was characterized by a rapid increase in the b/b_0 ratio, followed by a plateau during the majority of the fatigue life in stage II, and finally a fast increase in the last cycles up to failure (stage III). The duration of each stage was reduced with increasing applied stress amplitude. Curves of b/b_0 versus N under typical flight loading conditions also presented three stages, as shown in Fig. II.51 with N referred to the number of flights. XRD peak broadening resulted mainly from the build-up of microdeformations, which varied with fatigue cycling similarly to the b/b_0 versus N curve, as shown in Fig. II.52. The formation and progress of microcracks during fatigue cycling was related to the evolution of microdeformations. Microcracks were formed from early cycles and persisted until stage III, when microcracks were numerous and larger. The b/b_0 value at fatigue failure seemed to be independent of the loading procedure.

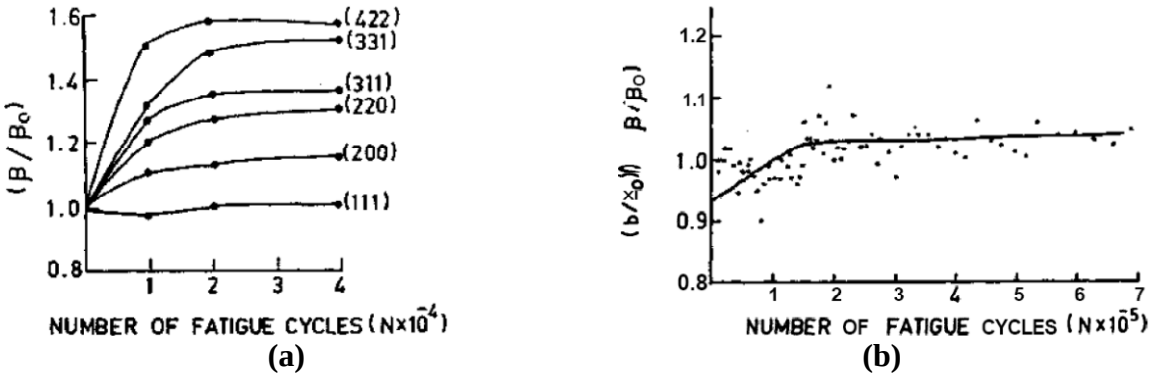

Figure II.49. Evolution (a) of (β/β_0) for XRD over different crystallographic planes and (b) of (b/b_0)/(β/β_0) for XRD over (422) planes during fatigue cycling of polycrystalline aluminum samples at stress amplitude of 46 MPa [28].

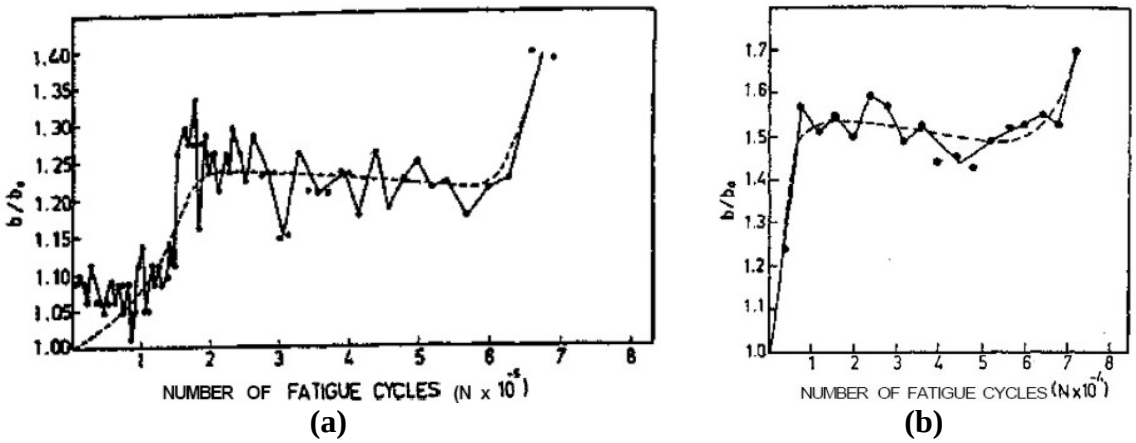

Figure II.50. (b/b_0) versus N at stress amplitudes of (a) 32 MPa (b) 46 MPa [28].

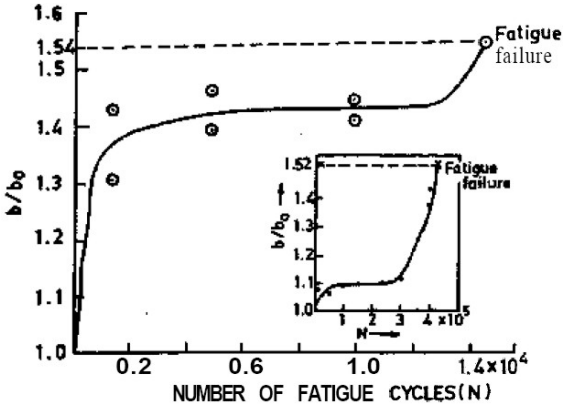

Figure II.51. (b/b_0) versus N curve under flight loading conditions [28].

The work presented in [35] evaluates the redistribution and relaxation of residual stresses induced by foreign object damage in Ti-6Al-4V alloy samples during high cycle fatigue loading using spatially resolved X-ray diffraction. Residual stress relaxation occurred

mainly in the first cycle, and with further cycles a slight relaxation was observed, as shown in Fig. II.53. The first cycle relaxation occurred when the superposition of applied and residual stresses exceeded the appropriate yield condition, leading to some plastic accommodation of pre-existing elastic strains associated with the initial residual stress state. Residual stress relaxation increased with increasing applied stress. Spatial maps of FWHM gave an indication of the degree of plasticity in the zone of impact. In the first cycle, some broadening of the diffraction peak was observed, more pronounced in the crater center. However, by the end of ten cycles, FWHM values returned to their initial values and were essentially stabilized with little evidence of further evolution. This suggested that the nature of the plasticity (dislocation substructure) was not significantly altered by fatigue cycles under these loading conditions and that the fatigue behavior was mainly influenced by relaxation of residual stresses.

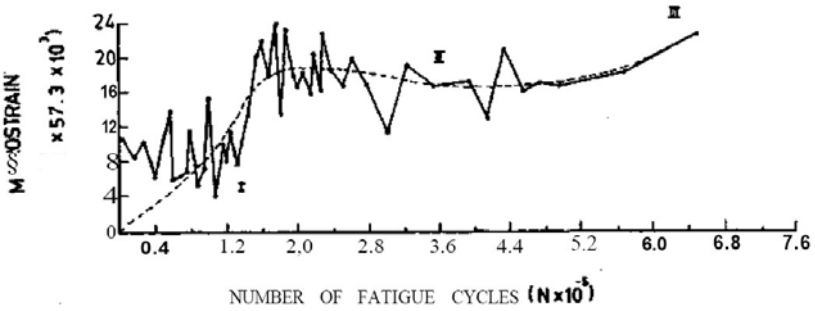

Figure II.52. Variation of microstrains with fatigue cycling at constant stress amplitude of 32 MPa (single line method) [28].

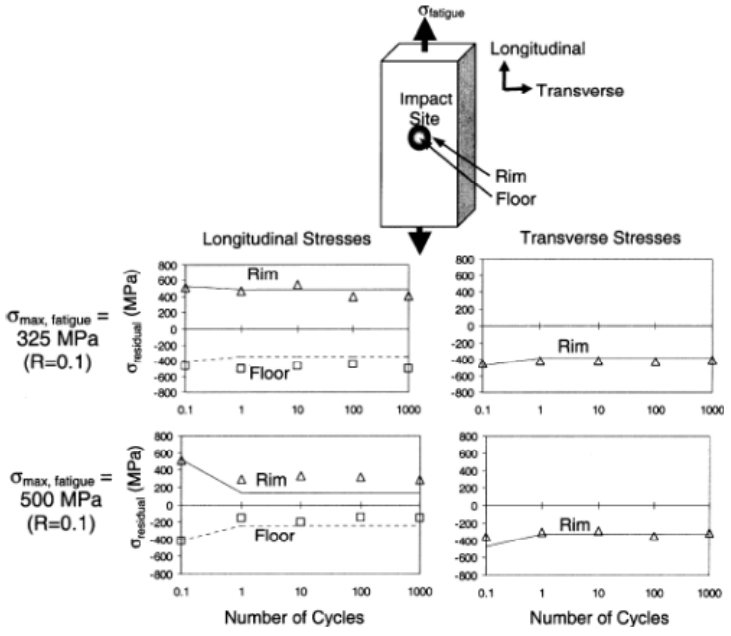

Figure II.53. Relaxation of residual stresses at damaged crater: spatially resolved XRD measurements (points) and finite element predictions (lines) [35].

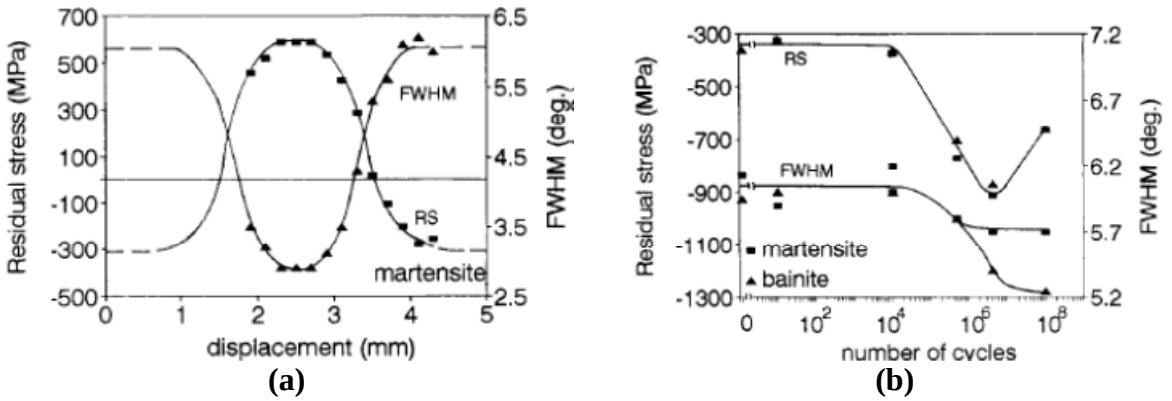

Figure II.54. Tangential residual stresses and FWHM values (a) across thermally affected zone of a martensitic ball bearing ring before fatigue and (b) in function of the number of cycles in thermally unaffected zone of bainitic and martensitic ball bearing rings under rolling contact fatigue [48].

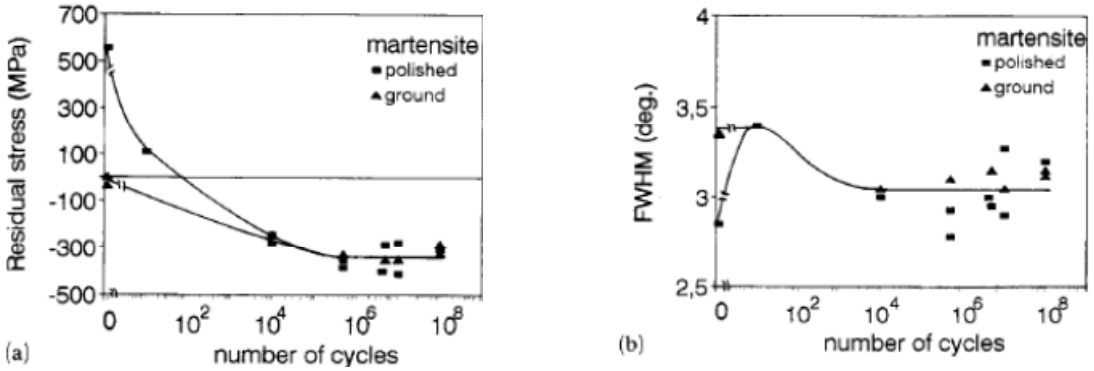

Figure II.55. (a) Tangential residual stresses and (b) FWHM values in the center of thermally affected zones of martensitic ball bearing rings under rolling contact fatigue as a function of the number of cycles [48].

In [48] the evolution of residual stresses and FWHM in defect zones in inner rings of ball bearings under rolling contact fatigue was studied. The ring of ball bearings is characterized by a thin surface layer with machining-induced compressive residual stresses. Ball bearing rings with martensitic and bainitic microstructures were employed and defects were induced as local thermal damage produced by laser irradiation (thermally affected zones). Thermally affected zones suffered changes in the ring geometry and in the near-surface microstructure, which led to lower material strength at the surface (lower hardness and FWHM), tensile residual stresses and significantly retained austenite decomposition (Fig. II.54(a)). In thermally unaffected zones, tangential surface residual stresses and FWHM remained unaffected up to 10^4 load cycles, during which the von Mises equivalent stress did not exceed the yield strength of the hardened material owing to machining-induced compressive residual stresses. With further cycling, compressive residual stresses increased

up to $5 \cdot 10^6$ cycles, when they started to relax for higher numbers of cycles (Fig. II.54(b)). After 10^4 cycles, FWHM decreased with further cycling, as shown in Fig. II.54(b); this effect was more pronounced for bainitic than for martensitic microstructure. In thermally affected zones, the von Mises equivalent stress increased owing to high tensile residual stresses, and then plastic deformation occurred within the first few cycles, leading to changes in the raceway geometry, residual stresses and FWHM. Fig. II.55 shows the evolution of residual stresses and FWHM in the centre of a thermally affected zone in a martensitic hardened ring. Residual stresses decreased with increasing number of cycles up to 10^4 cycles, when they became stable for higher numbers of cycles. After an increase in the first cycles, FWHM decreased up to 10^4 cycles, showing a stable behavior with further cycling. The stable behavior of residual stresses and FWHM in thermally affected zones for higher numbers of cycles resulted from decrease in the von Mises equivalent stress due to increasing compressive residual stresses and changes in the ring geometry. However, below the surface, the von Mises equivalent stress was higher than the local material strength, both in thermally affected and unaffected zones. Therefore, changes in residual stresses and FWHM were observed in subsurface layers even after a few load cycles.

CHAPTER III

MATERIAL AND EXPERIMENTAL TESTS

CHAPTER III

MATERIAL AND EXPERIMENTAL TESTS

This chapter presents the experimental work, comprising procedures for metallurgical and mechanical characterization of the material, preparation of fatigue test samples, experimental setup for fatigue tests, and X-ray diffraction study of microstructural changes during fatigue tests.

III. 1. METALLURGICAL AND MECHANICAL CHARACTERIZATION OF THE MATERIAL

Metallurgical and mechanical characterization of API 5L X60 grade steel was carried out by means of chemical composition analyses, metallographic analyses, uniaxial tension tests, and Vickers microhardness tests. Specific tests coupons were machined from a sample of seamless API 5L X60 grade steel pipe, with nominal diameter and thickness of 219.08 mm and 15.06 mm, respectively. The steel pipe was provided by the Subsea Technology Laboratory (LTS) of COPPE/Federal University of Rio de Janeiro. Figure III.1 shows the machining sketch of test coupons. The material properties acquired were compared with requirements provided by the standard API SPEC 5L – Specification for Line Pipe [6].

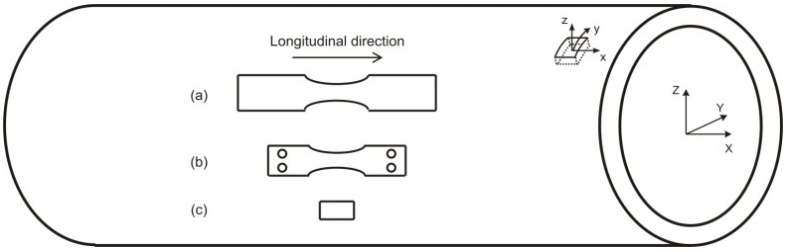

Figure III.1. Test coupons and samples cut off from an API 5L X60 grade steel pipe for: (a) uniaxial tension tests, (b) fatigue tests, and (c) other procedures of material properties characterization.

III. 1.1. CHEMICAL COMPOSITION ANALYSES

Chemical composition analyses were carried out according two different techniques: Castaing microprobe analysis, or electron probe micro-analysis (EPMA), and optical emission spectrometer analysis. Different techniques were employed in order to assure a more comprehensive detection of elements present in the chemical composition of the material.

Average results of chemical composition in percentage of weight (wt. %) obtained by optical emission spectrometer analysis and by electron probe micro-analysis are shown in Tables III.1 and III.2, respectively. Table III.3 presents the chemical composition requirements for API 5L X60 grade steel provided by the standard API SPEC 5L – Specification for Line Pipe [6], which also states that the sum of columbium (niobium, Nb), vanadium (V), and titanium (Ti) contents shall not exceed 0.15%. It was found that the chemical composition of the material is in agreement with these requirements.

Table III.1. Average chemical composition in percentage of weight (wt. %) estimated for API 5L X60 grade steel by optical emission spectrometer analysis.

C	Si	Mn	P	S	Cr	Ni	Mo	Al
0.148	0.28	1.32	0.032	0.012	0.05	0.02	0.06	0.039
Cu	**Co**	**Ti**	**Nb**	**V**	**W**	**Pb**	**Sn**	**Fe**
0.004	0.012	0.0028	0.08	0.039	0.013	< 0.003	0.014	Balance

Table III.2. Average chemical composition in percentage of weight (wt. %) estimated for API 5L X60 grade steel by electron probe micro-analysis (EPMA).

Si	Mn	Fe
0.298	1.286	97.802

Table III.3. Maximum chemical composition requirements in percentage of weight (wt. %) for API 5L X60 grade steel by the standard API SPEC 5L [6].

C	Mn	P	S	Fe
0.28	1.40	0.030	0.030	Balance

III. 1.2. METALLOGRAPHIC ANALYSES

Surfaces of small test coupons were prepared for metallographic examination by grinding with a sequence of SiC papers from 80 to 1200 grit numbers under water cooling, followed by wet grinding with diamond micro powders from 6 μm to 1 μm, electrolytic polishing with a standard perchloric-based acid solution (standard electrolyte Struers A2), and etching with 5% Nital. The material microstructure was then observed using optical microscope and scanning electron microscope (SEM). A ferritic matrix with homogeneous dispersion of pearlite bands was observed, as shown in Figs. III.2 and III.3. Some non-

metallic inclusions, such as small circular oxide inclusions can also be identified randomly distributed among the ferritic matrix.

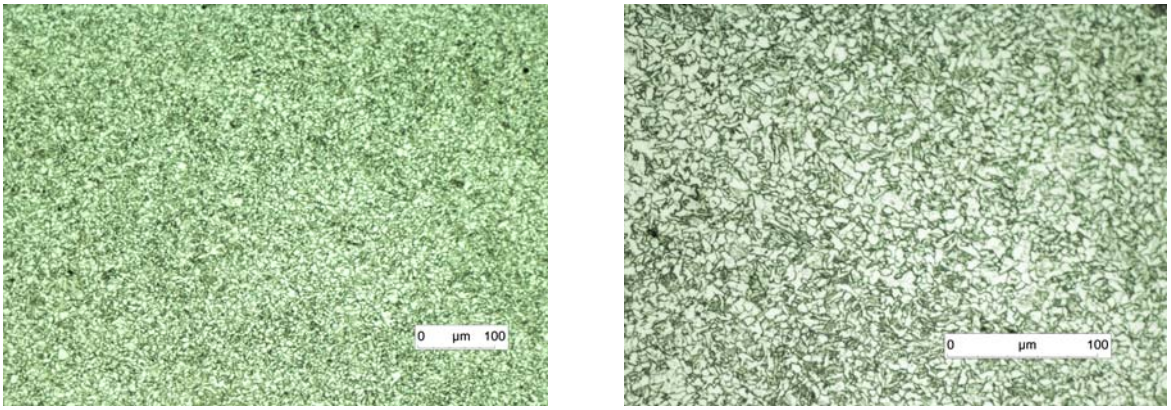

(a) **(b)**

Figure III.2. Microstructure observed through optical microscope, original magnification factor of (a) 100x and (b) 200x.

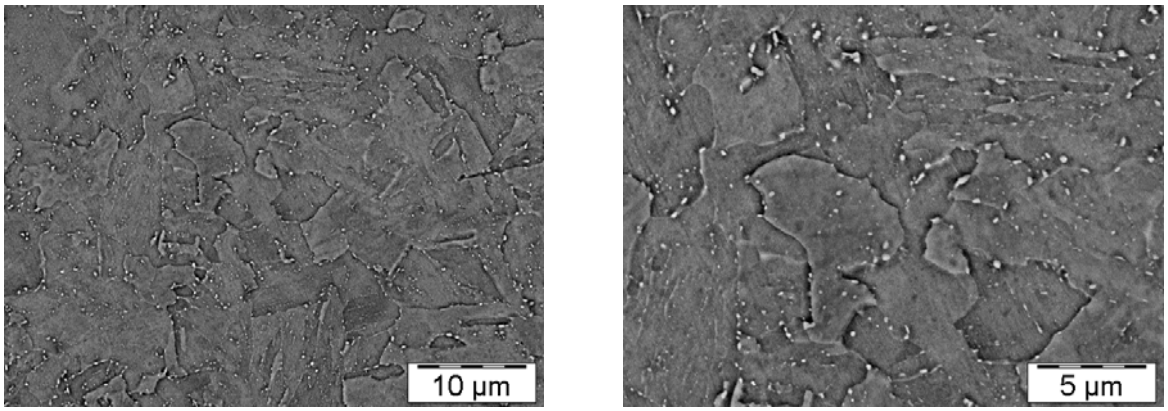

(a) **(b)**

Figure III.3. Microstructure observed through scanning electron microscope (SEM), original magnification factors of (a) 2500x and (b) 5000x.

III. 1.3. UNIAXIAL TENSION TESTS

Uniaxial tension tests were carried out to evaluate relevant mechanical properties of API 5L X60 grade steel. Six tension test coupons were machined in the longitudinal direction of the pipe sample (Fig. III.1). Tension test coupons were identified with the reference CPT followed by a sequential number (i.e., CPT1 to CPT6). The geometry and dimensions of tension test coupons are presented in Fig. III.4. Tension tests were conducted in a conventional servo-hydraulic machine (Instron 8802) with strain rate around $1.7 \cdot 10^{-4}$ m/m·s^{-1}, according to specifications of the ASTM E8M standard [96]. Strains were measured

throughout the tests with the aid of a video extensometer. The setup for the uniaxial tension tests is shown in Fig. III.5.

Figure III.6 presents the engineering stress-strain diagrams acquired for the six tension test coupons, which are shown after rupture in Fig. III.7. Table III.4 presents the average mechanical properties obtained, which are in agreement with the requirements of the standard API SPEC 5L – Specification for Line Pipe [6] shown in Table III.5.

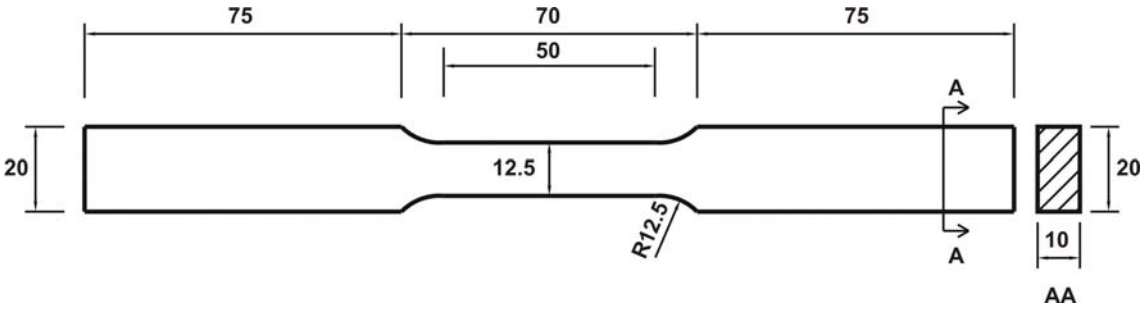

Figure III.4. Geometry and dimensions (in mm) of test coupons for uniaxial tension tests.

Figure III.5. Setup for uniaxial tension tests with a conventional servo-hydraulic machine (Instron 8802) and a video extensometer.

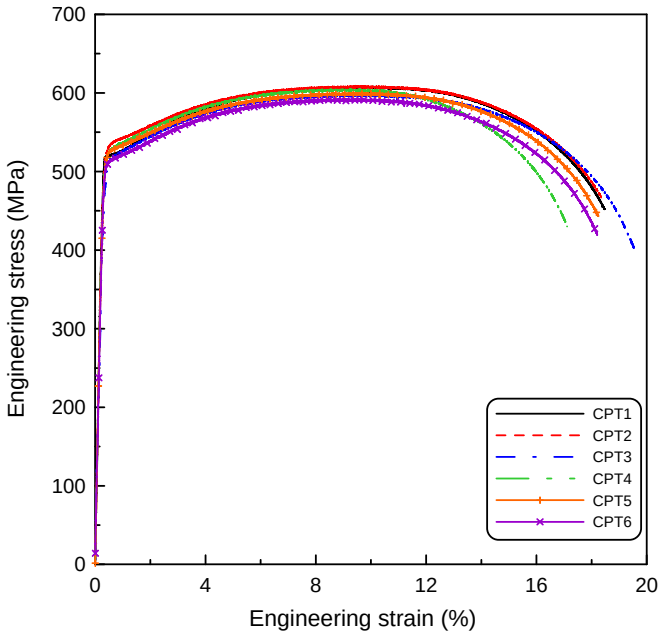

Figure III.6. Engineering stress-strain curves obtained for API 5L X60 grade steel.

Figure III.7. Tension test coupons after rupture.

Table III.4. Average mechanical properties obtained for API 5L X60 grade steel.

Young's modulus (GPa)	Yield strength[a] (MPa)	Ultimate tensile strength (MPa)	Y/T[b]	Elongation[c] (%)
183 ± 9	520 ± 6	602 ± 6	0.86	19 ± 1

[a]0.2% offset; [b]Y/T = yield strength/ultimate tensile strength; [c]50 mm gage length

Table III.5. Minimum tensile requirements for API 5L X60 grade steel [6].

Yield strength (MPa)	Ultimate tensile strength (MPa)	Elongation[d] (%)
414	517	20

[d]50.8 mm gage length

III. 1.4. VICKERS MICROHARDNESS TESTS

Surfaces of a small test coupon were prepared for Vickers microhardness tests by grinding with a sequence of SiC papers from 80 to 1200 grit numbers under water cooling, followed by wet grinding with diamond micro powders from 6 μm to 1 μm, and electrolytic polishing with a standard perchloric-based acid solution (standard electrolyte Struers A2).

Vickers microhardness tests are carried out with a diamond indenter in the form of a right pyramid with a square base and a top angle of 136° between opposite faces. Figure III.8 schematically illustrates a Vickers microhardness test. The length of the two impression diagonals are measured with the aid of an optical microscope. The Vickers microhardness (HV) is then calculated according to the following expression [84]

$$\mathrm{HV} = \frac{1.854F}{d^2} \qquad \textbf{(III.1)}$$

where F is the applied load (in kgf) and d is the average length between two impression diagonals (in mm).

Vickers microhardness tests were performed with the aid of the Duramim-1/Struers microhardness test device. Indentations were carried out with five different loads: 0.1 kg (0.9807 N), 0.2 kg (1.9610 N), 0.3 kg (2.9420 N), 0.5 kg (4.9030 N) and 1 kg (9.8070 N). The load was applied for a dwell time of 15 s. Ten indentations were performed for each load in three different directions, respectively, perpendicular to longitudinal (plane x-y), circumferential (plane y-z) and radial (plane x-z) directions of the original pipe sample (Fig. III.1).

Several publications have reported relationships between the ultimate tensile strength and hardness [97-101]. The ultimate tensile strength S_u can be correlated to the Vickers hardness HV according to the following expression

$$S_u \cong 3\mathrm{HV} \qquad \textbf{(III.2)}$$

with HV in kgf/mm^2 and S_u in MPa. This expression is verified for a broad range of steels, and over a wide range of strengths [100]. However, Eq. III.2 is no longer applicable for steels that exhibit appreciable work hardening, and a correction factor must be applied in this case [101].

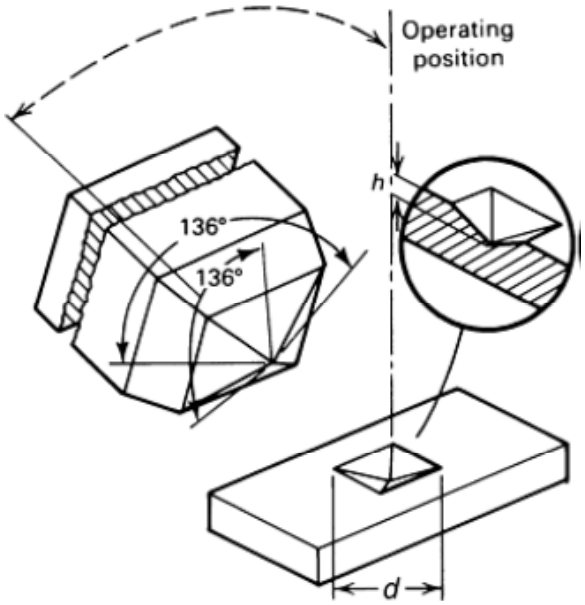

Figure III.8. Diamond pyramid indenter used for the Vickers microhardness test and resulting indentation in the sample [100].

Results obtained for indentations with 0.1 kg were neglected, in order to avoid size effects in Vickers indentations. The average results of Vickers microhardness obtained are listed in Table III.6, which also shows the estimated values of ultimate tensile strength. These values are close to the corresponding result obtained from uniaxial tensile tests in longitudinal direction (Table III.4). This suggests an almost isotropic material, even if the pipe manufacturing process is known to introduce some level of anisotropy.

Table III.6. Average results of Vickers microhardness for API 5L X60 grade steel.

Longitudinal direction		**Circumferential direction**		**Radial direction**	
HV	**S_u (MPa)**	**HV**	**S_u (MPa)**	**HV**	**S_u (MPa)**
195 ± 12	585 ± 36	196 ± 12	588 ± 36	200 ± 10	600 ± 30

III. 2. FATIGUE TESTS

API 5L X60 steel samples were submitted to high cycle fatigue tests with alternating bending loads under strain control at room temperature. Microdeformations as well as macro residual stresses during fatigue tests were evaluated from periodic X-ray diffraction (XRD) measurements.

Figure III.9. Experimental setup for fatigue tests.

III. 2.1. EXPERIMENTAL SETUP

The experimental setup for the fatigue tests is shown in Fig. III.9, comprising a fatigue testing machine Schenck model PWON [102] and a diffractometer Proto iXRD (portable mode). Figure III.10 schematically presents the alternating bending fatigue testing machine, showing (1) dial indicator gauges; (2) rotation measuring lever arm; (3) flexure leaf steel spring support; (4) axis of rotation; (5) test sample; (6) drive arm; (7) connecting rod; (8) dual eccentric; (9) preload adjustment by relocation (static stress), and (10) measuring spring-dynamometer. The fatigue test sample was clamped to the testing machine with the aid of fixing devices so that one extremity was constrained and the other was free to move in the vertical direction, following the dual eccentric oscillation.

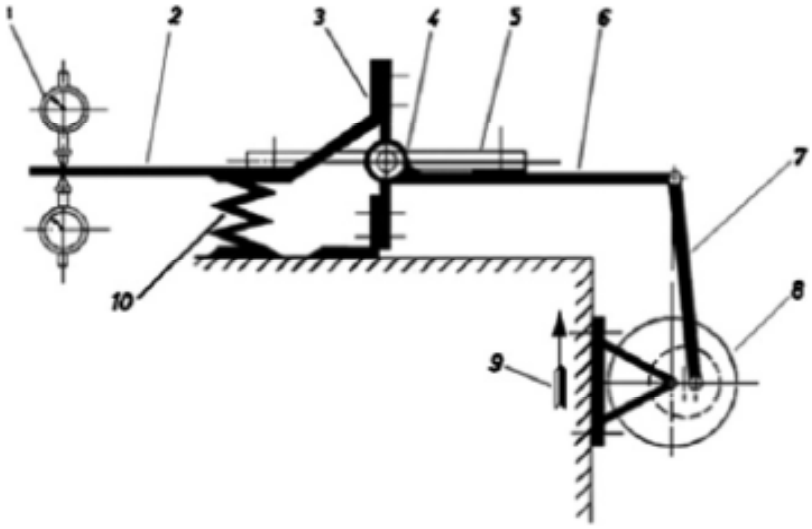

Figure III.10. Schematic representation of the alternating bending fatigue testing machine [102].

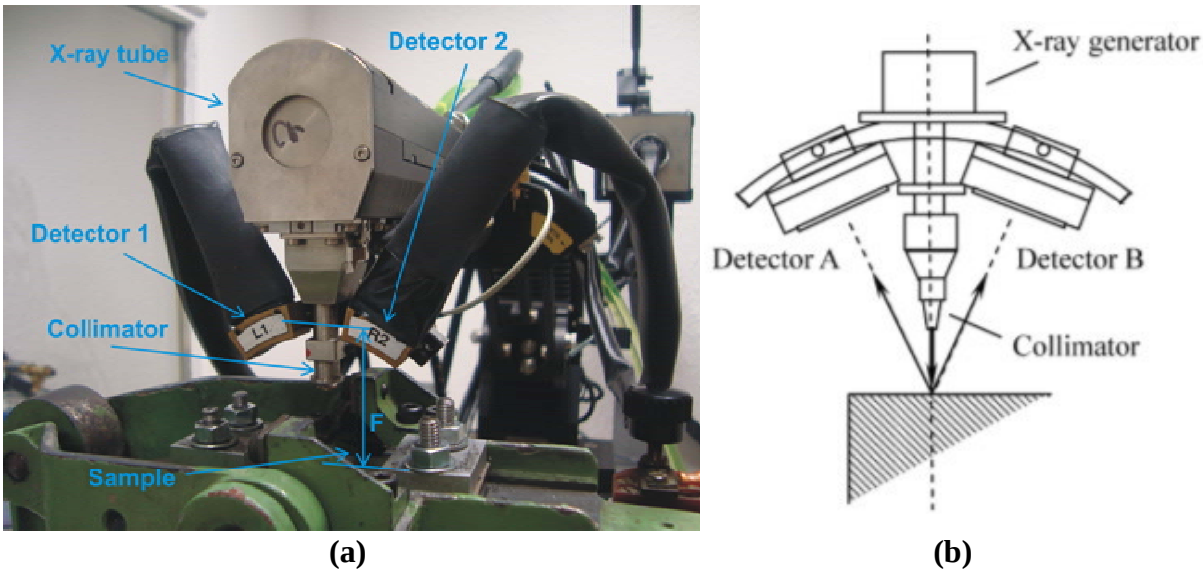

(a) **(b)**

Figure III.11. (a) Experimental setup for X-ray diffraction measurements in the sample longitudinal direction (X-ray detectors L1 and R2). Focal distance *F* = 40 mm. (b) Schematic representation of the X-ray diffractometer [103].

The fatigue testing machine Schenck model PWON is intended for fatigue strength evaluation of samples made of steels and non-ferrous metals in accordance with the German standard DIN 50142 [102]. Within tolerable capacity limits of the testing machine, static and dynamic bending moments in different superposition conditions can be applied [102].

Strain-controlled alternating bending loads were applied by prescribing the oscillation amplitude of the dual eccentric gear in the fatigue testing machine. Alternating bending loads followed a sinusoidal waveform at a frequency of approximately 25 Hz. The testing machine

was previously calibrated through loading tests with strain gage instrumentation of one sample to set the range of strain amplitudes for the fatigue tests.

Fatigue tests were regularly interrupted for XRD measurements at periods of 10,000 load cycles maximum up to sample failure. As shown in Fig. III.11, the experimental setup allowed XRD measurements to be carried out in real time during fatigue tests, i.e., without the need of removing the sample from the test machine. XRD measurements were taken at the center of the sample gage length.

XRD measurements were performed using a computer controlled Ω–diffractometer [21] employing Cr-Kα radiation (wavelength λ of 2.291 Å) generated at 20 kV and 4 mA. The incident beam was collimated by a circular aperture with 2 mm diameter, giving an irradiated area of 3.14 mm^2 at a focal distance F of 40 mm. XRD measurements were taken at (211) planes of the ferrite phase (α-Fe), under seven tilt angles ψ, 0, ±3.67, ±7.33 and ±11°, with ± 3° oscillations at each angle. Ten radiation expositions of 2 s each for every tilt angle were conducted. The penetration depth for chromium radiation in ferritic steels is approximately 6 μm at $\psi = 0$ [104]. Table III.7 summarizes the parameters adopted for XRD measurements.

Two X-ray detectors intercepted the diffraction cone from the sample and converted X-ray intensities into electronic data. Signals from X-ray detectors were transferred to a data acquisition system controlled by computational software. A Gaussian distribution function was used to fit XRD peaks and macro residual stresses and microdeformations were estimated. Figure III.12 shows the setup of the X-ray diffraction equipment with the data acquisition system and the screen display of software results, comprising diffraction peaks, diagrams of lattice spacing d versus $\sin^2\psi$ and listing of macro residual stresses and peak widths (integral width and FWHM).

Table III.7. Parameters of XRD measurements.

Tube voltage/current	Radiation	Diffraction plane	Irradiated area	Method	Exposition time	ψ
20 kV/4 mA	Cr-Kα	α-Fe (211)	3.14 mm^2	Multiple exposition (10 expositions)	2 s	0, ±3.67°, ±7.33°, and ±11°

From data concerning lattice spacing d versus orientation with respect to the surface normal ($\sin^2\psi$), macro residual stresses were calculated according to the $\sin^2\psi$ method [21],

considering the lattice spacing d_0 of 1.1702 Å, diffraction angle 2θ of 156.4°, and elastic constants $S_{1(211)} = -\nu/E = -1.28 \cdot 10^{-6}$ MPa^{-1} and $\frac{1}{2}S_{2(211)} = (1+\nu)/E = 5.92 \cdot 10^{-6}$ MPa^{-1} for the α-Fe phase (211) planes. FWHM values and macro residual stresses were considered in the sample longitudinal direction. Uncertainties were lower than 7% for measurements of FWHM values and within ± 10 MPa for measurements of residual stresses.

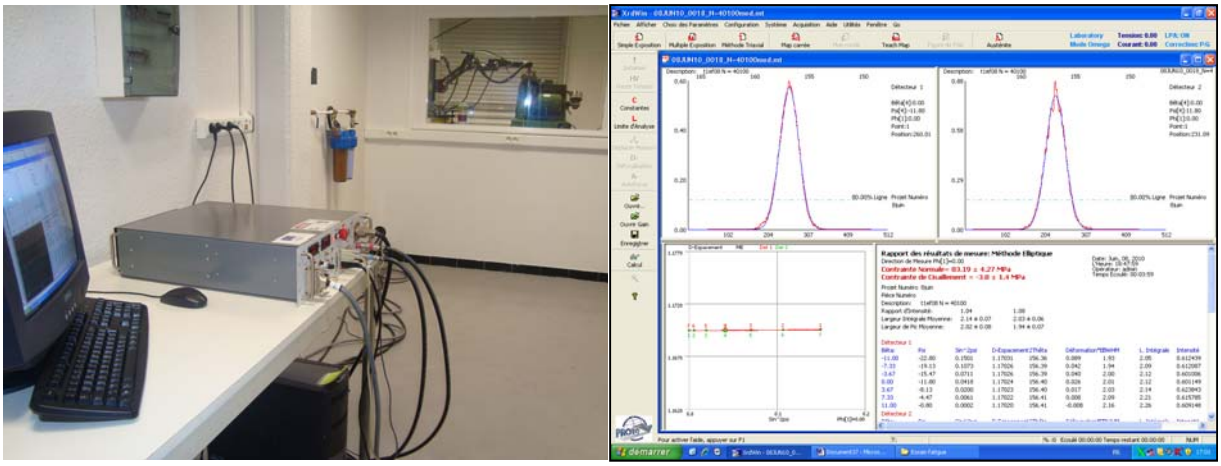

(a) **(b)**

Figure III.12. (a) Setup of the X-ray diffraction equipment with data acquisition system and (b) screen display of software results.

III. 2.2. ALTERNATING BENDING LOADING

To estimate the alternating stresses to be applied in fatigue tests, an S-N curve was estimated. In high cycle fatigue problems, the S-N curve, also known as Basquin equation, relates the number of stress cycles to failure (N) to the alternating stress (S_n) as

$$S_n = C N^b \qquad \textbf{(III.3)}$$

where parameters C and b depend on material properties and part geometry [73]. In logarithmic scale, the S-N curve renders itself as a straight line.

The Basquin equation was estimated assuming two points of the S-N curve. The first point was considered as the endurance limit point at $N = 10^6$ cycles. For the second point, it was assumed that at 10^3 cycles the alternating stress would correspond to a value between $0.8S_u$ and $0.9S_u$ [106]. The endurance limit of the fatigue test samples was estimated as [73]

$$S_e = S'_e \frac{k_a}{K_f} \qquad \textbf{(III.4)}$$

where K_t is the fatigue stress concentration factor, k_a is the surface condition factor, and S'_e is the endurance limit for standardized tests with small and polished test samples and zero mean stress. In these conditions, the endurance limit S'_e for steels can be inferred from the ultimate tensile strength (S_u) and is assumed as [73]

$$S'_e = \min\{0.5\, S_u\ ;\ 700\text{MPa}\} \qquad \textbf{(III.5)}$$

From tensile properties obtained for API 5L X60 grade steel (Table III.4) and assuming the fatigue stress concentration factor K_f as 1.0204 [105], for unitary notch sensitivity factor (i.e., $K_f = K_t$), and the surface condition factor k_a as 0.91705, for ground surface finish [73], an endurance limit S_e of 270 MPa was estimated for the fatigue test samples.

Finally, the Basquin equation was then estimated as

$$S_n = 1038\, N^{-0.0973} \qquad \textbf{(III.6)}$$

where S_n denotes the alternating stress amplitude (in MPa). In Fig. III.13 the estimated S-N curve is shown and compared with test results previously obtained and presented in [107], where the same material and identical testing conditions were used.

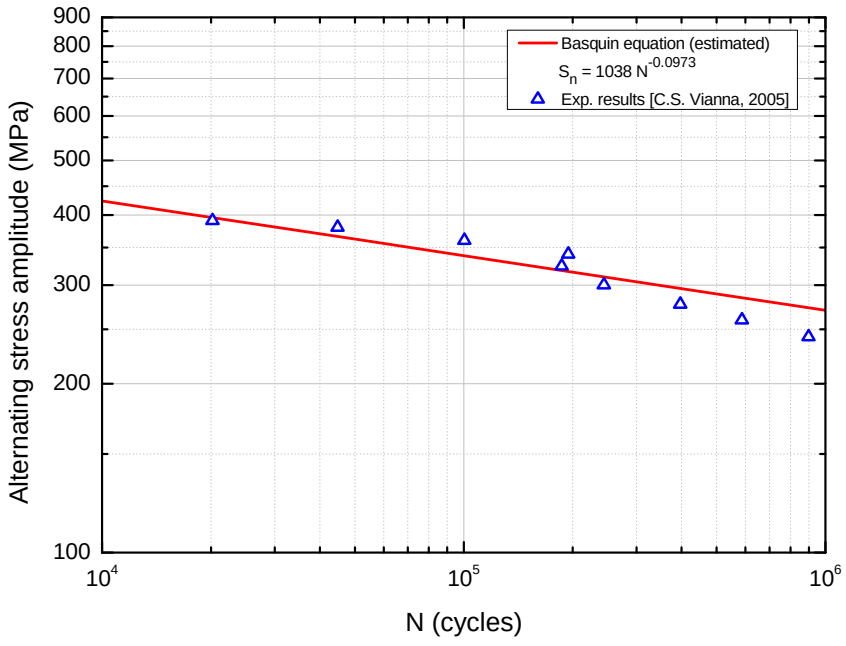

Figure III.13. S-N curve estimated and comparison with previous test results [107].

III. 2.3. FATIGUE TEST SAMPLES

Fatigue test samples were machined from the same pipe sample used to produce test coupons for material properties characterization (Fig. III.1). Flat samples were machined from the central region of the pipe wall thickness by cutting the internal and external walls. The nomenclature adopted for the fatigue test samples refers to the original pipe from which they were cut off (T1), followed by the mention EF and a sequential number, for instance T1EF01, T1EF02, T1EF03 and so forth.

III. 2.3.1. DIMENSIONING

Figure III.14 shows the geometry and dimensions of the fatigue test samples, which were defined in order to fit Schenck model PWO requirements [102]. To define the sample thickness, the maximum bending moment tolerable for the fatigue testing machine was verified. For fully reversed bending loads (zero mean stress), the maximum bending moment M_b reaches ± 15 Nm [102], which implies

$$-15\,\text{Nm} \le M_b \le 15\,\text{Nm}$$

The bending stress σ_b is given by

$$\sigma_b = \frac{M_b}{I_{Gz}} y_{max} \qquad \textbf{(III.7)}$$

where M_b is the bending moment about the axis Z, y_{max} is the maximum perpendicular distance from the neutral axis X and I_{Gz} is the second moment of area about the axis Z, expressed as

$$I_{Gz} = \frac{bh^3}{12} \qquad \textbf{(III.8)}$$

where h is the sample thickness. Substituting $y_{max} = h/2$ and I_{Gz} (Eq. III.8) in Eq. III.7 leads to

$$\sigma_b = 6\frac{M_b}{bh^2} \qquad \textbf{(III.9)}$$

The bending moment is then written as

$$M_b = \sigma_b \frac{bh^2}{6} \qquad \textbf{(III.10)}$$

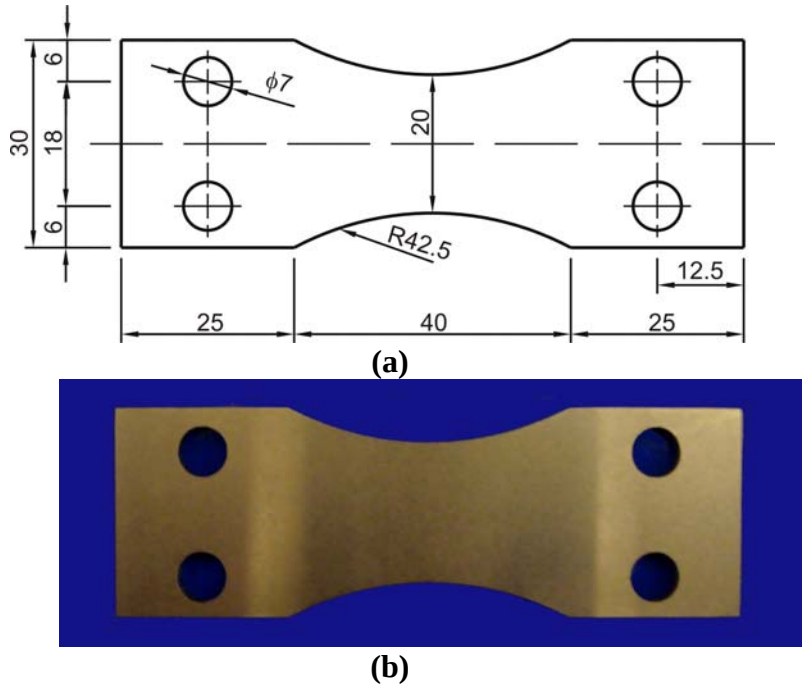

(a)

(b)

Figure III.14. (a) Geometry and dimensions (in mm) of fatigue test samples. Thickness: 2.90 mm. (b) Machined fatigue test sample.

The sample thickness was defined for the maximum alternating stress expected to be applied in the fatigue tests, corresponding to a fatigue life of 50,000 cycles. According to the S-N curve estimated, this fatigue life could be reproduced for alternating stress amplitude of 362 MPa. Then, with $M_b = |M_b| = 15$ Nm and $b = 30$ mm at the sample extremity (Fig. III.14), the sample thickness is restricted to $h \leq 2.90$mm. The sample thickness was then defined as 2.90 mm.

III. 2.3.2. POLISHING

The test samples were polished in order to reduce the surface roughness and uncertainties of X-ray diffraction measurements during fatigue tests. The surface roughness can affect XRD measurements since it reduces the density of diffracting crystallographic planes, and therefore the precision of diffraction peaks. Different polishing procedures were evaluated in view of a suitable reduction in the surface roughness without introducing additional residual stresses. The polishing procedures evaluated comprised grinding, grinding followed by electrolytic polishing, and electrolytic polishing. In the grinding procedure the

sample surface was ground with a sequence of SiC papers from 80 to 1200 grit numbers under water cooling. The electrolytic polishing procedure was performed in the Struers Lectropol 5 device at 25 V during 40 s, using a perchloric-based acid solution (standard electrolyte Struers A2). The electrolytic polishing was done within the gage length region of the sample surface with the aid of an adapted mask, as indicated schematically by the shaded area in Fig. III.15. Three fatigue test samples, T1EF01, T1EF02 and T1EF21, were used to evaluate the different polishing procedures. Residual stresses of the polished fatigue samples were measured by X-ray diffraction. The next section (III.2.3.3) describes the residual stress measurements and shows the results obtained. In addition, the surface roughness of the polished samples was measured and compared (section III.2.3.4).

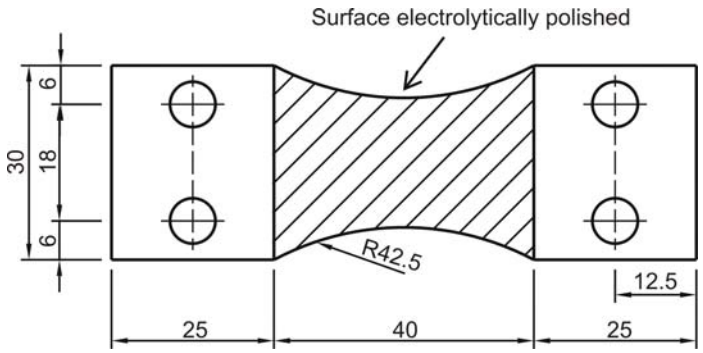

Figure III.15. Geometry and dimensions of the surface electrolytically polished.

Mechanical polishing was considered inadequate, since it can induce high compressive residual stresses (Table III.9), as already observed in previous works [47,108,109]. The role of grinding-inducing residual stresses can be important in fatigue resistance. Hamdi et al. [108] verified that conventional grinding processes in a steel workpiece lead to tensile superficial stresses while high speed grinding processes lead to compressive residual stresses. Surface residual stresses in a ground component can have three origins: mechanical traction, thermal flux and material phase transformation [109]. The mechanical effect generally induces compressive stresses whose magnitudes depend on the friction factor, a ratio between the normal and shearing force components. The strength of grinding heat, however, often produces unfavorable tensile stresses. As verified by Nguyen and Zhang [109], if the ground component experiences a critical temperature with rapid cooling, phase transformation may occur, often resulting in additional tensile stresses.

The electrolytic polishing technique was selected as the most suitable, since it helps to reduce the surface roughness and the near-surface residual stresses induced by machining (Table III.8), and therefore to reduce uncertainties of X-ray diffraction measurements.

III. 2.3.3. RESIDUAL STRESSES

Prior to fatigue tests, residual stresses of the fatigue test samples were measured by X-ray diffraction. Residual stresses were measured with a computer controlled Ω–diffractometer Proto iXRD. An X-ray tube operating at 20 kV and 4 mA was used for generating Cr-Kα radiation (wavelength λ of 2.291 Å). The incident beam was collimated by a circular aperture with 1 mm diameter (irradiated area of about 0.80 mm^2) at a focal distance F of 40 mm. Measurements were taken taken at (211) planes of the ferrite phase (α-Fe), with diffraction angle 2θ of 156.4°, under seven tilt angles ψ ranging from -30° to 30°, with ± 3° oscillation at each angle. For every tilt angle, measurements were made from 15 radiation expositions of 2 s each. The lattice spacing d_0 of α-Fe phase (211) planes is 1.1702 Å. A Gaussian distribution function was used to fit the diffraction peaks. Macro residual stresses were calculated according to the $\sin^2\psi$ method [21].

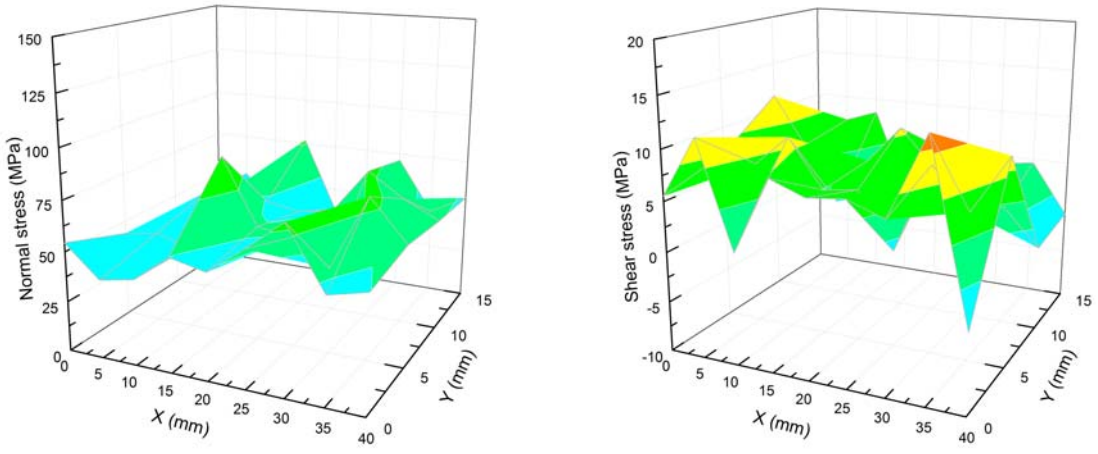

(a) **(b)**

Figure III.16. Profiles of residual stresses in sample T1EF01 as machined: (a) normal stresses and (b) shear stresses.

Measurements were taken over a mapping surface with 40 mm length and 15 mm width (area of 600 mm^2), comprising 36 points equally spaced by 5 mm. Residual stresses were measured in the sample longitudinal direction and results were evaluated in terms of

normal and shear stresses. The accuracy of residual stress measurements was of the order of ±10 MPa. Figures III.16 to III.19 present profiles of residual stresses measured in four fatigue test samples. Table III.8 presents the average residual stresses measured on fatigue test samples (machining surface finish). Neglecting residual shear stresses were measured.

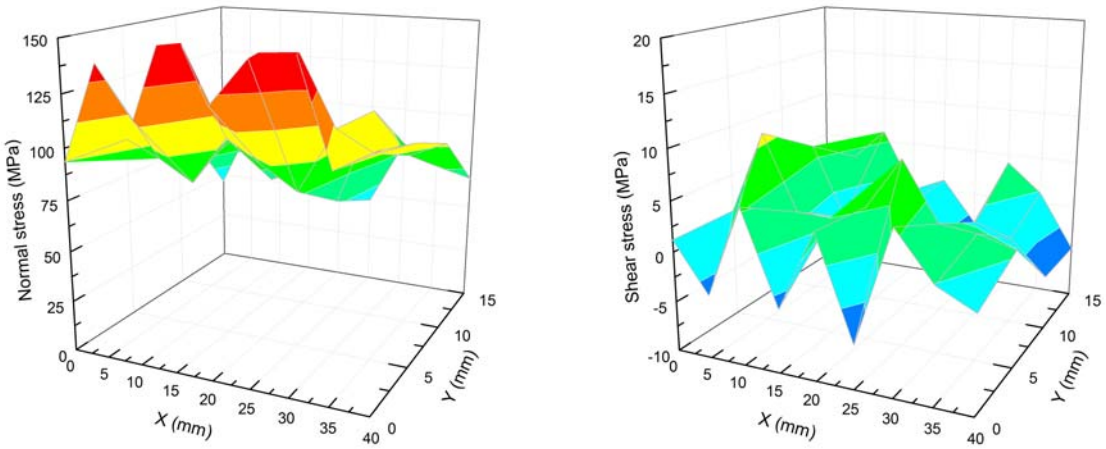

(a) **(b)**

Figure III.17. Profiles of residual stresses in sample T1EF02 as machined: (a) normal stresses and (b) shear stresses.

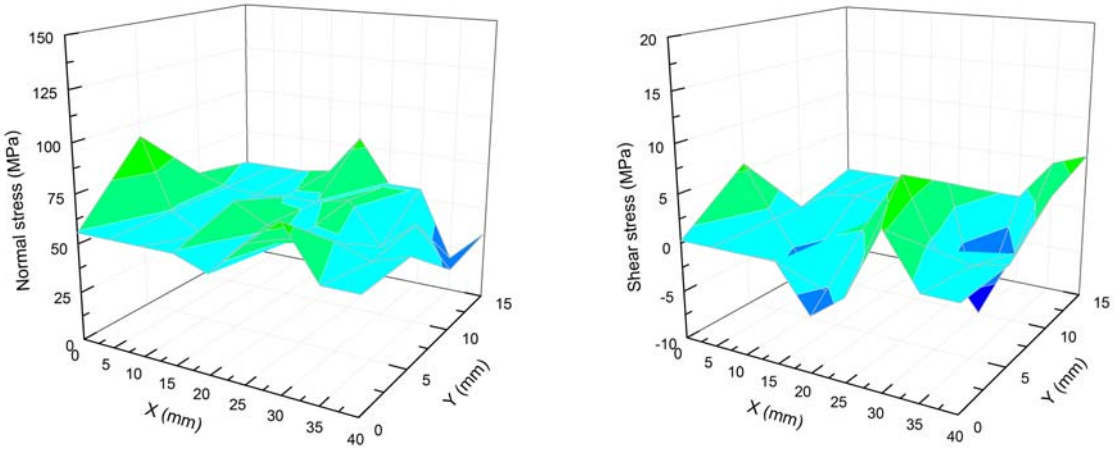

(a) **(b)**

Figure III.18. Profiles of residual stresses in sample T1EF07 as machined: (a) normal stresses and (b) shear stresses.

Residual stresses in fatigue test samples under different surface finish conditions (T1EF01 and T1EF02) were also measured in order to define the more suitable polishing procedure, which could sufficiently reduce surface roughness and uncertainties of XRD measurements, without introducing additional residual stresses. Profiles of residual stresses acquired for sample T1EF01 after grinding is shown in Fig. III.20. Table III.9 presents

residual stresses measured on fatigue samples T1EF01 and T1EF02 after different polishing procedures. Grinding introduced high compressive residual stresses, while electrolytic polishing attenuated residual stresses. Electrolytic polishing was then selected as the more suitable polishing procedure for the fatigue test samples. Table III.8 presents the average residual stresses of the fatigue test samples measured after electrolytic polishing. Electrolytic polishing attenuated the residual stresses of the samples and reduced uncertainties of XRD measurements.

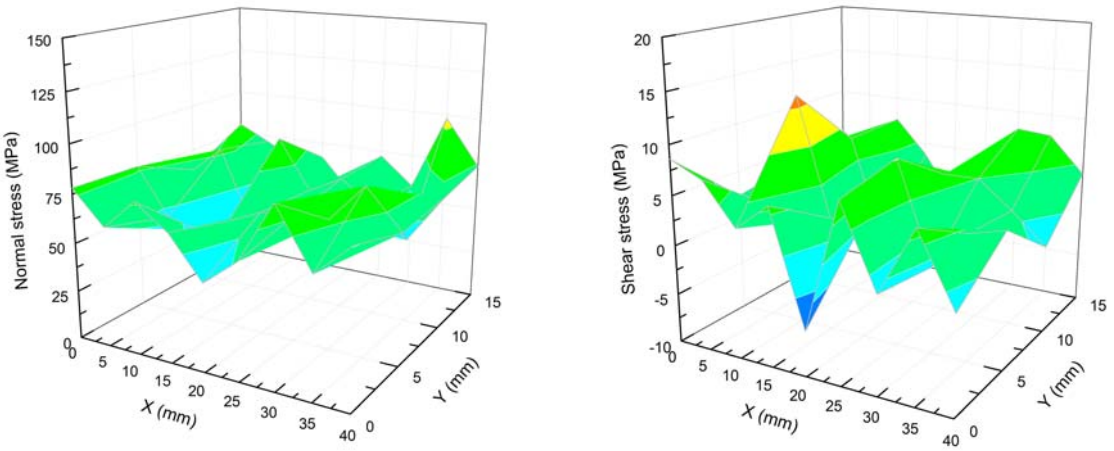

(a) **(b)**

Figure III.19. Profiles of residual stresses in sample T1EF15 as machined: (a) normal stresses and (b) shear stresses.

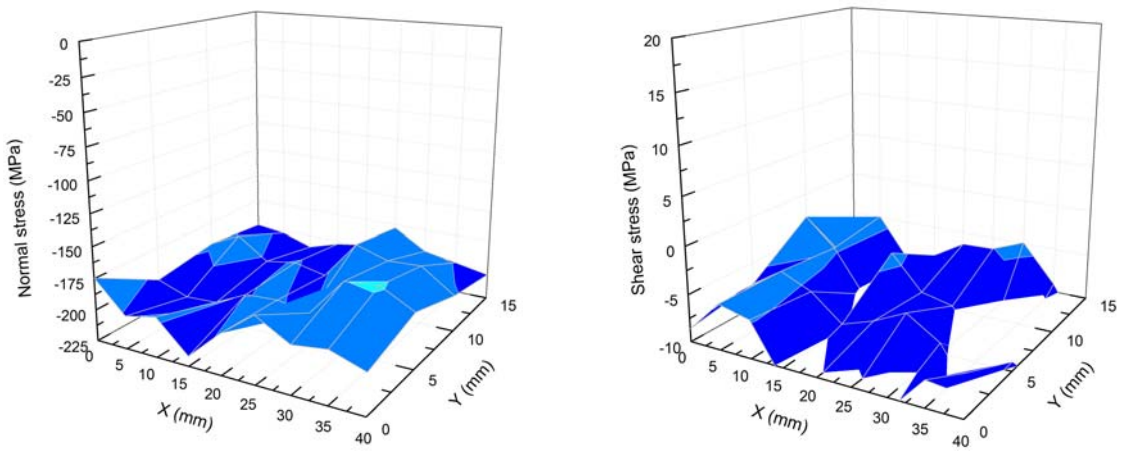

(a) **(b)**

Figure III.20. Profiles of residual stresses in sample T1EF01 after grinding: (a) normal stresses and (b) shear stresses.

Table III.8. Average residual stresses and average roughness R_a of fatigue test samples before and after electrolytic polishing.

Surface finish	Normal stress		R_a (µm)
	Normal stress (MPa)	Shear stress (MPa)	
Machining	60 ± 11	-10 ± 5	0.405
Electrolytic polishing	45 ± 6	3 ± 2	0.206

Table III.9. Residual stresses measured on fatigue test samples after different surface finish procedures.

Sample	Surface finish	Residual stress	
		Normal stress (MPa)	Shear stress (MPa)
T1EF01	Machining	54 ± 11	6 ± 5
T1EF01	Grinding	-192 ± 7	-9 ± 3
T1EF01	Grinding and electrolytic polishing	-73 ± 8	-9 ± 4
T1EF01	Electrolytic polishing	40 ± 10	-3 ± 5
T1EF02	Machining	93 ± 10	1 ± 5
T1EF02	Electrolytic polishing	20 ± 9	0 ± 4

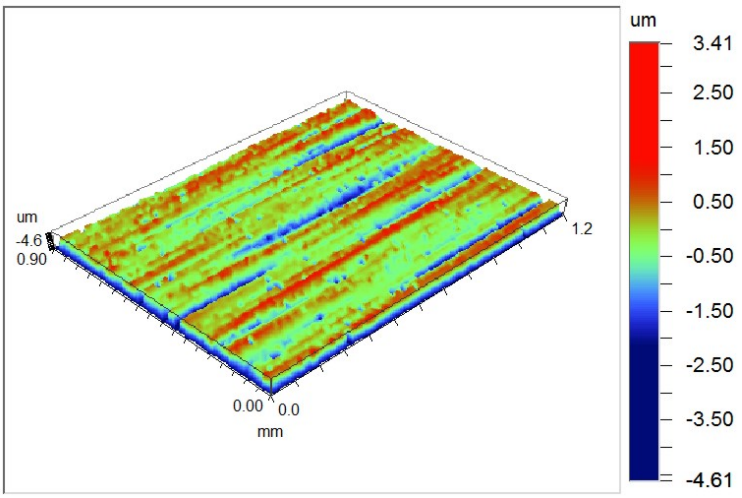

Figure III.21. Three-dimensional surface roughness profile of fatigue sample T1EF01 as machined (magnification 5x).

III. 2.3.4. SURFACE ROUGHNESS

Surface roughness of samples T1EF01, T1EF02 and T1EF21 was measured before and after different polishing procedures with the aid of VEECO instruments Wyko NT9100 optical profiler, which provides three-dimensional surface maps through scanning

interferometry. Figures III.21 and III.22 show, respectively, three-dimensional and two-dimensional surface roughness profiles acquired on sample T1EF01 as machined. Figure III.23 presents three-dimensional surface roughness profiles of sample T1EF01 after grinding and electrolytic polishing. The corresponding two-dimensional surface roughness profiles of this sample are shown in Figs. III.24 and III.25, respectively. Table III.10 presents average statistical parameters obtained from scanning data on samples with different surface finish conditions, where R_a is the average roughness, R_q is the root mean square roughness and R_t is the peak-to-valley roughness.

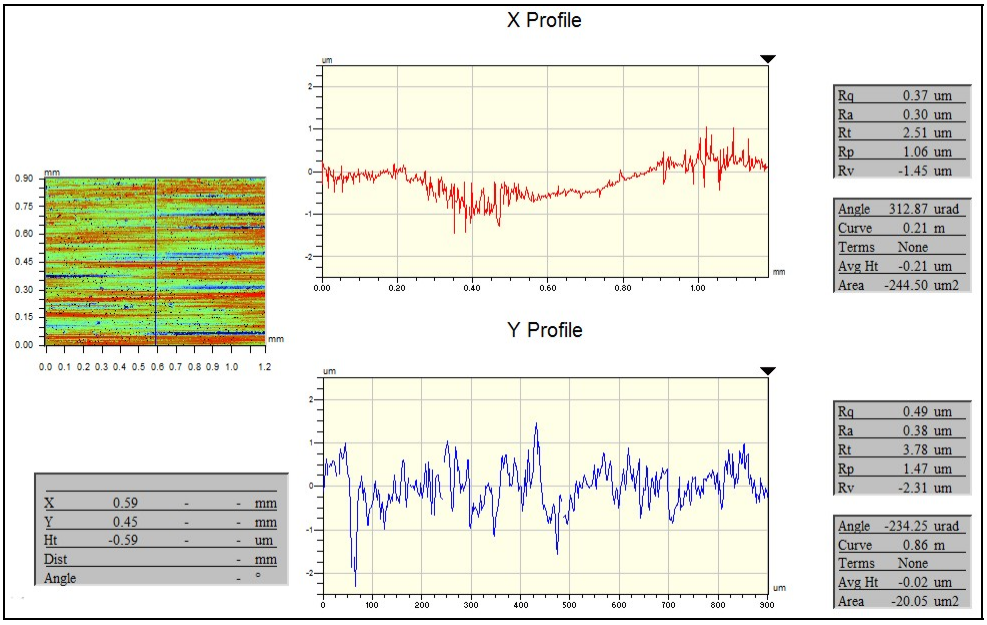

Figure III.22. Two-dimensional surface roughness profiles of fatigue sample T1EF01 as machined.

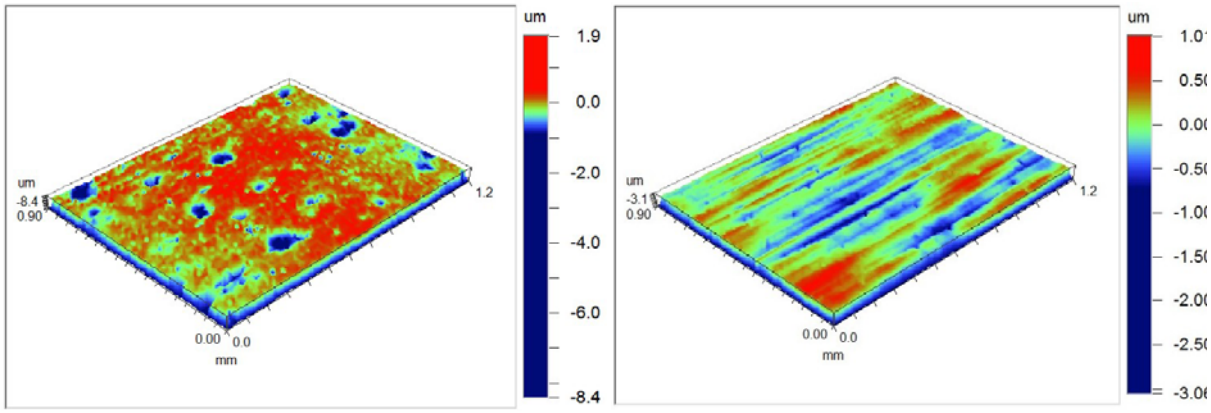

(a) **(b)**

Figure III.23. Three-dimensional surface roughness profiles of fatigue sample T1EF01 after (a) grinding and (b) electrolytic polishing (magnification 5x).

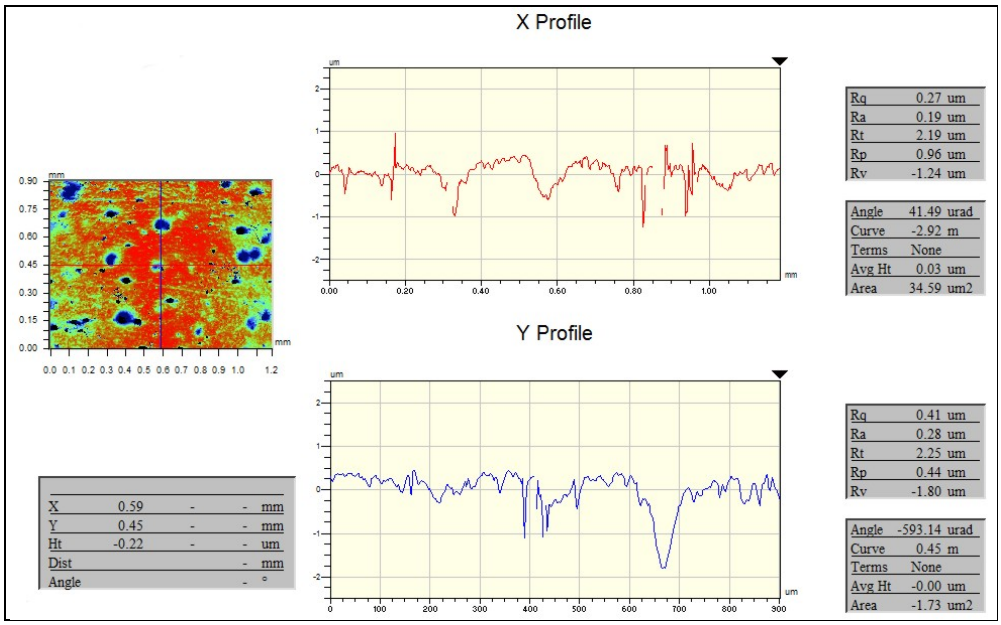

Figure III.24. Two-dimensional surface roughness profiles of fatigue sample T1EF01 after grinding.

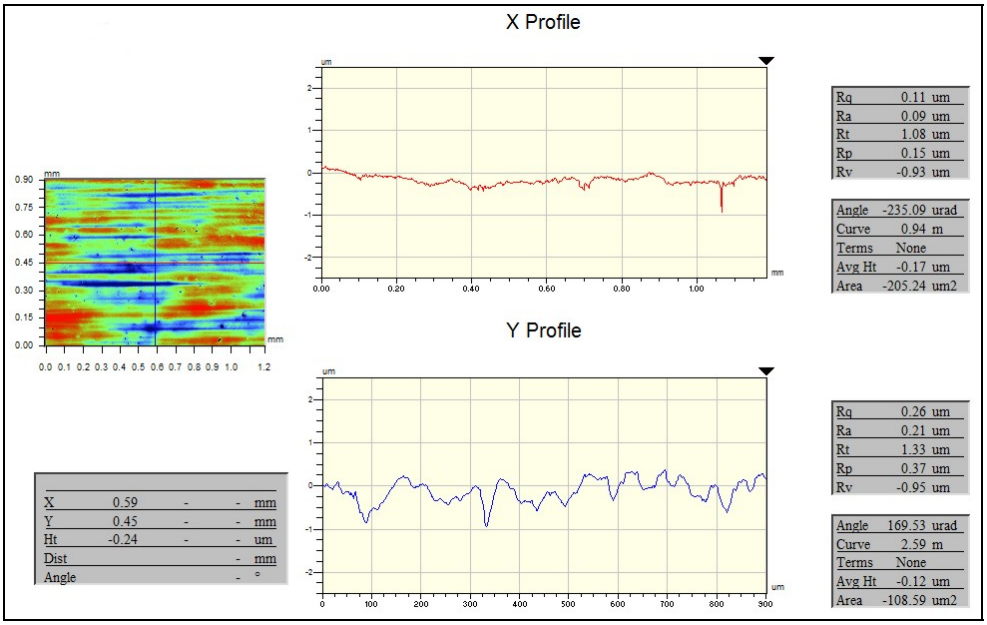

Figure III.25. Two-dimensional surface roughness profiles of fatigue sample T1EF01 after electrolytic polishing.

Table III.10. Average surface roughness statistical parameters.

Surface finish	R_a (µm)	R_q (µm)	R_t (µm)
Machining	0.405	0.524	6.670
Grinding	0.171	0.333	14.152
Electrolytic polishing	0.206	0.267	5.376

The average roughness R_a was considerably reduced after both grinding and electrolytic polishing. The average roughness R_a of 0.405µm in machined samples was reduced to 0.171µm and 0.206µm after grinding and electrolytic polishing, respectively. Even if greater reduction in R_a was induced by grinding, this polishing procedure led to an increase in the other statistical parameters, R_q and R_t. In contrast, electrolytic polishing was responsible for a reduction in all statistical parameters evaluated. Electrolytic polishing resulted in more homogenous and attenuated surface roughness when compared to grinding. Surface roughness attenuation was followed by higher precision of XRD peaks (better penetration of X-rays in the material) and lower uncertainties of residual stress measurements. Table III.8 summarizes the effects of electrolytic polishing on residual stresses and surface roughness.

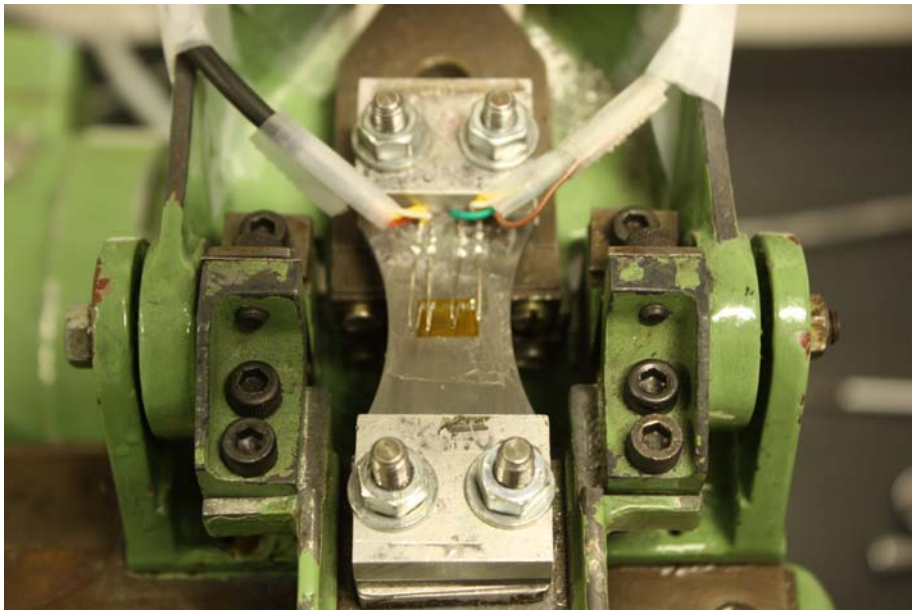

Figure III.26. Fatigue test sample instrumented with a biaxial strain gage.

III. 2.4. LOADING TESTS

Loading tests were carried out to calibrate the fatigue testing machine and to prescribe strain amplitudes for the applied alternating bending loads. With this purpose, one fatigue test sample was instrumented with a biaxial strain gage, as shown in Fig. III.26. Signals from the biaxial strain gage were transferred to a data acquisition system controlled by computational software. Figure III.27 exposes the experimental setup for the loading tests, which includes the fatigue testing machine, the strain gage instrumentation of a fatigue test sample, the data acquisition system and a PC. The calibration of the fatigue testing machine is summarized in

Fig. III.28, where the strain amplitude is correlated to the reference number of the dual eccentric.

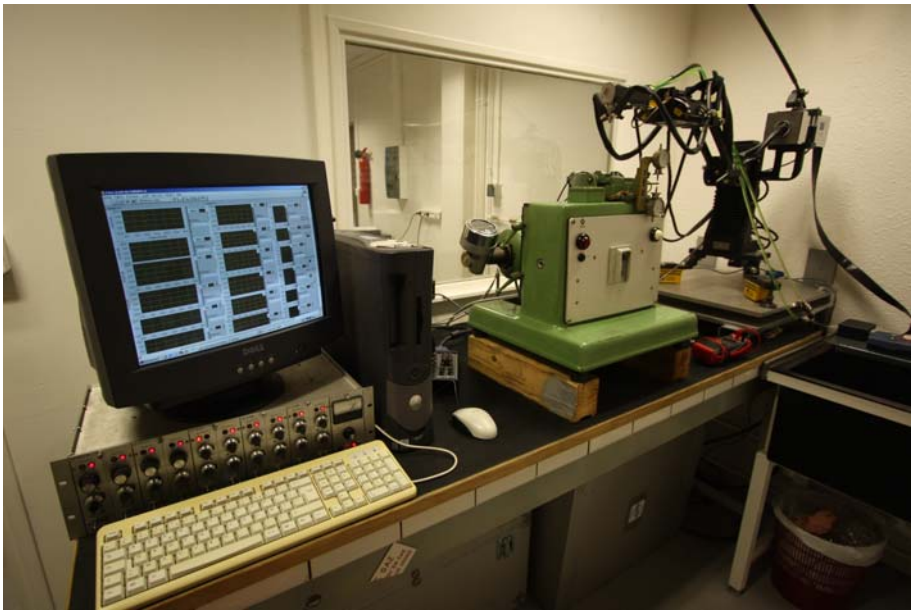

Figure III.27. Experimental setup for the loading tests.

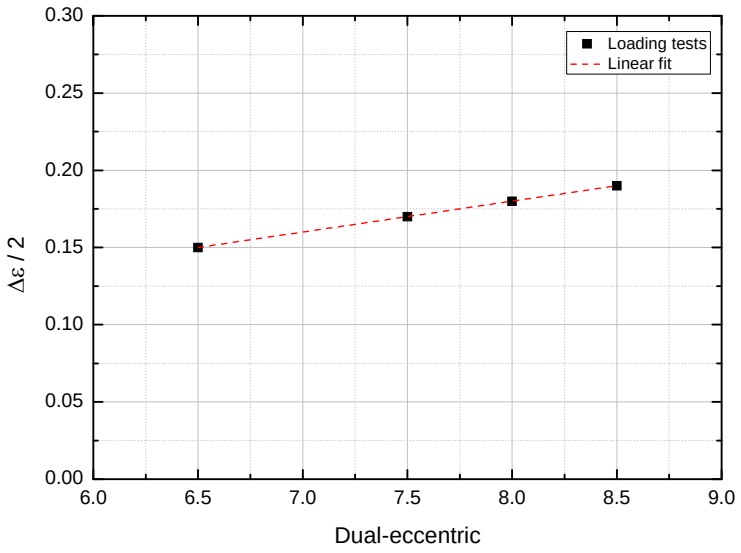

Figure III.28. Correlation between strain amplitude and reference number of the dual eccentric for calibration of the fatigue testing machine.

Table III.11 presents results of longitudinal strains obtained in loading tests with five different alternating bending loads, where ε_{min} and ε_{max} are the minimum and maximum strains, respectively, and $\Delta\varepsilon/2$ is the strain amplitude. For the highest strain amplitude,

alternating bending loads were applied with different mean stresses. As a result of the Poisson effect, neglecting transverse strains were observed.

Table III.11. Applied alternating bending loads acquired by loading tests (Exp.) and FE simulations.

Alternating bending load		Longitudinal strain Exp. (%) ε_{min} ε_{max}	$\Delta\varepsilon/2$	Longitudinal strain FE (%) ε_{min} ε_{max}	$\Delta\varepsilon/2$	Error (%)	Longitudinal stress FE (MPa) σ_{min} σ_{max}	σ_a	R
1	M+	-0.1355	0.1500	-0.1338	0.1497	1.23	-247	277	-0.8
	M-	0.1646		0.1655		0.57	306		
2	M+	-0.1819	0.1700	-0.1830	0.1724	0.63	-338	319	-1.1
	M-	0.1581		0.1619		2.39	299		
3	M+	-0.2375	0.1855	-0.2335	0.1836	1.69	-432	340	-1.7
	M-	0.1334		0.1338		0.25	247		
4	M+	-0.1923	0.1922	-0.1939	0.1950	0.82	-358	361	-1
	M-	0.1920		0.1961		2.12	363		
5	M+	-0.3058	0.1914	-0.3120	0.1984	2.06	-542	367	-2.8
	M-	0.0786		0.0848		8.00	193		

III. 2.5. NUMERICAL SIMULATIONS

Numerical simulations were carried out according to the finite element (FE) method to estimate stress amplitudes corresponding to strain-controlled applied loadings and stress distributions on fatigue test samples. A finite element model was generated with the aid of the code ABAQUS version 6.8 [110] to reproduce one cycle of the fatigue test.

III. 2.5.1. FE MESH

The FE mesh is composed of quadratic continuum solid elements C3D20R [110], with twenty nodes, three degrees of freedom per node and reduced integration. The mesh comprises 41,209 nodes and 8,144 elements. The mesh is more refined along the gage length, were higher stresses are expected to occur. Figure III.29 shows the FE mesh, highlighting the elements corresponding to the strain gage area (loading tests). The spring support of the fatigue testing machine (Fig. III.10) was modeled with the aid of spring elements SPRING1 [110]. Element type SPRING1 was used to model a spring between a reference node and the ground, acting in a fixed direction associated with vertical displacement.

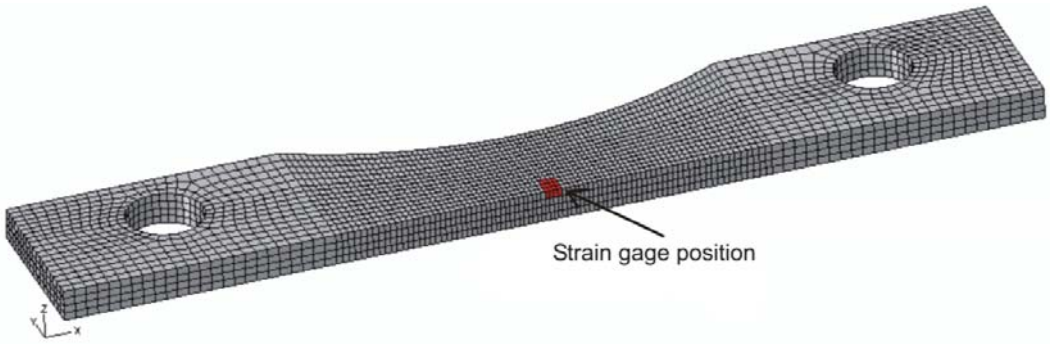

Figure III.29. FE mesh and highlight of elements in the strain gage area (loading tests).

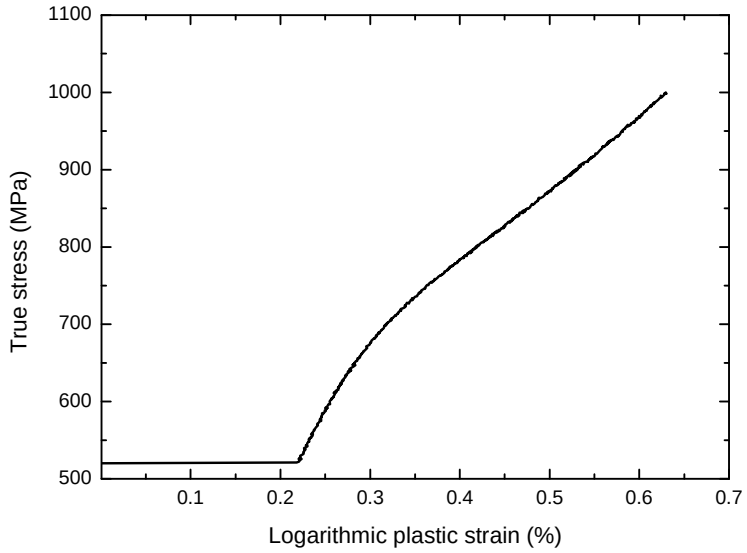

Figure III.30.True stress versus logarithmic plastic strain of API 5L X60 grade steel.

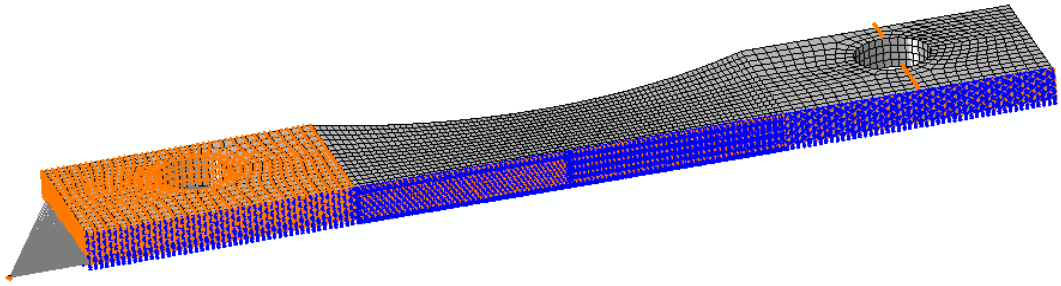

Figure III.31. Boundary conditions of the FE model.

III. 2.5.2. CONSTITUTIVE MODEL

The FE model assumes infinitesimal plasticity and allows finite rotations. A plastic constitutive behavior was adopted within the potential flow rule, assuming the von Mises yield function under combined isotropic and kinematic hardening. An average stress-strain

curve was used as input to the model in terms of true stress versus logarithmic plastic strain data, as shown in Fig. III.30. Since cyclic uniaxial tensile tests were not carried out, an approximation routine using only half cycle was adopted within the kinematic hardening theoretical approach [110].

III. 2.5.3. BOUNDARY CONDITIONS AND LOADING

Vertical displacements are coupled to the spring deflection in one extremity and prescribed in the other extremity in order to apply the alternating bending load. Considering the symmetry in the transverse direction, only one-half of the sample geometry was modeled. Figure III.31 shows the boundary conditions adopted, where orange symbols mean constrained or prescribed displacements and blue symbols represent constrained rotations.

The spring rate was estimated considering the energy associated with the spring in the Castigliano's theorem [73]. The total strain energy of a helical spring is composed of torsional and shear components and is given by

$$U = \frac{T^2 l}{2GJ} + \frac{F^2 l}{2AG} \qquad \textbf{(III.11)}$$

where T and F are the torque and the axial force acting in the spring, respectively, $G = E/[2(1+\nu)]$ is the shear modulus, l is the length of the spring, and A and J are the area and the polar second moment of area of the cross section of the spring, respectively. Defining

$$T = \frac{FD}{2} \qquad \textbf{(III.12)}$$

and

$$l = \pi DN \qquad \textbf{(III.13)}$$

where D is the mean coil diameter and N is the number of active coils. Substituting Eqs. III.12 and III.13 in Eq. III.11 results in

$$U = \frac{\pi F^2 DN}{2Gbh}\left[\frac{3D^2}{(b^2+h^2)}+1\right] \qquad \textbf{(III.14)}$$

where *b* and *h* are the width and height of the cross section of the spring, respectively. Then, using the Castigliano's theorem to find the total deflection *y* leads to [73]

$$y = \frac{\partial U}{\partial F} = \frac{\pi DN}{Gbh}\left[\frac{3D^2}{(b^2+h^2)}+1\right]F \qquad \textbf{(III.15)}$$

Defining

$$C = \left[\frac{3D^2}{(b^2+h^2)}+1\right] \qquad \textbf{(III.16)}$$

the spring rate $k = F/y$ can then be obtained as

$$k = \frac{F}{y} = \frac{Gbh}{\pi CDN} \qquad \textbf{(III.17)}$$

With G = 70 GPa (for Poisson's ratio ν = 0.3 and E given in Table III.4), b = 4.7 mm, h = 5.85 mm, and N = 2.25, Eq. III.17 gives k = 300 N/mm.

The model reproduces one cycle of the fatigue test with a load step of alternating bending load of sinusoidal waveform with frequency of 25 Hz. The first half-cycle of the load step applies positive moment M+ followed by negative moment M- in the second half-cycle.

III. 2.5.4. FE RESULTS

Figures III.32 and III.33 show FE results of longitudinal stress distribution at applied stress amplitudes of 319 MPa (R = -1.1) and 361 (R = -1), corresponding to loadings 2 and 4 in Table III.11. The undeformed contour, represented by the thicker line, is superposed to the deformed configuration. FE results of longitudinal strains were averaged over the strain gage fixation area in order to correlate them to results from loading tests and to verify the validity of the FE model. In Table III.11, strain results acquired by numerical simulations (FE) and loading tests (Exp.) are compared; an average error of less than 2% was obtained. The FE model can then reproduce strain amplitudes from fatigue tests with engineering accuracy. Stress amplitudes corresponding to the alternating bending loads considered were then estimated by FE simulations. Table III.11 presents longitudinal stresses estimated by FE simulations, where σ_{min} and σ_{max} are the minimum and maximum stresses, respectively, and σ_a is the stress amplitude.

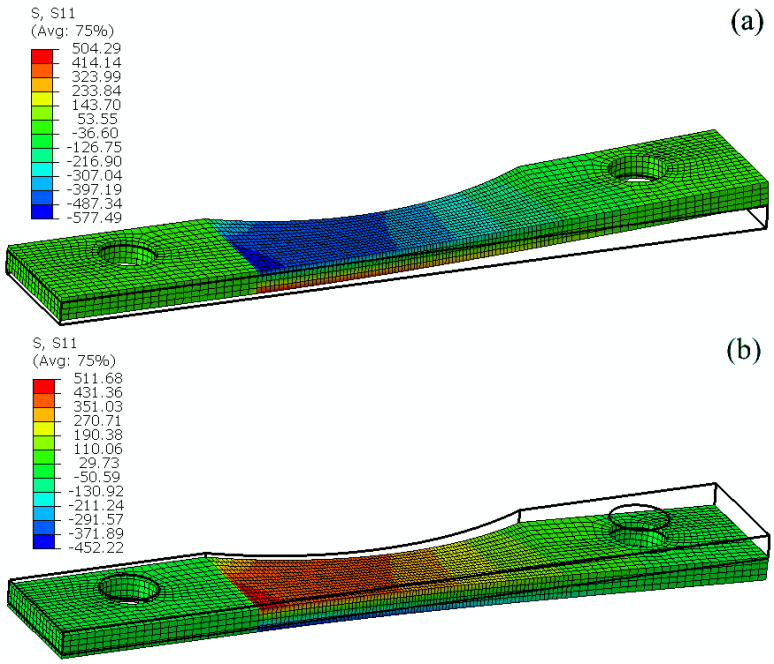

Figure III.32. FE results of longitudinal stress distribution (in MPa) at stress amplitude of 319 MPa (*R* = -1.1) for (a) positive and (b) negative maximum bending moments.

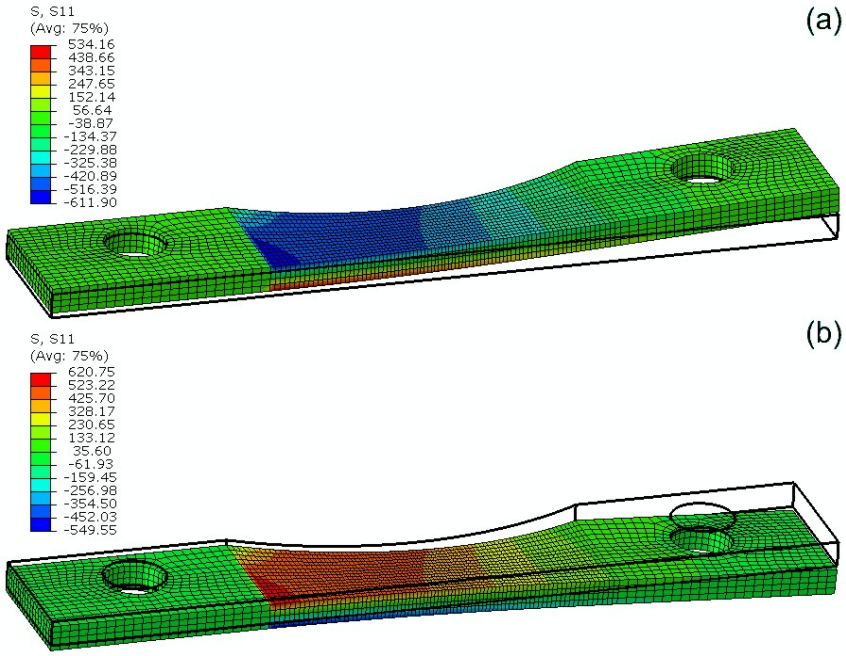

Figure III.33. FE results of longitudinal stress distribution (in MPa) at stress amplitude of 361 MPa (*R* = -1) for (a) positive and (b) negative maximum bending moments.

III. 3. FATIGUE TESTS ON ANNEALED SAMPLES

The effects of restoration of the nonstressed dislocation network state were studied by submitting samples to annealing treatment previously to fatigue tests. The initial dislocation

network state of the machined samples was affected by cold working during pipe manufacturing.

When a metal is cold worked (deformed at room temperature), the dislocation density increases and the microstructure becomes severely distorted [73]. The strength and hardness of metals are increased due to cold working, also referred to as work hardening or strain hardening, while the ductility is reduced. Cold worked materials with highly distorted microstructures are in a high-energy state and are thermodynamically unstable. Annealing of steels involves heating to a temperature above the upper critical temperature (about 50°C above this temperature), followed by very slow cooling. Annealing process transforms the material to a lower-energy state through thermal activation energy provided by heating. Since during annealing the hardening effect is eliminated by reducing the dislocation density and relieving internal lattice strains, the strength and hardness decrease while the ductility increases [73]. Annealing also results in reduction of fatigue life and strength [74]. There is also a significant reduction in machining-induced residual stresses due to annealing [74].

Four alternating bending fatigue tests were carried out on annealed samples. Fatigue test samples were annealed for 1h at 850°C under protective atmosphere, followed by cooling in the furnace. Before fatigue tests, metallographic analyses and Vickers microhardness tests were carried out to evaluate the microstructure and hardness of the annealed API 5L X60 grade steel. With this purpose, tests coupons were produced from the same steel pipe sample used previously to produce test coupons and fatigue test samples (Fig. III.1).

III. 3.1. METALLOGRAPHIC ANALYSES

The surface of a small test coupon was prepared for metallographic examination by grinding with a sequence of SiC papers from 80 to 1200 grit numbers under water cooling, followed by wet grinding with diamond micro powders from 6 μm to 1 μm, electrolytic polishing with a standard perchloric-based acid solution (standard electrolyte Struers A2), and etching with 5% Nital. The microstructure of the annealed material, observed through optical microscope, is shown in Fig. III.34. A fine-grained pearlitic-ferritic microstructure was observed.

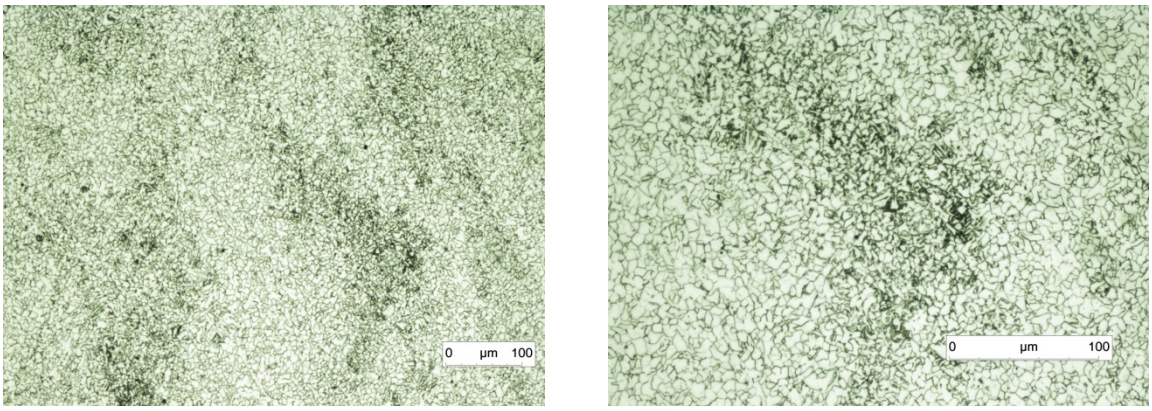

(a) **(b)**

Figure III.34. Microstructure of annealed API 5L X60 grade steel observed through optical microscope, original magnification factor of (a) 100x and (b) 200x.

III. 3.2. VICKERS MICROHARDNESS TESTS

The surface of test coupon of the annealed material was prepared for Vickers microhardness tests with the same metallographic preparation adopted for the original material. Vickers microhardness tests were performed with the aid of the Duramim-1/Struers microhardness test device with five different loads (0.1, 0.2, 0.3, 0.5 and 1 kg) applied for a dwell time of 15 s. Ten indentations were performed perpendicular to longitudinal direction (plane x-y) of the original pipe sample (Fig. III.1). Results obtained for indentations with 0.1 kg were neglected, in order to avoid size effects. Table III.12 compares results of Vickers microhardness obtained for hardened and annealed materials. The ultimate tensile strength S_u was estimated from correlation with the Vickers hardness according to Eq. III.2. Table III.12 shows the estimated value of ultimate tensile strength for the annealed material (longitudinal direction), which is lower than the ultimate tensile strength of the hardened material (602 MPa) obtained from uniaxial tensile tests (Table III.4). The reduction in strength and hardness confirms the effects produced by annealing.

Table III.12. Average results of Vickers microhardness for hardened and annealed API 5L X60 grade steel.

Machined samples		**Annealed samples**	
Longitudinal direction		**Longitudinal direction**	
HV	**S_u (MPa)**	**HV**	**S_u (MPa)**
195 ± 12	585 ± 36	154 ± 7	462 ± 21

CHAPTER IV

RESULTS AND DISCUSSION

CHAPTER IV

RESULTS AND DISCUSSION

In this chapter the experimental results are presented and discussed, including results of changes in residual stresses and microdeformations measured by X-ray diffraction during fatigue tests, analysis of fatigue fracture surfaces, and transmission electron microscopy (TEM) observations of dislocation structures.

IV. 1. RESULTS OF FATIGUE TESTS

Five different alternating bending loads were applied in the fatigue tests (Table III.11). Four different alternating bending loads were applied with stress ratios R around -1 (fully reversed stress). Additionally, fatigue tests were performed with R = -2.8 at the highest strain amplitude (0.19%). At least three fatigue tests were carried out for each loading. The obtained fatigue test results are presented in Table IV.1. Fatigue lives were determined at the rupture of the samples, after complete sample separation. Figure IV.1 shows a fatigue sample after rupture.

A non-statistically evaluated Basquin equation was obtained from fatigue test results, given as

$$S_{\mathrm{n}} = 1955\, N^{-0.1520} \qquad \textbf{(IV.1)}$$

with S_{n} in MPa. Since small variations in mean stress were found among the applied alternating bending loads 1-4 (Table III.11), fatigue tests results were corrected according to Gerber mean stress criterion [73] to bring every result to the condition of fully reversed bending stress load (R = -1). The Gerber mean stress criterion gives the alternating stress associated with failure at a particular number of cycles under a mean stress σ_{m} as [73]

$$\sigma_{\mathrm{a}} = \left[1 - \left(\frac{\sigma_{\mathrm{m}}}{S_{\mathrm{u}}}\right)^2\right] C N^{b} \qquad \textbf{(IV.2)}$$

where S_{u} is the ultimate tensile strength. Stress amplitudes corrected by the Gerber mean stress criterion are indicated in Table IV.1, where σ_{o} is the yield strength (Table III.4). When

small mean stresses are present, alternating stresses remained almost unchanged after correction.

Table IV.1. Results of fatigue tests.

Sample	Strain amplitude	Stress amplitude (MPa)			*R*	*N* (cycles)
		Applied	Corrected			
T1EF03	0.15%	277	277	$0.53\sigma_o$	-0.8	296,200
T1EF09						306,600
T1EF10						288,300
T1EF04	0.17%	319	319	$0.61\sigma_o$	-1.1	147,300
T1EF05						106,600
T1EF08						143,200
T1EF15						191,100
T1EF11	0.18%	340	348	$0.67\sigma_o$	-1.7	56,300
T1EF12						59,400
T1EF13						62,700
T1EF22	0.19%	361	361	$0.69\sigma_o$	-1	63,600
T1EF23						190,400
T1EF24						48,100
T1EF06	0.19%	367	401	$0.77\sigma_o$	-2.8	60,200
T1EF07						59,300
T1EF14						41,700

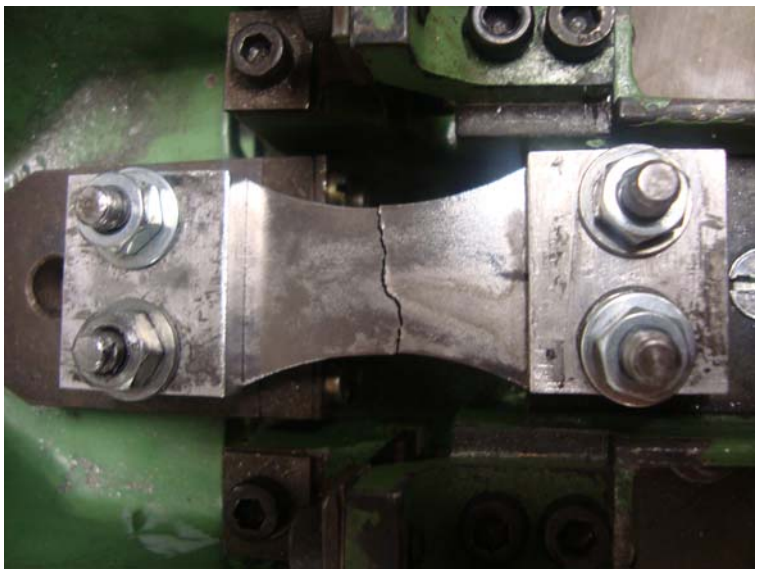

Figure IV.1. Fatigue test sample after rupture.

Figure IV.2 shows average fatigue test results for each alternating bending load applied, the obtained non-statistically S-N curve (Eq. IV.1) and the previously estimated Basquin equation (Eq. III.6). Even with small variations among applied strain amplitudes (0.02% maximum), a consistent range of resulting fatigue lives was observed, which also

confirms the reliability of alternating stress amplitudes estimated by FE simulations. The S-N diagram in Fig. IV.2 also shows that the fatigue test results are in good agreement with test results previously obtained and presented in [107], where the same material and identical testing conditions were used.

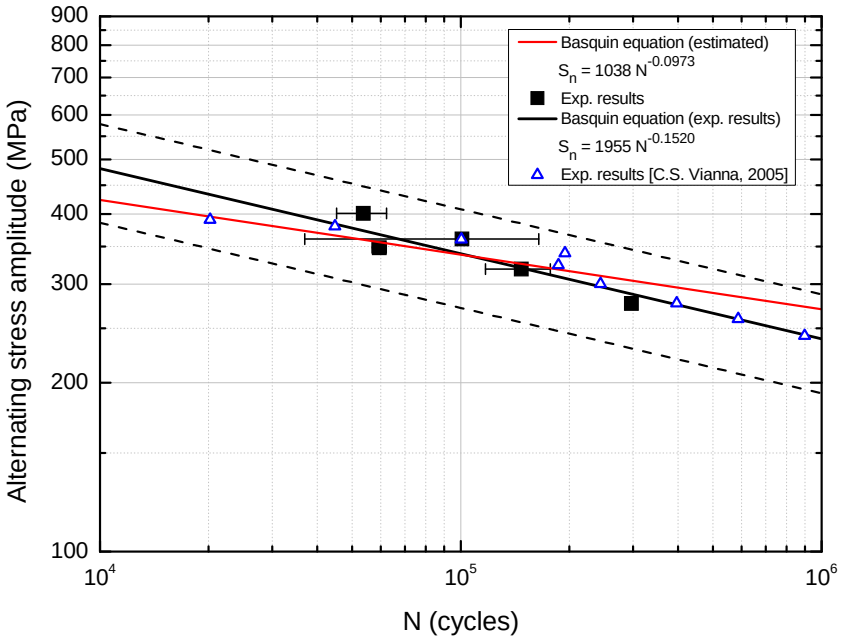

Figure IV.2. Results of alternating bending fatigue tests and non-statistically S-N curve.

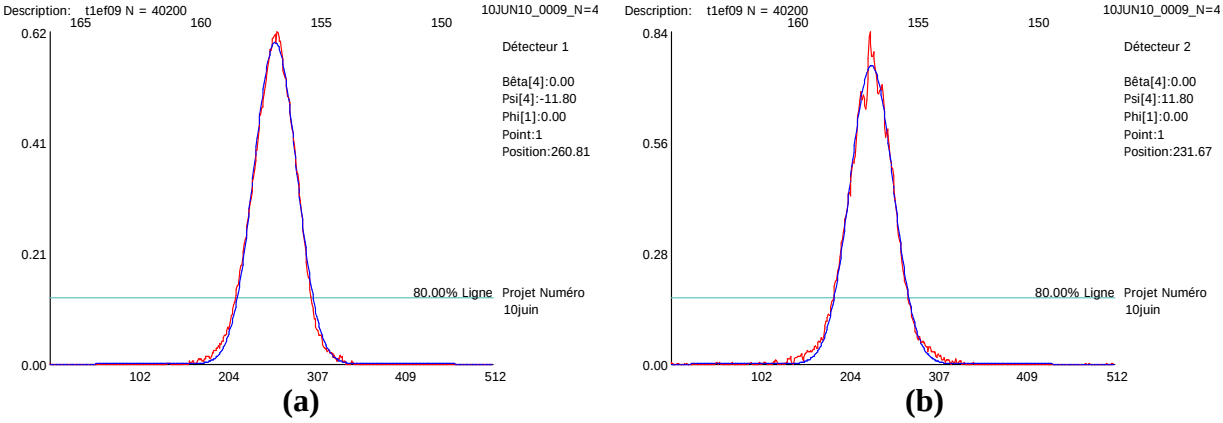

Figure IV.3. XRD peaks obtained by detectors (a) L1 and (b) R2 for alternating stress of 277 MPa at *N* = 40,200 cycles (sample T1EF09).

X-ray diffraction peaks obtained for alternating stress of 277 MPa at *N* = 40,200 cycles are shown in Fig. IV.3 (sample T1EF09). Figure IV.4 presents X-rays diffraction peaks detected for alternating stress of 319 MPa at different numbers of cycles (sample T1EF08). It can be noted that the peak width slightly decreased between *N* = 0 and *N* = 20,000 cycles (as

indicated by the 80% line), and thereafter the peak width remained almost constant. X-rays diffraction peaks obtained for alternating stress of 361 MPa at different numbers of cycles are shown in Fig. IV.5 (sample T1EF24). A small decrease in the peak width can be observed between N = 0 and N = 10,000 cycles, and for higher numbers of cycles no significant changes can be noted.

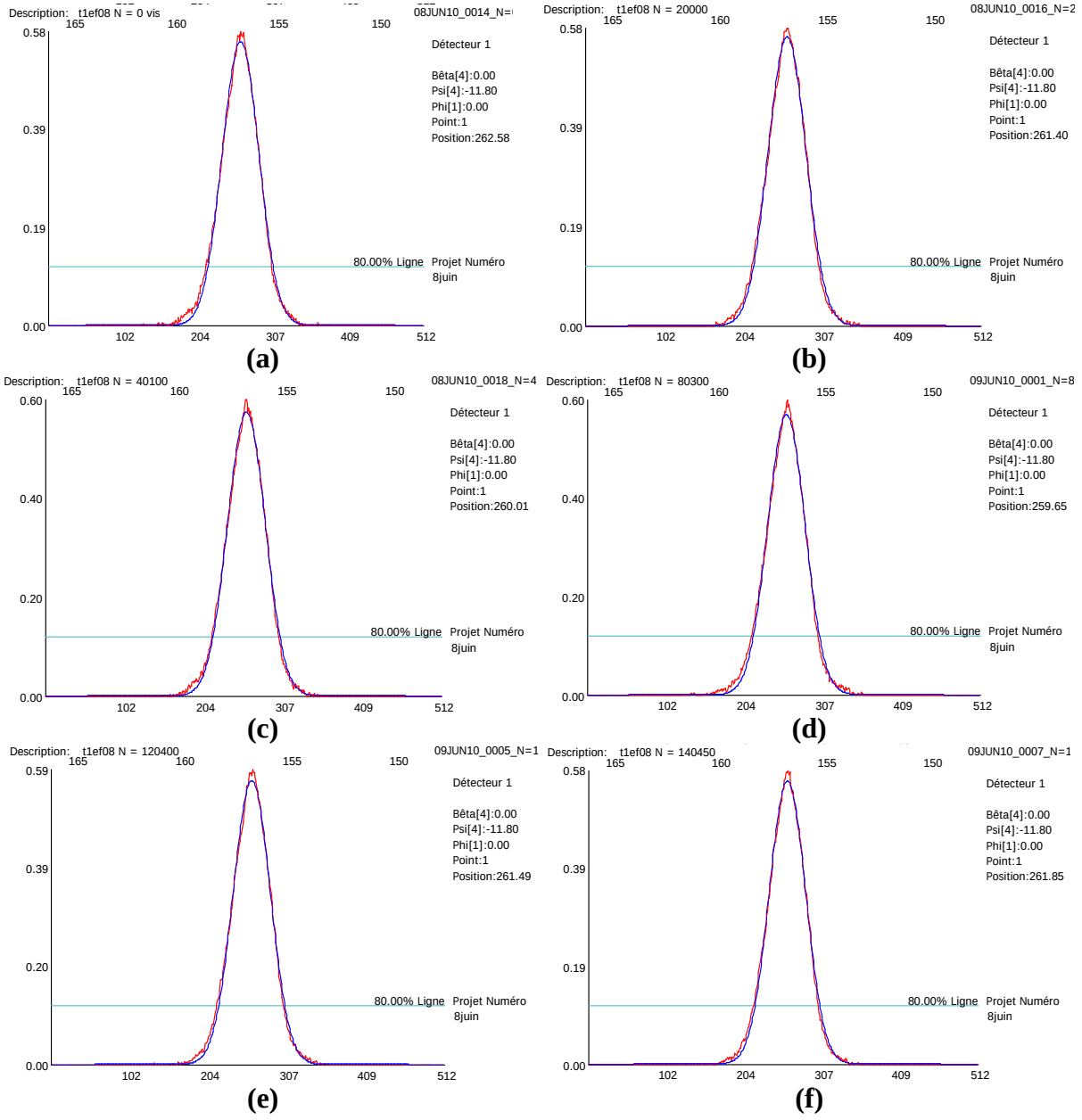

Figure IV.4. XRD peaks obtained by detector L1 for alternating stress of 319 MPa at (a) N = 0, (b) N = 20,000, (c) N = 40,100, (d) N = 80,300, (e) N = 120,400, and (f) N = 140,450 cycles (sample T1EF08).

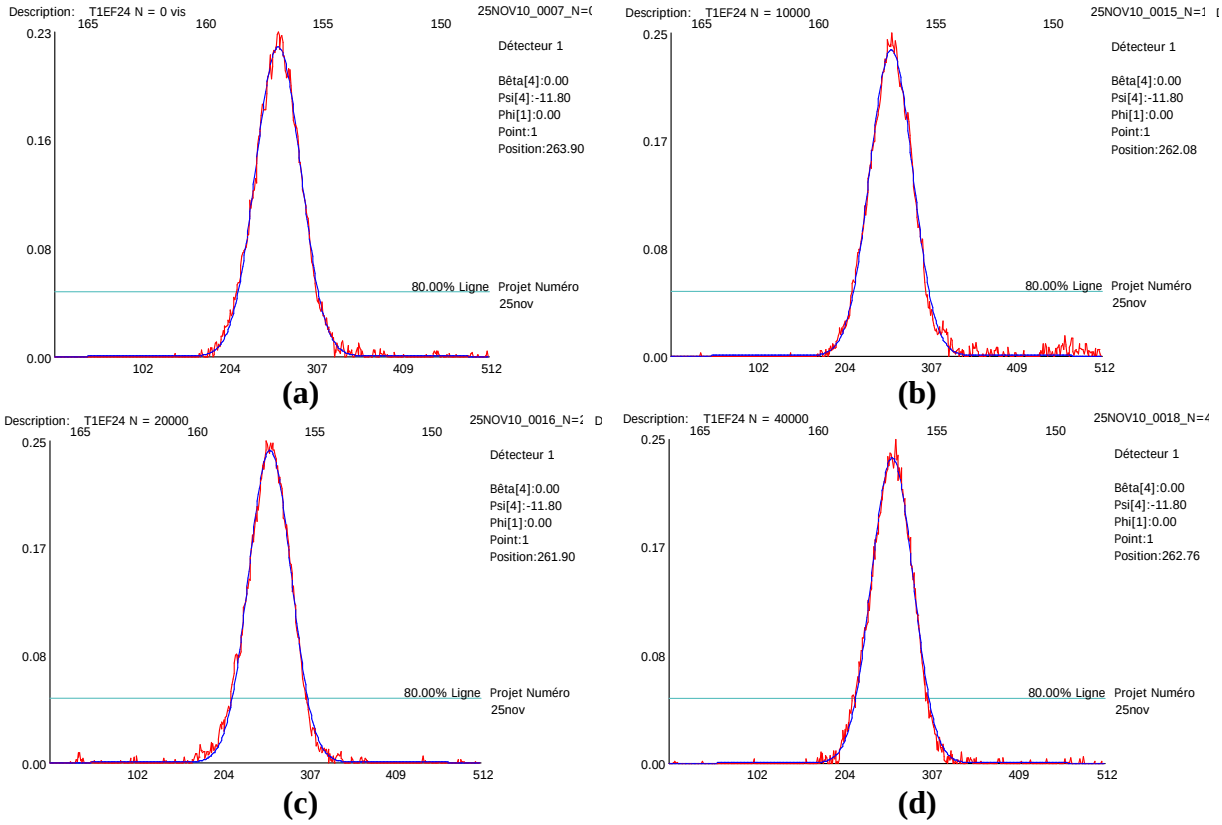

Figure IV.5. XRD peaks obtained by detector L1 for alternating stress of 361 MPa at (a) N = 0, (b) N = 10,000, (c) N = 20,000, and (d) N = 40,000 cycles (sample T1EF24).

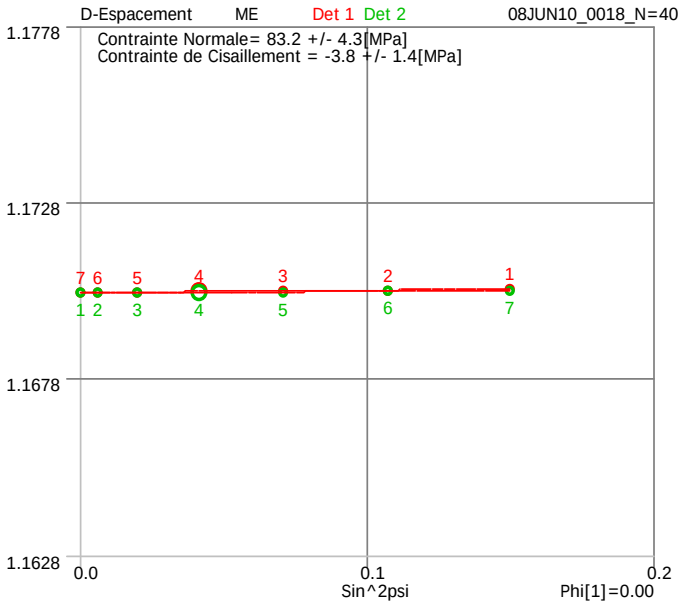

Figure IV.6. Diagrams of lattice spacing d versus $\sin^2\psi$ at N = 40,100 cycles for alternating stress of 319 MPa obtained by X-ray detectors L1 (Det1) and R2 (Det2) (sample T1EF08).

A diagram of lattice spacing d versus $\sin^2\psi$ at N = 40,100 cycles for alternating stress of 319 MPa (sample T1EF08) is shown in Fig. IV.6. This diagram presents results from the two X-ray detectors, with each result point corresponding to a different tilt angle. The absence of oscillations indicates the absence of crystallographic texture and elastic anisotropy, which would limit the use of the $\sin^2\psi$ method. As indicated in Table III.7, multiple expositions were performed under seven tilt angles.

In Figs. IV.7 to IV.11 variations in FWHM of X-ray diffraction peaks measured during fatigue tests at different stress amplitudes are presented. The FWHM change measured at a given number of cycles is defined as the difference between FWHM values at this point and at N = 0, i.e., FWHM – $FWHM_0$. Figure IV.8 shows three additional results obtained with run out of tests at 20,000 (T1EF16), 80,000 (T1EF17) and 120,000 (T1EF18) cycles. These fatigued samples were prepared for transmission electron microscopy (TEM) observations to investigate dislocation densities and structures.

For all stress amplitudes, three stages can be identified in FWHM changes during fatigue cycling. The first stage (Stage 1) takes place in the early cycles and is characterized by a fast decrease in FWHM. In the second stage (Stage 2), the rate of FWHM decrease is considerably reduced. This stage comprises the major fraction of fatigue life (about 50%). Finally, the third stage (Stage 3) occurs in the last cycles with a rapid decrease in FWHM until complete fracture. Average curves of FWHM changes obtained during fatigue tests at four different stress amplitudes (R = -1) are shown in Fig. IV.12. Increasing the stress amplitude accentuates FWHM changes and reduces the duration of each stage. Figures IV.7 to IV.11 also show the evolution of macro residual stresses with fatigue cycling, which presents three stages with durations similar to those observed in FWHM variations for a given stress amplitude. Average curves of changes in residual stresses with fatigue cycling at four different stress amplitudes (R = -1) are shown in Fig. IV.13.

The number of cycles delimiting the transition between Stages 1 and 2 is defined as N_1, while N_2 refers to the number of cycles delimiting Stages 2 and 3. Numbers of cycles characterizing N_1 and N_2 for the four stress amplitudes under R = -1 are plotted in Fig. IV.12 and listed in Table IV.2, where N_f is the number of cycles at failure. In general, fatigue life fractions N_1/N_f and N_2/N_f correspond to approximately 30% and 80% of the fatigue life, respectively. Table IV.2 also points out the FWHM decrease at N_1, defined as $FWHM_1$ – $FWHM_0$. Figure IV.14 shows that N_1 and N_2 can be well correlated to the stress amplitude by linear fits.

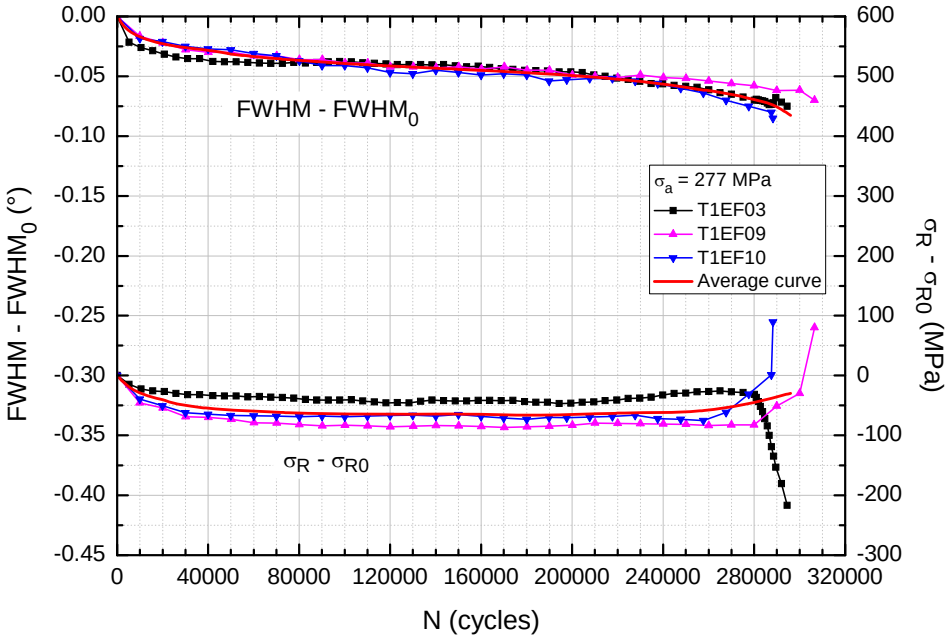

Figure IV.7. Evolution of FWHM and residual stresses σ_R with fatigue cycling at σ_a = 277 MPa (R = -1).

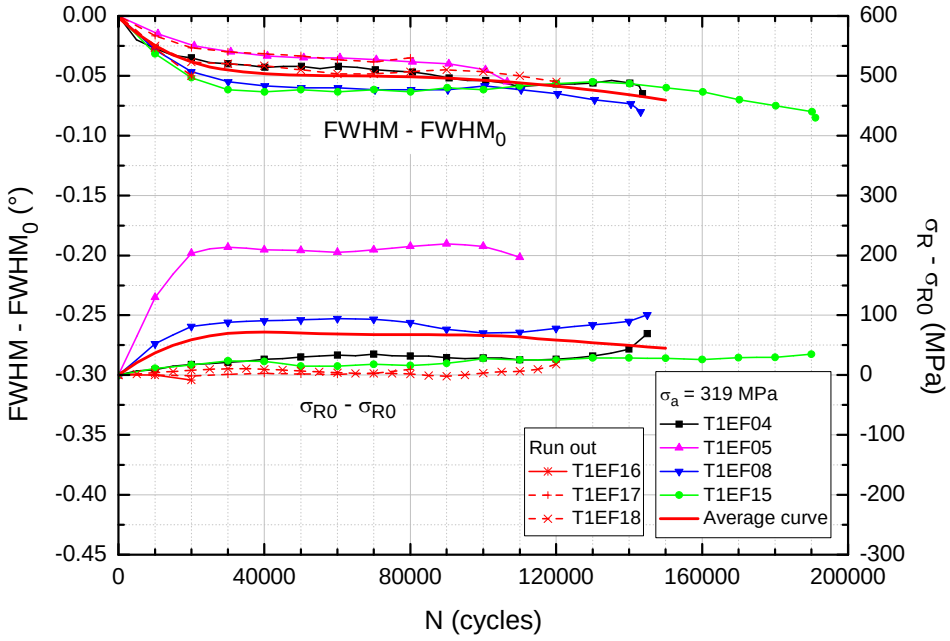

Figure IV.8. Evolution of FWHM and residual stresses σ_R with fatigue cycling at σ_a = 319 MPa (R = -1).

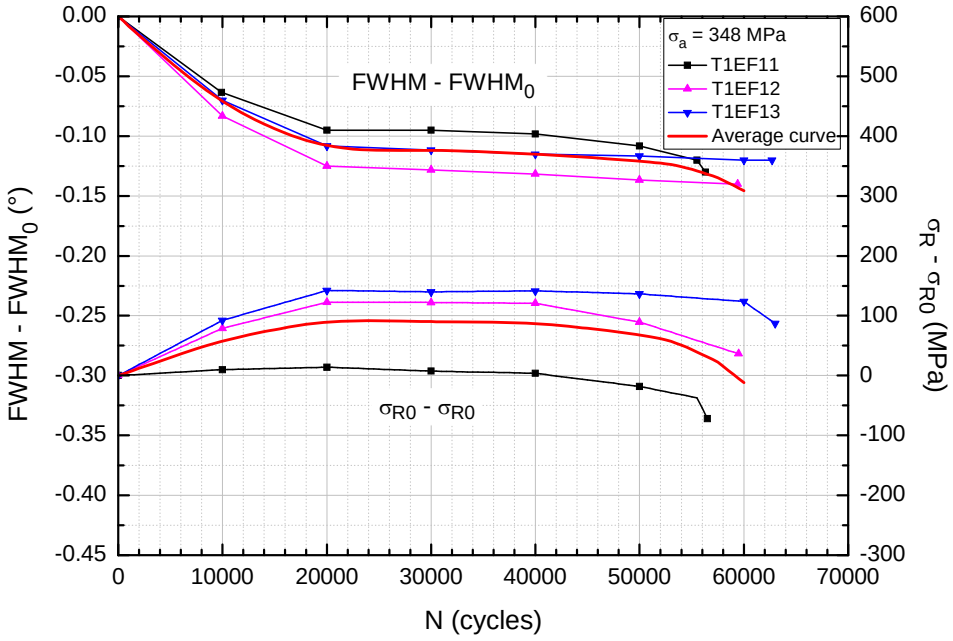

Figure IV.9. Evolution of FWHM and residual stresses σ_R with fatigue cycling at σ_a = 348 MPa (R = -1).

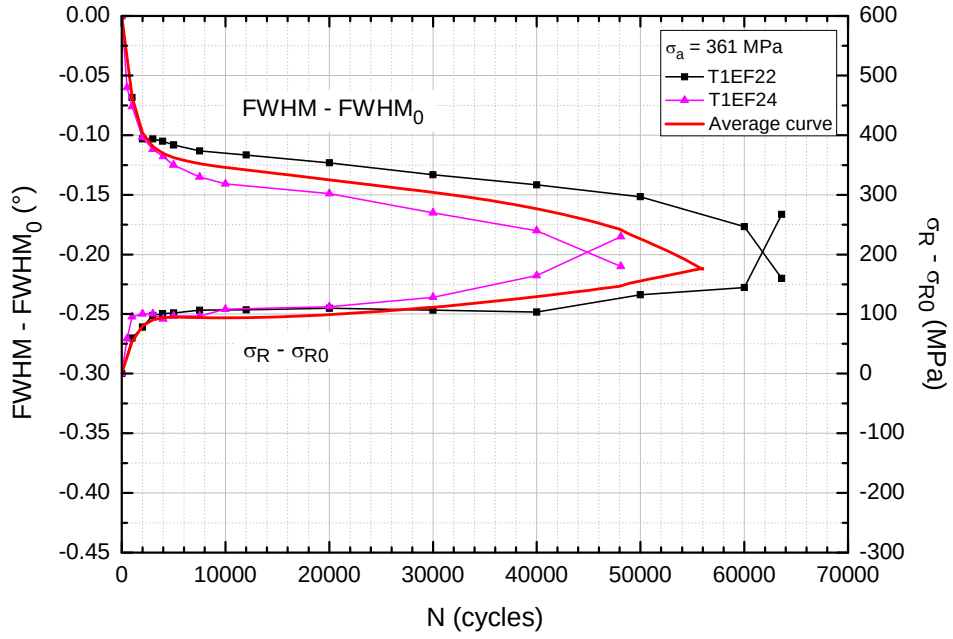

Figure IV.10. Evolution of FWHM and residual stresses σ_R with fatigue cycling at σ_a = 361 MPa (R = -1).

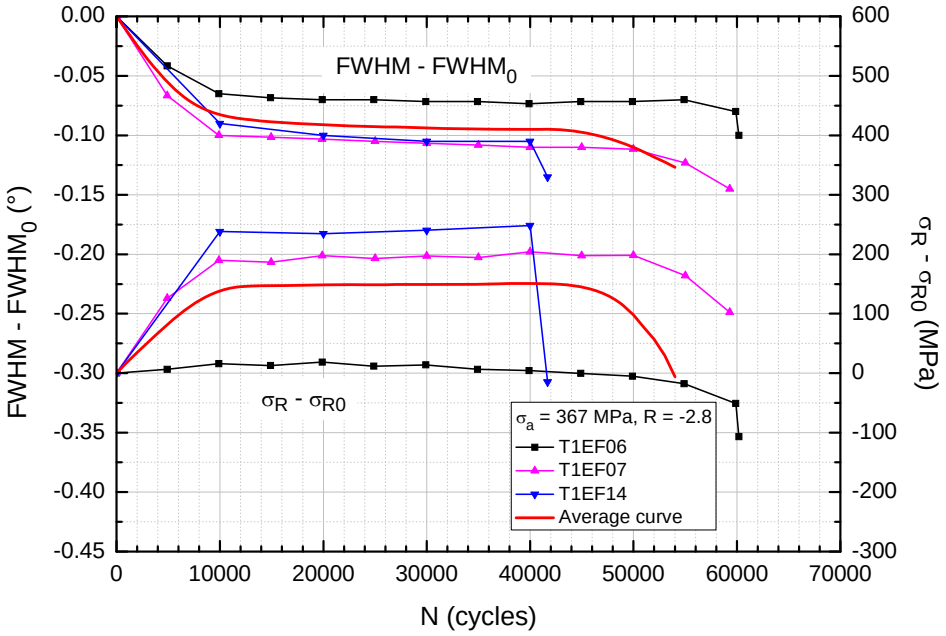

Figure IV.11. Evolution of FWHM and residual stresses σ_R with fatigue cycling at σ_a = 367 MPa (R = - 2.8).

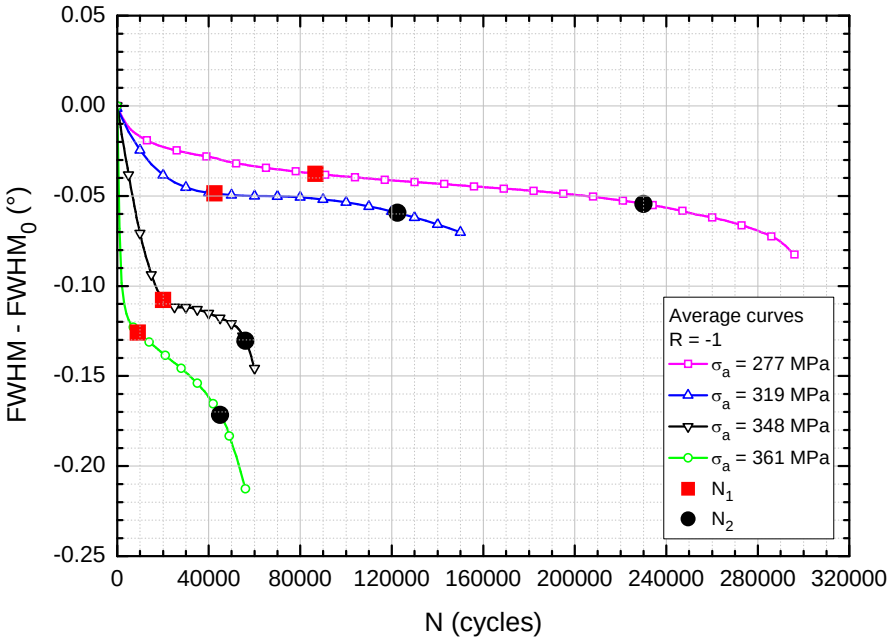

Figure IV.12. Average curves of FWHM changes during fatigue tests at different stress amplitudes (R = -1).

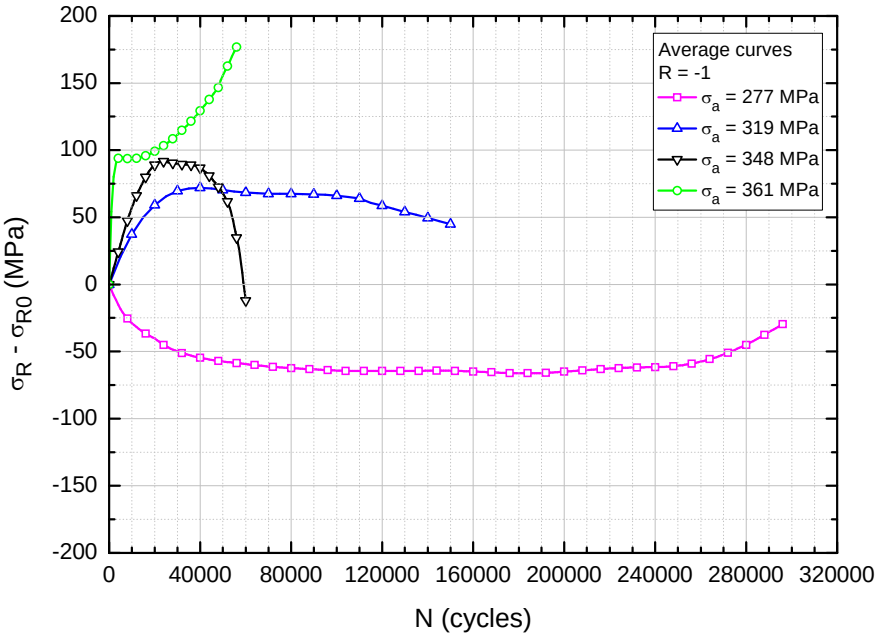

Figure IV.13. Average curves of changes in residual stresses σ_R during fatigue tests at different stress amplitudes (R = -1).

Table IV.2. Number of cycles delimiting stages of FWHM changes during fatigue testing.

σ_a (MPa)	R	$FWHM_1$-$FWHM_0$ (°)	N_1 (cycles)	N_2 (cycles)	N_f (cycles)	N_1/N_f	N_2/N_f
277	-1	-0.0377	86,667	230,000	297,033	0.29	0.77
319	-1	-0.0487	42,500	122,500	147,050	0.29	0.83
348	-1	-0.1078	20,000	56,000	59,467	0.34	0.94
361	-1	-0.1259	9,000	45,000	55,850	0.16	0.81
367	-2.8	-0.08265	10,000	44,000	53,733	0.19	0.82

It is well known that damage mechanisms observed during high cycle fatigue can be generally described by three distinct phases, namely initiation of microcracks, microcracking (microcrack propagation and coalescence), and macrocrack propagation [72]. In the first phase, strain localization leads to the formation of persistent slip bands (PSBs), extrusions and intrusions, which act as initiation sites for microcracks. The second phase is characterized by microcracking and microcrack propagation, usually along PSBs or slip planes of the crystalline structure with high shear stress [72]. The rate of microcrack propagation is very low (on the order of nm/cycle), and microcracks are frequently interrupted at grain boundaries that they cannot easily overcome, when adjacent grains are not favorably oriented [72]. In the last phase, macrocracking and macrocrack propagation take place. Macrocrack propagation

(on the order of μm/cycle) occurs in a direction normal to the maximum tensile stress applied and leads to sudden failure.

Considering that the microstructural changes measured in terms of variations in FWHM present three regular successive stages (Fig. IV.12), it can be supposed that a connection could exist between them and the three phases of fatigue damage mechanisms previously described.

In Stage 1 of the microstructural changes observed, the decrease in FWHM can be associated with the movement and multiplication of dislocations and rearrangement of the initial dislocation network. A part of the initial dislocation network is produced during the pipe manufacturing process by cold working. Another part may come from the sample preparation (machining, grinding, and polishing), which is also likely to induce some level of residual stresses. Microstructural changes during the early stages of fatigue are connected to movement and reorganization of dislocations, and strain localization [10,70]. The level of microdeformations can be estimated by observation of the X-ray diffraction peak: a decrease in FWHM is related to a reduction in microdeformations, while an increase in FWHM is generally associated with an increase in microdeformations [9,38,39].

From a macroscopic point of view, these changes are characterized by cyclic hardening or softening, depending on the initial structural state of the material [10]. For instance, an increase in FWHM during cyclic deformation of AA6110 aluminum alloy was accompanied by cyclic hardening [34]. Decrease in FWHM related to cyclic softening in a cold rolled high strength low alloy steel was observed during fatigue cycling in [47]. For strain amplitudes lower than 0.3%, pronounced softening in pearlitic steel is seen during the first few cycles in [39]. At this level of strain amplitude, the looser and consequently more flexible network created may explain the initial softening, which is the typical behavior of pearlitic steels [39]. In [20] cyclic softening in ferritic steel occurred during the major low cycle fatigue life fraction, followed by the saturation stage at higher number of cycles until the surface crack initiation and propagation impairs the load bearing capacity of the specimen, leading to a rapid fall in residual stress. On the other hand, at higher strain amplitudes the denser dislocation network created is associated with initial hardening [47].

The evolution of FWHM was found to decrease in regular successive stages with fatigue cycling of cold worked, shot peened, deep rolled, and laser shot peened steel samples [19,36-44]. In general, a decrease in FWHM is observed in the early stage of fatigue for hardened materials [69]. In contrast, FWHM may increase for annealed materials, since cyclic loading will most likely increase lattice distortion, which entails an increase in dislocation

density and microdeformations [10]. Here, the decrease in FWHM can be associated with reduction of microdeformations.

During Stage 2, the decreasing rate of FWHM is considerably reduced. This stage represents the major part of the fatigue life, especially for the lower alternating stress applied. This stage probably corresponds to the process of microcracks initiation and propagation. This process, which entails the creation of new free surfaces, can be considered as the propagation of a virtual crack, assuming that this crack would be the sum of individual microcracks propagating at a very low rate (on the order of nm/cycle). Considering that the macrocrack size at the end of Stage 2 is of the order of one or two grain sizes, i.e., 20-40 µm, it is possible to roughly estimate an apparent microcrack propagation rate during this stage. From the data given in Fig. IV.12 and Table IV.2, propagation rates would be about 0.14 and 0.60 nm/cycle for the highest and lowest stress amplitudes, respectively. This represents a very interesting perspective, since after the end of the initiation stage (Stage 1) it would be possible to calculate the duration of Stage 2, until the beginning of macrocrack propagation. This has to be confirmed on various materials and loading conditions in order to verify the possible quantification of fatigue damage before macroscopic cracking, which takes place during Stage 3. Stage 2 could also be associated with cyclic saturation of the material.

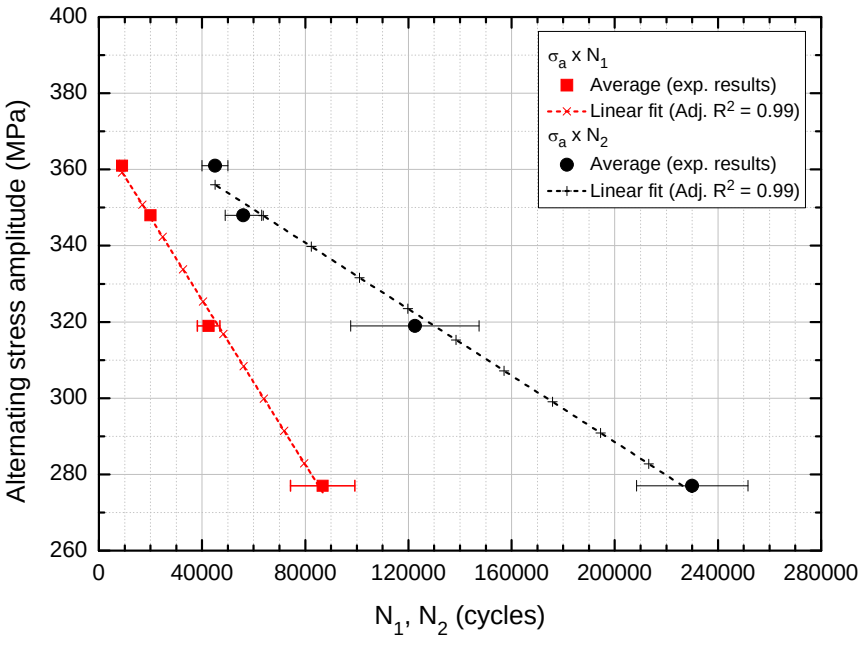

Figure IV.14. Number of cycles delimiting Stages 1 and 2 (N_1) and Stages 2 and 3 (N_2) during fatigue tests at different stress amplitudes.

Finally, Stage 3 occurs in the last cycles with a rapid decrease in FWHM until complete fracture. This behavior can be attributed to relaxation of microstresses due to macroscopic crack initiation and propagation (on the order of μm/cycle), preceding final failure.

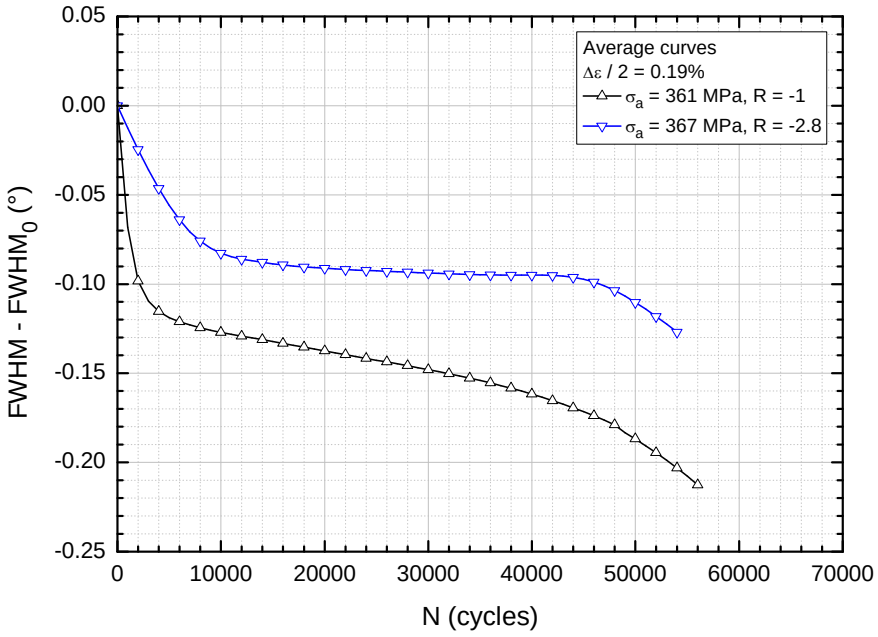

Figure IV.15. Evolution of FWHM with fatigue cycling at strain amplitude of 0.19% with different stress ratios.

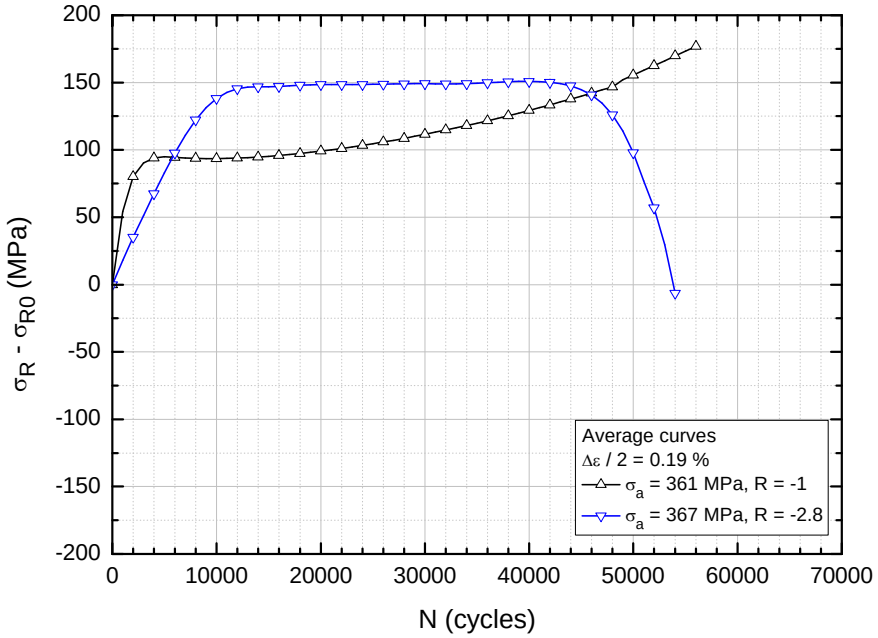

Figure IV.16. Evolution of residual stresses σ_R with fatigue cycling at strain amplitude of 0.19% with different stress ratios.

In Fig. IV.15, average curves of FWHM changes during fatigue tests obtained at the same strain amplitude (0.19%) with two different stress ratios *R* are compared. Even if the duration of each stage seems to remain unchanged, the decrease of the stress ratio (from -1 to -2.8) considerably reduces the amplitude of FWHM variations. It is considered that this behavior can be due to the lower tensile maximum stress at *R* = -2.8, which would result in less microstructural changes during fatigue cycling and consequently lower amplitude of FWHM variations. In Fig. IV.16, changes in residual stresses with fatigue cycling at strain amplitude of 0.19% with different stress ratios are compared.

It can be considered that there is a direct correlation between variations in FWHM and changes in residual stresses for all stress amplitudes. The evolution of residual stresses in the first cycles (Stage 1) could be different depending on the level of stress amplitude applied. For low stress amplitudes (277 MPa) residual stresses tend to decrease, while for high stress amplitudes (319-367 MPa) residual stresses tend to increase.

In Stage 3 the evolution of residual stress seems to be related to macrocrack initiation and propagation. In the last cycles, macroscopic cracking is followed by release of residual stresses (top surface). Generally, increasing residual stresses are observed when the crack propagates in the bottom surface, and decreasing residual stresses are measured when the crack propagates in the top surface. This is in agreement with the consideration that crack propagation would be accompanied by residual stress release along the crack.

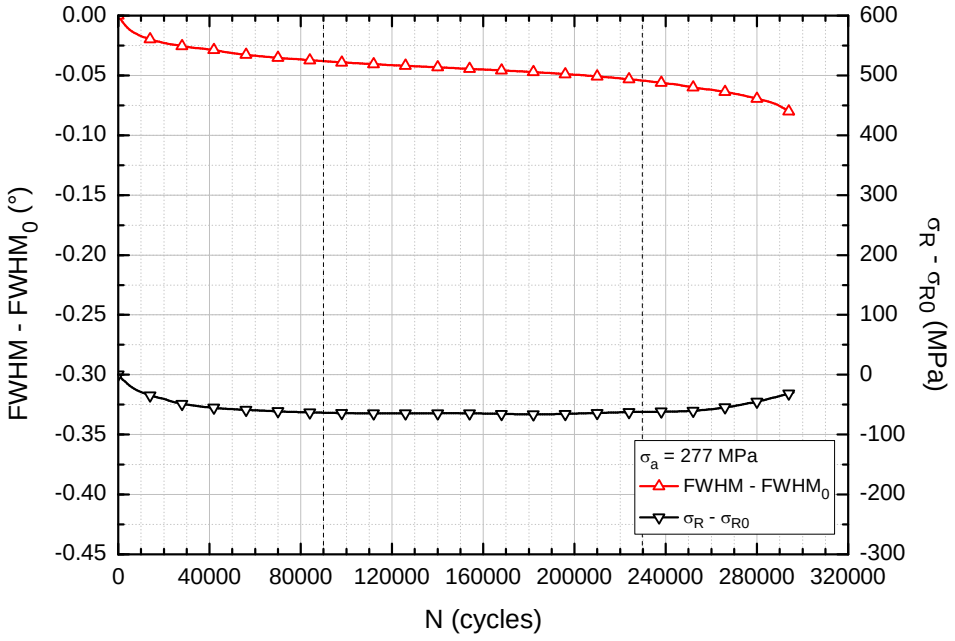

Figure IV.17. Average curves for the evolution of FWHM and residual stresses σ_R with fatigue cycling at σ_a = 277 MPa (*R* = - 1).

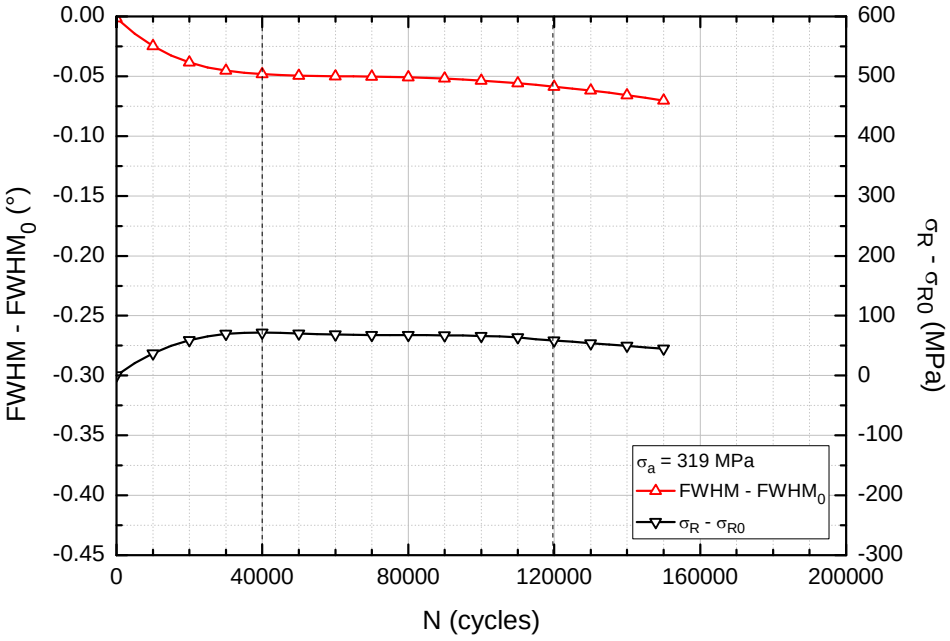

Figure IV.18. Average curves for the evolution of FWHM and residual stresses σ_R with fatigue cycling at σ_a = 319 MPa (R = - 1).

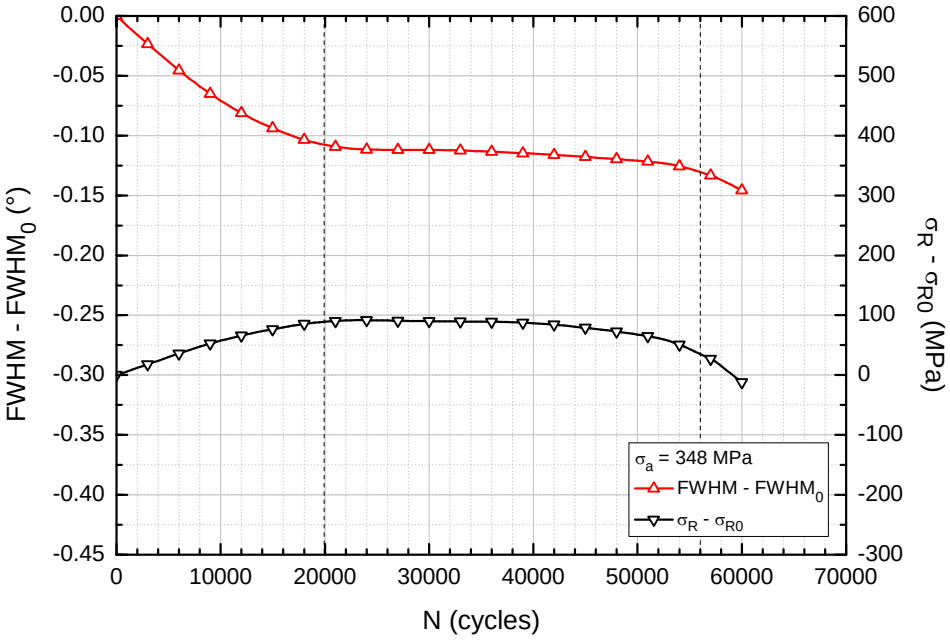

Figure IV.19. Average curves for the evolution of FWHM and residual stresses σ_R with fatigue cycling at σ_a = 348 MPa (R = - 1).

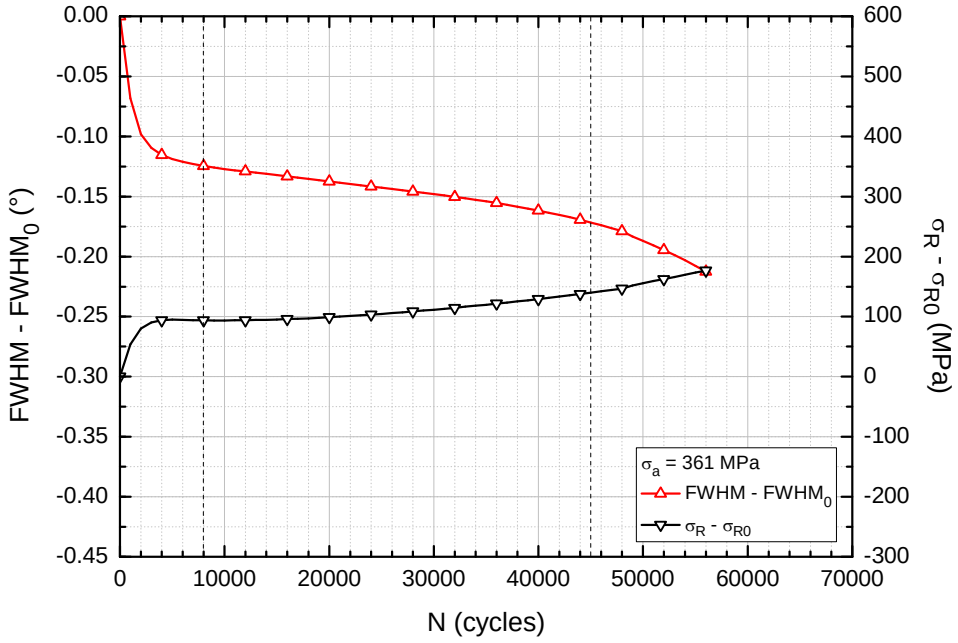

Figure IV.20. Average curves for the evolution of FWHM and residual stresses σ_R with fatigue cycling at σ_a = 361 MPa (R = - 1).

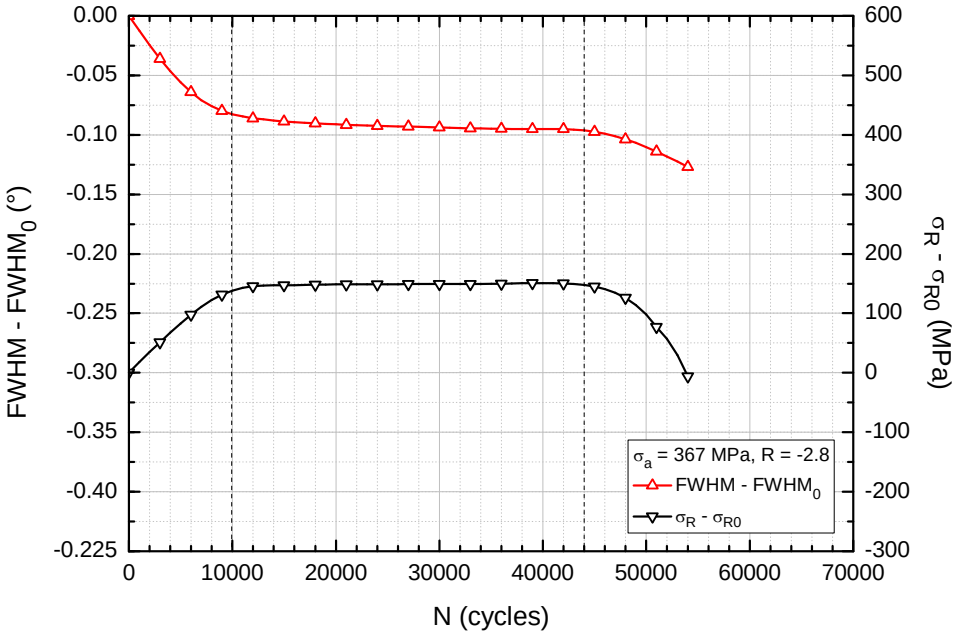

Figure IV.21. Average curves for the evolution of FWHM and residual stresses σ_R with fatigue cycling at σ_a = 367 MPa (R = - 2.8).

Figures IV.17 to IV.21 show average curves of the evolution of FWHM and residual stresses with fatigue cycling for the five alternating loadings applied. It can be observed that the durations of the three stages are similar for both evolutions.

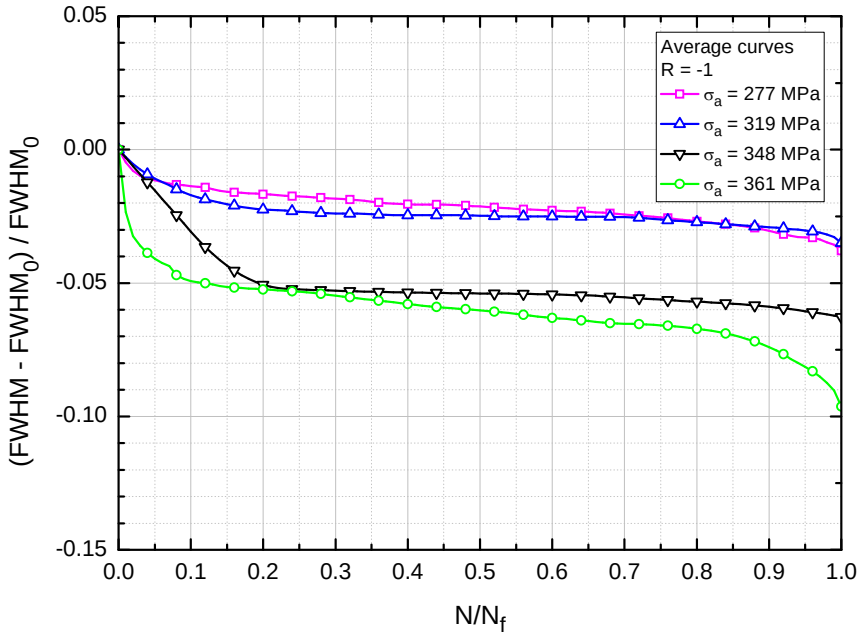

Figure IV.22. Average curves of (FWHM-FWHM$_0$)/FWHM$_0$ changes during fatigue tests at different stress amplitudes (R = -1).

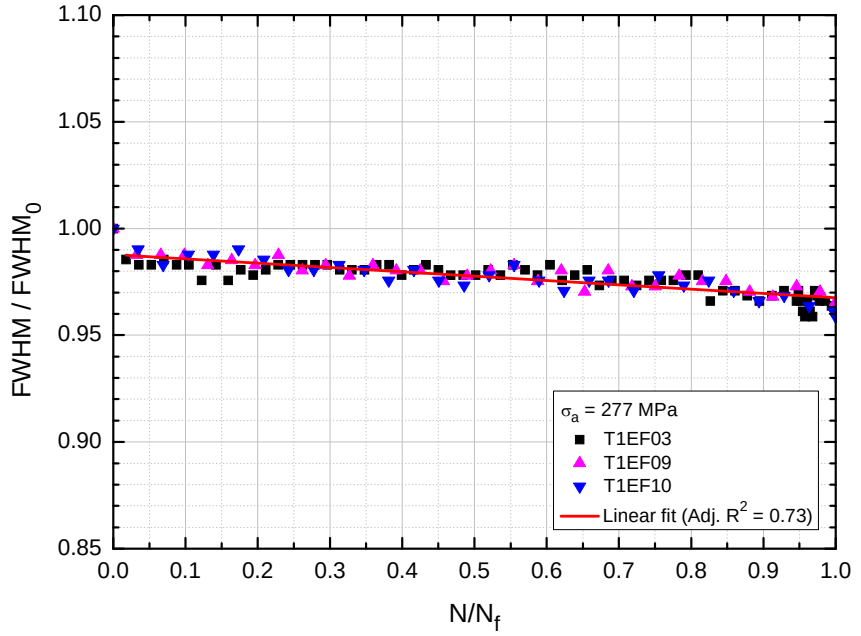

Figure IV.23. FWHM/FWHM$_0$ versus N/N_f at σ_a = 277 MPa (R = -1).

In Fig. IV.22 average curves of (FWHM-FWHM$_0$)/FWHM$_0$ versus N/N_f at different stress amplitudes (R = -1) are shown. The evolution of (FWHM-FWHM$_0$)/FWHM$_0$ versus N/N_f also presents three stages, with similar durations in each stage at all stress amplitudes. The duration of the first stage is approximately 30% of the fatigue life (N_f), while the second

stage persists until nearly 80% of N_f. The decrease in (FWHM-FWHM$_0$)/FWHM$_0$ during the three stages is accentuated with increasing stress amplitude.

Figures IV.23 to IV.27 show that a linear correlation can be found between FWHM/FWHM$_0$ and the fatigue life fraction N/N_f for $N > 0$ at all stress amplitudes applied in the fatigue tests.

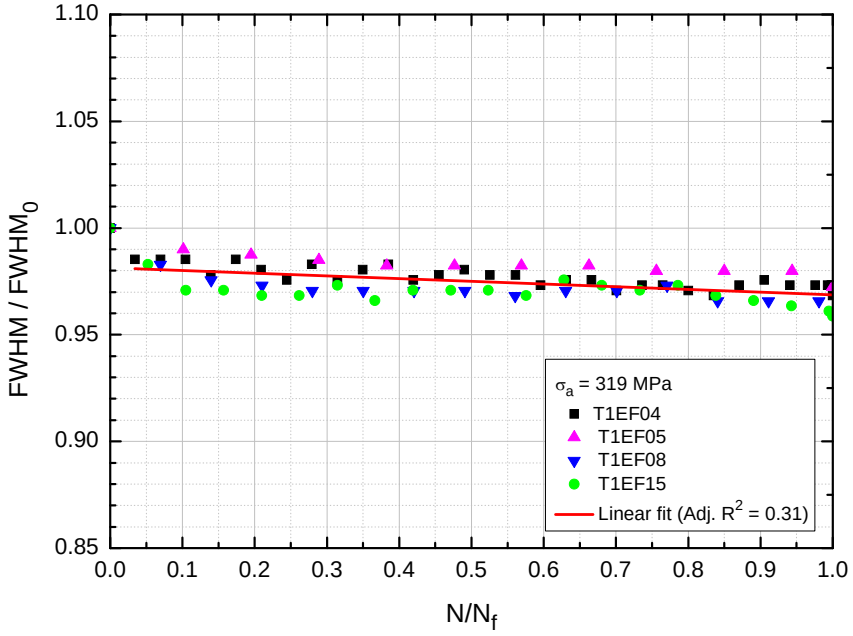

Figure IV.24. FWHM/FWHM$_0$ versus N/N_f at σ_a = 319 MPa (R = -1).

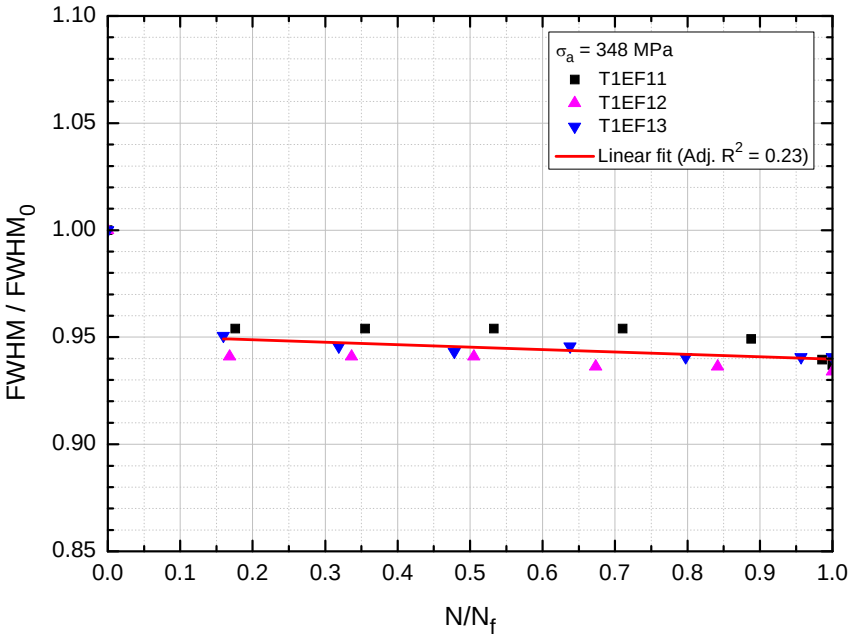

Figure IV.25. FWHM/FWHM$_0$ versus N/N_f at σ_a = 348 MPa (R = -1).

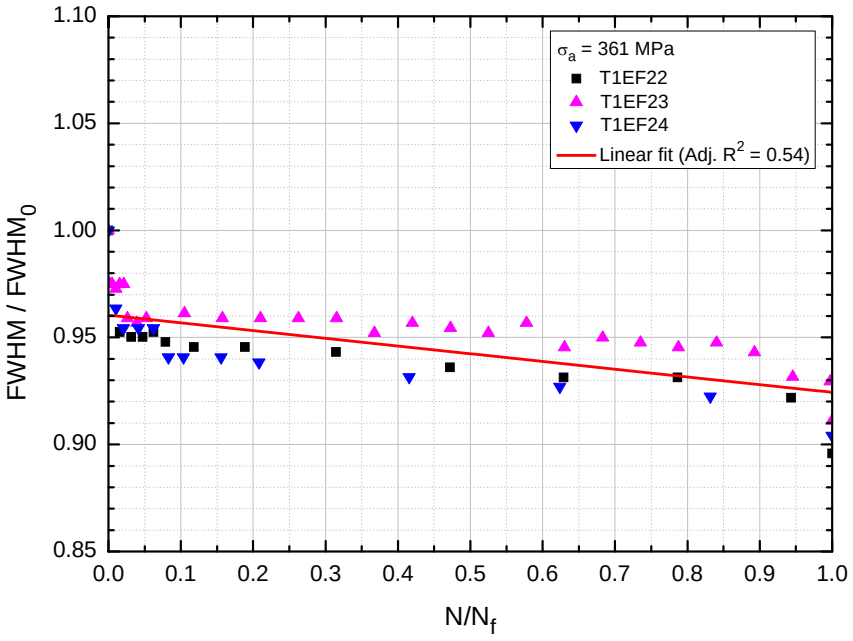

Figure IV.26. FWHM/FWHM$_0$ versus N/N_f at σ_a = 361 MPa (R = -1).

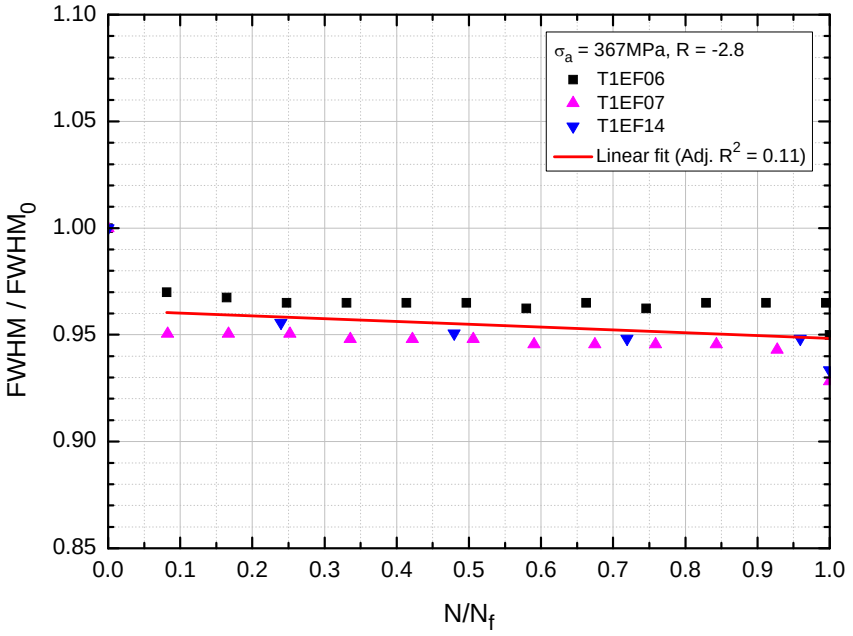

Figure IV.27. FWHM/FWHM$_0$ versus N/N_f at σ_a = 367 MPa (R = -2.8).

The evolution of the ratio σ_R/σ_{R0}, between the residual stresses at a given number of cycles N and at N = 0, with fatigue cycling is shown in Figs. IV.28 to IV.32 for the five stress amplitudes applied.

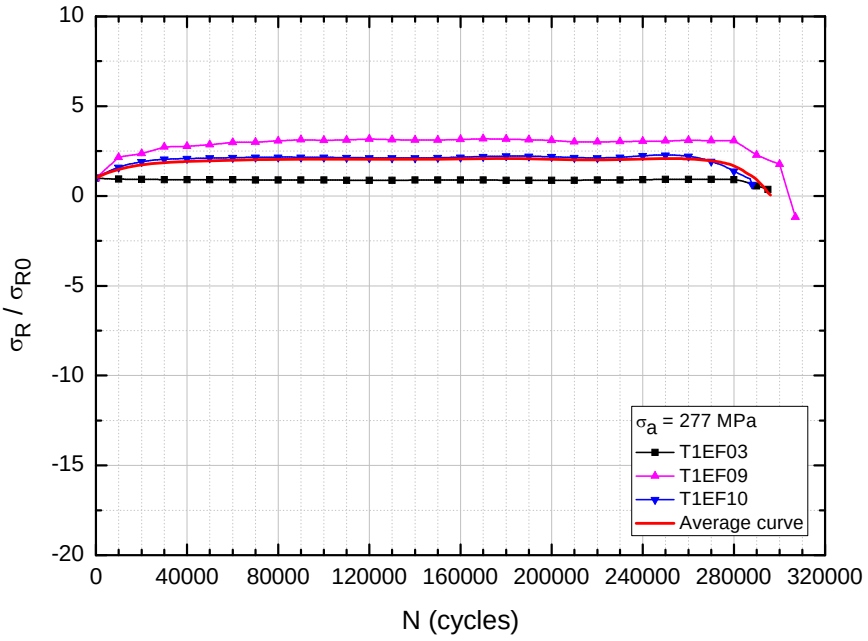

Figure IV.28. Evolution of residual stress ratio σ_R/σ_{R0} with fatigue cycling at σ_a = 277 MPa (R = - 1).

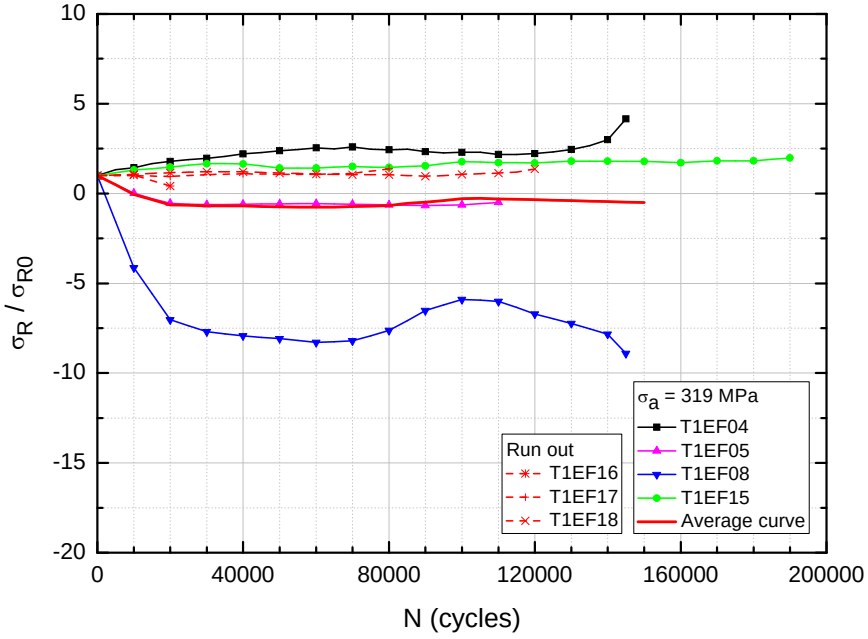

Figure IV.29. Evolution of residual stress ratio σ_R/σ_{R0} with fatigue cycling at σ_a = 319 MPa (R = - 1).

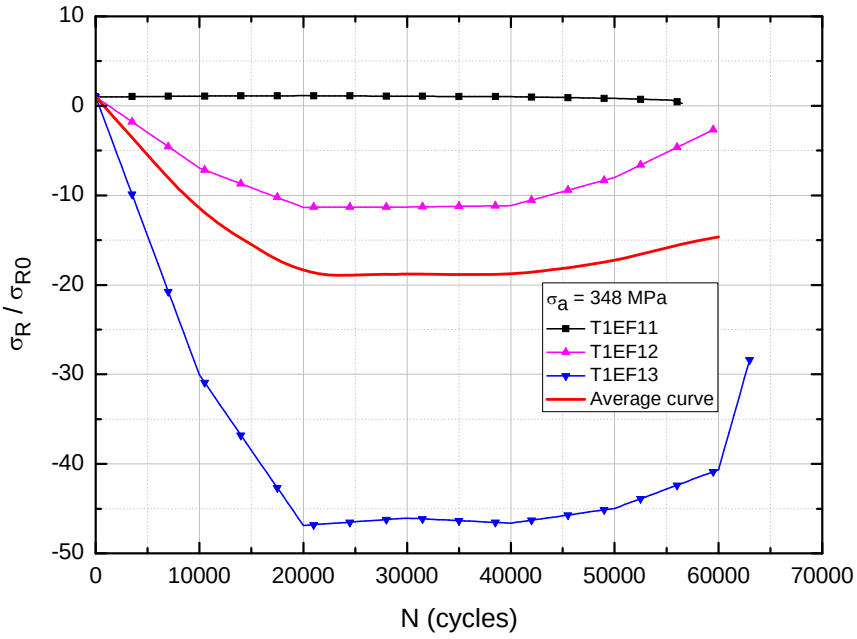

Figure IV.30. Evolution of residual stress ratio σ_R/σ_{R0} with fatigue cycling at σ_a = 348 MPa (R = - 1).

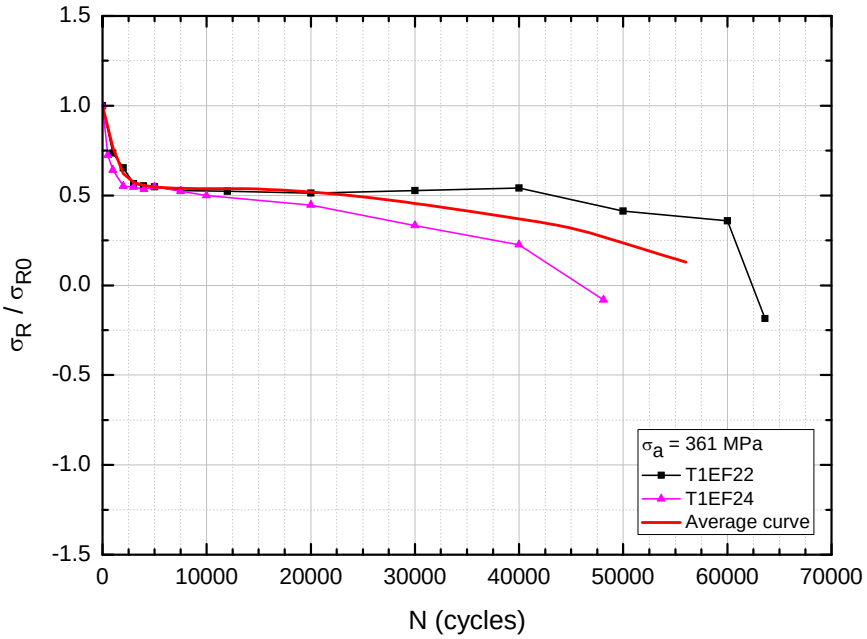

Figure IV.31. Evolution of residual stress ratio σ_R/σ_{R0} with fatigue cycling at σ_a = 361 MPa (R = - 1).

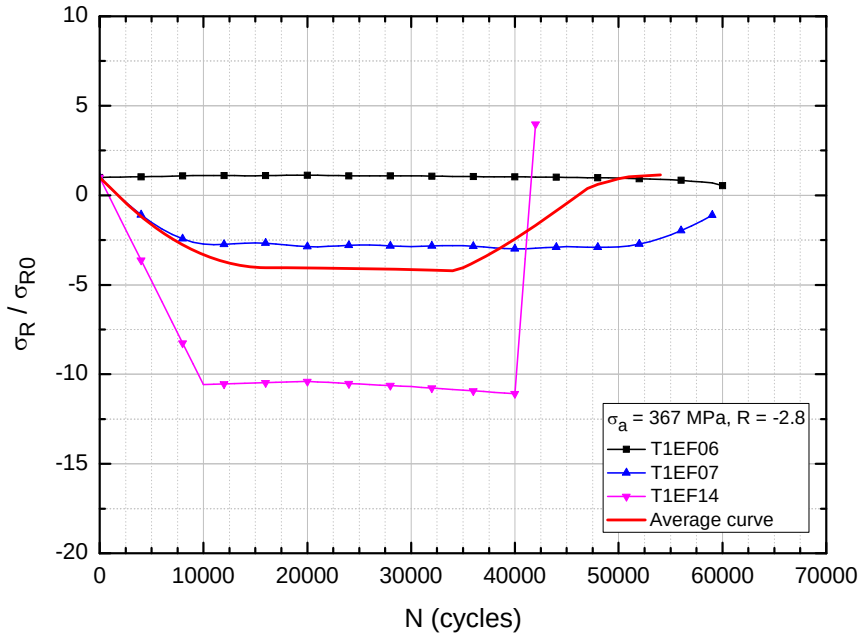

Figure IV.32. Evolution of residual stress ratio σ_R/σ_{R0} with fatigue cycling at σ_a = 367 MPa (R = - 2.8).

IV. 2. FRACTOGRAPHY

Analyses of fracture surfaces of fatigued samples were carried out for the five stress amplitudes. Fractography images were obtained using scanning electron microscope (SEM). For each stress amplitude, one fatigued sample was selected for analysis. In the SEM images presented in Figs. IV.33 to IV.37, the upper sample surface (electrolytically polished) is on the right hand side. In these images it can be observed the division line between regions of fatigue crack initiation and propagation on fracture surfaces.

Figure IV.33 presents SEM images of fracture surface for stress amplitude of 277MPa, R = -1 (sample T1EF10). These images indicate that in this sample the fatigue crack initiated in the lower sample surface, located on the left hand side of Figs. IV.33(a) and (b). Figure IV.33(c) shows the crack propagation near the region of crack initiation, which is shown in the top of Fig. IV.33(b), and Fig. IV.33(d) focus on the region of crack initiation.

SEM images of fracture surface for stress amplitude of 319 MPa, R = -1 (sample T1EF08), are presented in Fig. IV.34. It is found from these images that the fatigue crack initiation in this sample occurred in the upper sample surface, located on the right hand side of Figs. IV.34(a) and (b). Figure IV.34(c) shows the region of crack initiation, and Fig. IV.34(d) focus on a zone of fatigue striations near the crack initiation region.

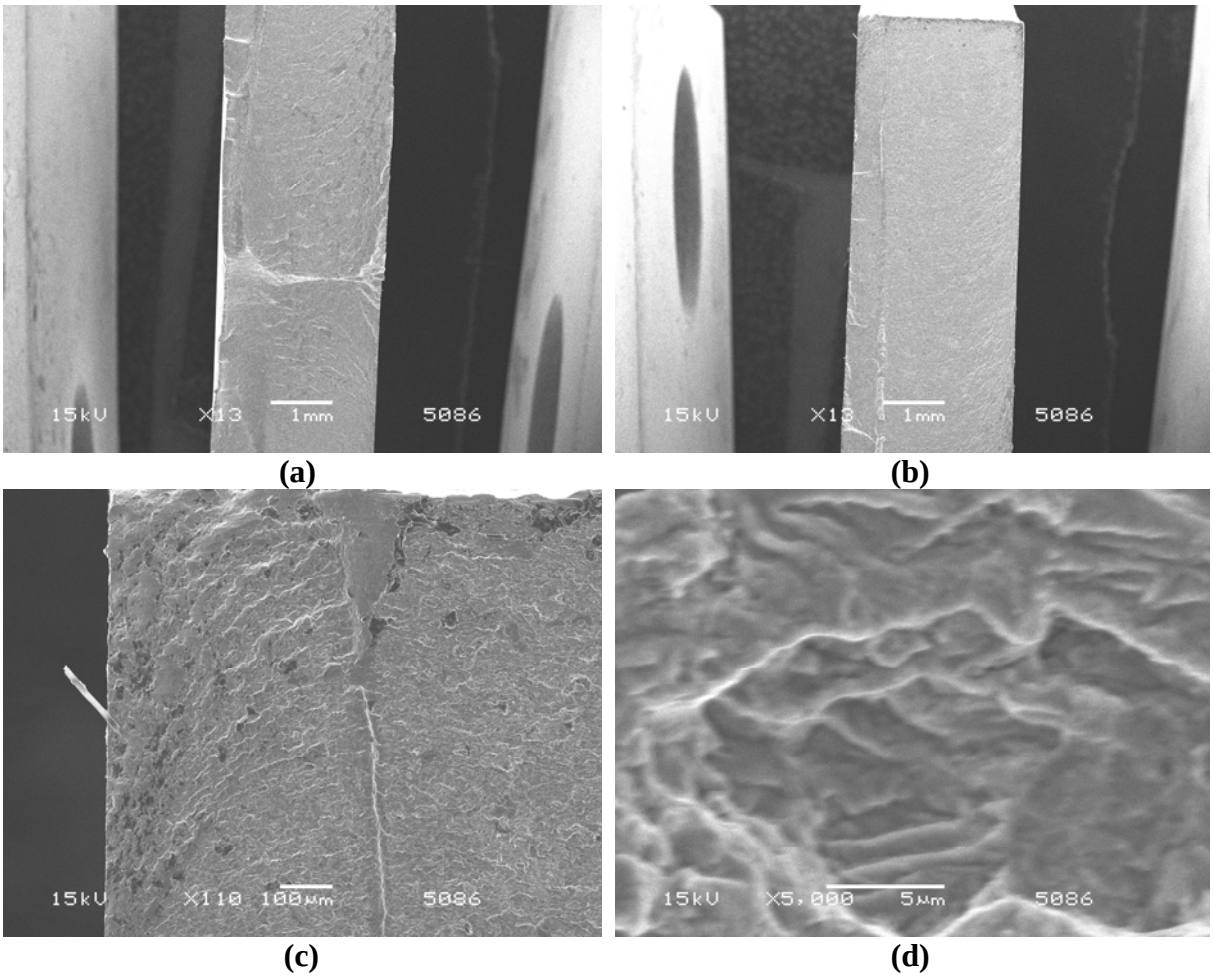

Figure IV.33. Fracture surface of sample T1EF10 fatigued at σ_a = 277 MPa (R = - 1).

In Fig. IV.35 are shown SEM images of fracture surface for stress amplitude of 348 MPa, R = -1 (sample T1EF11). In this sample, the fatigue crack initiated in the upper surface, located on the right hand side of Figs. IV.35(a) and (b). Figure IV.35(b) focus on the top region of Fig. IV.35(a), near the region of crack initiation.

Figure IV.36 shows SEM images of fracture surface for stress amplitude of 361 MPa, R = -1 (sample T1EF22). In this sample, the fatigue crack initiated in the lower surface, located on the left hand side of Figs. IV.36(a) and (b). Figure IV.36(b) focus on the top region of Fig. IV.36(a), near the region of crack initiation.

SEM images of fracture surface for stress amplitude of 367 MPa, R = -2.8 (sample T1EF06) are shown in Fig. IV.37. In this sample, the fatigue crack initiated in the upper surface, located on the right hand side of Figs. IV.37(a)-(d). Figure IV.37(b) focus on the bottom region of Fig. IV.37(a), near a region of crack initiation. Figure IV.37(d) focus on the top region of Fig. IV.37(c), near a region of crack initiation.

From observation of SEM images of fracture surfaces presented in Figs. IV.33 to IV.37 and the evolution of the σ_R/σ_{R0} ratio with fatigue cycling shown in Figs. IV.28 to IV.32 for the five stress amplitudes applied, it is suggested that the behavior of the σ_R/σ_{R0} ratio versus N curve at the end of fatigue life (Stage 3) can be correlated to the origin of fatigue crack initiation. At stress amplitudes of 277 and 361 MPa (R= - 1), the crack initiated in the lower surface sample and a descending σ_R/σ_{R0} ratio versus N curve is observed in Stage 3. In contrast, at stress amplitudes of 319, 348 MPa (R= - 1) and 367 MPa (R= - 2.8) crack initiation occurred in the upper surface sample and ascending σ_R/σ_{R0} ratio versus N curve is observed.

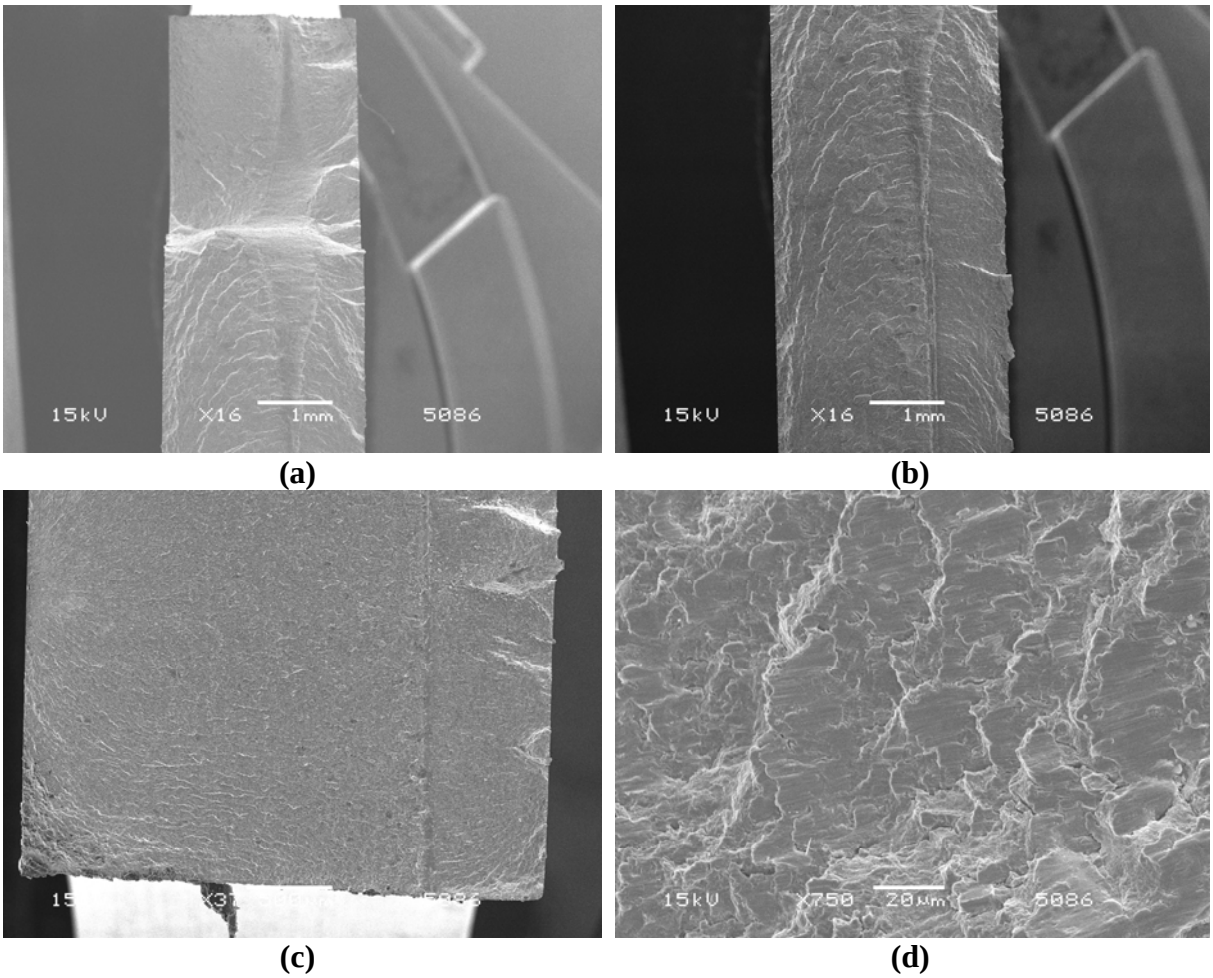

(a) **(b)** **(c)** **(d)**

Figure IV.34. Fracture surface of sample T1EF08 fatigued at σ_a = 319 MPa (R = - 1).

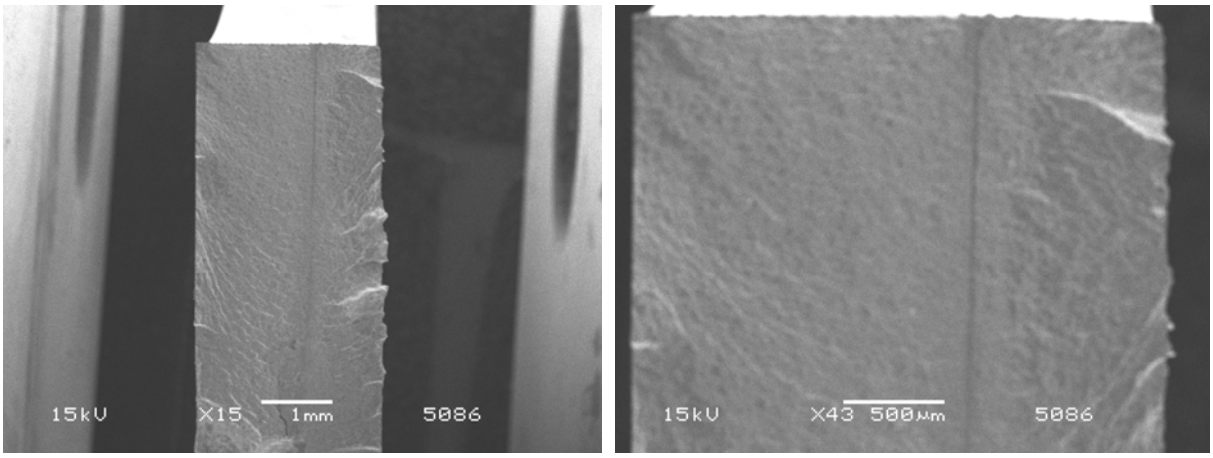

(a) **(b)**

Figure IV.35. Fracture surface of sample T1EF11 fatigued at σ_a = 348 MPa (*R* = - 1).

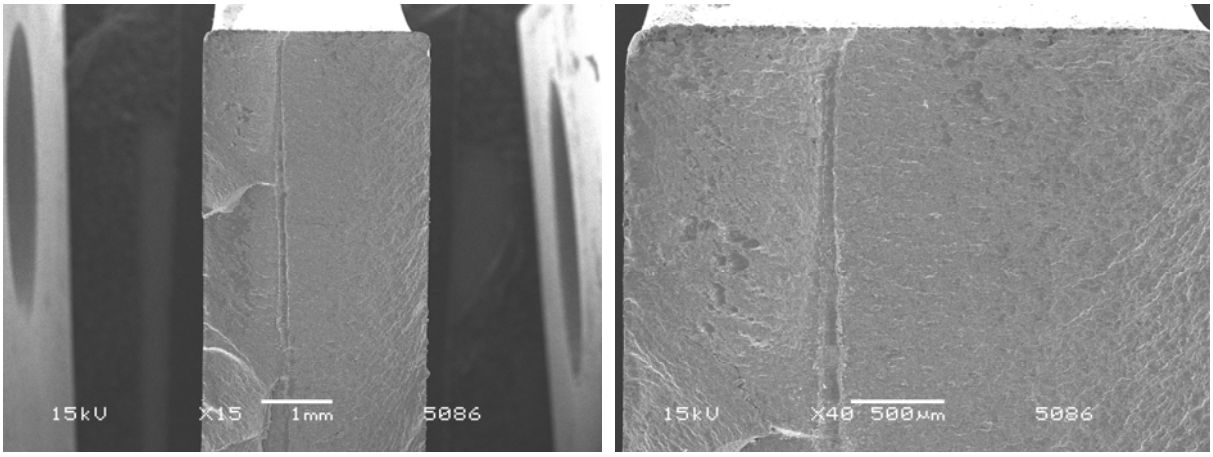

(a) **(b)**

Figure IV.36. Fracture surface of sample T1EF22 fatigued at σ_a = 361 MPa (*R* = - 1).

At the same time, the surface where the fatigue crack initiates can be related to the occurrence of tensile residual stresses. At stress amplitudes of 319, 348 MPa (*R*= - 1) and 367 MPa (*R*= - 2.8) tensile residual stresses were present in the upper sample surface (surface considered for XRD measurements), where the fatigue crack initiated. At stress amplitudes of 277 and 361 MPa (*R*= - 1) compressive residual stresses were measured in the upper sample surface and the crack initiation occurred in the lower surface sample.

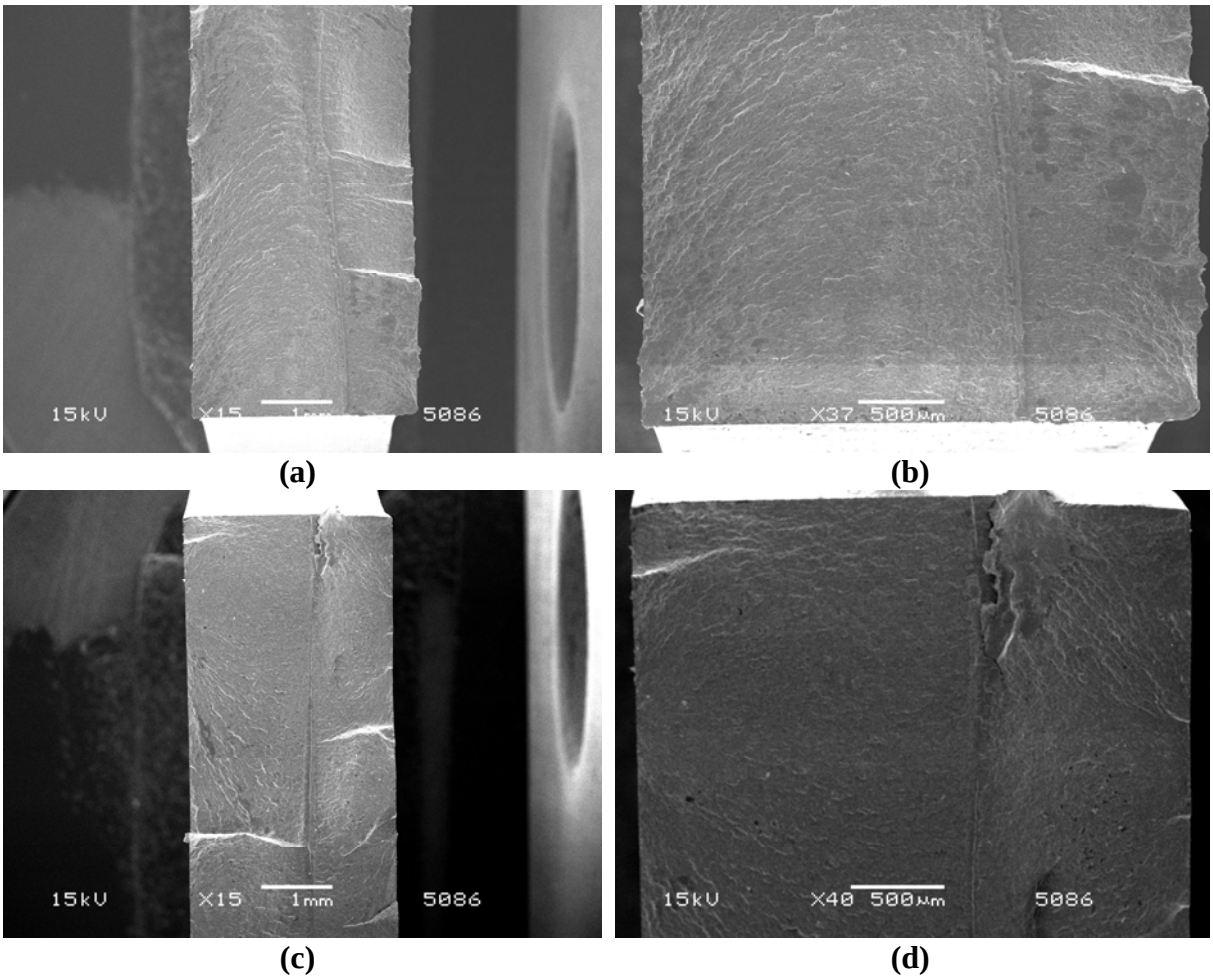

(a) **(b)**

(c) **(d)**

Figure IV.37. Fracture surface of sample T1EF06 fatigued at σ_a = 367 MPa (R = - 2.8).

IV. 3. TRANSMISSION ELECTRON MICROSCOPY ANALYSES

Samples fatigued to specific numbers of cycles, characteristic of the three stages of microstructural changes (Fig. IV.8), were prepared for transmission electron microscopy (TEM) examination combined with focused ion beam (FIB) technique to investigate the correlation between the evolution of FWHM values and microstructural changes (dislocation density and structure). Fatigued samples were cycled at a stress amplitude of 319 MPa (R = - 1) until 20,000 (T1EF16), 80,000 (T1EF17), and 120,000 cycles (T1EF18). FEI Focused Ion Beam-Dual Beam [111] was used to produce thin electron transparent lamellae to be analyzed by means of TEM. The lamellae were prepared from the center of the gage length surface area of fatigued samples. Lamellae preparation and TEM analyses were carried out at the Interdepartmental Laboratory of Electron Microscopy (LIME), University of Rome TRE, with the assistance of Prof. Edoardo Bemporad.

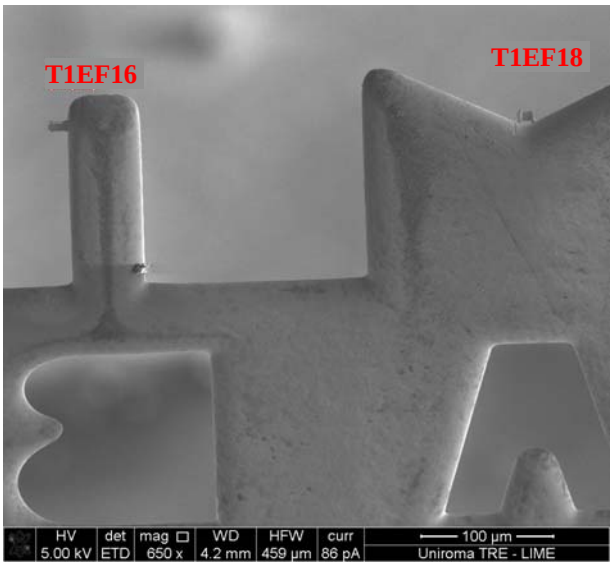

Figure IV.38. The lamellae produced were stuck to the TEM specimen-holder.

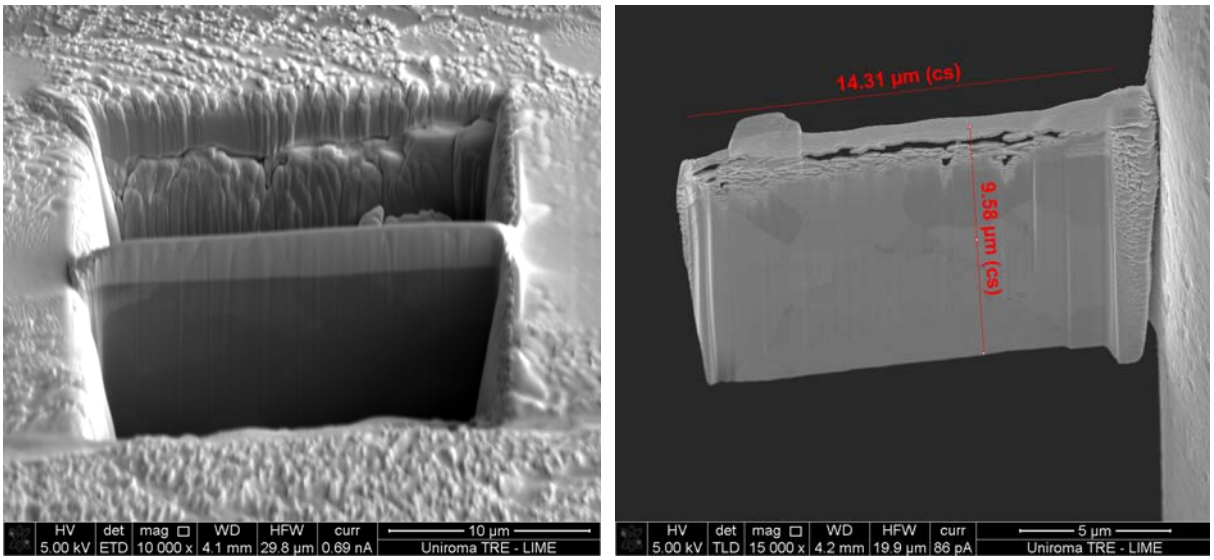

(a) **(b)**

Figure IV.39. (a) Lamella preparation with FIB and (b) lamella produced from sample T1EF16.

Application of the focused ion beam (FIB) technique for three-dimensional material characterization resides in precise ion milling through the sample, combined with characterization capabilities of transmission electron microscopy (TEM) [112]. FIB devices scan sample surfaces with finely focused ion beams and, by detecting generated secondary ions, enable observation of microscope images and process sample surfaces [111]. TEM analyses complement results obtained from X-ray diffraction measurements to investigate microstructural changes during fatigue cycling. However, in TEM analyses only a small

amount of material is observed in each thin lamella, and the demanding and time-consuming lamellae preparation restricts their applicability.

Two lamellae were produced, one from sample T1EF16 and other from sample T1EF18. In Fig. IV.38 the two lamellae produced are shown in the TEM specimen-holder. Figures IV.39 and IV.40 show steps for lamella preparation with focused ion beam (FIB) and the lamellae produced from samples T1EF16 and T1EF18, respectively. Lamella preparation involved milling the surface with gallium ions to obtain the lamella section, extraction of the lamella with the aid of a mechanical needle, thinning, and sticking the electron transparent lamella 80-100 nm thick to the TEM specimen-holder.

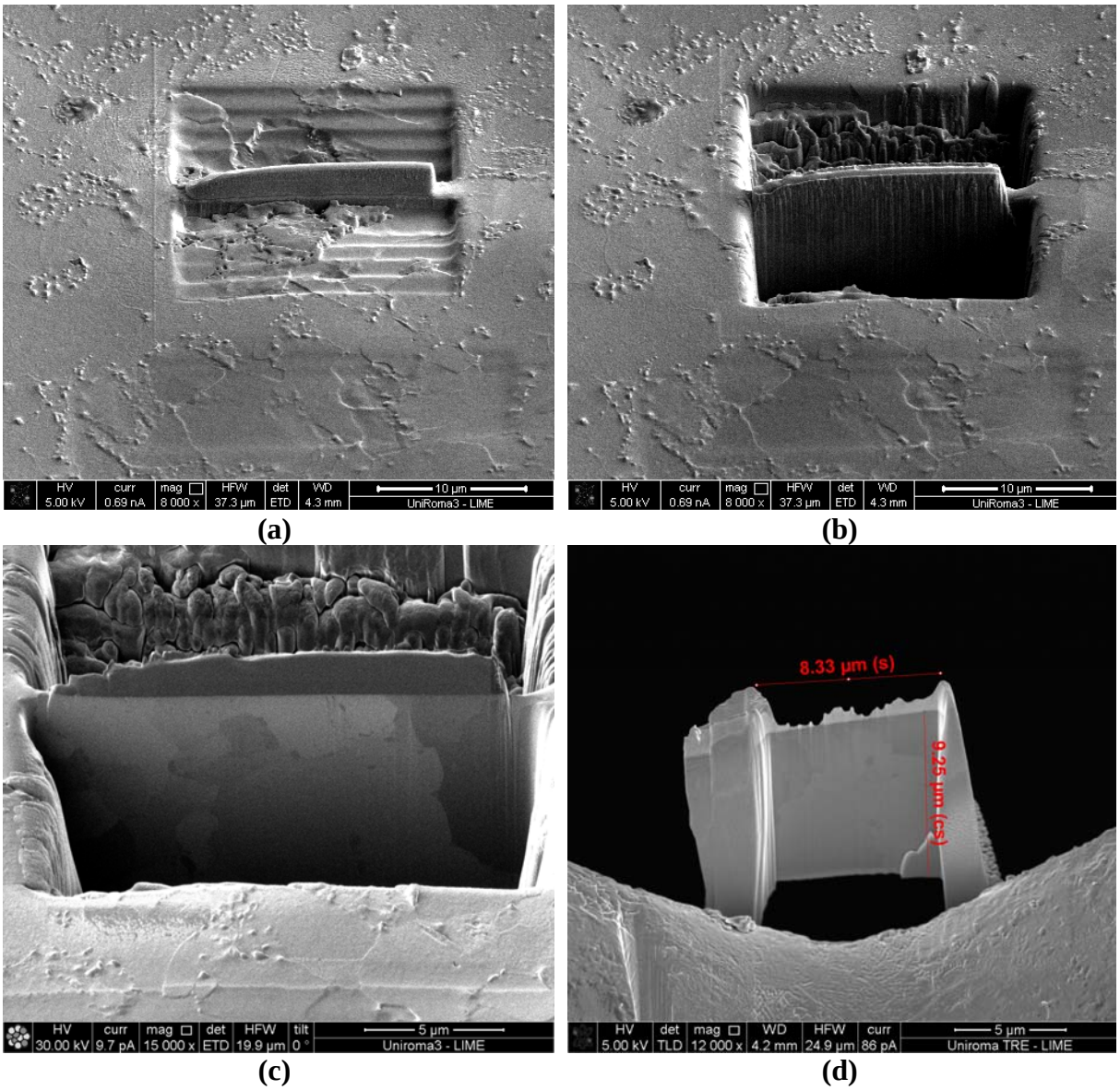

Figure IV.40. (a)-c) Lamella preparation with FIB and (d) lamella produced from sample T1EF18.

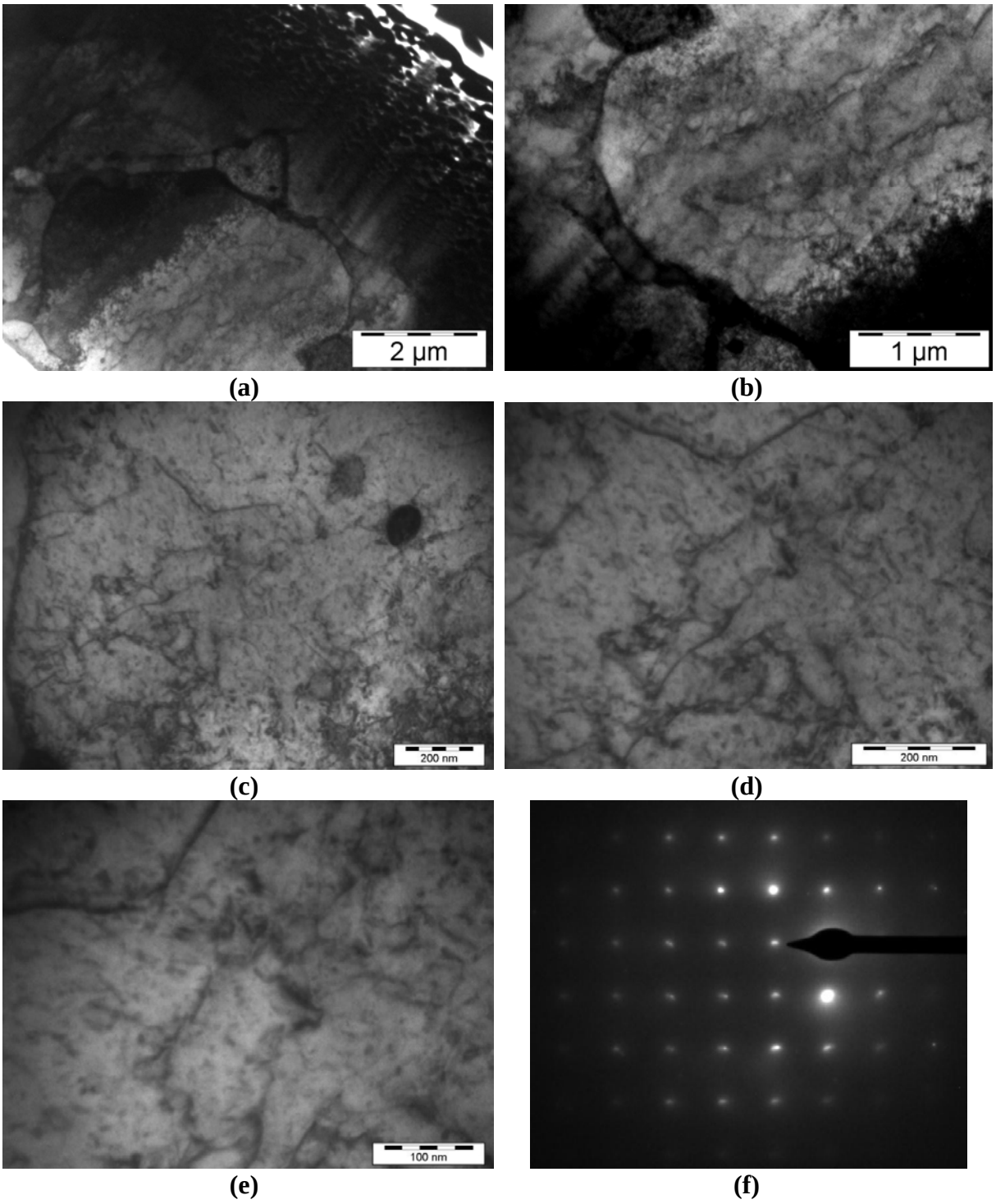

Figure IV.41. (a)-(e) Dislocation structures and (f) selected area electron diffraction (SAED) pattern obtained from analyses of lamella produced from sample T1EF16 cycled at σ_a = 319 MPa (R = - 1) to 20,000 cycles.

Figures IV.41 and IV.42 present TEM images obtained from analyses of lamellae produced from samples T1EF16 and T1EF18, respectively. A qualitative evaluation of dislocation structures observed in these images suggests that the dislocation density increased between 20,000 (T1EF16) and 120,000 cycles (T1EF18). From comparison of images from

samples T1EF16 and T1EF18, it is possible to observe the fatigue damage effect, considering how nested and close to each other are dislocations in sample T1EF18, fatigued to 120,000 cycles, with respect to sample T1EF16, fatigued to 20,000 cycles.

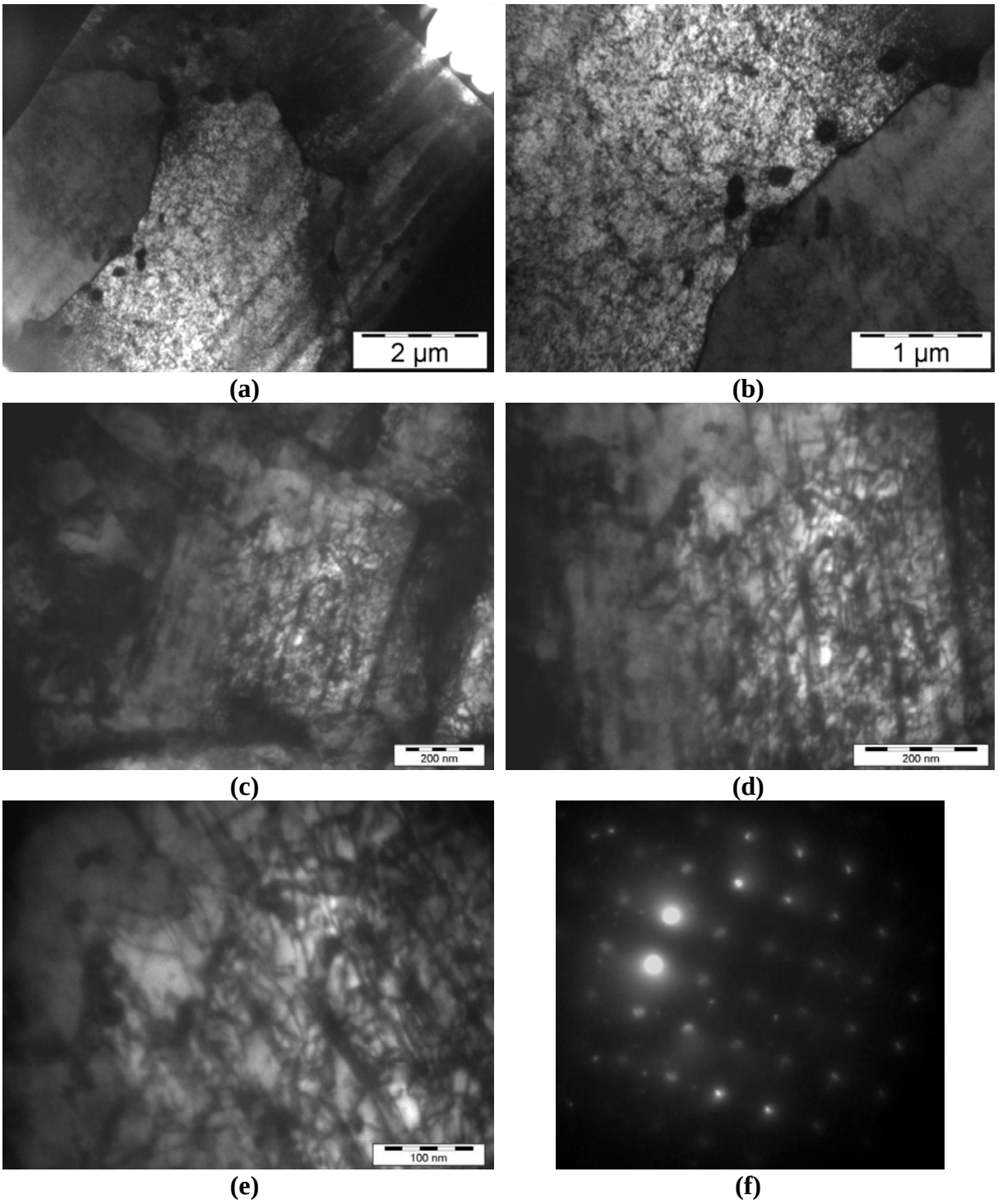

Figure IV.42. (a)-(e) Dislocation structures and (f) selected area electron diffraction (SAED) pattern obtained from analyses of lamella produced from sample T1EF18 cycled at σ_a = 319 MPa (R = - 1) to 120,000 cycles.

In order to be able to carry out a quantitative evaluation of changes in the dislocation density, additional analyses are envisaged. With this purpose, future works are expected to be carried out, including:

- improvement of TEM lamellae preparation in order to reach a thinner sampling and brighter images, and also to accurately distinguish the very surface morphology and microstructure;
- production and analyses of thin lamellae from sample T1EF17, fatigued to 80,000 cycles, and from other samples fatigued at different stress amplitudes, and
- analyses on a non-fatigued sample.

IV. 4. RESULTS OF FATIGUE TESTS ON ANNEALED SAMPLES

Table IV.3 compares average values of FWHM and residual stresses for machined (hardened) and annealed API 5L X60 grade steel samples measured before fatigue tests. These values were measured after electrolytic polishing. Annealing reduced the work hardening effect generated during the pipe manufacturing process, as confirmed by the decrease in FWHM of annealed samples with respect to machined samples. The annealing process is expected to result in annihilation of dislocations, reduction of the dislocation density, and, consequently, lower FWHM values. The average residual stress of annealed samples was slightly higher than that of machined samples. It should be noted that the average residual stress of annealed samples should not necessarily be lower than that of machined samples, since the machined-induced residual stresses of these samples before annealing should differ.

Table IV.3. Average values of FWHM and residual stresses for machined and annealed API 5L X60 grade steel samples measured before fatigue tests.

Machined samples		**Annealed samples**	
FWHM (°)	**Residual stress (MPa)**	**FWHM (°)**	**Residual stress (MPa)**
2.0582	45 ± 6	1.8250	66 ± 7

Four alternating bending fatigue tests were carried out at two different stress amplitudes, σ_a = 319 and 361 MPa (R = -1). Two tests were conducted for each loading level. Table IV.4 presents the results of fatigue tests on annealed samples. Fatigue lives of annealed samples were lower than those of machined samples (Table IV.1) for the same stress

amplitude. This is due to annealing effects, which lead to reduction of fatigue life and strength [74].

The evolution of FWHM and residual stresses with fatigue cycling on annealed samples at stress amplitudes of 319 and 361 MPa (R = -1) is shown in Figs. IV.43 and IV.44, respectively. Average curves of FWHM changes during fatigue tests at these stress amplitudes (R = -1) are shown in Fig. IV.45, while Fig. IV.46 presents average curves of (FWHM-$FWHM_0$)/$FWHM_0$ versus N/N_f. Similarly to results obtained for machined samples, the evolution of FWHM with fatigue cycling on annealed samples also presents three stages. However, instead of a decrease in FWHM in the first and third stages observed for machined samples, an increase in FWHM is observed for annealed samples. In the second stage, a decrease is observed for both machined and annealed samples. The comparison between FWHM changes for machined and annealed samples is shown in Figs. IV.47 and IV.48 at stress amplitudes of 319 and 361 MPa (R = -1), respectively.

The transformation of the material to a lower-energy state and restoration of the dislocation network state by annealing reduced the work hardening effect generated by the pipe manufacturing process, as confirmed by lower FWHM values of annealed samples (Table IV.3). As a result, the first stage of the evolution of FWHM for annealed samples is characterized by an increase in FWHM, as fatigue loading enhances the energy state of the material. This stage (Stage 1) could be related to multiplication of dislocations, intensification of their interactions and hardening of the material, which results in a fast increase of FWHM values in the early cycles. Stage 1 could be associated with the development of persistent slip bands, extrusions and intrusions. In the second stage (Stage 2), the decrease in FWHM can be associated with the rearrangement of the dislocation network, with preponderant annihilation of dislocations, and microcracking (microcrack propagation). Finally, FWHM values increased in the third stage (Stage 3) until complete fracture. The rate of changes in FWHM in the three stages is accentuated with increasing stress amplitude.

Table IV.4. Fatigue test results on annealed samples.

Sample	Strain amplitude	Stress amplitude (MPa)			R	N (cycles)
		Applied	Corrected			
T1EF19	0.17%	319	319	$0.61\sigma_0$	-1.1	173,500
T1EF25						68,500
T1EF26	0.19%	361	361	$0.69\sigma_0$	-1	34,100
T1EF27						26,500

Figures IV.49 and IV.50 show that a linear correlation can be found between FWHM/FWHM$_0$ and the fatigue life fraction N/N_f for $N > 0$ for annealed samples.

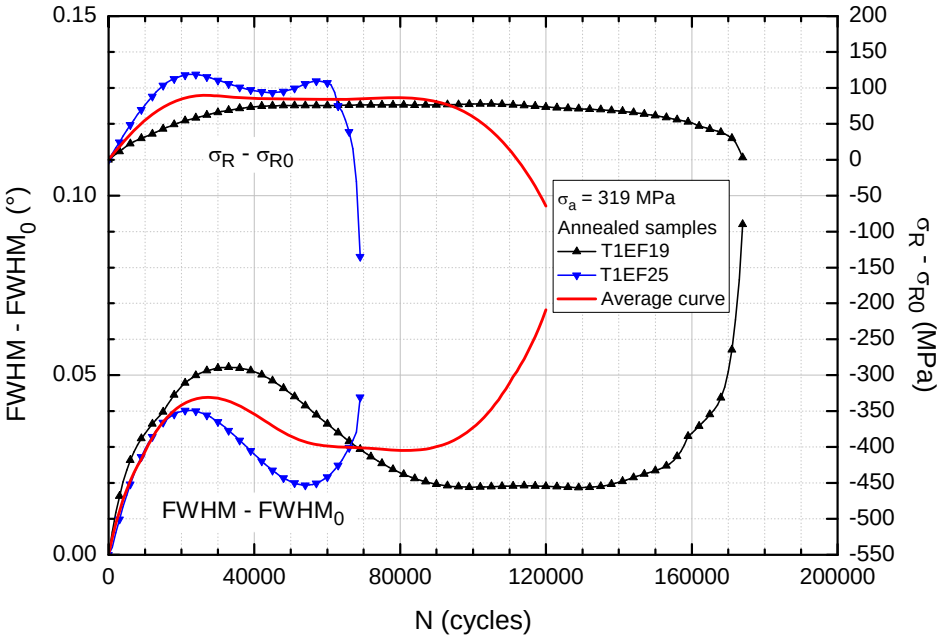

Figure IV.43. Evolution of FWHM and residual stresses σ_R with fatigue cycling at σ_a = 319 MPa (R = -1).

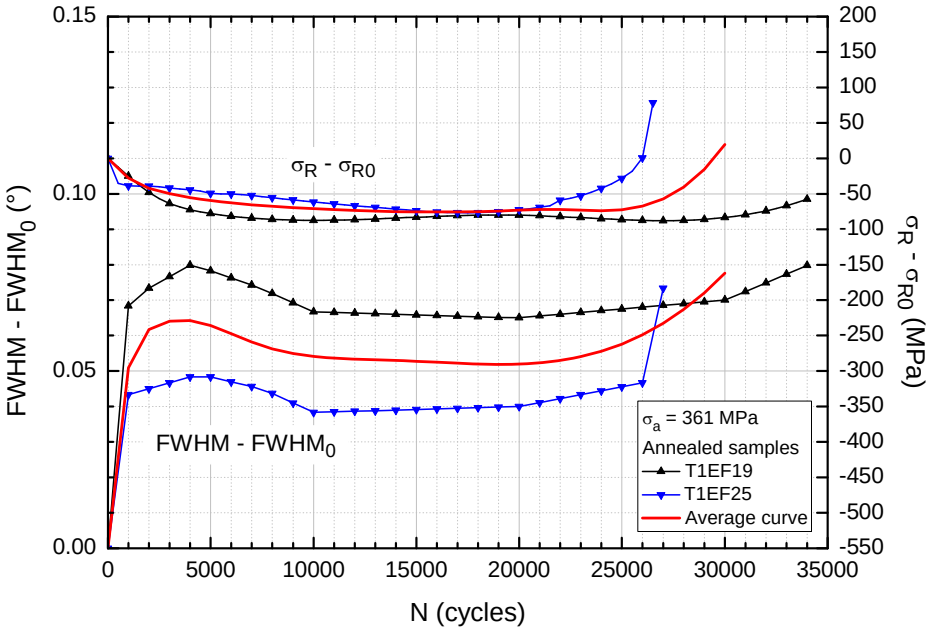

Figure IV.44. Evolution of FWHM and residual stresses σ_R with fatigue cycling at σ_a = 361 MPa (R = -1).

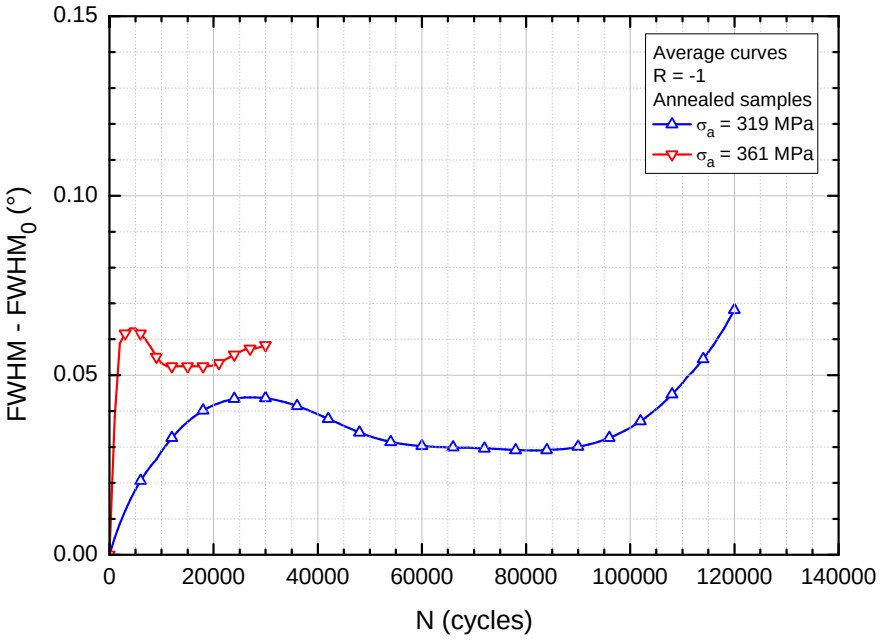

Figure IV.45. Average curves of FWHM changes during fatigue tests on annealed samples at different stress amplitudes (*R* = -1).

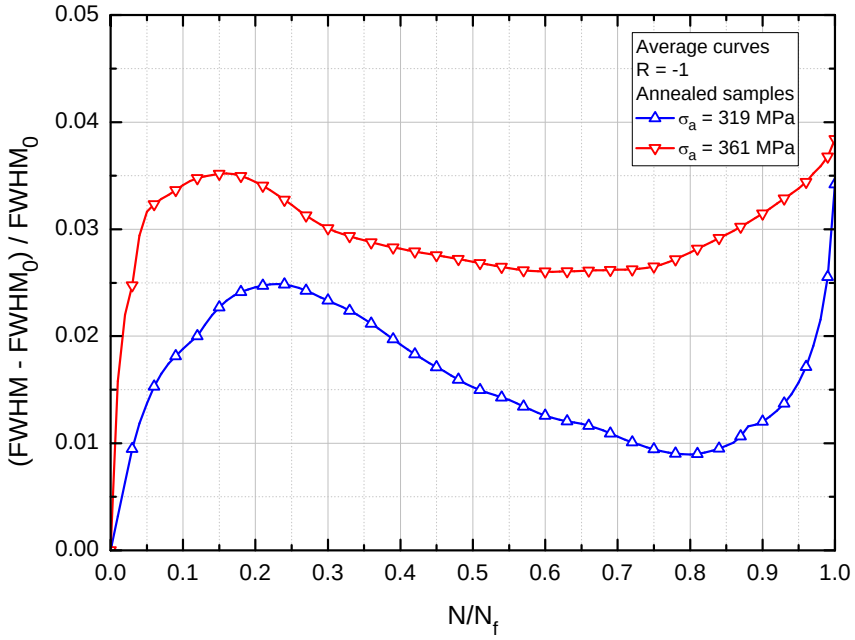

Figure IV.46. Average curves of (FWHM-FWHM$_0$)/FWHM$_0$ versus N/N_f for annealed samples at different stress amplitudes (*R* = -1).

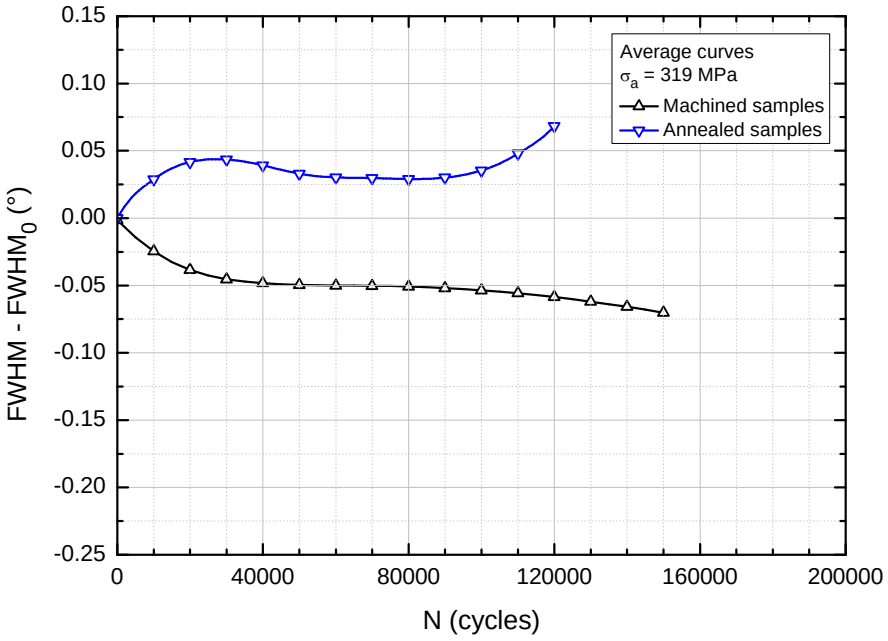

Figure IV.47. Comparison between evolutions of FWHM with fatigue cycling on machined and annealed samples at σ_a = 319 MPa (R = -1).

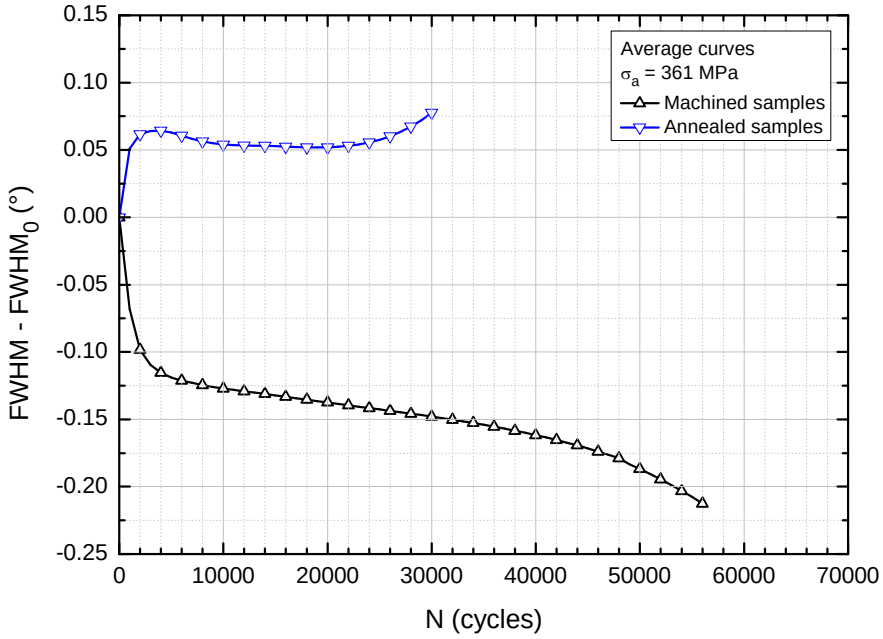

Figure IV.48. Comparison between evolutions of FWHM with fatigue cycling on machined and annealed samples at σ_a = 361 MPa (R = -1).

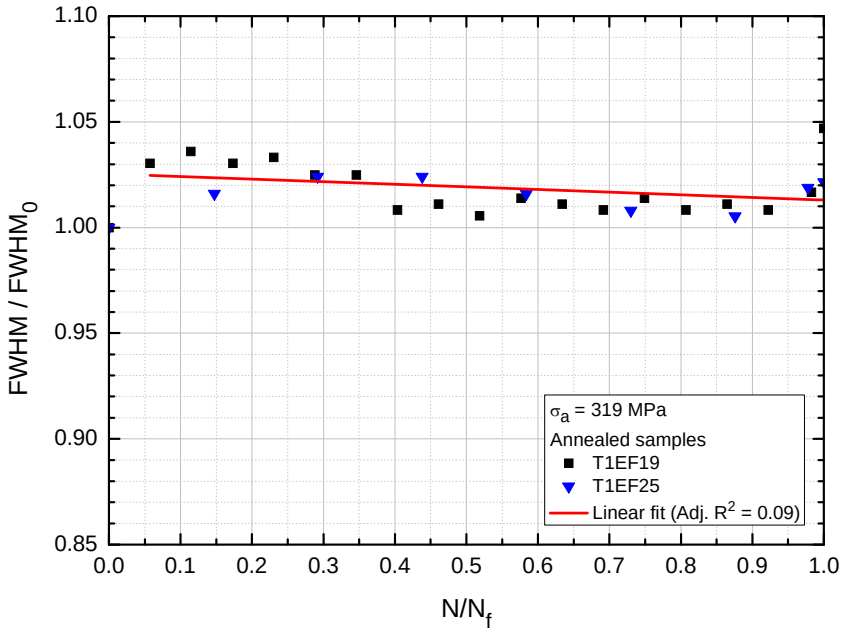

Figure IV.49. FWHM/FWHM$_0$ versus N/N_f for annealed samples under fatigue cycling at σ_a = 319 MPa (R = -1).

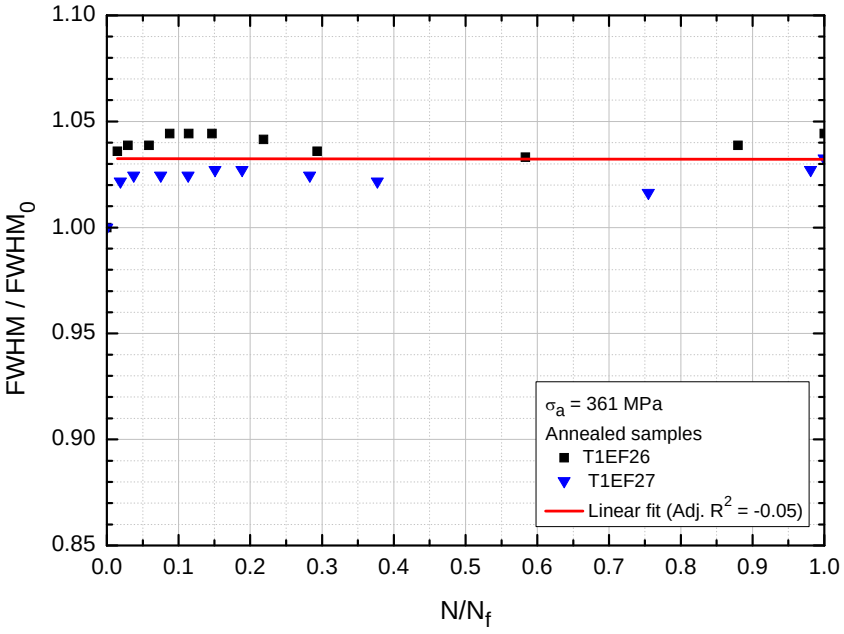

Figure IV.50. FWHM/FWHM$_0$ versus N/N_f for annealed samples under fatigue cycling at σ_a = 361 MPa (R = -1).

CONCLUSIONS AND PERSPECTIVES

CONCLUSIONS AND PERSPECTIVES

The aim of this work is to evaluate and quantify the evolution of microdeformations and macro residual stresses during high cycle fatigue life of API 5L X60 grade steel samples, using X-ray diffraction technique. Samples are submitted to strain-controlled alternating bending fatigue tests at room temperature. Five different alternating bending loadings are applied, and at least three fatigue tests are carried out for each loading level. Microdeformations are evaluated from measurements of the full width at half maximum (FWHM) of X-ray diffraction peaks and macro residual stresses are estimated according to the $\sin^2\psi$ method.

For the five stress amplitudes applied, three stages are identified in FWHM changes during fatigue cycling. The first stage (Stage 1) takes place in the early cycles and is characterized by a fast decrease in FWHM. In the second stage (Stage 2), the rate of FWHM decrease is considerably reduced. This stage comprises the major fraction of fatigue life (about 50%). Finally, the third stage (Stage 3) occurs in the last cycles with a rapid decrease in FWHM until complete fracture. Microstructural changes are well correlated to the level of stress amplitude applied. Increasing the stress amplitude accentuates FWHM changes and reduces the duration of each stage. It can be supposed that a connection could exist between variations in FWHM and the three phases of fatigue damage mechanisms, characterized by initiation of microcracks, microcracking (microcrack propagation and coalescence), and macrocrack propagation. The evolution of macro residual stresses with fatigue cycling also presents three stages, with durations similar to those observed in FWHM variations for a given stress amplitude.

In Stage 1, the decrease in FWHM can be associated with the movement and multiplication of dislocations and rearrangement of the initial dislocation network. The initial dislocation network is generated essentially during the pipe manufacturing process by cold working, as well as during sample preparation (machining, grinding, and polishing). In Stage 2, representing the major part of the fatigue life, the decreasing rate of FWHM is considerably reduced. This stage probably corresponds to the process of microcracks initiation and propagation. This process, which entails the creation of new free surfaces, can be considered as the propagation of a virtual crack, assuming that this crack would be the sum of individual microcracks propagating at a very low rate (on the order of nm/cycle). Considering that the macrocrack size at the end of Stage 2 is of the order of one or two grain sizes, i.e., 20-40 µm,

it is possible to roughly estimate an apparent microcrack propagation rate during this stage. Finally, Stage 3 occurs in the last cycles with a rapid decrease in FWHM until complete fracture. This behavior can be attributed to relaxation of microstresses due to macroscopic crack initiation and propagation (on the order of μm/cycle), preceding final failure.

Effects of restoration of the nonstressed dislocation network state are studied by submitting samples to annealing treatment previously to fatigue tests. Alternating bending fatigue tests on annealed samples are carried out at two different stress amplitudes; two tests are conducted for each loading level. The evolution of FWHM with fatigue cycling on annealed samples also presents three stages. However, instead of a decrease in FWHM in the first and third stages as observed for machined (hardened) samples, an increase in FWHM is observed for annealed samples. In the second stage, a decrease is observed for both machined and annealed samples. Annealing brings the material to a lower-energy state and reduces the work hardening effect generated by the pipe manufacturing process, as confirmed by lower FWHM values for annealed samples. As a result, the first stage of the evolution of FWHM for annealed samples is characterized by an increase in FWHM, as fatigue loading enhances the energy state of the material. This stage (Stage 1) could be related to multiplication of dislocations, intensification of their interactions and hardening of the material, which results in a fast increase of FWHM values in the early cycles. In the second stage (Stage 2), the decrease in FWHM can be associated with the rearrangement of the dislocation network, with preponderant annihilation of dislocations, and microcracking (microcrack propagation). Finally, an increase in FWHM is observed in the third stage (Stage 3) until complete fracture, suggesting that additional energy are needed for macrocrack propagation on annealed samples.

From transmission electron microscopy (TEM) analyses of fatigued test samples, it is possible to observe the fatigue damage effect, considering that dislocations become more nested and close to each other with increasing number of cycles. TEM analyses carried out are only qualitative, and in order to be able to carry out a quantitative evaluation of changes in dislocation density and structure, additional analyses are envisaged.

With the purpose of quantifying the initiation phase preceding macrocracking, a very new approach is suggested here in terms of the propagation of a virtual crack during Stage 2, which could allow the estimation of the duration of this stage. This virtual crack could be considered as the sum of the contributions of individual microcracks to the creation of new free surfaces. This has to be confirmed on various materials and loading conditions in order to

verify the possible quantification of fatigue damage before macroscopic cracking, which takes place during Stage 3.

Nevertheless, the interpretation of changes in FWHM and residual stresses that appear in the different stages is not evident and care should be taken in connecting them to changes in dislocation density and structure under fatigue loading conditions. To date, this was only established under monotonic loading conditions. In order to appreciate the validity of such a new concept, further TEM analyses needed. These analyses would allow the estimation of the density of microcracks and their propagation rate during Stage 2.

The results obtained in this work show that the X-ray diffraction technique, even if it cannot elucidate by itself the whole nature of fatigue damage, can be used as a tool to evaluate damage in real time. This was rendered possible by the portability and fastness of the X-ray diffraction equipment used. These results offer interesting perspectives for future works in the objective of quantifying changes in microdeformations and macro residual stresses in API 5L X60 grade steel pipes submitted to cyclic loadings, which can allow a consistent evaluation of the residual life before macroscopic cracking and help to increase their reliability.

REFERENCES

REFERENCES

[1] **P.H. Wertheim**, *Brazilian pre-salt reserves bring role of oil industry into question*, Oil Gas Financ. J. 6(7) (2009), http://www.ogfj.com/index/article-display/6444410005/articles/oil-gas-financial-journal/e-__p/offshore/brazilian-pre-salt.html.

[2] **D. Lyons**, *Western European Cross-country Oil Pipelines 30-year Performance Statistics*, Report No. 1/02, CONCAWE, Brussels, 2002.

[3] **K. Paulson**, *Focus on Safety and Environment, A Comparative Analysis of Pipeline Performance 2000-2003*, National Energy Board, Alberta, 2005.

[4] **S.B. Cunha, I.P. Pasqualino, B.C. Pinheiro**, *Stress-life fatigue assessment of pipelines with plain dents*, Fatigue Fract. Eng. Mater. Struct. 32 (2009) 961-974.

[5] **B.C. Pinheiro, I.P. Pasqualino**, *Fatigue analysis of damaged steel pipelines under cyclic internal pressure*, Int. J. Fatigue 31 (2009) 962-973.

[6] **American Petroleum Institute**, *API Specification 5L*, 42nd ed., Washington, D.C., 2004.

[7] **P. Paris, F. Erdogan**, *Critical analysis of crack propagation laws*, J. Basic Eng. 85 (1963) 528-534.

[8] **Det Norske Veritas**, *Fatigue Design of Offshore Steel Structures*, Recommended Practice DNV-RP-C203, Høvik, 2008.

[9] **N. Ji, J.L. Lebrun**, *Microstructural study of static and dynamic deformed polycrystalline copper by X-ray diffraction profile analysis*, Scr. Metall. Mater. 24(8) (1990) 1547-1552.

[10] **J. Lesage, D. Chicot, P. Perez, J.M. Chatelet**, *X-ray diffraction study of microstructural modifications during fatigue*, Proc. 11th Conference on Materials Testing, Balatonszéplak, Hungary, 1994, pp. 616-620.

[11] **T. Magnin, J. Driver, J. Lepinoux, L.P. Kubin**, *Aspects microstructuraux de la déformation cyclique dans les métaux et alliages C.C. et C.F.C. I. Consolidation Cyclique*, Rev. Phys. Appl. 19 (1984) 467-482.

[12] **P.K. Liaw, H. Wang, L. Jiang, et al.**, *Thermographic detection of fatigue damage of pressure vessel at 1,000 Hz and 20 Hz*, Scr. Mater. 42 (2000) 389-395.

[13] **S. Luxemburger, W. Arnold**, *Laser ultrasonic absorption measurement in fatigue-damaged materials*, Ultrasonics 40 (2002) 797-801.

[14] **H. Ogi, T. Hamaguchi, M. Hirao**, *Ultrasonic attenuation peak in steel and aluminum alloy during rotating bending fatigue*, Metall. Mater. Trans. A 31 (2000) 1121-1128.

[15] **A. Gilanyi, K. Morishita, T. Sukegawa, M. Uesaka, K. Miya**, *Magnetic nondestructive evaluation of fatigue damage of ferromagnetic steels for nuclear fusion energy systems*, Fusion Eng. Des. 42 (1998) 485-491.

[16] **E.S. Palma, T.R. Mansur, S.F. Silva Jr, A. Alvarenga Jr**, *Fatigue damage assessment in AISI 8620 steel using Barkhausen noise*, Int. J. Fatigue 27 (2005) 659-665.

[17] **A. Benrabah, C. Langlade, A.B. Vannes**, *Residual stresses and fretting fatigue*, Wear 224 (1999) 267-273.

[18] **Y. Isobe, A. Kamimura, K. Furuta, E. Ikuta, K. Aoki, F. Nakayasu**, *Fatigue damage characterization in alloy 718, Superalloys 718, 625, 706 and various derivatives*, E.A. Loria (Ed.), (1994) 607-618.

[19] **B. Scholtes**, *Residual stress analysis - A useful tool to assess the fatigue behavior of structural components*, Adv. X Ray Anal. 43 (2000) 39-47.

[20] **S. Rai, B.K. Choudhary, T. Jayakumar, K. Rao, B. Raj**, *Characterization of low cycle fatigue damage in 9Cr–1Mo ferritic steel using X-ray diffraction technique*, Int. J. Press. Vessels Pip. 76 (1999) 275-281.

[21] **N. Broll**, *Caractérisation de Solides Cristallisés par Diffraction X, PE 1080*, Techniques de l'Ingénieur, Traité Analyse et Caractérisation, 1996.

[22] **P.S. Prevéy**, *Problems with Non-destructive Surface X-ray Diffraction Residual Stress Measurement*, Practical Applications of Residual Stress Technology, ed. C. Ruud, ASM International, Materials Park, Ohio, 1991, pp 47-54.

[23] **P.S. Prevéy**, *Current Applications of X-ray Diffraction Residual Stress Measurement*, Developments in Materials Characterization Technologies, eds. G. Vander Voort, J. Friel, ASM International, Materials Park, Ohio, 1996, pp 103-110.

[24] **T. Ungár**, *Dislocation densities, arrangements and character from X-ray diffraction experiments*, Mater. Sci. Eng., A 309-310 (2001) 14-22.

[25] **G. Maeder, J.L. Lebrun, J.M. Sprauel**, *Present possibilities for the X-ray diffraction method of stress measurement*, NDT Int. 14(5) (1981) 235-247.

[26] **B. Hoffmann, 0. Vijhringer, E. Macherauch**, *Effect of tempering on the microstructure and strength of martensitically hardened plain carbon steels*, Mater. Sci. Eng. A 234-236 (1997) 707-710.

[27] **M.B. Kerber, E. Schafler, M. Zehetbauer**, *Processing and evaluation of X-ray line profiles measured from nanostructured materials produced by severe plastic deformation*, Rev. Adv. Mater. Sci. 10(2005) 427-433.

[28] **K. Vijayan, A. Mani, C. Balasingh, A.K. Singh**, *X-ray analysis of polycrystalline aluminium subjected to fatigue cycling*, Bull. Mater. Sci. 10(3) (1998) 205-216.

[29] **P. Juijerm, I. Altenberger, B. Scholtes**, *Effect of Deep Rolling on the Fatigue Behavior of Under-, Peak- and Over-aged AA6110 at Room Temperature*, in: Proc. 9th International Conference and Exhibition on Shot Peening, Paris, 2005, pp. 302-307.

[30] **P. Juijerm, I. Altenberger, B. Scholtes**, *Fatigue and residual stress relaxation of deep rolled differently aged aluminium alloy AA6110*, Mater. Sci. Eng., A 426 (2006) 4-10.

[31] **P. Juijerm, I. Altenberger**, *Residual stress relaxation of deep rolled Al–Mg–Si–Cu alloy during cyclic loading at elevated temperatures*, Scr. Mater. 55 (2006) 1111-1114.

[32] **P. Juijerm, I. Altenberger**, *Effect of temperature on cyclic deformation behavior and residual stress relaxation of deep rolled under-aged aluminium alloy AA6110*, Mater. Sci. Eng., A 452-453 (2007) 475-482.

[33] **P. Juijerm, U. Noster, I. Altenberger, B. Scholtes**, *Fatigue of deep rolled AlMg4.5Mn (AA5083) in the temperature range 20–300°C*, Mater. Sci. Eng., A 379 (2004) 286-292.

[34] **P. Juijerm, I. Altenberger**, *Cyclic Deformation Behaviour and Its Optimization at Elevated Temperature*, in: Aluminium Alloys, Theory and Applications, ed. Tibor Kvackaj, InTech, 2011, pp. 183-198.

[35] **B.L. Boyce, X. Chen, J.O. Peters, J.W. Hutchinson, R.O. Ritchie**, *Mechanical relaxation of localized residual stresses associated with foreign object damage*, Mater. Sci. Eng., A 349 (2003) 48-58.

[36] **H. Holzapfel, V. Schulze, O. Vöhringer, E. Macherauch**, *Residual stress relaxation in an AISI 4140 steel due to quasistatic and cyclic loading at higher temperatures*, Mater. Sci. Eng., A 248 (1998) 9-18.

[37] **A. Wick, V. Schulze, O. Vöhringer**, *Effects of warm peening on fatigue life and relaxation behaviour of residual stresses in AISI 4140 steel*, Mater. Sci. Eng., A 293 (2000) 191-197.

[38] **K. Dalaei, B. Karlsson, L.-E. Svensson**, *Stability of residual stresses created by shot peening of pearlitic steel and their influence on fatigue behavior*, Procedia Engineering 2 (2010) 613-622.

[39] **K. Dalaei, B. Karlsson, L.-E. Svensson**, *Stability of shot peening induced residual stresses and their influence on fatigue lifetime*, Mater. Sci. Eng., A 528 (2011) 1008-1015.

[40] **A. Cherif, Y. Pyoun, Scholtes**, *Effects of Ultrasonic Nanocrystal Surface Modification (UNSM) on Residual Stress State and Fatigue Strength of AISI 304*, J. Mater. Eng. Perform. 19(2) (2010) 282-286.

[41] **I. Nikitin, M. Besel**, *Correlation between residual stress and plastic strain amplitude during low cycle fatigue of mechanically surface treated austenitic stainless steel AISI 304 and ferritic–pearlitic steel SAE 1045*, Mater. Sci. Eng., A 491 (2008) 297-303.

[42] **I. Nikitin, M. Besel**, *Residual stress relaxation of deep rolled austenitic steel*, Scr. Mater. 58 (2008) 239-242.

[43] **I. Nikitin, I. Altenberger**, *Comparison of the fatigue behavior and residual stress stability of laser-shock peened and deep rolled austenitic stainless steel AISI 304 in the temperature range 25-600°C*, Mater. Sci. Eng., A 465 (2007) 176-182.

[44] **I. Nikitin, B. Scholtes, H.J. Maier, I. Altenberger**, *High temperature fatigue behavior and residual stress stability of laser-shock peened and deep rolled austenitic steel AISI 304*, Scr. Mater. 50 (2004) 1345-1350.

[45] **Y. Akiniwa, S. Machiya, K. Tanaka**, *Fatigue damage evaluation in SiCp/2024 by X-ray diffraction method*, Int. J. Fatigue 28 (2006) 1406-1412.

[46] **Y. Akiniwa, S. Machiya, H. Kimura, K. Tanaka, N. Minakawa, Y. Morii, T. Kamiyama**, *Evaluation of material properties of SiC particle reinforced aluminum alloy composite using neutron and X-ray diffraction*, Mater. Sci. Eng., A 437 (2006) 93-99.

[47] **D.J., Quesnel, M. Meshii, J.B. Cohen**, *Residual stress in high strength low alloy steel during low cycle fatigue*, Mater. Sci. Eng. 36 (1978) 207-215.

[48] **S. Dorn, T. Hirsch, P. Mayr**, *Structural alterations of local damage in ball bearings subjected to rolling contact fatigue*, Mater. Sci. Eng., A 189 (1994) 181-189.

[49] **M. Krauss, B. Scholtes**, *Thermal shock damage of hot-work tool steel AISI H11 in hard turned, electroeroded, shot peened or deep rolled surface conditions*, J. Mater. Sci. Technol. 20(1) (2004) 93-96.

[50] **M.J. Hadianfard**, *Low cycle fatigue behavior and failure mechanism of a dual-phase steel*, Mater. Sci. Eng., A 499 (2009) 493-499.

[51] **I.F. Pariente, M. Guagliano**, *Contact fatigue damage analysis of shot peened gears by means of X-ray measurements*, Eng. Fail. Anal. 16 (2009) 964-971.

[52] **H. Yaguchi, H. Mitani, K. Nagano, T. Fujii, M. Kato**, *Fatigue-damage evaluation in aluminum heat-transfer tubes by measuring dislocation cell-wall thickness*, Mater. Sci. Eng., A 315 (2001) 189-194.

[53] **K.B. Yoo, K.T. Hwang, J.C. Chang, J.H. Kim**, *Residual Stress Evaluation and Fatigue Life Prediction in the Welded Joint by X-ray Diffraction*, in: Proc. 2nd International Conference on Smart Materials and Nanotechnology in Engineering, SPIE, Weihai, eds. J. Leng, A.K. Asundi, W. Ecke, 2009, pp. 749374-1-7.

[54] **R.K. Nalla, I. Altenberger, U. Noster, G.Y. Liu, B. Scholtes, R.O. Ritchie**, *On the influence of mechanical surface treatments-deep rolling and laser-shock peening-on the fatigue behavior of Ti-6Al-4V at ambient and elevated temperatures*, Mater. Sci. Eng., A 355 (2003) 216-230.

[55] **P.M. Fourspring, R.N. Pangborn**, *An X-ray diffraction study of microstructural deformation induced by cyclic loading of selected steels*, Fatigue Fract. Mech., ASTM STP 1321, v. 28, eds. J.H. Underwood, B.D. Macdonald, M. R. Mitchell, American Society for Testing and Materials, New York, 1997.

[56] **A. Olchine, H. Stamm, F. dos Santos Marques**, *Fatigue damage monitoring of laser surface treated steel by x-ray diffraction methods*, Surf. Eng. 14(5) (1998) 386-390.

[57] **A. Dias, J.L. Lebrun, G. Maeder, H.P. Lieurade**, *Etude de l'endommagement en fatigue thermique par diffractometrie X*, pp. 113-126.

[58] **S. Taira**, *X-ray examination during fatigue*, Met. Sci. 8 (1974) 234-236.

[59] **A. Evans, S-B. Kim, J. Shackleton, G. Bruno, M. Preuss, P.J. Withers**, *Relaxation of residual stress in shot peened Udimet 720Li underhigh temperature isothermal fatigue*, Int. J. Fatigue 27 (2005) 1530-1534.

[60] **O.S. Zaroog, A. Ali, B.B. Sahari, R. Zahari**, *Modeling of residual stress relaxation of fatigue in 2024-T351 aluminium alloy*, Int. J. Fatigue 33 (2011) 279-285.

[61] **O.S. Zaroog, A. Ali, B.B. Sahari, R. Zahari**, *Relaxation of residual stress. Part 2: Relaxation of stage 2*, American J. of Eng. Appl. Sci. 2(4) (2009) 759-763.

[62] **I. Nikitin, I. Altenberger, B. Scholtes**, *Effect of Deep Rolling at Elevated and Low Temperatures on the Isothermal Fatigue Behavior of AISI 304*, Proc. 9th International Conference on Shot Peening, ICSP9, Paris, 2005, pp. 185-190.

[63] **R.N. Pangborn, S. Weissmann, I.R. Kramer**, *Prediction of fatigue life by X-ray diffraction methods*, Fat. Eng. Mater. Struct, 1 (1979) 363-369.

[64] **P. Juijerm, I. Altenberger**, *Fatigue behavior of deep rolled Al–Mg–Si–Cu alloy at elevated temperature*, Scr. Mater. 55 (2006) 943-946.

[65] **U. Martin, I. Altenberger, B. Scholtes, K. Kremmer, H. Oettel**, *Cyclic deformation and near surface microstructures of normalized shot peened steel SAE 1045*, Mater. Sci. Eng., A 246 (1998) 69-80.

[66] **D. Löhe, O. Vöhringer**, *Stability of Residual Stresses, in: ASM International Handbook of Residual stress and Deformation of Steel*, eds. G. Totten, M. Howes, T. Inoue, ASM International, Materials Park, Ohio, 2002, pp. 54-69.

[67] **K. Tanaka**, *Recent x-ray diffraction studies of metal fatigue in Japan*, J. Strain Anal. 10(1) (1975) 32-41.

[68] **T. Goto**, *Material strength evaluation and damage detection by X-ray diffraction*, Adv. X Ray Anal. 35 (1992) 489-501.

[69] **R. Lemaitre, J.-L. Lebrun, J. Maeder**, *Contraintes Résiduelles et Fatigue*, in: Matériaux et Techniques, 70 (1982) 297-304.

[70] **D. Chicot, J. Lesage**, *Diffraction X et Modifications Microstructurales en Cours de Fatigue, X-ray Diffraction and Microstructural Modifications during Fatigue*, Proc. Innovation Technologique pour les Transports Terrestres, Technological Innovation for Land Transportation, TILT 2003, Lille, 2003, pp. 803-810.

[71] **J. Lesage, D. Chicot, G. Mesmacque**, *Etude par Diffraction des Rayons X des Modifications Microstructurales Intervenant au cours de la Fatigue d'aciers Durcis Superficiellement*, Proc. Symposium Franco-Brésilien sur la Science des Matériaux, Ouro Preto, 1992.

[72] **G.E. Dieter**, Mechanical Metallurgy, SI Metric ed., McGraw-Hill, London, 1988.

[73] **J.E. Shigley, C.R. Mischke**, Mechanical Engineering Design, 6th ed., McGraw-Hill, New York, 2001.

[74] **D. Löhe, O. Vöhringer**, *Residual Stresses and Fatigue Behavior*, in: ASM International Handbook of Residual stress and Deformation of Steel, eds. G. Totten, M. Howes, T. Inoue, ASM International, Materials Park, Ohio, 2002, pp. 27-53.

[75] **P.J.E. Forsyth**, *Fatigue damage and crack growth in aluminium alloys*, Acta Metall. 11 (1963) 703-715.

[76] **H. Mughrabi**, *Cyclic plasticity of matrix and persistent slip bands in fatigued metals*, eds. O. Brulin, R.K.T. Hsieh, North-Holland, Proc. 4th International Conference on Continuum Models of Discrete Systems, Stockholm, 1981, pp. 241-257.

[77] **A.H. Cottrell, D. Hull**, *Extrusion and intrusion by cyclic slip in copper*, Proc. R. Soc. of London, Series A, Mathematical and Physical Sciences, The Royal Society, London, 1957, v. 242, pp. 211-213.

[78] **W.A. Wood**, Bull. Inst. Met., 3 (1955) 5-6.

[79] **R.W. Cahn, P. Haansen**, Physical Metallurgy, v. 3, 4 ed., Elsevier Science, Amsterdam, 1996.

[80] **M. Bao-Tong, C. Laird**, *Overview of fatigue behavior in copper single crystals-I. Surface morphology and stage I crack initiation sites for tests at constant strain amplitude*, Acta Metall. 37(2) (1989) 325-336.

[81] **G.R. Irwin**, *Analysis of stresses and strains near end of crack traversing plate*, American Society of Mechanical Engineers, J. Appl. Mech. 24(3) (1957) 361-364.

[82] **M.A. Miner**, *Cumulative damage in fatigue*, J. Appl. Mech. 12 (1945) 159-164.

[83] **J.L. Chaboche, P.M. Lesne**, *A non-linear continuous fatigue damage model*, Fatigue Fract. Eng. Mater. Struct. 11(1) (1988) 1-17.

[84] **W.D. Callister Jr.**, Materials Science and Engineering: An Introduction, 7th ed., John Wiley & Sons, New York, 2001.

[85] **B. E. Warren, B. L. Averbach**, *The effect of cold-work distortion on X-ray patterns*, J. Appl. Phys. 21 (1950) 595-599.

[86] **T Ungár, S. Ott, P.G. Sanders, A. Borbely, J.R. Weertman**, *Dislocations, grain size and planar faults in nanostructured copper determined by high resolution X-ray diffraction and a new procedure of peak profile analysis*, Acta Mater. 46 (1998) 3693-3699.

[87] **G.K. Williamson, W.H. Hall**, *X-ray line broadening from filed aluminium and wolfram*, Acta Metall. 1 (1953) 22-31.

[88] **A. Boberly, J.H. Driver**, *Dislocation measurements by X-ray profile analysis in texture components of deformed metals*, Arch. Metall. Mater. 50(1) (2005) 65-76.

[89] **A.J.C. Wilson**, *On variance as a measure of line broadening in diffractometry general theory and small particle size*, Proc. Phys. Soc. 80 (1962) 286-294.

[90] **I. Groma**, *X-ray line broadening due to an inhomogeneous dislocation distribution*, Phys. Rev. B 57(13) (1998) 7535-7542.

[91] **L.V. Azaroff**, Elements of X-ray Crystallography, Mc Graw-Hill, New York, 1968, pp. 549-558.

[92] **B.E. Warren**, X-ray diffraction, Dover Publications, New York, 1990, pp. 251-252.

[93] **E.J. Mittemeijer**, *The relation between residual macro- and microstress and mechanical properties of case-hardened steels*, Proc. 3rd International Congress on Heat Treatment of Materials, Shangai, 1983, pp. 161-187.

[94] **J. Barralis, L. Castex, J.C. Chaize**, *Influence des conditions de traitement sur la distribution des phases et des contraintes résiduelles dans les couches nitrurées*, Mém. Et. Sci. Rev. Mét. 83 (1986) 629-641.

[95] **N. Ji, J.L. Lebrun, H.P. Lieurade**, *Etude de la microstructure d'un acier eutectoïde déformé par traction monotone ou par fatigue oligo-cyclique en utilisant la technique de l'analyse des profils de raies de diffraction X*, Méc. Matér. Electr. 433 (1990) 32-37.

[96] **ASTM International**, Standard Test Methods for Tension Testing of Metallic Materials, ASTM Standard E 8M-04, West Conshohocken, USA, 2004.

[97] **D. Tabor**, *The hardness and strength of metals*, J. Inst. Met. 79 (1951) 1-18.

[98] **J.R. Cahoon**, *An improved equation relating hardness to ultimate strength*, Metall. Trans. 3 (1972) 3040.

[99] **J. Moteff, R.K. Bhargava, W.L. McCullough**, *Correlation of the hot-hardness with the tensile strength of 304 stainless steel to temperatures of 1200°C*, Metall. Trans. A 6A (1975) 1101-1104.

[100] **H.E. Boyer, T.L. Gall** (eds.), Metals Handbook, ASM International, Metals Park, Ohio, 2005.

[101] **I. Brooks, P. Linb, G. Palumbo, G.D. Hibbard, U. Erb**, *Analysis of hardness–tensile strength relationships for electroformed nanocrystalline materials*, Mater. Sci. Eng., A 491 (2008) 412-419.

[102] **C. Schenck**, Wechselbiegemaschine PWON, Maschinenfabrik GmbH, Darmstadt, Germany, 1971.

[103] **F. Yang, J.Q. Jiang, F. Fang, Y. Wang, C. Ma**, *Rapid determination of residual stress profiles in ferrite phase of cold-drawn wire by XRD and layer removal technique*, Mater. Sci. Eng., A 486 (2008) 455-460.

[104] **AFNOR**, Association Française de Normalisation, Essais non destructifs – Méthodes d'essais pour l'analyse des contraintes résiduelles par diffraction des rayons X, XP A 09-285, Paris, 1999.

[105] **W.D. Pilkey**, Peterson's Stress Concentration Factors, 2nd ed., John Wiley & Sons, New York, 1997.

[106] **J.A Graham**, SAE Fatigue Design Handbook, Society of Automotive Engineers, New York, 1968.

[107] **C.S. Vianna**, Mechanical Behavior of the API 5L X-60 Steel with and without Hydrogen, M.Sc. Thesis, COPPE/UFRJ, Rio de Janeiro, Brazil, 2005.

[108] **H. Hamdi, H. Zahouani, J.-M. Bergheau**, *Residual stresses computation in a grinding process*, J. Mater. Process. Technol. 147 (2004) 277-285.

[109] **T. Nguyen, L.C. Zhang**, *An assessment of the applicability of cold air and oil mist in surface grinding*, J. Mater. Process. Technol. 140 (2003) 224-230.

[110] **ABAQUS**, User's and Theory Manuals, Release 6.8, Hibbitt, Karlsson, Sorensen, Inc, USA, 2008.

[111] **FEI Company**, Focused ion beam technology, capabilities and applications, 2006 (available in http://www.fei.com/).

[112] **M. Hradilova, A. Jäger, T. Vystavel, P. Lejcek**, *3D Characterization of Material Structure Using Scanning Electron Microscopy and Focused Ion Beam*, in: Proc. Metal 2010, Rožnov pod Radhoštěm, Česká republika, 2010.

Titre :

ETUDE PAR DIFFRACTION DES RAYONS X DES MODIFICATIONS MICROSTRUCTURALES EN COURS DE FATIGUE

Title:

X-RAY DIFFRACTION STUDY OF MICROSTRUCTURAL CHANGES DURING FATIGUE

Résumé :

Le travail présenté ici a pour but d'évaluer les mécanismes microstructuraux liés à l'amorçage de l'endommagement par fatigue d'un acier à usage pétrolier. Les microdéformations et les contraintes résiduelles (macrocontraintes) ont été déterminées par diffraction des rayons X en temps réel pendant des essais de fatigue en flexion alternée sur des éprouvettes plates prélevées dans la paroi d'un tube neuf. Les microdeformations sont estimées à partir de mesures de la largeur de corde à mi-hauteur (LCMH) d'un pic de diffraction et les contraintes résiduelles à partir du déplacement du pic. Les essais de fatigue sont réalisés pour cinq niveaux de contraintes différents. On observe trois stades de variation pendant l'évolution des microdeformations. On montre que leur amplitude et leur durée sont proportionnelles au niveau de contrainte alternée. Des variations similaires sont observées pour les contraintes résiduelles, avec des durées identiques à celles des microdéformations. Des évolutions dans la densité et la répartition des dislocations ont été observées par microscopie électronique en transmission à l'aide de la technique du faisceau d'ions focalisés. Pour comprendre le rôle de la structure initiale, des essais de fatigue sur éprouvettes recuites ont été réalisés dans les mêmes conditions d'essai. Là encore trois stades d'évolution sont observés mais avec un premier stade inversé du fait de l'état initial du réseau de dislocations. Les résultats obtenus sont très encourageants pour la prise en compte des évolutions microstructurales dans l'établissement d'un futur indicateur de dommage de la phase d'amorçage en fatigue à grand nombre de cycles des matériaux.

Abstract:

The present work aims to evaluate the microstructural mechanisms associated with the initiation of fatigue damage of steels used in the petroleum industry. Microdeformations and residual stresses (macrostresses) were evaluated by X-ray diffraction in real time during alternating bending fatigue tests performed on flat test pieces taken from a pipe sample. Microdeformations were estimated from measurements of the full width at half maximum (FWHM) of the diffraction peak and residual stresses from the peak displacement. The fatigue tests were performed at five different stress levels. Three stages of changes during the evolution of microdeformation were detected. We show that their amplitude and duration are proportional to the level of alternating stress. Similar variations were observed for the residual stresses, with duration identical to those of the microdeformation. Changes in the density and distribution of dislocations were observed by transmission electron microscopy using the technique of focused ion beam. To understand the role of the initial structure, fatigue tests on annealed samples were performed under the same test conditions. Again, three stages of changes are observed but with an increase of the microdeformations instead of a decrease during the first stage due to the initial state of the dislocation network. The results are very encouraging for the consideration of the microstructural evolutions in the construction of a future counter of fatigue damage initiation in materials.

Mots-clés :

Fatigue ; Fatigue à grand nombre de cycles ; Amorçage de l'endommagement par fatigue ; Diffraction des rayons X ; Largeur de corde a mi-hauteur ; Microdéformations, Contraintes résiduelles ; Acier API 5L X60 ; Pipelines

Keywords:

Fatigue; High cycle fatigue; Fatigue damage initiation; X-ray diffraction; Full width at half maximum; Microdeformations; Residual stresses; API 5L 60 grade steel; Pipelines

Encadrements : Professeurs Jacky LESAGE et Noureddine BENSEDDIQ